Measuring Nanoscale Exciton Transport and Carrier Recombination in Organic Solar Cells

A DISSERTAION

SUBMITTED TO THE FACULTY OF THE

UNIVERSITY OF MINNESOTA

BY

Ian John Curtin

IN PARTIAL FULFILLMENT OF THE REQUIREMENTS

FOR THE DEGREE OF

DOCTOR OF PHILOSOPHY

Russell J. Holmes, Advisor

August 2018

Acknowledgements

I would first like to acknowledge my advisor, Russ Holmes, whose passion for research is inspiring and provided me with the fortitude to be successful throughout this experience. His guidance, support, and mentorship has molded me both personally and professionally in ways that will stay with me for the rest of my life. The members of the Holmes group, both past and present, deserve recognition for their help in lab, camaraderie, and thoughtful discussion – Nick, Matt, Tyler, Yunlong, Nathan, Yi, Meng, Tom, Kyle, Abbey, Gang, Tao, Deepesh, Catherine, John, and Kaicheng. I would especially like to thank those who contributed directly to the work presented in this dissertation, Tyler, Tao, and Kaicheng, as well as Matt, whose mentorship over my first two years was truly invaluable. Successful research requires many areas of expertise and I would like to thank the people who collaborated with this work, Wayne Blaylock and Professor David Blank and his research group, for helping me gain a deeper understanding of my own work with tools, measurements, and perspectives that I would not have otherwise had access to. Bob and Beverley Sundahl generously supported me throughout my Ph.D. with the Sundahl Fellowship. The few times I got to meet Bob his unique perspective challenged me to think about science and life in a more pragmatic way. Lastly, I need to thank my family Rita, Deane, Evan, Brogan, and Emily. I would not have been able to get through this experience or get to where I am today without their constant love and support.

This dissertation is dedicated to my family – Rita, Deane, Evan, Brogan and Emily

Abstract

Organic photovoltaic devices (OPVs) have the potential to provide low cost solar energy to unique applications which are not accessible by traditional photovoltaics. These devices are made from abundant materials and can be deposited on lightweight flexible substrates with low cost roll-to-roll manufacturing techniques. However, to date they have suffered from relatively low power conversion efficiencies compared to their inorganic counterparts. As such, a deeper understanding of the fundamental processes which govern photoconversion in OPVs is needed in order to better inform materials and device design and realize more efficient devices. Optical absorption in OPVs leads to the formation of Coulombically bound electron-hole pairs, called excitons, which must be dissociated into free carriers to collect photocurrent. Inefficiencies in these devices result from the short diffusion length (L_D) of excitons and the subsequent recombination of generated carriers. In this dissertation, material parameters which affect the magnitude of L_D and new techniques to quantify and decouple transport and recombination mechanisms will be presented. Covered topics include the effects of molecular impurities on L_D, techniques to measure L_D and the exciton lifetime in previously inaccessible dark (non-luminescent) materials through photovoltage measurements, methodologies to quantitatively decouple recombination mechanisms at device relevant operating conditions, and the effects of polycrystalline grain size on L_D in singlet fission materials, which are capable of producing two excitons per absorbed photon. These studies provide tools to better understand the underlying physics which govern photoconversion and material parameters which can be manipulated to enhance exciton transport to realize more efficient devices.

Table of Contents

List of Tables

List of Figures

List of Abbreviations

η_A ……Absorption efficiency

η_{CS} ……Charge separation efficiency

η_{CT} …… Charge transfer efficiency

η_D …….. Diffusion efficiency

η_{EQE} ……. External quantum efficiency

η_{FC} ……..….. Free carrier collection efficiency

η_{PL} …… Photoluminescence efficiency

λ ….……... Wavelength of light

τ ……..… Exciton lifetime

Al…….... Aluminum

BHJ ……..……. Bulk heterojunction

BCP …….. Bathocuproine

CT state …….. Charge-transfer state

CuPc……..... Copper phthalocyanine

D... …….. Diffusivity

D-A ……...…. Donor-Acceptor

FF…….. Fill factor

HATCN ……..... Dipyrazino[2,3-f:2',3'-h]quinoxaline-2,3,6,7,10,11-hexacarbonitrile

HOMO…….. Highest occupied molecular orbital

ITO……. Indium tin oxide

J_{SC}……..... Short-circuit current density

k_B…….….. Boltzmann constant

k_{fis} …….. Rate of singlet fission

k_{fus}…… Rate of triplet fusion

k_{NR}.... ……..... Non-radiative exciton decay rate

k_R…….. Radiative exciton decay rate

L_D……... Exciton diffusion length

LUMO……... Lowest unoccupied molecular orbital

OPV……...…….. Organic photovoltaic device

PHJ…….. Planar heterojunction

PL……Photoluminescence

S_0……...… Singlet ground state

S_1……...… First excited singlet state

SubPc……..... Boron Subphthalocyanine Chloride

T_1…… First triplet excited state

V_{OC}……... Open-circuit voltage

1. Introduction to photovoltaics

1.1 Generation of electricity and global climate change

Modern society has a dependence on electricity which has led to global climate change, causing a multitude of adverse environmental effects. The combustion of fossil fuels has led to dramatic increases in greenhouse gasses in the atmosphere. According to the Intergovernmental Panel on Climate Change, CO_2 levels in the atmosphere have increased from 280 ppm to over 400 ppm over the last 150 years, exceeding the highest levels of atmospheric CO_2 in centuries.[1] The energy and heating sector is responsible for 25% of these emissions due to the burning of coal, oil, and natural gas. This has caused the average surface temperature of the earth to rise by about 2.0 degrees Fahrenheit since the late 19th century, a trend which is only accelerating. Current projections suggest an increase of 6.7 to 8.6 degrees Fahrenheit could occur by year 2100; furthermore 16 of the last 17 years have been the hottest on record.[1,2] This has caused a variety of environmental problems including, but not limited to, the shrinking of polar ice caps, causing rises in the sea level, the warming and acidification of the earth's oceans, and an increase in the frequency and intensity of extreme weather events.[1,2] These problems are only projected to get worse unless a dramatic shift to low-carbon and renewable energy sources occurs over the next century.[1]

Compounding these issues is the growing demand for electricity. In 2015 the global power consumption was around 22 TW and is projected to increase to 25 TW by 2040, with the majority of this increase coming from developing countries.[3] With the intrinsically limited supply of fossil fuels the development of renewable energy technologies is imperative to meeting this demand. The production of electricity from photovoltaic

devices, which harness energy from the sun to produce electricity, has the potential to be a major part of this solution.

The sun continuously delivers 174000 TW to the earth's upper atmosphere at a power density of 1366 W m^{-2}.[4] When light reaches the earth's surface, this value is reduced to about 1000 W m^{-2} due to absorption and scattering of light traveling through the atmosphere. Taking into account seasonal variations, the diurnal nature of sunlight, and weather related cloud coverage, an average of 188 W m^{-2} or 4.5 kWh m^{-2} is incident at the average latitude of the continental U.S. (38 ºN).[5] With current commercially available photovoltaic panels it would only take an area of 17,500 sq. mi, or roughly 0.6% of the surface area of the continental United States, to produce the 4,000 TWh necessary to provide electricity to the entire country for the year.[6] While this calculation is impractical for a variety of reasons, including the intermittency of solar electricity generation and electrical transmission limitations, it highlights the vast potential for photovoltaic installations to be a major part of the global energy solution.

1.2 The photovoltaic market

Even with this vast potential, the deployment of solar energy is relatively small. In 2015 renewable energy sources generated only 7.12% of the total electrical production in the United States and solar energy constituted only 0.61%. This is because energy production is cost driven industry and renewable energy technologies must be able to compete financially with traditional fossil fuel sources on a $/kWh basis. For photovoltaics this is calculated by the levelized cost of energy, which is determined from the ratio of the life cycle cost of the module to the total amount of energy produced, including costs associated with construction, operation, maintenance, and decommission.[7] This will depend on the

lifetime of the solar cell, its efficiency, cost of manufacturing, cost of hardware, and soft costs, such as labor and overhead.

In the United States, the average cost of energy from a utility company is currently \$0.13/kWh residentially and \$0.11/kWh commercially.[8] A recent economic analysis of solar electricity estimates that unsubsidized photovoltaic installations in the United States range from about \$0.11-0.16/kWh for utility scale systems and \$0.19-0.29/kWh for residential systems.[9] With federal tax subsidies, these numbers can be reduced to \$0.07-0.13/kWh for utility and \$0.12-0.23/kWh for residential, nearing a price point necessary to be competitive with traditional energy technologies.[9] This has caused a tremendous amount of growth in the market over the last two decades, where the globally installed solar photovoltaic capacity has increased from 4 to 227 GW from 2000-2015.[10]

Currently, the photovoltaic market is dominated by crystalline silicon technologies, which controlled 90% of the marketplace in 2014.[5] However, this technology is starting to reach a fundamental limit, as the cost is dominated not by the price of the panels, but by balance of system costs including hardware, inverters, wiring, racking, and labor, which constitutes 80% of residential and 60% of utility scale system costs.[9] Additionally, recently imposed import tariffs on crystalline silicon photovoltaic panels threaten the technology's economic viability in United States.[11] Consequently, the need to develop next generation photovoltaic technologies is now more important now ever in order to ensure the continued growth of this renewable energy resource.

1.3 Emerging photovoltaic technologies

To reduce the levelized cost of energy research and development efforts of new technologies should focus on increasing device efficiencies, reducing the cell thickness,

both for reduced material costs and weight which will reduce the balance of system costs, improving device lifetimes, and reducing manufacturing complexity and costs.[5] There are a vast number of thin film technologies under development which aim to address these issues. Early research efforts focused on amorphous silicon, but this technology has not been able to achieve efficiencies high enough to compete with its crystalline predecessors. The most widely deployed commercially available thin film technology is cadmium telluride, which controlled 5% of the global PV market in 2013.[12] These devices have displayed record efficiencies of 21.0% in cells and 17.5% for modules, compared to 26.7% and 22.4% for cell and module efficiencies, respectively, for single crystalline silicon.[12] However, large scale deployment of this technology is affected by the toxicity of cadmium and scarcity of tellurium.[5] The next major technology in the thin film market is copper indium gallium diselenide which controlled a 2% market share of the global photovoltaic market in 2013.[12] This technology has achieved cell and module efficiencies of 21.7% and 17.5%, respectively, but worry about the scarcity of indium could hinder large scale development.[12] Of the emerging thin film technologies, metal-halide perovskites have shown perhaps the most promise, demonstrating rapid increases in efficiency over the last few years, with certified lab scale efficiencies of 22.1%.[13] These devices have tunable band gaps and can be deposited from solution or low temperature vapor deposition, but are highly sensitive to moisture and currently contain toxic lead compounds.

1.4 Organic photovoltaics

Organic photovoltaic devices (OPVs) are made out of small molecule or polymer organic semiconductors. These synthetic materials have high absorption coefficients, which can be tuned throughout the visible light spectrum, allowing for thin active layers

on the order of tens of nanometers.[14–16] Additionally, they are compatible with high-throughput, large area, roll-to-roll processing techniques and can be deposited out of solution or low temperature evaporation on cheap flexible plastic substrates.[15,17–19] Furthermore, the active materials can be synthesized from non-toxic, abundant feedstock.[20] These materials also have a high defect tolerance, allowing for facile fabrication of multijunction cells with broad absorption across the visible spectrum.[21,22] However, current efficiencies lag behind their inorganic counterparts as the record efficiency for a multijunction OPV is 13.2%.[23] Additionally, these devices traditionally suffer from relatively short device lifetimes and issues with device yield and scaling.[19] With that being said, significant progress has been made to address these issues. Heliatek, one of the leading commercial OPV manufacturers currently produce module efficiencies at 7-8% with extrapolated lifetimes of >25 years.[23]

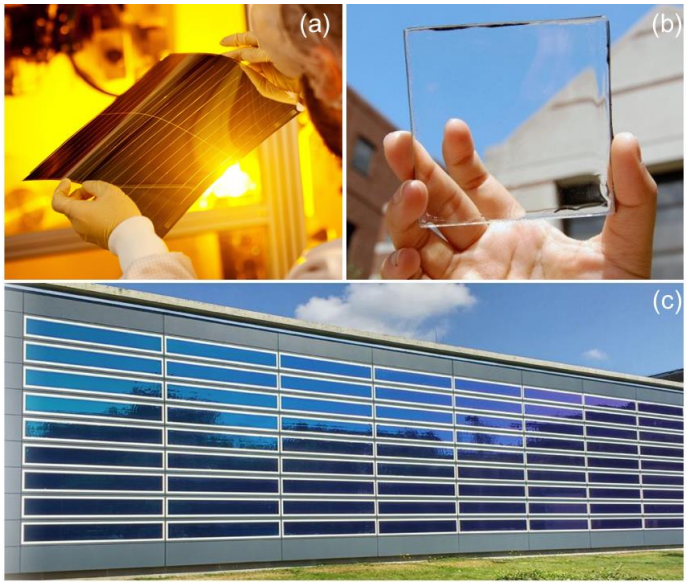

Figure 1.1 Organic photovoltaic devices displaying (a) flexible form factors (Heliatek),[23] (b) transparent (Ubiquitous Energy),[25] and (c) building integrated applications (Heliatek).[23]

Current efficiency trends suggest OPVs are not going to replace rooftop solar; however, their unique characteristics allow them to penetrate markets which are not accessible by traditional photovoltaics. For example, there are a variety of companies starting to come to market which aim to manufacture visibly transparent OPVs which absorb UV and infrared

light.[24,25] These devices can then be used in building integrated applications such as window coatings which generate electricity and passively cool the building. This same sort of technology can also be implemented into electronic devices like mobile phones, smartwatches, or even electric cars to constantly charge and extend battery life. The flexible form factor also allows for the potential of photovoltaic textiles for off the grid applications. With this technology nearing the point of commercialization, the market will ultimately test whether OPVs can be a commercially viable technology.

1.5 Scope of this dissertation

This dissertation is focused on understanding the underlying physics of OPV device operation by elucidating and decoupling the various recombination losses which limit the performance of small molecule OPVs. First, an introduction into the physical properties which produce the semiconducting behavior of OPV active materials will be discussed. This is followed by an in depth look into how optically generated excited states, called excitons, are transported in organic semiconductors. Once these fundamental concepts have been established, the implementation of organic semiconductors into OPV device architectures, the operation of these devices, and methods to characterize various aspects of their performance will be presented. The remainder of the dissertation presents specific studies which focus on how material properties can be manipulated to optimize the transport of excitons and the development of new techniques to characterize transport and recombination losses in these devices with the goal of providing a better understanding of device physics to enhance power conversion efficiencies of OPVs.

2. Physics of organic semiconductors

This chapter will provide a foundation for the work presented in this dissertation by giving insight into the fundamental properties of the materials which make up OPVs. First the bonding environment and energy levels of the materials which constitute organic semiconductors will be presented. This is followed by a discussion of the optical properties and generated excited states which, in part, dictate the performance of OPV devices. With this knowledge, a deeper understanding of how these materials can be combined to effectively harvest solar radiation and produce useable electricity in device architectures can be achieved.

2.1 Bonding and energy levels of organic semiconductors

Organic semiconductors are made of highly conjugated organic molecules, where alternating single and double covalent bonds give rise to their semiconducting behavior.[26] As organic materials, these molecules are made primarily out of carbon, which is a tetravalent atom with a $1s^2 2s^2 2p^2$ electron configuration.[27] In a molecule, carbon atoms will seek to create four covalent bonds with the surrounding atoms in order to achieve a closed electron shell configuration. The two main types of bonds that are present in these molecules are sigma (σ) bonds and pi (π) bonds. Sigma bonds arise from orbital hybridization, where the 2s, $2p_x$, and $2p_y$ orbitals hybridize to form three degenerate sp^2 orbitals which are coplanar and separated by 120°.[26,27] The remaining $2p_z$ orbital is perpendicular to the plane of the σ bonds and the overlap of these orbitals atoms form π bonds. While σ bonds confine the electron density between two atoms, π bonds form highly delocalized electron densities above and below the plane of atoms.[27] These can be

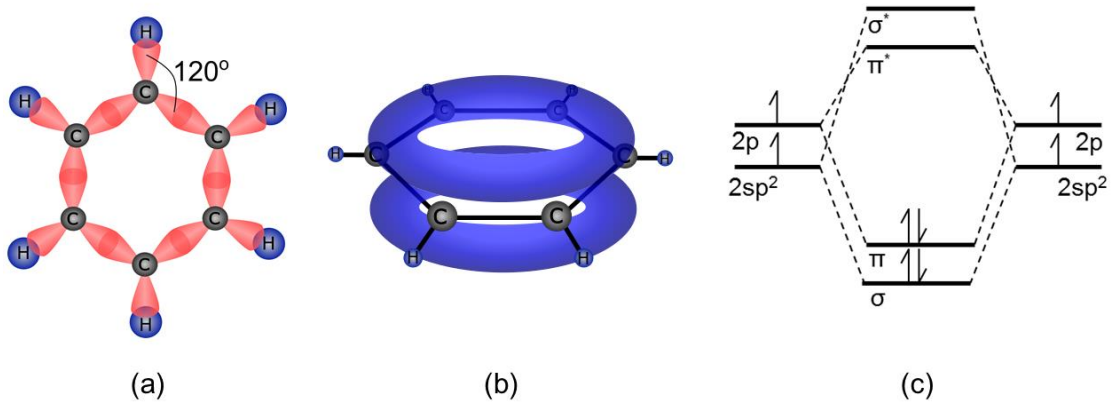

Figure 2.1 (a) Coplanar σ bonds between sp^2 hybrid orbitals in benzene. (b) π bonds form a delocalized electron density above and below the plane of atoms. (c) Electronic structure of a double bond between two carbon atoms, resulting in a filled bonding π orbital, called the highest occupied molecular orbital, separated by an energy gap from the anti-bonding π* orbital, referred to as the lowest unoccupied molecular orbital.

visualized in a benzene molecule, shown in Fig. 2.1a, b, consisting of a ring of six carbon atoms, where each carbon forms three σ bonds and one π bond, generating a delocalized electron cloud above and below the plane of atoms due to the overlap of π-orbitals between all of the carbon atoms.

When two electron wavefunctions overlap with one another the linear combination of the two wavefunctions forms two distinct energy levels, a low energy bonding state which shares the electron density between the two atoms, as described in the previous paragraph, and a higher energy anti-bonding state which creates a node in the electron densities between the two atoms.[27] An energy level diagram of a double bond between two carbon atoms is shown in Fig. 2.1c, where doubly occupied σ- and π-orbitals are separated by an energy gap from unfilled antibonding π* and σ* orbitals. The π-orbital is referred to as the highest occupied molecular orbital (HOMO), corresponding the ionization potential of the molecule, and the π*-orbital is referred to as the lowest unoccupied molecular orbital (LUMO), corresponding to the electron affinity.[28] When these molecules are incorporated into a thin film, the HOMO and LUMO can be thought of as analogous to the valence and

conduction bands in traditional inorganic semiconductors; however, it should be noted that they are not continuous bands, but rather discrete energy states, where the ensemble of excitonic energies have some finite energetic width.[29] As shown in Fig 2.1c, a covalent bond between two atoms forms two energy levels. In inorganic semiconductors, covalent bonds between *N* atoms will form *N* energy levels. As *N* becomes very large, continuous energy bands are formed. While covalent bonds between atoms form molecules, films of these molecules are bound together by weak van der Waals bonds, yielding a distribution of discrete HOMO and LUMO energies.[26] The semiconducting behavior of these materials is generated by electronic transitions which bridge the energy gap between the filled HOMO and empty LUMO combined with the overlap in the electron density of the π-orbitals between adjacent molecules, which provide a continuous pathway for electron transport.[26]

2.2 Exciton generation in organic semiconductors

In addition to the formation of discrete energy levels, another major difference between inorganic and organic semiconductors are the excited states which are generated from optical absorption. Generally for inorganic semiconductors, when a photon with energy greater than the band gap is absorbed a free electron is promoted to the conduction band, leaving behind a hole in the valence band.[30] Alternatively, when light is absorbed by an organic semiconductor and an electron is promoted from the HOMO to the LUMO of the molecule, the negatively charged electron and positively charged hole remain Coulombically bound to each other, creating what is called an exciton.[26] While an exciton technically refers to the total electronic structure of the excited molecule, it is easier in some respects to think of it as the bound charge neutral electron-hole pair.

The Coulomb force between two charged particles is inversely proportional to the dielectric constant of the surrounding medium, given by $\epsilon = \epsilon_R \epsilon_0$ where ϵ_R is the relative dielectric constant and ϵ_0 is the vacuum permittivity, and the square of the distance between the charged particles.[30] Both of these factors contribute to the formation of excitons. Organic semiconductors typically have low ϵ_R (~2-5) compared to inorganic semiconductors (~12-16).[31] This is partially due to the fact that organic semiconductors are primarily made up of atoms with low atomic numbers like hydrogen, carbon, and nitrogen which have strong electron binding energies and are less polarizable.[32] Additionally, the van der Waals forces which bind organic molecules together restrict the extent of the electron wavefunction compared to covalently bonded inorganic semiconductors, limiting the electron-hole separation.[29]

There are three types of excitons that exist in semiconducting materials which are characterized by the spatial extent of the electron-hole pair and the exciton binding energy. Wannier-Mott excitons are typically found in inorganic semiconductors and are characterized by a large exciton radius (~40 – 100 Å) and low binding energies. In silicon for example, the exciton binding energy is 14.7 meV.[30] These excitons are quickly dissociated into free carriers by the 25 meV of available thermal energy at room temperature. Charge-transfer excitons are found in highly crystalline organic semiconductors or at an interface between two energetically dissimilar materials and have an exciton radius on the order of a few molecular lengths (~5 – 20 Å).[26,33] Lastly, Frenkel excitons, which are the type of exciton which will be considered throughout this text, are confined to a molecule with a small exciton radius (< 5 Å) and a large binding energy ranging between ~0.4 - 1.4 eV.[26,28,34] The nature of the Frenkel exciton, including both the

binding energy and the distance over which they can travel, strongly dictates the architecture of OPV devices as will be outlined in the next chapter.

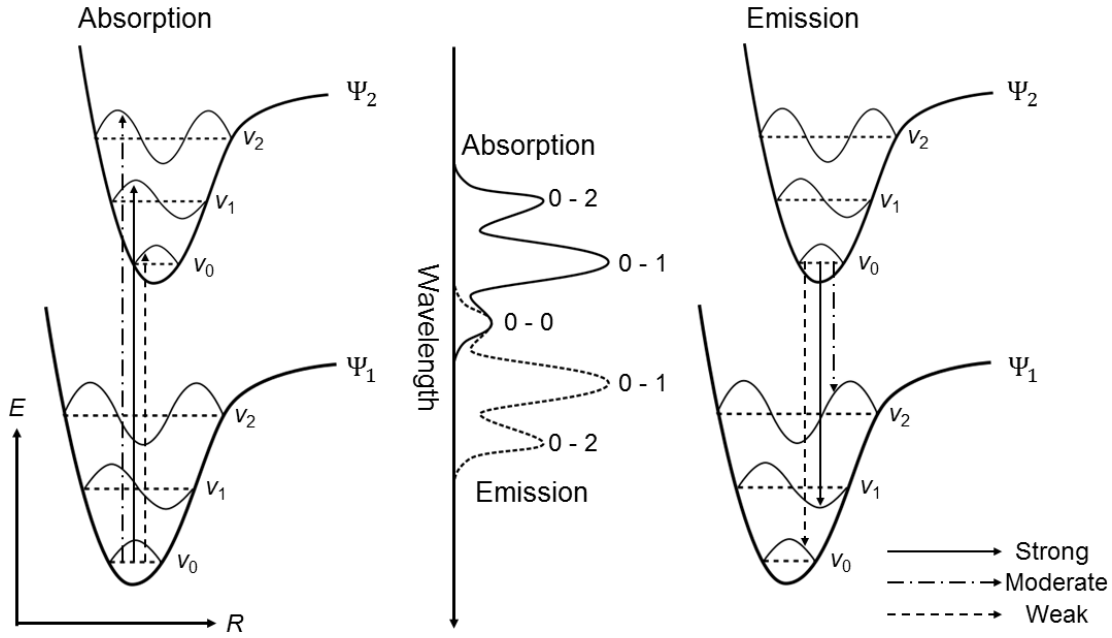

Figure 2.2 Vibronic energy levels as function of nuclear position (R). Electronic transitions between the ground state (Ψ_1) and first excited state (Ψ_2) give rise to the unique absorption and emission spectra of organic semiconductors. Absorption originates out of the lowest vibronic state (v_0) and the strength of the transition depends on the vibrational wavefunction overlap. Before emission occurs, molecules undergo vibronic relaxation and emit out of v_0 in Ψ_2, creating a shift between the emission and absorption spectra.

2.3 Absorption and emission

The previous section described the transition from a ground state to an excited state in a molecule as the promotion of electron from the HOMO to LUMO. Within each of these energy states, there exists a manifold of different vibrational energy states due to nuclear vibrational motion in the molecule, which generates the unique absorption and emission spectra of organic semiconductors.[28] Figure 2.2 shows a schematic of a molecular energy diagram where the ground state (Ψ_1) and first excited state (Ψ_2) wavefunctions are

represented as a function of nuclear coordinate. Within each of these energy levels the first three vibronic energy levels are shown and transitions between these levels correspond to absorption and emission from the molecule.

The Born-Oppenheimer approximation allows for electronic and vibrational wavefunctions, corresponding to electron and nuclear motion, respectively, to be treated separately when solving Schrödinger's equation.[28,30] In other words, nuclear motion is considered fixed when treating electron motion due to the fact that the nuclear mass is much larger than the electron mass. Consequently, electronic transitions are treated as instantaneous relative to changes in nuclear position and molecular energy states can be calculated as a function of nuclear position.[28] In Fig. 2.2, Ψ_1 and Ψ_2 correspond to the total wavefunction of the molecule, including both electron and vibrational wavefunctions. Vertical transitions correspond to electronic transitions, *i.e.* the promotion of electron from HOMO to LUMO and v_0, v_1, and v_2 correspond to the energies of the first three pictured nuclear vibrational wavefunctions.

When a photon is absorbed, the molecule transitions from Ψ_1 to Ψ_2. Absorption transitions generally occur out of the lowest vibrational energy state, v_0, since this is usually the most populated energy level in the ground state due to rapid vibronic relaxation.[28] The relative strength of the transitions between vibrational energy levels in Ψ_1 and Ψ_2 are dictated by the Franck-Condon principle. This principle states that the most probable transitions occur between energy levels where the overlap integral of the vibrational wavefunctions is maximized.[26,28] Equivalently, transitions will be the strongest between states that possess similar nuclear configurations and vibrational momentum. From Fig. 2.2, we see that the 0-1 transition maximizes the wavefunction overlap, producing stronger

transitions relative to 0-0 and 0-2, which is reflected in the strength of the absorption spectrum.

Similar rules govern radiative transitions from Ψ_2 to Ψ_1, which release energy in the form a photon. In this case, the crucial overlap occurs between v_0 in Ψ_2 and the vibrational energy levels of Ψ_1. This is due to the fact that electrons in higher energy states in Ψ_2 quickly undergo vibrational relaxation to the lowest vibrational energy level on time scales much faster the lifetime of the exciton (~10^{-15} – 10^{-12} s), known as Kasha's rule.[35] This causes luminescence to occur at a lower energy than absorption, generating a shift between the absorption and emission spectra known as a Franck-Condon shift.

2.4 Exciton spin

Excitons can exist in different spin states that can result in dramatic differences in their photophysical properties. In a simple explanation, the intrinsic angular momentum of an electron is described by its spin, which can either be spin up or spin down, taking on values of +½ or -½, respectively.[36] The Pauli Exclusion Principle states that electrons in a filled, doubly occupied orbital must have antiparallel spins, one spin up and one spin down, giving a net spin of zero.[27,28] However, when an exciton is formed, an electron is transferred to the empty LUMO of the molecule, leaving behind an unpaired electron in the HOMO. These two uncorrelated electrons need not obey the Pauli Exclusion Principle. If these two electrons have a net spin of zero, they are referred to as singlet excitons and if they have a net spin of one, they are referred to as triplet excitons.

The relation between these two electrons is more complicated than this simple explanation. Electron spin angular momentum is a quantized vectorial quantity which couples according to the rules of quantum mechanics.[28,37] For a single electron, the total

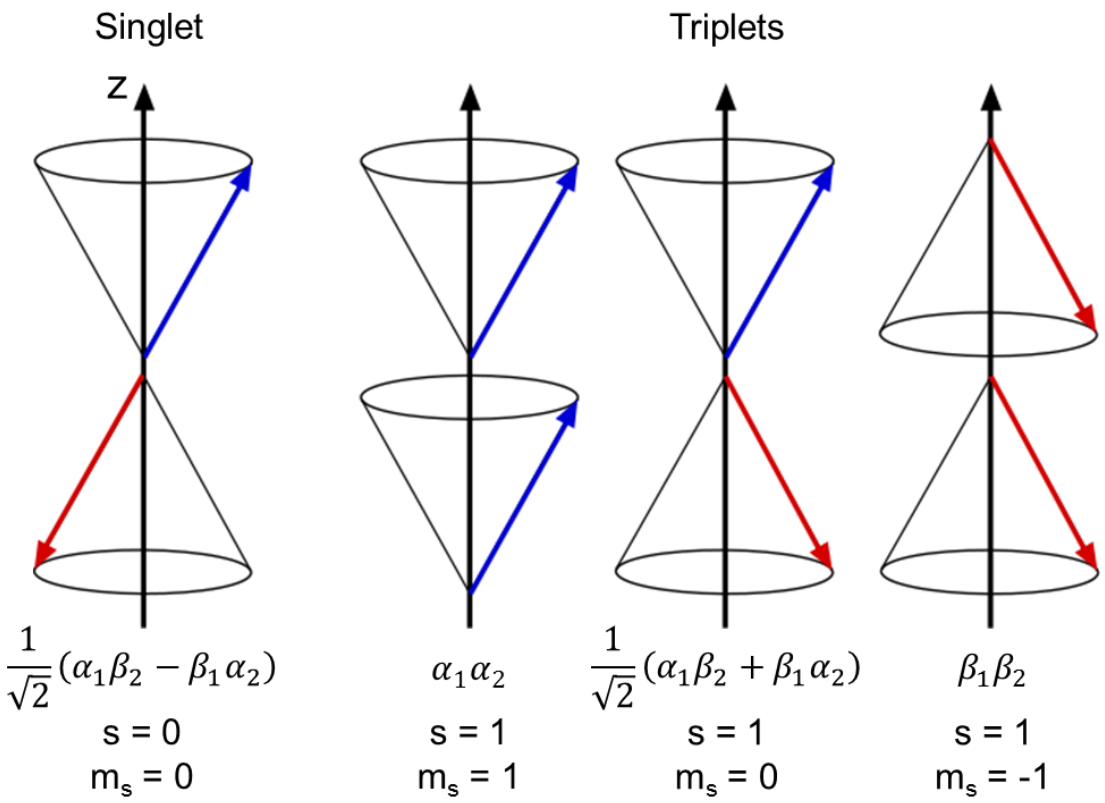

Figure 2.3 Spin combinations of a two electron system that generate singlet and triplet excitons. Electrons can either be spin up (α) with a spin quantum number of s = ½ and z-component spin quantum number of m_s = + ½, or spin down (β) with s = ½ and m_s = -½. The singlet state involves a superposition of α and β where the electron spins are completely out of phase leading to net s = 0. Three spin combinations result in degenerate triplet states with total s = 1.

wavefunction can be expressed as the product of the spatial wavefunction, describing the electrons position in space, and the spin wavefunction, which describes the electron spin.[37] The spin wavefunction is determined by two quantum numbers, the spin quantum number, *s*, which is equal to ½ for electrons, and m_s which gives the z-component of the spin and is equal to ± ½. Since these two numbers completely determine the spin state, the spin wavefunction of the electron can be written as $|s, m_s\rangle$, in bra-ket notation, where the spin-up electron wavefunction, α, is given by $|{}^1/_2, {}^1/_2\rangle$, and a spin-down electron wavefunction, β, is given by $|{}^1/_2, -{}^1/_2\rangle$.[36,37] When the spin operator $\hat{\boldsymbol{S}}^2$ acts on the wavefunction it produces an eigenvalue which gives the square of the total spin angular

momentum of the electron, given by $\widehat{\boldsymbol{S}}^2|s,m_s\rangle = \hbar^2 s(s+1)|s,m_s\rangle = {}^3/_4\,\hbar^2|s,m_s\rangle$. A similar operator, S_z, determines the z-component of the spin angular momentum as $S_z|s,m_s\rangle = \hbar m_s|s,m_s\rangle$.[36]

An exciton consists of a coupled two particle system, where the total spin of the system must be equal to either zero or one.[28] The multiplicity of each of these states is given by M = (2*s* + 1); as such, there is one configuration which yields *s* = 0, referred to as the singlet state, and three degenerate configurations which yield *s* = 1, called triplet states. The four spin wavefunctions of this two particle system and their resulting quantum numbers are:

$$|s,m_s\rangle = \begin{cases} \alpha_1\alpha_2 = |1,1\rangle \\ \frac{1}{\sqrt{2}}(\alpha_1\beta_2 + \beta_1\alpha_2) = |1,0\rangle \\ \beta_1\beta_2 = |1,-1\rangle \\ \frac{1}{\sqrt{2}}(\alpha_1\beta_2 - \beta_1\alpha_2) = |0,0\rangle \end{cases} \tag{2.1}$$

where 1 and 2 refer to electron 1 and electron 2. For the case where one electron is spin up and one electron is spin down, a superposition of the two states is needed in order to satisfy the strong statement of the Pauli Exclusion Principle, which requires two electrons to be indistinguishable upon exchange.[28] In Eqn. 2.1, we see that the first three states correspond to the *s* = 1 triplet state and the last wavefunction corresponds to the singlet state. These states can be visualized as spin vectors, shown in Fig. 2.3. Note that for the triplet wavefunctions the spins are always in phase and couple, such that the magnitude of their total spin angular momentum is given by $\sqrt{2}\hbar$ when added together, whereas the singlet state is completely out of phase so the magnitude of the spin angular momentum is precisely zero. Additionally, a cone is used to represent the spin vector in the x-y plane in order to account for the uncertainty principle, which states that if a value of S_z is measured, then the azimuthal angle of the spin state will be completely indeterminable.[28,36]

This relationship between the spin of two electrons has some remarkable consequences on the physics of organic semiconductors. The ground state of a molecule is usually a singlet state because of their closed shell configuration with filled covalent bonds, as discussed in Section 2.2. Spin selection rules of quantum mechanics state that electronic transitions where $\Delta s = 0$ are allowed and are probable to occur, whereas transitions where $\Delta s \neq 0$ are forbidden and are less probable to occur.[28] Consequently, when a photon is absorbed (with zero spin), only singlet excited states are efficiently generated. This also affects the decay of excitons back to the ground state, as singlets have a high probability of radiative decay back to the ground state and triplet excitons do not, leading to much longer exciton lifetimes for triplet excitons and negligible emission in the absence of significant spin-orbit coupling.

In OPVs, excitons are generated optically; consequently, triplet states must be populated from optically generated singlet states through intersystem crossing by flipping the spin of the excited electron. This can be accomplished in molecules incorporating heavy-metal atoms, exhibiting strong spin-orbit coupling,[28,38,39] or which exhibit thermally activated delayed fluorescence,[40–43] singlet fission,[44–47] or a high degree of symmetry, such as in C_{60}.[48–50] Spin-orbit coupling results from an interaction of the electron with the nucleus of an atom. While we commonly think of an electron orbiting a stationary nucleus; however, in the reference frame of the electron, the positively charged nucleus orbits around the electron, creating a current loop that induces a magnetic field. This magnetic field then interacts with the spin magnetic dipole moment, creating a torque on the electron.[36] If the interaction is strong enough, this can mix the singlet and triplet states and induce a spin flip.[28] In this interaction spin angular momentum itself is not conserved, but

the total angular momentum of the system is conserved by coupling the electron spin angular momentum with the orbital angular momentum.[36] The probability of a spin flip can be increased with the incorporation of a heavy metal atom, often Ir or Pt in organic molecules, because the magnitude of this interaction is proportional to Z^4, where Z is the atomic number.[28,36] Spin orbit coupling also makes it possible for triplet excited states to radiatively couple to the singlet ground state, emitting a photon is process called phosphorescence.

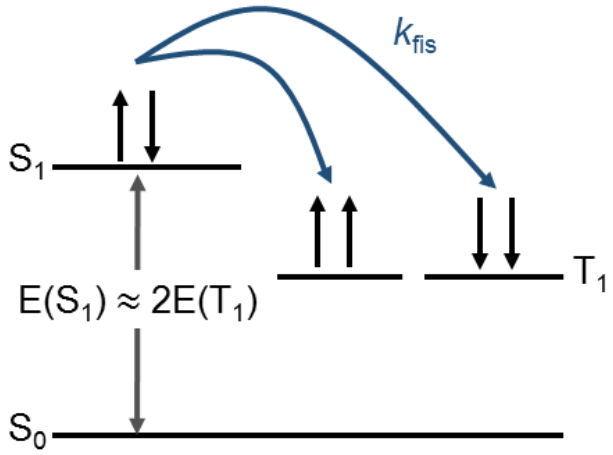

Figure 2.4 Process of singlet fission where a molecule in the singlet excited state (S_1) shares it energy with a neighboring molecule in the ground state (S_0) to produce two triplet excitons (T_1), each with roughly half the energy of S_1 and a net overall singlet character.

Singlet fission is a process that only occurs in a small subset of organic semiconductors, where a singlet exciton is able to share its energy with an adjacent molecule to produce two triplets, each with roughly half the energy of the initial singlet state, as shown in Fig. 2.4.[51,52] This is a spin-allowed process, as the resulting triplet pair has net overall singlet character, so that $\Delta s = 0$ for the transition. As a spin-allowed transition, this process can occur efficiently on timescales of 80 fs to 25 ps.[52]

2.5 Molecular excited state diagram

This chapter has focused on the properties of optically generated excitons in the molecules which comprise organic semiconductors. The relationship between all of these processes and their relative time scales can be visualized in a molecular excited state

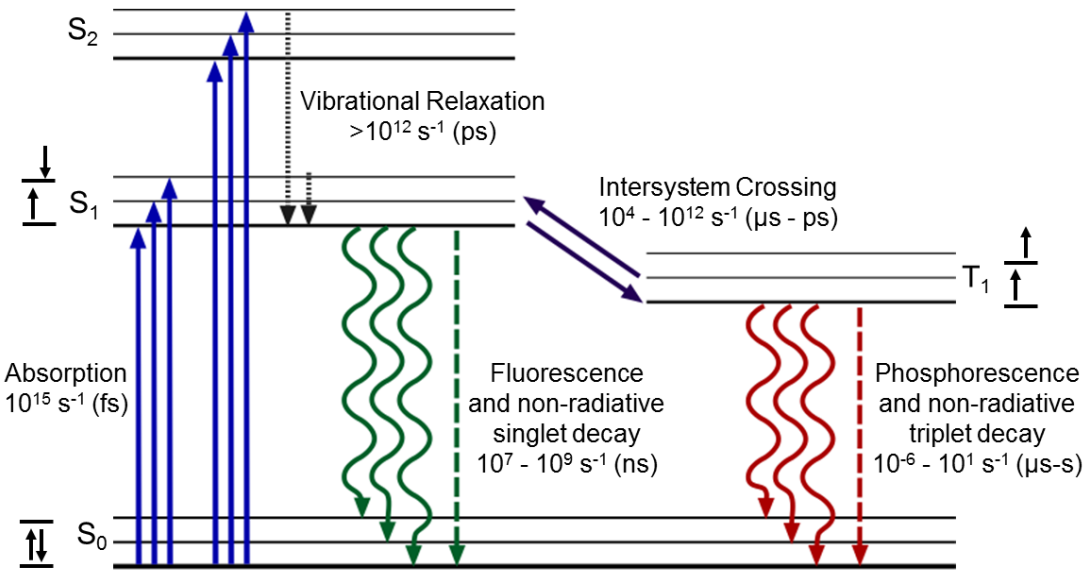

Figure 2.5 Jablonski diagram showing the transitions and relative rates between the ground (S_0) and excited molecular states.[3] Singlet excited states (S_1, S_2) are generated from optical absorption and the triplet state (T_1) must be populated through intersystem crossing.

diagram, called a Jablonski diagram, shown in Fig. 2.5.[28] Here, bold lines represent the lowest vibronic energy level of the ground state (S_0), first and second excited singlet states (S_1 and S_2), and the first excited triplet state (T_1), and the thinner lines represent higher energy vibronic states.

Upon the absorption of light, the molecule is excited from S_0 to a higher energy singlet state, forming a singlet exciton. This can either be S_1 or a higher singlet energy level depending on the energy of the incident photon. If the molecule is excited to a higher energy vibronic state in S_1 or a higher energy singlet state, it will quickly relax back to the lowest vibronic state of S_1 through vibrational relaxation.[28,35] Once the molecule is in S_1 it can decay back to the ground state S_0, either radiatively with rate $k_{R,S}$, in a process known as fluorescence, or non-radiatively with rate $k_{NR,S}$, releasing its energy as heat through lattice vibrations to surrounding molecules. The probability of radiative decay from S_1 determines the photoluminescence efficiency and is given by:

$$\eta_{PL,S} = \frac{k_{R,S}}{k_{R,S}+k_{NR,S}}. \quad (2.2)$$

Additionally, the natural lifetime of the exciton is given by the inverse of all the deactivation rates from S_1, traditionally excluding the rate of intersystem crossing, as:

$$\tau_S = \frac{1}{k_{R,S}+k_{NR,S}}. \quad (2.3)$$

Similar equations for the triplet $\eta_{PL,T}$ and τ_T using the radiative ($k_{R,T}$) and non-radiative ($k_{NR,T}$) triplet decay rates.

In some molecules which display intersystem crossing rates (k_{ISC}) that are competitive with $k_{R,S}$ and $k_{NR,S}$, the triplet excited state can be efficiently populated. It should be noted that the energy of T_1 is always less than S_1 due to the exchange interaction. This results from the overlap of the electron wavefunctions for the electron in the HOMO and LUMO and has to do with the Pauli Exclusion Principle. Two electrons with the same spin do not want to occupy the same place in space, the exchange interaction reduces the overlap of these two wavefunctions and consequently reduces electron repulsion, lowering the energy of the system.[37] Once the molecule is in T_1 it can either decay radiatively in materials with strong spin-orbit coupling as phosphorescence, or non-radiatively back to S_0. In certain systems reverse intersystem crossing back to S_1 is also possible. Decay from T_1 to S_0 requires a spin flip, which is quantum mechanically unfavorable.[28] Consequently, τ_T is generally much longer than τ_S. While this chapter has focused on the generation of excitons in organic semiconductors, the next chapter will focus on the movement of excitons between molecules.

3. Exciton energy transfer and diffusion

The motion of localized excitons in organic semiconductors can be thought of as a three-dimensional random walk, where excitons hop from molecule to molecule through a series of successive energy transfer events. In OPVs, often the performance of a device depends on how far an exciton can travel before it recombines. As such, there is a need to understand the fundamental mechanism which govern the motion of excitons in order to be able to design materials and devices which maximize the distance excitons can move from the point of photogeneration.

There are three different mechanisms by which energy transfer can occur in these materials: cascade energy transfer, Förster transfer, and Dexter transfer, which are shown schematically in Fig. 3.1. Here, D and A are used to denote the donor molecule, which transfers its energy, and the acceptor molecule, which receives the energy, respectively. An asterisk is used to represent a molecule in the excited state, *i.e.* an exciton. These three mechanisms differ in the length scale over which excitonic energy is transferred and the physical nature of the process. Each process can occur between two molecules of the same type in a homogenous film, or between two different types of molecules either in a mixture or at an interface, so long as both energy and angular momentum are conserved.[28]

Cascade energy transfer (Fig. 3.1a) involves the radiative decay of an excited donor molecule, emitting a photon, which is subsequently absorbed by an acceptor molecule, transferring its energy over length scales comparable to the absorption path length.[26,28] Förster energy transfer (Fig 3.1b) involves a dipole-dipole interaction, where the electromagnetic field produced from excited donor molecule couples to the ground state of an acceptor molecule, transferring its energy non-radiatively over length scales of up to

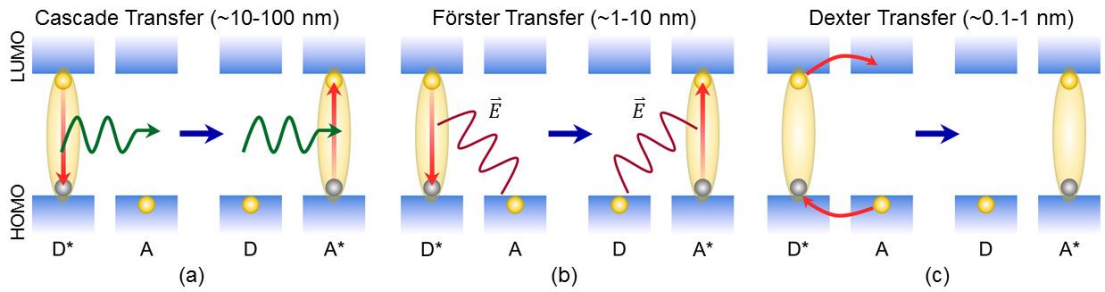

Figure 3.1 Energy transfer mechanisms where excitonic energy is transferred from an excited donor molecule (*D**) to a ground state acceptor molecule (*A*) leading to the motion of excitons. (a) Cascade energy transfer involves the emission of a photon by *D** that is then absorbed by *A*, generating an exciton on the acceptor (*A**). (b) Förster energy transfer is a dipole mediated mechanism where the electromagnetic field ($\vec{E}$) generated by a transition dipole on *D** couples to the ground state dipole of *A*, transferring energy non-radiatively. (c) Dexter transfer involves the physical exchange of an electron in the LUMO of *D** with an electron in the HOMO of *A*, occurring on nearest neighbor length scales.

tens of nanometers.[53–55] Dexter transfer (Fig. 3.1c) relies on the physical exchange of electrons, requiring electron wavefunction overlap, occurring on a nearest neighbor length scale.[56,57] In reality, all three of these processes likely occur to some extent in a given material, but often, depending on the photophysical properties of the material, one type of mechanism will be dominant.[28,37] In this chapter, the physics of each of these energy transfer processes will be explored and material parameters which can be manipulated to optimize energy transfer will be discussed. Once these mechanisms have been established, a connection between nanoscopic energy transfer events and mesoscopic exciton transport will be presented in order to describe exciton diffusion in films of organic semiconductors. Lastly, the fundamental limits of exciton diffusion occurring from Förster and Dexter transfer will be compared.

3.1 Cascade energy transfer

The process of cascade energy transfer involves the emission of a photon from a donor molecule that is absorbed by an acceptor molecule, generating an exciton on the acceptor. The efficiency of this mechanisms depends on η_{PL} of the donor molecule, the overlap

between the emission spectrum of the donor molecule and the absorption spectrum of the acceptor, such that energy is conserved, and the thickness of the film.[26,28] While this mechanism is capable of transferring energy over the longest length scale, organic semiconductors typically have a low η_{PL} and a large Stokes shift, making this mechanism often the least efficient form of energy transfer in a material.[26] Additionally, if k_R is shorter than the total hopping rate due to Förster or Dexter transfer, these shorter range mechanisms will dominate. As such, this form of energy transfer is often neglected when other modes of energy transfer are possible.

3.2 Fermi's golden rule and energy transfer rates

Förster and Dexter transfer arise from quantum mechanical Coulomb and exchange interactions, respectively. In the weak coupling limit, which permits the use of perturbation theory, the transfer rates for these processes can be calculated by Fermi's golden rule:[28,37,56,58–60]

$$k_{ET} = \frac{2\pi}{\hbar} |\langle f|H'|i\rangle|^2 \rho, \tag{3.1}$$

where $|i\rangle$ is the wavefunction describing the initial state of the system, $\langle f|$ is the wavefunction of final state, *H'* is the perturbing Hamiltonian operator which mixes $|i\rangle$ and $\langle f|$, and ρ is the density of final states, meaning the number of available resonant energy states during the transition. In this case $|i\rangle$ is given by $|\psi(D^*)\psi(A)\rangle$, the overall electronic wavefunction corresponding to an excited donor molecule and ground state acceptor and $\langle f|$ is given by $\langle\psi(D)\psi(A^*)|$, representing the wavefunction after energy has been transferred to the acceptor. The operator *H*' can be expressed in terms of the sum of the Coulomb interaction operator H_{coul} and exchange interaction operator H_{ex}. The electronic interaction that promotes Förster transfer arises from the coupling of transition dipole

moments between D^* and A *via* a Coulombic interaction.[55] A transition dipole is the electric dipole that is associated with a transition between two states, in this case the dipole that arises from the change in electron density associated with $D^* \rightarrow D$ and $A \rightarrow A^*$ transitions.[26,28] The exchange interaction, which drives Dexter transfer, results from the overlap of the electronic orbitals of two indistinguishable particles and is related to the Pauli Exclusion Principle.[28,55] Equation 3.1 can then be rewritten as:

$$k_{ET} = \frac{2\pi}{\hbar}[\langle\psi(D^*)\psi(A)|H_{ex} + H_{coul}|\psi(D^*)\psi(A)\rangle^2]\,\rho. \qquad (3.2)$$

Therefore, there will always exist exchange and Coulomb interactions associated with an energy transfer event, but depending on the distance and nature of the exited state, often one mechanism will be dominant. Generally, the exchange interaction will dominate at short distances when the molecules are in contact with one another and the Coulomb interaction will dominate at larger distances. Additionally, the Coulomb interaction requires spin allowed transitions between the excited state and singlet ground state with large transition dipole moments. Transitions from a triplet excited state to a singlet ground state are spin forbidden and therefore carries no appreciable oscillator strength, so the Coulomb term will be negligible in the absence of strong spin-orbit coupling.[37] For this reason, it is generally thought that singlet energy transfer is dominated by Förster transfer and triplet energy transfer is dominated by Dexter transfer; however, some organometallic materials with appreciable spin-orbit coupling have demonstrated rate constants with distance dependences consistent with Förster transfer for triplet excitons.[61,62]

3.3 Förster energy transfer

Förster transfer occurs when a transition dipole moment on an excited donor molecule generates an oscillating electric field which couples to the ground state of an acceptor

molecule, inducing a transition dipole on the acceptor molecule, transferring energy non-radiatively through empty or molecularly occupied space. Original work by Förster in the 20th century used Eqn. 3.1 to derive a rate equation for this mechanism in terms of measurable photophysical molecular properties.[53,54] In this work, the molecules are approximated as weakly coupled point dipoles and the energy transfer rate is expressed in terms of the intermolecular separation (d), the exciton lifetime (τ), and the Förster radius (R_0) as:[28,53,55]

$$k_F = \frac{1}{\tau}\left(\frac{R_0}{d}\right)^6, \tag{3.3}$$

where R_0 is defined as "the critical distance for which excitation transfer and spontaneous deactivation of the sensitizer (donor) are of equal probability," meaning that at a distance R_0 from the donor the rate of Förster transfer is equal the rate of all other excitonic decay pathways.[53] This term can be expressed as:

$$R_0^6 = \frac{9\eta_{PL}\kappa^2}{128\pi^5 n^4}\int \lambda^4 F_D(\lambda)\sigma_A(\lambda)d\lambda, \tag{3.4}$$

where η_{PL} is the photoluminescence efficiency, κ is the dipole orientation factor, λ is the wavelength of light, F_D is the area normalized emission spectrum, σ_A is the absorption cross section, and n is the index of refraction at the wavelength where the overlap of F_D and σ_A is maximized. The absorption cross section can be calculated from the extinction coefficient (k) as:

$$\sigma_A = \frac{4\pi k}{\lambda \rho_A}, \tag{3.5}$$

where ρ_A is the molecular density of the acceptor.

Being a dipole-dipole mediated energy transfer process, Eqn. 3.4 can be thought of in terms of two separate components: the pre-factor, which describes the electrostactic

interaction between the transition dipoles, and the overlap integral, shown in Fig. 3.2, which is equivalent to ρ in Eqn. 3.1 and can be thought of as an overlap in the density of states between the donor and acceptor molecules, providing a measure of the number of available resonant energy states, so that energy is conserved in the process

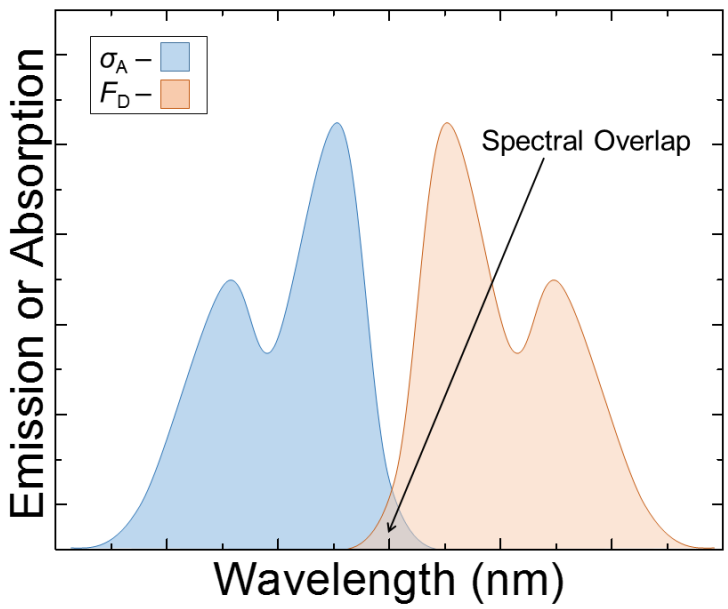

Figure 3.2 Spectral overlap between the area normalized emission spectrum (F_D) of a donor molecule and the absorption cross section (σ_A) of an acceptor molecule. This overlap determines the number of resonant energy states available during Förster transfer.

While k_F is calculated using η_{PL}, it should be noted that Förster transfer does not involve the emission of a photon. The photoluminescence efficiency can be rewritten as $\eta_{PL} = k_R\tau$. Using this relation and inserting Eqn. 3.4 into Eqn. 3.3, τ cancels leaving k_F proportional to k_R. Therefore, η_{PL} provides a measure of the oscillator strength of transition dipole, which establishes the electromagnetic field and drives Förster transfer. The more efficiently the donor molecule radiates, the more efficiently it will be able to transfer its energy. The efficiency of this energy transfer process is also dependent on the relative orientation of the transition dipole moments between the donor and acceptor molecules, which is encapsulated in κ. This can be calculated by:[26,55,63]

$$\kappa^2 = (\cos(\varphi_{AD}) - 3\cos(\varphi_A)\cos(\varphi_D))^2, \tag{3.6}$$

where φ_{AD} is the angle between the donor and acceptor dipoles and φ_A and φ_D are the angles between the respective dipoles and direction of molecular stacking, as shown in Fig. 3.3. The value of κ^2 can range from zero, for perpendicular dipoles, to four for head-to-tail parallel dipoles. For randomly oriented rigid dipoles, like those found in a solid amorphous material, $\kappa^2 = 0.476$.[64] In materials where Förster transfer is the dominant energy transfer mechanism, L_D can be increased by optimizing parameters that determine k_F. In accord with Eqn. 3.4, this can be accomplished by decreasing the molecular separation,[65,66] increasing η_{PL},[67–69] optimizing the alignment of κ through molecular ordering and crystallization,[70] and decreasing the stokes shift.[66,67,71]

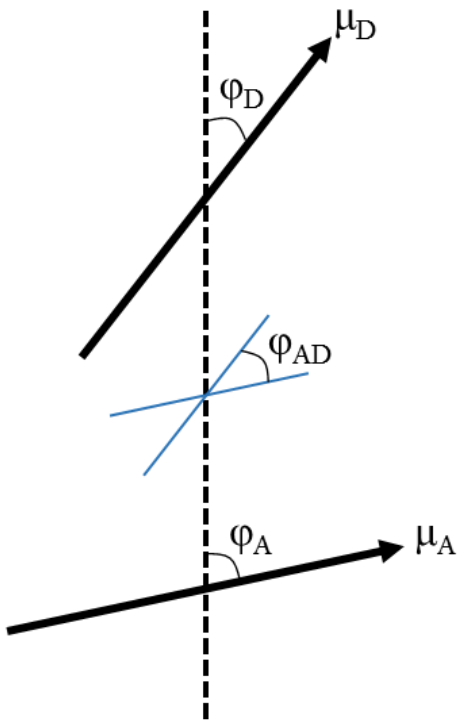

Figure 3.3 Angles which determine the dipole orientation factor between donor (μ_D) and acceptor (μ_A) transition dipoles in Eqn. 3.6

3.4 Dexter energy transfer

Dexter transfer is driven by the exchange interaction and involves the simultaneous transfer of an electron in the LUMO of donor to the empty LUMO of the acceptor and the transfer of a ground state electron from HOMO of the acceptor to the HOMO of the donor molecule.[28,37,57] In this process the spin state of the exciton is conserved, such that for a singlet exciton the transferred electrons will have the same spin and for a triplet exciton

the transferred electrons will have opposite spin in order to satisfy the Pauli Exclusion Principle in the filled singlet ground state.

Since this process involves the physical exchange of electrons, it requires electron wavefunction overlap between D^* and A and is therefore a nearest neighbor process occurring on the length scale of 0.5 – 1 Å, with documented values up to 3 nm.[28,40,55,72–74] A useful rate equation for Dexter transfer can be derived by approximating the electron wavefunctions of the donor and acceptor as two spheres, causing the wavefunction overlap to decrease exponentially as a function of the center to center distance d. Using this approximation, the rate of Dexter energy transfer can be expressed as:[28]

$$k_D(R) = KJe^{\left(\frac{-2d}{L}\right)} \tag{3.7}$$

where L is the van der Waals radius, K is a parameter related to the specific orbital interaction, and J is the spectral overlap integral featuring an area-normalized extinction coefficient of the ground state acceptor and an area-normalized emission spectrum of the excited state. The normalized overlap terms in J mean that significant optical emission or absorption of the molecules involved is not required, merely the presence of resonant states.[28] Since efficient absorption and emission are not required for Dexter transfer, it is thought that singlet excitons in materials with negligible fluorescence quantum yields as well as triplet excitons transfer their energy *via* this method. Optimizing Dexter transfer to increase L_D can be achieved by reducing the intermolecular spacing,[75] improving wavefunction overlap, and reducing energetic disorder to reduce exciton trapping.[47,76,77]

3.5 Connecting energy transfer and exciton diffusion

The discussion thus far has focused on nanoscopic energy transfer events where an exciton undergoes a three-dimensional random walk, transferring its energy from molecule

to molecule. In a film material, the random motion of an ensemble of excitons can be well described by diffusion.[78] In the simplest form, three dimensional exciton diffusion can be modeled with a second order differential equation as:

$$\frac{\partial n(\vec{r},t)}{\partial t} = D\nabla^2 n(\vec{r},t) - \frac{n(\vec{r},t)}{\tau} + G(\vec{r}), \tag{3.8}$$

where n is the exciton density, τ is the natural exciton lifetime, D is the diffusivity, $\vec{r}$ is the position, t is the time, and G is exciton generation rate.[63,79,80] On the right side of Eqn. 3.8, the first term represents exciton motion by diffusion, the second term represents exciton recombination, and the third term represents the optical generation of excitons due the absorption of light. Additional linear and second order terms can be added onto this equation to account for generation and loss processes other than optical absorption and natural decay, including, but not limited to, exciton-polaron quenching, exciton-exciton annihilation, singlet fission, and the quenching of excitons by impurity molecules, as will be demonstrated in future chapters.

In OPVs, often device performance is only sensitive to exciton diffusion in one direction, normal to an exciton dissociating interface. In this case, Eqn. 3.8 can be reduced to one-dimension as:

$$\frac{\partial n(x,t)}{\partial t} = D\frac{\partial^2 n(x,t)}{\partial x^2} - \frac{n(x,t)}{\tau} + G(x). \tag{3.9}$$

The diffusion length (L_D) is a critical parameter to device performance and represents the characteristic distance over which an exciton migrates during its lifetime and is given by:

$$L_D = \sqrt{D\tau}. \tag{3.10}$$

Intuitively, D determines how fast the exciton hops from molecule to molecule, which is proportional to the energy transfer rate, and τ determines how many hops can occur before the exciton recombines.

The diffusivity can be related to the energy transfer rate (k_{ET}) by modeling exciton diffusion as an ensemble of self-energy transfer events.[60,63,78] Starting from a first principles rate equation and assuming isotropic energy transfer on a three-dimensional cubic lattice, it can be shown that D is proportional to k_{ET} by:

$$D = \frac{1}{6}\sum_N r^2 k_{ET}(r), \tag{3.11}$$

where r is the distance of a single hop, or energy transfer event, and is summed over the total number of molecules, N. This equation can be further simplified by assuming that energy transfer can only occur to the 6 nearest neighbors on this cubic lattice, yielding:

$$D = \frac{A}{6}(6k_{ET}d^2) = Ad^2k_{ET}, \tag{3.12}$$

where d is the lattice constant and A is a prefactor which is added to account for anisotropy on the length scale of L_D which is not accounted for in this model, such as energetic disorder. For purely diffusive behavior A = 1, but can be reduced in more disordered systems.[81] An analogous expression can be given in terms of the mean time between hops (τ_H), where ${\tau_H}^{-1} = 6k_{ET}$, accounting for multiple hopping sites, yielding $D = Ad^2/6\tau_H$.

For luminescent materials, where energy transfer is dominated by the Förster mechanism, this model allows for predictions of L_D to be made in terms of physically measureable quantities. Assuming that $k_{ET} = k_F$ and inserting Eqn. 3.4 into Eqns. 3.3 and 3.12, L_D can be predicted by:

$$L_D = A\frac{{R_0}^3}{d^2} = \frac{A}{d^2}\sqrt{\frac{9\eta_{PL}\kappa^2}{128\pi^5 n^4}\int \lambda^4 F_D(\lambda)\sigma_A(\lambda)d\lambda}. \tag{3.13}$$

Several studies have demonstrated that in certain systems where Förster transfer is dominant, this model is capable of accurately predicting the magnitude of L_D.[67–70]

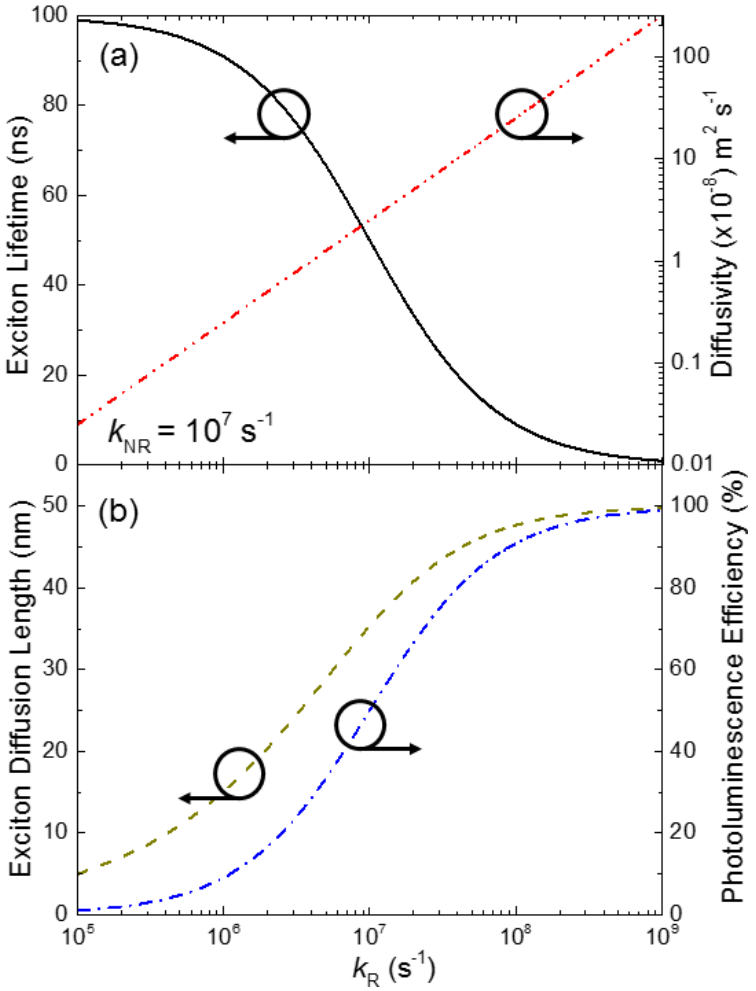

Figure 3.4 Photophysical parameters for excitons diffusing *via* a Förster mechanism. (a) The exciton lifetime and diffusivity have opposite dependences on the radiative rate (k_R). (b) When k_R is much greater than the non-radiative exciton decay rate (k_{NR}), the photoluminescence efficiency and diffusion length begin to plateau, fundamentally limiting the maximum diffusion length for Förster transfer. Diffusivity and diffusion length values were calculated using Eqns. 3.10 and 3.12 with A = 1, d = 0.5 nm, and $k_{ET} = k_R \times 10^3$ s^{-1}.

3.6 The limits of diffusion by Dexter and Förster mechanisms

Luminescence efficiency is often viewed as the deciding factor for whether a material will transfer energy by a Dexter or Förster mechanism due to the requirement for luminescence in Eqn. 3.4. The relatively long-range dipole-dipole interactions of Förster transfer, compared to the nearest-neighbor exchange interaction of Dexter transfer, usually

results in a higher hopping rate and D for Förster materials; however, this does not necessarily translate to a longer L_D.

Interestingly, the longest values of L_D for organic semiconductors are reported for triplet excitons in crystalline materials.[47,77,82] These materials can exhibit L_D on the order of microns, whereas singlet L_D are typically reported as tens of nanometers.[63,70,80,83] This has led some to speculate that there is a fundamental limit in place for excitons diffusing *via* a Förster mechanism. As noted in a study by Yost *et al.*, the Förster rate and the exciton lifetime have an inverse dependence on the magnitude of the transition dipole moment.[59] Examination of Eqn. 3.13 demonstrates that L_D in a Förster material is proportional to $\sqrt{\eta_{PL}}$. It is perhaps more instructive in this case to express η_{PL} as τ/τ_{rad}, where $\tau_{rad} = {k_R}^{-1}$ is the radiative lifetime. Then, Eqn. 3.12 can be rewritten as:

$$D = \frac{A}{d^4}\frac{9k_R\kappa^2}{128\pi^5 n^4}\int \lambda^4 F_D(\lambda)\sigma_A(\lambda)d\lambda. \tag{3.14}$$

From this equation it is clear that $D \propto k_R$; however, $\tau \propto k_R^{-1}$. This implies that for materials with high η_{PL}, where k_R is much greater than k_{NR}, increases in τ will not lead to a longer L_D because there will be an equivalent reduction in D (Fig. 3.4a), causing L_D to plateau (Fig. 3.4b).

Conversely, the rate of Dexter energy transfer is independent of τ_{rad}, so the energy transfer rate and τ are not coupled. Therefore, there is no theoretical maximum L_D for excitons diffusing via a Dexter mechanism. Generally, for non-radiative triplets with long lifetimes $k_R \ll k_{NR}$ and $\tau \approx {k_{NR}}^{-1}$. In this limit, L_D in materials dominated by Dexter transfer will be able to maintain a constant D and display unbounded behavior as a function increasing τ, as shown in Fig. 3.5 where $L_D \propto {k_{NR}}^{-1/2}$. Despite orders of magnitude lower hopping rates than Förster transport, the spin forbidden transition to the ground state for

triplet excitons can lead to τ ranging from microseconds to milliseconds, which can result in much longer values of L_D.

As we will see in the next chapter, longer values of L_D allow for thicker active layers to be used in the device, which absorb more light and lead to more efficient devices. Therefore, triplet excitons offer the best opportunity to increase the efficiency OPVs through enhancements in the photocurrent due to increased exciton harvesting. However, it should be noted that achieving the long τ necessary to generate microscopic L_D often requires highly ordered crystalline films which are difficult to implement into device architectures.[37,47,84] Additionally, the lower energy of triplet excitons, compared to singlets, will reduce the maximum attainable open-circuit voltage of the device, which must be taken into account.[37]

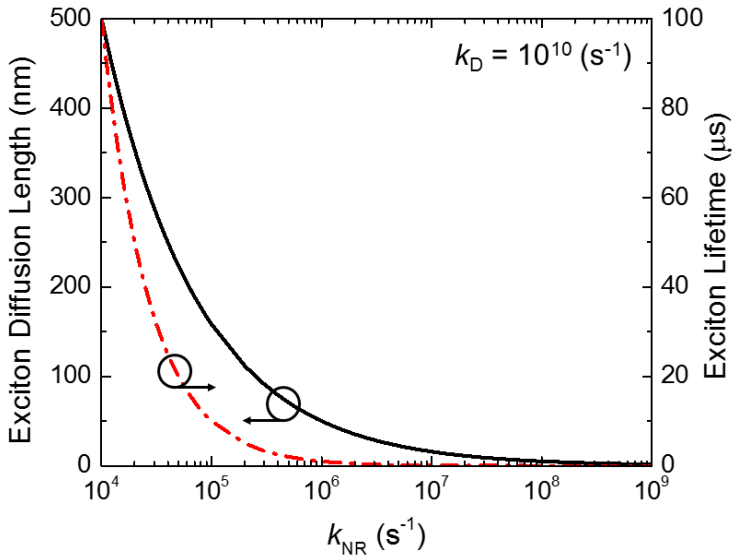

Figure 3.5 Dependence of the diffusion length on the non-radiative exciton decay rate (k_{NR}) for excitons traveling *via* a Dexter mechanism. For non-luminescent triplets, the radiative rate is much smaller than k_{NR} and the exciton lifetime is approximately k_{NR}^{-1}. Given that there is no dependence of the diffusivity on k_{NR}, the diffusion length displays unbounded behavior in contrast to Förster transfer. The diffusion lengths were calculated using Eqns. 3.10 and 3.12 with A = 1, d = 0.5 nm, and $k_D = 10^{10}$ s^{-1}.

4. Organic photovoltaic device operation

As discussed in the previous chapters, the absorption of light by organic semiconductors produces molecular excited states called excitons, where an excited electron is Coulombically bound to a ground state hole. The goal of an OPV is to convert solar radiation from the sun into useable electricity by collecting the electron and hole at opposite contacts of the device, producing an electrical photocurrent. In order to accomplish this, the exciton must be dissociated into free carriers.[16,18,85] Consequently, the architecture of these devices are strongly dictated by necessity to dissociate excitons. In this chapter, the processes which lead to photoconversion in OPVs, device architectures which are able to accomplish these processes efficiently, and methods to analyze device performance will be discussed in detail. This broader context will motivate the experimental work presented in this dissertation, which aims to provide a deeper understanding of the factors that determine the component efficiencies of the photoconversion process and methods to quantify these processes.

4.1 Photoconversion in organic photovoltaic devices

Modern OPVs are based on an organic heterojunction between two energetically dissimilar materials designed to dissociate excitons. This bilayer architecture was first discovered by Tang in 1985 and yielded a power conversion efficiency of about 1%, which was an order of magnitude increase over previous incarnations of OPVs.[86,87] In their simplest form, these devices consist of two organic layers, with roughly 50 – 100 nm total thickness, deposited between a transparent conducting anode on a glass substrate, usually indium tin oxide (ITO), and some sort of metallic cathode, generally aluminum or silver, as shown in Fig. 4.1a.[16,18,86,88] Within these devices, an organic heterojunction is formed

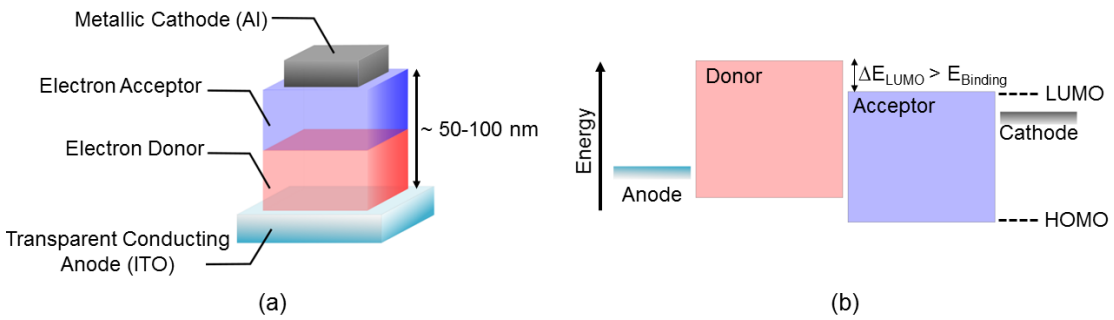

Figure 4.1 (a) Bilayer device architecture consisting of an organic heterojunction between an electron donating and electron accepting material, deposited between a transparent conducting anode, usually indium tin oxide (ITO) on glass, and a metallic cathode, often aluminum (Al). (b) Energetic structure of bilayer device, where an offset in the HOMO and LUMO (ΔE_{LUMO}) energies of the donor and acceptor exceed the binding energy of an exciton ($E_{Binding}$).

between an electron donating and electron accepting material, referred to as a donor-acceptor (D-A) heterojunction. These two materials are selected such that there is an offset in their respective HOMO and LUMO energies which exceeds the exciton binding energy (Fig. 4.1b).[18,85] When an optically generated exciton reaches the D-A interface it can be dissociated by either transferring an electron from the LUMO of the donor to the LUMO of the acceptor if the exciton originates on the donor, or equivalently, transferring a hole from the HOMO of the acceptor to the HOMO of the donor, for excitons originating on the acceptor.

The process of photoconversion in these devices occurs through a five step mechanism, where each step is characterized by its own efficiency. First an incident photon is absorbed by the active layers of the device, generating an exciton (Fig. 4.2a). This process occurs with an absorption efficiency $\eta_A(\lambda)$, which depends on the absorption coefficient of the material at the wavelength of the incident light (λ) and the thickness of the material.[16,79] This value can also be affected by optical interference effects caused by varying reflections and transmissions at each interface, which will be discussed in more detail in the next chapter.[79] In Fig. 4.2a, the exciton has been drawn in the optical bandgap (E_{Opt}) of the layer.

After the absorption of a photon, the exciton will relax from the electrical gap (E_{Elec}), given by the difference in HOMO and LUMO energies, due to the exciton binding energy (E_B), where:[89]

$$E_{Elec} = E_{Opt} + E_B = E_{LUMO} - E_{HOMO}. \quad (4.1)$$

Additionally, the energy levels of the active layers have been drawn to represent the built in electric potential generated by the equilibration of the fermi level due to the difference in work function between the anode and cathode.[16] The active layers are treated as insulators, where the built in field is dropped linearly over the active layers and band bending caused by the build of charge or interface dipoles are ignored.[16,37,90,91]

After the exciton is generated, it must diffuse to the D-A interface, with efficiency η_D (Fig. 4.2b). In these materials, the diffusion length (L_D ~ 10 nm) is typically much shorter than the absorption length of light (L_A ~ 100 nm).[63,80,83] This restricts the thickness of the active layers, as excitons generated more than L_D away from the D-A interface will likely recombine before being dissociated, wasting the absorbed energy. The use of optically thin layers limits η_A and the power conversion efficiency of these bilayer devices, which is known as the exciton bottleneck.[14]

Once the exciton reaches the D-A interface an electron is transferred from the LUMO of the donor to the LUMO of the acceptor, with efficiency η_{CT}, forming an intermediate Coulombically bound charge-transfer (CT) state (Fig. 2.1c). The process of charge transfer can be described by Marcus theory, where the rate of charge transfer depends on the magnitude of the D-A LUMO or HOMO offset.[92] If the offset is greater than E_B, then this

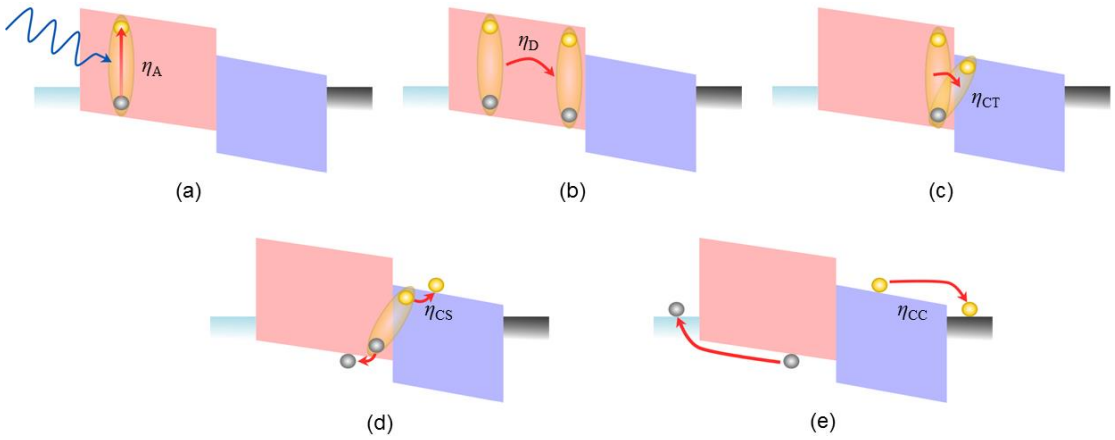

Figure 4.2 Five steps of photoconversion in an OPV and their associated efficiencies. (a) Optical absorption generates a Coulombically bound exciton (η_A). (b) The generated exciton must diffuse to the interface between the electron donor and electron acceptor (η_D). (c) Charge transfer occurs when an electron is transferred from the LUMO of the donor to the LUMO of the acceptor, or when a hole is transferred from the HOMO of the acceptor to the HOMO of the donor, forming and interfacial charge transfer state (η_{CT}). (d) The charge transfer state is dissociated into free carriers (η_{CS}). (e) Free carriers are collected at their respective electrodes as photocurrent. (η_{CC}).

exothermic process happens fast, occurring on rate scales of $10^8 - 10^{12}$ s^{-1} and it is often assumed that $\eta_{CT} = 100\%$.[89]

After the CT state is formed, it must be dissociated into a free electron and hole with charge separation efficiency η_{CS} (Fig. 2.1d). In order for this to occur, the binding energy of the CT state must be overcome by either absorbing thermal energy or being aided by electric field assisted dissociation.[93,94] The binding energy of the CT state is less than E_B due to the increased separation of the charges; however, thermal energy alone may not be enough to dissociate the CT state efficiently. Assuming that the CT state binding energy depends on the charge separation, a binding energy of 25 meV, the amount of thermal energy available at room temperature, implies a CT state radius of about 16 nm.[93] This separation is likely unphysical in most systems, so the built in electric field of the device also assists in the dissociation process. Both of these processes can be described by the Onsager-Braun theory of field assisted dissociation.[95] Here, the rate of CT state dissociation is by:

$$k_{CS} = \frac{3q\langle\mu\rangle}{4\pi a^3\langle\epsilon\rangle} e^{-E_{CT}/k_B T} \frac{J_1(2\sqrt{-2b})}{\sqrt{-2b}} \text{ and } b = \frac{q^3 E}{8\pi\epsilon {k_B}^2 T^2}, \quad (4.2)$$

where q is the elementary charge, a is the initial charge separation, $\langle\mu\rangle$ and $\langle\epsilon\rangle$ are the average carrier mobility and dielectric constant across the D-A interface, respectively, E_{CT} is the CT state binding energy, T is the temperature, E is the electric field, and J_1 is a first order Bessel function.

Once the CT state is dissociated the generated carriers, or more precisely generated polarons, can be collected at their respective electrodes with a charge collection efficiency η_{CC} (Fig. 2.1e). A polaron is a quasiparticle which accounts for the charge on the ionized molecule as well as the induced polarization of the surrounding medium. The one-dimensional current density ($J(x)$) in these devices can be expressed as:[85]

$$J(x) = q\left(n_{pol}(x)\mu_n \nabla U(x) + k_B \mathrm{T}\mu_n \nabla n_{pol}(x)\right), \quad (4.3)$$

where n_{pol} is the polaron density, either electrons or holes, μ_n is the polaron mobility, and U is the electrical potential. Here ∇U corresponds to carrier drift and ∇n_{pol} corresponds to carrier diffusion. In an OPV, both of these forces act in the same direction. The built in electric field will cause electrons and holes to drift to the cathode and anode, respectively. The generation of electrons and holes is confined at the D-A interface, which will cause a photoinduced carrier concentration gradient, generating a diffusional force in the same direction. This is in contrast to traditional inorganic photovoltaics, where these forces act in opposite directions.[85]

The product of these five efficiencies determines the device external quantum efficiency (η_{EQE}). This gives the ratio of the number of charges collected at the electrodes to the total number of incident photons as:

$$\eta_{EQE} = \eta_A(\lambda)\eta_D(L_D)\eta_{CT}(V)\eta_{CS}(V)\eta_{CC}(V). \quad (4.4)$$

4.2 Photocurrent loss mechanisms

4.2.1 Exciton-polaron quenching

During the photoconversion process there are a variety of photocurrent loss mechanisms which can limit the efficiency of OPVs. It has already been established that radiative and non-radiative exciton decay will reduce the fraction of harvested excitons. Diffusing excitons can also be lost to a mechanism called exciton-polaron quenching. This is a bimolecular process where excitonic energy is transferred to a nearby molecule containing a polaron. This results in the quenching of the exciton to the ground state, transferring its energy to the polaron, which can then rapidly thermalize.[96–99] For emissive singlet excitons, this process is thought to occur over relatively long ranges through Förster transfer.[99,100] Interestingly, it has been shown that this type of exciton-polaron energy transfer can be even more efficient than exciton-exciton Förster transfer, due to lattice relaxation effects which cause a red-shift in the absorption spectrum of ionized molecule relative to the neutral ground state absorption, increasing the Förster radius of the energy transfer event.[96,99] Non-emissive triplet excitons, which cannot undergo Förster transfer, can be quenched by polarons via the nearest neighbor Dexter mechanism.[97,101–103] This process is thought to occur at a slower rate than singlet exciton-polaron quenching, at a given L_D, due to the shorter length scale of the interaction.[97,101]

4.2.2 Exciton-exciton annihilation

Another possible excitonic loss pathway is exciton-exciton annihilation. This is a bimolecular process similar to exciton-polaron quenching, except excitonic energy is

transferred to a molecule containing an exciton, instead of a polaron, resulting in one quenched exciton and one high energy exciton, which then undergoes vibrational relaxation.[28] This process has a quadratic dependence on the exciton density and therefore generally only occurs at high exciton densities on the order to 10^{17} - 10^{19} cm^{-3}.[62,102,104,105] For singlet excitons with relatively short lifetimes, establishing an exciton density of this magnitude is rare under typical OPV illumination intensities and is often ignored.[106,107] This process is more detrimental to long lived triplet excitons, especially in an organic light-emitting device, where this mechanism has been shown to cause detrimental effects contributing to the efficiency roll-off at high voltages.[102,104,108,109] There are two different reaction mechanisms by which this can occur. When two triplet excitons annihilate to form one triplet exciton, $D^*(T_1) + A^*(T_1) \xrightarrow{k_{TT}} D(S_0) + A^*(T_n) \xrightarrow{k_{vib}} D(S_0) + A^*(T_1)$, where D and A represent the donor and acceptor molecules, respectively, * represents a molecule in the excited state, k_{TT} is the rate of triplet-triplet annihilation, and k_{vib} is the rate of vibronic relaxation. For certain triplet spin pairings it is also possible for two triplets to produce one singlet as, $D^*(T_1) + A^*(T_1) \xrightarrow{k_{TT}} D(S_0) + A^*(S_n) \xrightarrow{k_{vib}} D(S_0) + A^*(S_1)$. When this happens, two triplet excitons with a net overall singlet character, *i.e.* $\uparrow\uparrow + \downarrow\downarrow$ and total spin = 0, annihilate and are capable of forming an excited singlet state, provided that the energy of the triplet is greater than twice the energy of the singlet.[28] This mechanism is especially important in certain singlet fission materials and reduces the overall triplet yield.[51]

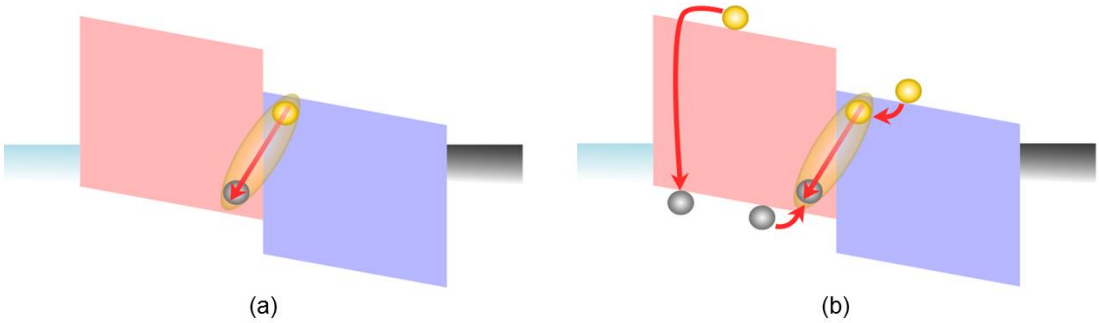

Figure 4.3 (a) Geminate recombination involves the recombination of an electron and hole originating from the same absorption event. This most commonly happens when an interfacial charge transfer states recombines before dissociation can occur. (b) Non-geminate recombination involves two carriers originating from separate absorption events. This can happen if two charges near the interface form a charge transfer state which recombines, or occur through band to band Langevin recombination in the bulk of one of the materials.

4.2.3 Geminate and non-geminate recombination

In addition to excitonic losses, the photocurrent in an OPV can also be reduced due to the recombination of charge carriers through geminate and non-geminate recombination. Geminate recombination is defined as the recombination of two charge carriers which originate from the same absorption event, or exciton, and non-geminate recombination is defined as the recombination of two charges which originate from different absorption events. Practically, geminate recombination generally involves recombination of an interfacial CT state before it can it is dissociated, as shown in Fig. 4.3a. Just like CT state dissociation, discussed in Section 4.1, this process is described by Onsager-Braun theory and is dependent on the amount of thermal energy available relative to the CT state binding energy and the magnitude of the built in electric field.[94,95,110–112]

Non-geminate recombination can involve direct band to band recombination between two oppositely charged carriers, called Langevin recombination, or when two dissociated carriers arrive at the D-A interface and form a CT state, which then recombines, as shown in Fig 4.3b. Langevin recombination assumes that the rate of recombination is limited by

the time it takes the carriers to diffuse within a close enough proximity to each other for recombination to occur and is given by:

$$k_{rec} = \frac{q}{\epsilon}\left(\frac{\mu_n+\mu_p}{2}\right)np, \tag{4.5}$$

where n and μ_n, p and μ_p are the electron and hole density and mobility, respectively.[113] This mechanism is also a function of voltage, as a decrease in the internal field will cause a buildup charge in the active layer and lead to increased non-geminate recombination.[114–118] Given that the minority carrier density in an OPV is generally very low, geminate recombination is often a more dominant loss mechanism than non-geminate recombination in simple bilayer OPVs.

4.3 Organic photovoltaic device architectures

The bilayer devices discussed hereto, shown in Fig 4.1a, are called planar heterojunction devices (PHJ), which represented a large advancement in the field over the previous single layer Schottky style devices.[88] This style of device utilizes simple fabrication techniques and provides a continuous pathway for charge collection; however, they are often limited by the magnitude of L_D, as discussed at the beginning of the chapter. In order to overcome this bottleneck, devices can be fabricated which utilize an active layer that consists of a mixture of donor and acceptor materials, referred to as a bulk heterojunction device (BHJ), shown in Fig. 4.4a. These devices significantly increase the surface area of the D-A interface and reduce the average distance which an exciton must diffuse in order to be dissociated, with some reports of η_D reaching 100%.[18,21,119–121] Most high efficiency devices utilize some version of this architecture; however, it requires precise control of the nano-morphology, which often requires significant optimization in order to ensure that the domain size of the donor and acceptor is on the order of L_D.

Additionally, there must exist a continuous pathway for charge collection after dissociation to ensure that charge does not get trapped on an island of material without a pathway to an electrode. In these devices, η_{FC} is completely determined by the internal electric field, as these devices do not have a strong diffusive contribution to charge collection, which can lead to increased non-geminate recombination compared to PHJ devices.[122]

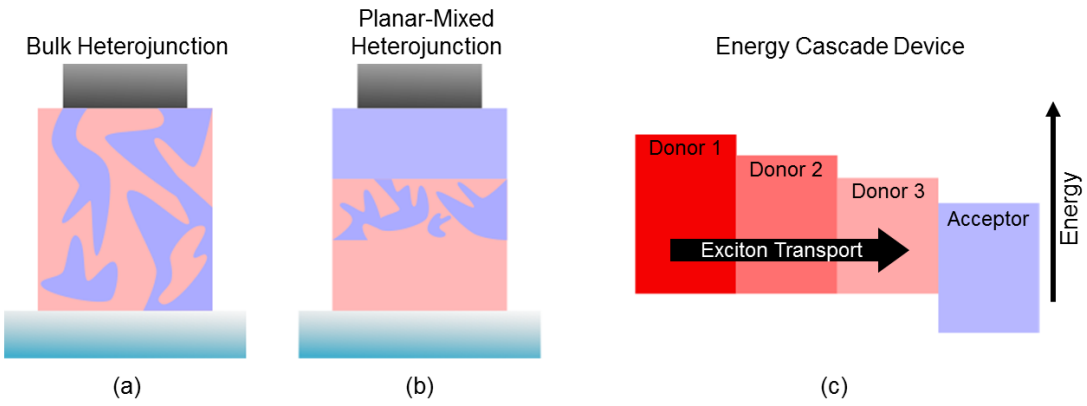

Figure 4.4 In addition to planar heterojunction devices shown in Fig 4.1a, OPVs can be made in (a) bulk heterojunction architectures, (b) Planar-mixed heterojunctions, and multilayer cells like (c) energy cascade devices. Bulk and planar mixed heterojunctions increase the donor-acceptor interface surface area and reduce the distance an exciton needs to diffuse to be dissociated. Energy cascade devices utilize multiple absorbing layers to achieve broadband absorption and increase diffusion efficiencies with long range Förster transfer between layers and an exciton gating effect which prevents back transfer of excitons.

Another disadvantage of BHJ devices is that when one material provides a continuous pathway between both electrodes, it removes the potential energy barrier of the D-A heterojunction which can lead to charge leakage, *i.e.* electrons to the anode or holes to the cathode, which reduces the operating voltage of the device.[123] To address this issue, BHJ and PHJ devices can be combined to form a planar-mixed heterojunction, shown in Fig. 4.4b, where a mixed layer is deposited between two planar layers. This architecture can reduce charge leakage effects, improving rectification, and aid in charge collection by ensuring a continuous pathway to the electrode.

Lastly, organic semiconductors have the advantage of being able to form multilayer stacks without the need for the rigorous lattice matching which is often necessary in inorganic devices.[5] This allows for relatively easy processing of devices which utilize multiple layers in order to achieve broadband absorption across solar spectrum. One example of this type of device is an energy cascade OPV. These devices consist of multiple planar layers with a single dissociating interface, incorporating multiple donors or acceptors with decreasing excitonic energy trending toward the dissociating interface, as shown in 4.4c.[124] These multilayer devices have been shown to achieve broad spectral absorption throughout the visible spectrum, internal quantum efficiencies approaching 100%, and high power conversion efficiencies.[125–127] The mechanism upon which they operate relies on cascading excitonic energies, such that there is sufficient overlap between the emission spectra of one layer and the absorption spectra of the next, for efficient long range Förster transfer to occur. This configuration also creates an exciton gating effect, biasing exciton transport toward the dissociating interface.[128] This results from the fact that an exciton residing immediately to the left of an interface will have a non-zero probability of moving either left or right; however, an exciton residing to the right of the interface in the smaller gap material will only move right, due to conservation of energy. These two effects result in very high values of η_D, while being able to fabricate simple PHJ architectures with efficient charge collection.

4.4 Device performance characterization

The performance of a photovoltaic device is determined by the current-voltage characteristics under illumination. In order to provide a standard to compare the performance of photovoltaic devices, the current-voltage behavior is typically measured

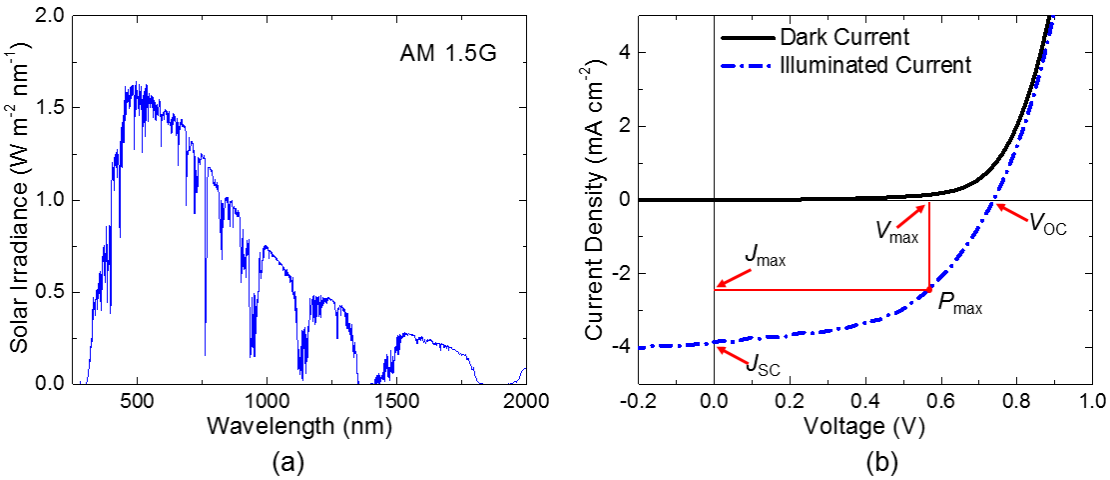

Figure 4.5 (a) The AM 1.5G solar spectrum at 1000 W m^{-2}, which represents a standard irradiance for which photovoltaic device performance are compared. (b) Current voltage characteristics of an OPV displaying the short-circuit current density (J_{SC}), open-circuit voltage (V_{OC}), maximum operating power point (P_{max}), its associated current density (J_{max}) and voltage (V_{max}).

under standard reporting conditions, which are Air Mass 1.5 Global (AM 1.5G) solar irradiance spectrum at 25 ºC with a total irradiance of 1000 W m^{-2}, referred to as 1 sun, which is shown in Fig 4.5a. AM 1.5G represents the light spectrum of the sun that is incident on the earth's surface and 1000 W m^{-2} is a representative intensity. As light passes through the earth's atmosphere, different molecules will scatter and absorb certain wavelengths of light more than others. Consequently, the spectrum that arrives at the earth's surface is dependent on the amount of atmosphere it has to travel through; 1.5 implies a path length of 1.5 times the thickness of the atmosphere vertically upwards, or the zenith, and a solar angle of 48.2º, which is representative of a yearly average for mid-latitude locations. A generic current-voltage (*J*-*V*) plot is shown in Fig. 4.5b. Here, positive current flow is defined as holes flowing from anode toward the cathode and electrons from the cathode toward the anode. Under illumination there are two contributions to this behavior. The first is the photocurrent generation which is produced by the five step mechanism described in Section 4.1, producing a negative current in the power generating

fourth quadrant. The rectifying behavior of the device occurs from the dark current contribution, where the device behaves like a diode in the dark. This is caused by injection of electrons and holes from the cathode and anode, respectively, which subsequently recombine when they meet at the D-A interface.

On this plot there are several points of merit which determine the performance of these devices. The short-circuit current density (J_{SC}) represents the maximum current that can be extracted from the device at a given illumination, occurring at zero volts. Given that the dark current is generally zero at short-circuit, J_{SC} gives the photocurrent that is produced when the anode and cathode are connected externally with no load resistance, *i.e.* short circuited. Consequently, this is inherently related the η_{EQE} described by Eqn. 4.4. The η_{EQE} can be determined by measuring the current produced by the device at zero applied bias as a function of monochromatic illumination, from which the ratio of collected charges to incident photons can be determined. This is usually done with a lock-in measurement to filter out the dark current and provide greater sensitivity to the measurement at low illumination intensities. Once the η_{EQE} has been measured, J_{SC} can be accurately predicted from the integrated spectrum as:

$$J_{SC} = \frac{q}{hc} \int \lambda \eta_{EQE}(\lambda) P(\lambda) d\lambda, \tag{4.6}$$

where h is Plank's constant, c is the speed of light, and P is the solar spectrum, *i.e.* AM 1.5G.

The open-circuit voltage (V_{OC}) represents the maximum voltage at which the device can operate in the power generating fourth quadrant. This is the voltage where the photocurrent is exactly canceled by the dark current, leading to no net current flow through

the device. Equivalently, this can be thought of as the voltage that is produced by the device when the anode and cathode are connected with an infinite load resistance.

Between these two extremes lies the maximum operating power point of the device (P_{max}). This is the point where the product of J and V is optimized ($J_{max}V_{max}$). Using these four values the fill factor (FF) of the device is determined by:

$$FF = \frac{J_{max}V_{max}}{J_{SC}V_{OC}}. \tag{4.7}$$

The FF reflects inefficiencies in the photoconversion process at forward bias voltages. Processes which contribute to this reduction are increased excitonic losses due to exciton-polaron annihilation, increased geminate recombination causing a larger fraction of CT states to recombine, or increases in non-geminate recombination leading to more charge carrier recombination.[100,110,117,126] Lastly, the power conversion efficiency (η_P), which is the most important figure merit, determines the fraction of incident optical power (P_0) that is converted into usable electrical power and is given by:

$$\eta_P = \frac{J_{SC}V_{OC}FF}{P_0} \times 100\% = \frac{J_{max}V_{max}}{P_0} \times 100\%. \tag{4.8}$$

For state of the art OPVs, J_{SC} values of ~12-16 mA cm^{-2} , V_{OC} ~0.8-1.2 V, FF > 65%, and η_P > 9% have been demonstrated, with a record efficiency of 13.2% for a multijunction cell.[22,127,129,130] In order for OPVs to become an economically viable technology, improvements in efficiency, device lifetime, and fabrication costs must be made so that the levelized cost of energy is competitive with traditional energy sources. From a device performance perspective, improvements in efficiencies should focus on optimizing J_{SC} and FF through innovations in device architecture and molecular engineering.

5. Experimental probes of exciton diffusion

The generation of photocurrent in OPVs relies on optically generated excitons diffusing to a D-A interface. As such, it is critically important to be able to accurately characterize the magnitude of L_D in order to build an understanding of how exciton diffusion limits device performance, as well as how material properties and device architectures can be manipulated to optimize diffusion and yield more efficient devices. However, measuring exciton diffusion is inherently difficult. In the vast majority of organic semiconductors excitons exist for only a few nanoseconds before decaying and diffuse very short distances, often on the order of ~10 nm.[68,70,80,83,105,131–136] Additionally, due the charge-neutral nature of the electron-hole pair, excitons are difficult to directly probe by electrical measurements. Consequently, exciton transport is usually characterized by measuring end of life products, namely, charge carriers resulting from exciton dissociation or photons resulting from radiatively decaying excitons which do not reach a dissociating interface. Here, a variety of different L_D measurement techniques broadly characterized by photon or charge carrier measurements will be discussed. In addition to presenting the method for extracting L_D, the advantages, disadvantages, constraints and assumptions of each technique will also be considered.

5.1 Optical modeling and the diffusion equation

Most L_D measurement techniques rely on combining some sort of experimentally generated data related to exciton quenching with a solution to an exciton diffusion equation. The most general form of this equation is given by Eqn. 3.8 and in many cases can be reduced to a single dimension (Eqn. 3.9). Additional first order and second order terms can be added to these equations to account for processes like exciton-exciton

annihilation, exciton-polaron quenching, or singlet fission, as we will see in subsequent chapters. This equation can be solved analytically (Appendix G); however, as additional terms are added to the equation it becomes necessary to use a numerical solution (Appendix E and H). Appropriate boundary conditions must also be employed in order accurately reflect the exciton dynamics of the system. It is often assumed that interfaces are either perfectly quenching ($n = 0$) or reflecting ($\frac{dn}{dx} = 0$) to excitons.[67,70,86,137] In reality, many interfaces may be partially quenching; however, this remains understudied. If an interface is indeed partially quenching, it will result in an overestimate or underestimate of L_D depending on whether the interface is modeled as perfectly reflecting or quenching, respectively.

One of the most important aspects of accurately modeling exciton diffusion is to properly account for the optical exciton generation term, $G(x)$. For films which are thicker than the optical absorption length, this can be approximated by a Beer-Lambert type absorption term.[70,77] Here, the optical exciton generation rate under monochromatic illumination is given by:

$$G(x) = \frac{I_0 \alpha}{cos(\theta)} e^{\frac{-\alpha x}{cos(\theta)}}, \tag{5.1}$$

where I_0 is the incident photon flux, θ is the angle of incident light, x is the position in the layer, and α is the absorption coefficient, given by $4\pi k/\lambda$, where k is the extinction coefficient and λ is the wavelength of light.

In device relevant architectures however, there are often multiple adjacent layers with thicknesses less than the wavelength of light, each with different indices of refraction. The amount light reflected and transmitted at each interface and propagated through each layer will be different, causing complex constructive and destructive interference patterns which

must be strictly accounted for using a transfer matrix formalism.[18,79] This approach relies on the following assumptions: (1) layers in the system are homogenous and isotropic, such that their optical response can be described by a scalar complex index of refraction; (2) interfaces are parallel and flat compared to the wavelength of light; and (3) the incident light can be described by a plane wave.

Figure 5.1 shows a generic, multi-layered structure for a series of films deposited onto a substrate. Each given layer (*j*) is described by its thickness (d_j) and complex index of refraction ($\tilde{n}_j = n_j + ik_j$), which can both be determined from spectroscopic ellipsometry. The total generating optical electric field at any point *x* in a given layer *j* can be expressed in terms of two component fields, one propagating in the positive *x* direction,$E_j^+(x)$, and one propagating in the negative *x* direction, $E_j^-(x)$.

At each interface, light can be transmitted and reflected. At an interface between layers *j and k*, Fresnel complex coefficients determine the fraction of the optical electric field that

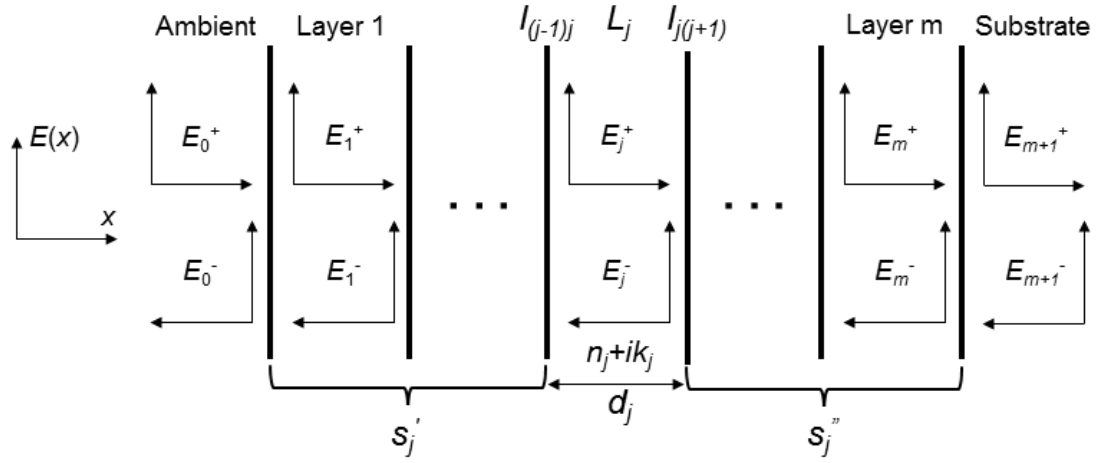

Figure 5.1 Representation of the transfer matrix method used to determine the optical electric field and exciton generation rate in an arbitrary stack of material consisting of *m* layers deposited on a substrate. Layer thicknesses (*d*) and optical constants (*n* + *ik*) are input for each layer. The generating electric field in each layer is expressed in terms two component fields, one propagating in the positive *x* direction (E^+) and one propagating in the negative *x* direction (E^-), which are calculated by the product of a series of matrices (*S',S"*) that describe the amount of light propagated at each interface (*I*) and through each layer (*L*).

is either reflected (r_{jk}) or transmitted (t_{jk}). For light with an electric field perpendicular to the plane of incidence (s-polarized), the coefficients are given by

$$r_{jk} = \frac{q_j - q_k}{q_j + q_k} \text{ and } t_{jk} = \frac{2q_j}{q_j + q_k}. \tag{5.2}$$

For light with an electric field parallel to the plane of incidence (p-polarized), the coefficients are given by

$$r_{jk} = \frac{-\tilde{n}_k{}^2 q_j + \tilde{n}_j{}^2 q_k}{\tilde{n}_k{}^2 q_j + \tilde{n}_j{}^2 q_k} \text{ and } t_{jk} = \frac{2\tilde{n}_k{}^2 \tilde{n}_j{}^2 q_j}{\tilde{n}_k{}^2 q_j + \tilde{n}_j{}^2 q_k}, \tag{5.3}$$

where

$$q_j = \tilde{n}_j cos\varphi_j = \sqrt{\tilde{n}_j{}^2 - n_0{}^2 sin^2\varphi_0}, \tag{5.4}$$

and n_0 is the refractive index of the transparent ambient, φ_0 is the angle of incidence, and φ_j is the angle of refraction in layer j. Using these coefficients, light propagation at each interface can be described by a 2×2 matrix:

$$I_{jk} = \frac{1}{t_{jk}} \begin{bmatrix} 1 & r_{jk} \\ r_{jk} & 1 \end{bmatrix}. \tag{5.5}$$

Additionally, light propagation and the phase change through each layer can be described by

$$L_j = \begin{bmatrix} e^{-i\frac{2\pi}{\lambda} q_j d_j} & 0 \\ 0 & e^{i\frac{2\pi}{\lambda} q_j d_j} \end{bmatrix}. \tag{5.6}$$

Using these matrices, the propagation of the optical electric field through the all of the layers can be determined from a total transfer matrix (S), calculated from the product of all the interface and layer matrices:

$$\begin{bmatrix} E_0^+ \\ E_0^- \end{bmatrix} = S \begin{bmatrix} E_{m+1}^+ \\ E_{m+1}^- \end{bmatrix} \tag{5.7}$$

and

$$S = \begin{bmatrix} S_{11} & S_{12} \\ S_{21} & S_{22} \end{bmatrix} = \left(\prod_{v=1}^{m} I_{(v-1)v} L_v\right) I_{m(m+1)}. \tag{5.8}$$

In order to calculate the electric field within a given layer, *S* can be expressed in terms of partial system transfer matrices where

$$S = S_j' L_j S_j''. \tag{5.9}$$

Extending Eqns. 5.2 through 5.9, the electric field in layer *j* as a function of *x* can be determined as:

$$E_j(x) = E_j^+(x) + E_j^-(x) = \frac{S_{j11}'' e^{-i\frac{2\pi}{\lambda} q_j (d_j - x)} + S_{j21}'' e^{i\frac{2\pi}{\lambda} q_j (d_j - x)}}{S_{j11}' S_{j11}'' e^{-i\frac{2\pi}{\lambda} q_j d_j} + S_{j12}' S_{j21}'' e^{i\frac{2\pi}{\lambda} q_j d_j}} E_0^+. \tag{5.10}$$

Next, the generating optical electric field profile must be converted to an exciton generation rate throughout the active layers. The number of excitons generated at a given position will be proportional to the amount of energy absorbed by the material. The time averaged absorbed energy of the electromagnetic field is determined from the modulus squared of the electric field, refractive index, and absorption coefficient as:

$$Q_j(x) = \frac{1}{2} c \epsilon_0 \alpha_j n_j \left| E_j(x) \right|^2, \tag{5.11}$$

where $\epsilon_0$is the permittivity of free space and *c* is the speed of light. Finally, the exciton generation rate can be calculated:

$$G(x) = \frac{Q_j(x)}{h\nu}, \tag{5.12}$$

where $h\nu$ is the energy of the incident photons. Example calculations of *E*(*x*) and *G(x*) in a PHJ OPV based on the D-A pairing of boron subphthalocyanine chloride (SubPc) and C_{60} is shown in Fig. 5.2. Devices based on this D-A pairing will be used to demonstrate many of the methods developed throughout this work. The device used for this example consists of a 15-nm-thick donor layer of SubPc deposited onto an indium tin oxide (ITO) covered

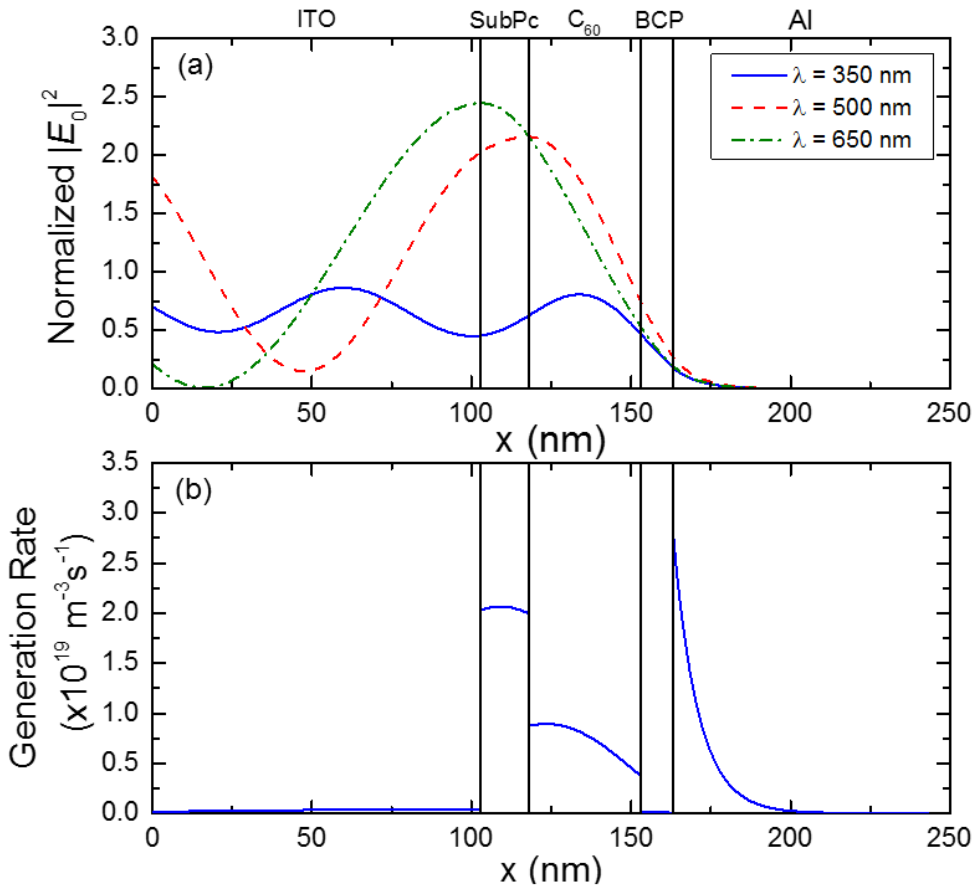

Figure 5.2 (a) Normalized electric field intensity in a planar heterojunction device based on donor and acceptor layers of SubPc and C_{60}, respectively, displaying the variation of the generating field in the active layers of the device at different incident wavelengths. (b) The total exciton generation rate in the device under AM 1.5G illumination at 100 mW cm^{-2}.

glass substrate, with a 35-nm-thick acceptor layer of C_{60}, a 10-nm-thick exciton blocking layer of bathocuproine (BCP) and an 80-nm-thick aluminum cathode. Figure 5.2a shows the modulus squared electric field normalized to the incident electric field (E_0^+) at three different incident wavelengths, demonstrating that interference within the device at different excitation wavelengths can cause drastically different optical field profiles throughout the device. Figure 5.2b displays the total generation rate throughout the device when AM1.5G illumination at 100 mW cm^{-2} is incident on the device. While the discussion thus far has focused on monochromatic illumination, the total generation rate under broadband illumination is given by $\int G(x,\lambda)d\lambda$. In addition to aiding in the fitting of L_D,

this type of model can also be used to guide device optimization by tuning layer thicknesses to maximize the generating electric field near the D-A interface.

5.2 Photoluminescence based diffusion length measurements

Photoluminescence quenching based measurements are perhaps the most widely used and arguably among the most accurate methods to determine L_D in materials of interest to OPVs. [67–70,80,105,132,135,136,138–145] These techniques generally rely on the interaction of optically generated excitons with an exciton-quenching material. Ideal exciton quenching materials should have a large energy offset with respect to the material of interest, so that excitons are exothermically quenched by charge transfer and a large enough energy gap to prevent Förster transfer to quencher, simplifying the fitting process.[146] Emitted photons represent radiatively decaying excitons which have failed to reach a dissociating interface; thus, L_D is inversely proportional the magnitude of the remaining PL. The exciton quenching material can be placed at an interface in a bilayer structure[67,68,70,105,135,136,138,139,144,145] or distributed throughout the bulk of the material[80,132,140–143] and PL is measured in either the steady-state[40,68–70,135,144,145] or transient regimes[80,105,132,136,138–143]. These measurements can be conducted with simple film architectures and experimental set ups. Additionally, because these techniques only require that a quenching material facilitates efficient charge transfer, and not necessarily dissociation, they are not subject to the charge carrier recombination losses that affect charge carrier based techniques, as we will see in Section 5.3. Therefore, PL quenching measurements offer an intrinsic value of L_D for the material under study without having to make assumptions about charge collection. However, they are incapable of measuring L_D

in a large class of organic semiconductors with exceedingly low η_{PL}, restricting the scope of materials that able to be accessed by these methods.

5.2.1 Thickness dependent photoluminescence quenching

Thickness dependent PL quenching measurements are conducted in the steady-state regime using a bilayer architecture, as shown in Fig. 5.3. In these measurements, films are excited with monochromatic illumination and PL spectra are measured for films both with (quenched) and without (unquenched) an adjacent exciton quenching material, as shown for a set of SubPc films in Fig. 5.4a. With these spectra, an experimental PL ratio can be constructed by dividing the integrated emission spectra of the quenched film (PL_Q) by the integrated spectra of the unquenched film (PL_{UQ}):

$$Exp.PL_{ratio} = \frac{\int PL_Q(\lambda)d\lambda}{\int PL_{UQ}(\lambda)d\lambda}. \tag{5.13}$$

The PL ratio is inversely proportional to the magnitude of L_D. As L_D is increased in the system, a larger fraction of excitons will reach the dissociating interface within their

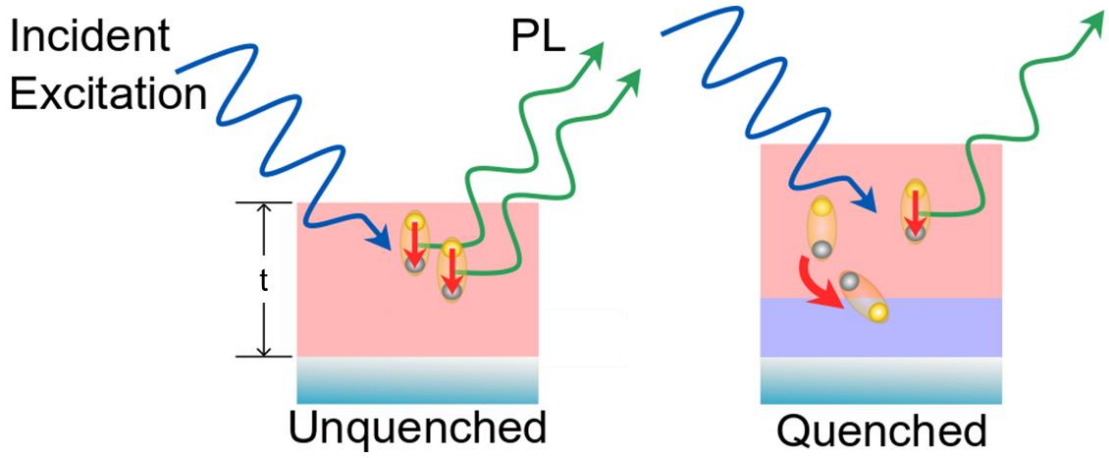

Figure 5.3 Schematic representing bilayer photoluminescence (PL) quenching. Photoluminescence is measured for a film both with (quenched) and without (unquenched) an adjacent exciton quenching layer. Reduction in PL of the quenched sample is proportional to the fraction of excitons which reach the dissociating interface and thus, the exciton diffusion length. The diffusion length is extracted by modeling the ratio of PL from the quenched to unquenched sample as a function of film thickness (t) or incident excitation wavelength.

lifetime, leading to a lower fraction of excitons which are capable of undergoing radiative recombination in the bulk of the film. Additionally, by constructing a ratio it can be assumed that the incident excitation and photon collection efficiency between the two samples is the same, eliminating the need to quantitatively determine these parameters, which can be difficult to accurately measure.

To extract L_D from these measurements, a calculated PL ratio is determined by solving a one-dimensional exciton diffusion equation, like Eqn. 3.9. Appropriate quenching and reflecting boundary conditions are applied to the quenched and unquenched films, respectively, and $G(x)$ is determined using the transfer matrix method outlined in Section 5.1, resulting in exciton density profiles as shown in Fig. 5.4b. The calculated PL ratio is then given by the ratio of the integrated exciton densities:

$$Calc.PL_{ratio} = \frac{\int n_Q(x,L_D)dx}{\int n_{UQ}(x,L_D)dx}, \tag{5.14}$$

which is equal to the ratio of integrated photoluminescence provided that η_{PL} of the two films is the same. Values of L_D are then iterated until Eqn. 5.14 matches Eqn. 5.13. It should be noted that in the steady state the fraction of excitons which reach the interface is only proportional the product of D and τ and not the magnitude of either individual component. While the magnitude of the exciton density will certainly be proportional to balance of D and τ, the PL ratio will only be proportional to the product; therefore, L_D is the only fit parameter in these experiments.

In order to provide a robust and confident fit for L_D, the PL ratio measured over a statistically significant number of samples with an increasing film thickness for the layer of interest, causing a large variation in the PL ratio. For the optically thin films used in these measurements, excitons are generated throughout the bulk of the film. As the

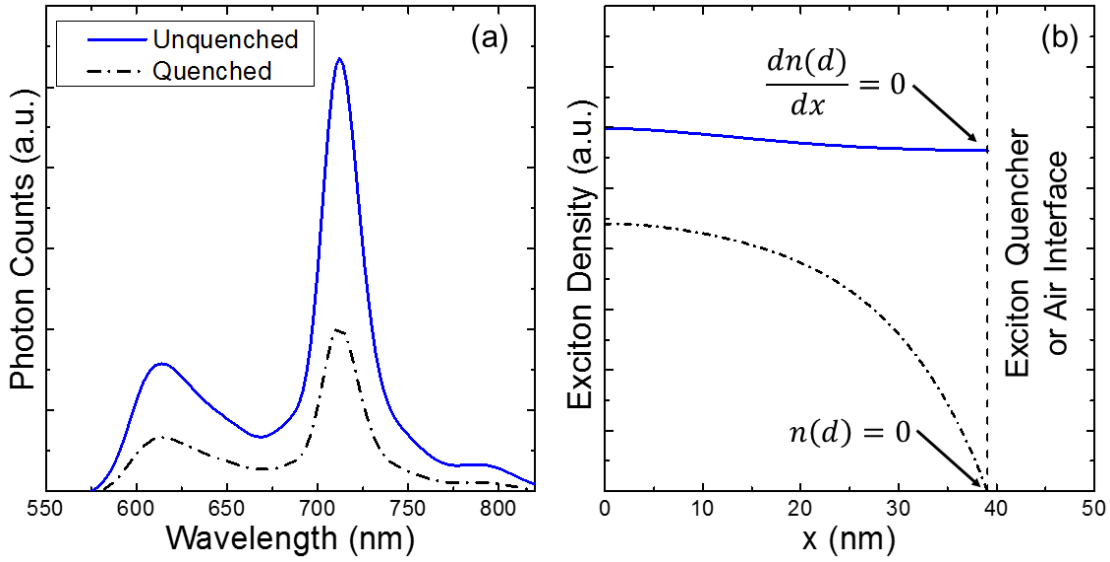

Figure 5.4 (a) Photoluminescence (PL) of a quenched and unquenched film of SubPc, used to construct an experimental PL ratio. (b) Modeled exciton densities in the quenched and unquenched films used to determine a calculated PL ratio. Exciton density profiles are modeled using the transfer matrix formalism coupled to solutions to the diffusion equation with appropriate reflecting and quenching boundary conditions. Values of L_D are iterated until the calculated and experimental PL ratios are equal.

thickness of the film increases, a smaller fraction of the total exciton population will be generated within L_D of the interface and consequently, a smaller fraction of excitons will reach the dissociating interface, leading to a larger PL ratio. Film thicknesses should be chosen such that they result in a large range of PL ratios, generally spanning thicknesses both above and below the value of L_D. An example of calculated PL ratios under varying values of L_D for a series of SubPc films is shown in Fig. 5.5. The value of L_D is then determined from a least squares fit of the difference between the calculated and experimental PL ratios.

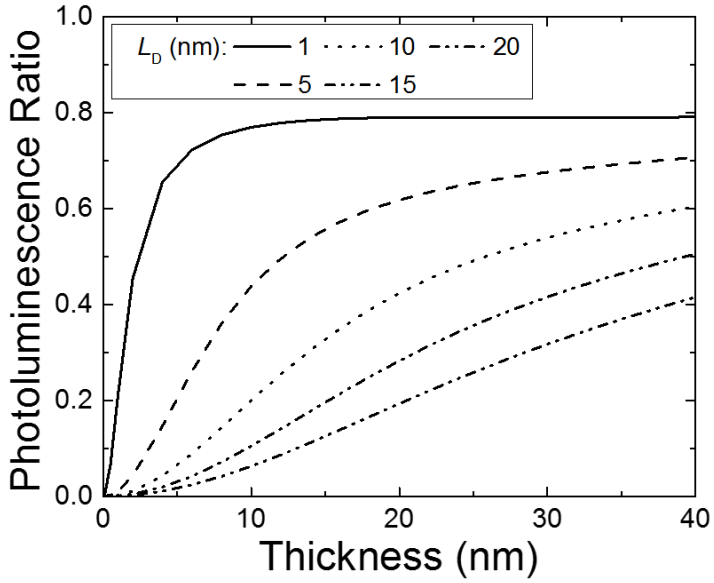

Figure 5.5 Simulated photoluminescence ratios as a function of film thickness for SubPc under varying values of the exciton diffusion length (L_D).

5.2.2 Spectrally resolved photoluminescence quenching

In addition to varying the thickness of the emitting film, the PL ratio can also be varied by changing the incident excitation wavelength and tracking the change in PL intensity at a single emission wavelength. This type of measurement is referred to as spectrally resolved photoluminescence quenching and is also conducted in bilayer architectures at steady-state.[70,135,144,145] The technique of mapping PL intensity as a function of excitation wavelength is called an excitation scan, an example of which for SubPc is shown in Fig. 5.6a. The shape of the excitation scan will generally look like the absorption spectrum of the film, but can be smeared out if the absorption length is less than thickness of the film. For these measurements, the PL ratio is not integrated, but rather kept as a spectral quantity. The model and fitting algorithm used in these measurements is nearly identical to thickness dependent measurements, the only difference being that excitation wavelength is varied instead of film thickness. In order to achieve a unique fit with these measurements, large

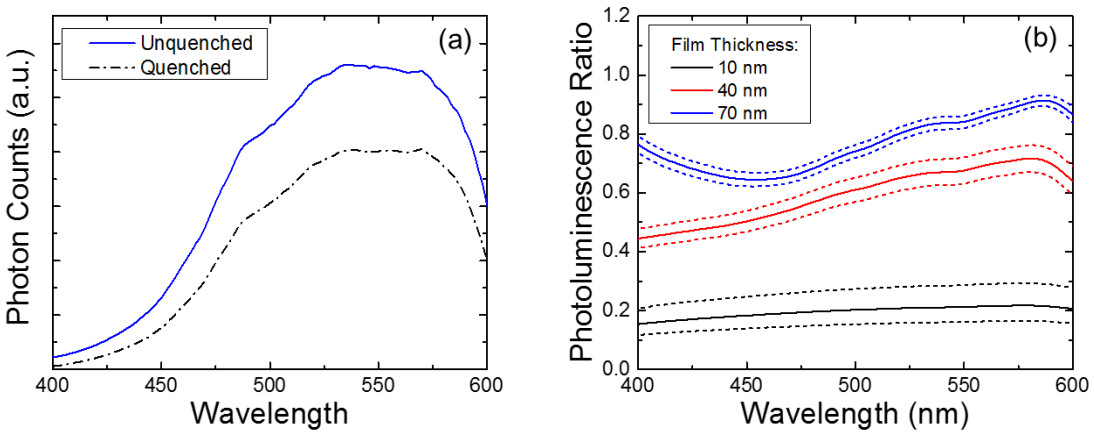

Figure 5.6 (a) Experimental excitation spectra of 40 nm quenched and unquenched films of SubPc used to determine experimental spectrally resolved photoluminescence ratios. (b) Simulated spectrally resolved photoluminescence ratios in films of SubPc with an L_D of 10 nm at varying film thicknesses. Dotted lines represent ±2 nm of L_D. As the film thickness is increased the spectral variation in the PL ratio increases, but the resolution of L_D decreases.

wavelength ranges should be measured spanning the absorption spectra of the layer of interest.

Additionally, care must be taken in choosing an appropriate film thickness which causes a large variation in optical field between the quenched and unquenched samples, producing a spectral variation in the PL ratio. Figure 5.6b displays spectrally resolved PL ratios for a SubPc film at three different film thicknesses. Solid lines represent the PL ratio with L_D = 10 nm and dashed lines represent ± 2nm on L_D. As the film thickness increases, so does the variation in the PL ratio, providing good spectral resolution; however, this plot also demonstrates that the resolution of L_D decreases as a function of film thickness. As such, film thicknesses should be chosen to balance the variation in PL ratio and resolution of L_D in order to achieve robust and unique fits. The advantage of this method is that an L_D measurement can be performed on a single film, rather than multiple films of varying thickness; however, this makes the technique sensitive to sample to sample variations in the PL intensity. As such, a statistically significant number of samples, which can be prepared in a single deposition, should be measured in order to eliminate this error.

5.2.3 Transient photoluminescence measurements

Similar to the steady-state PL quenching measurements discussed in the previous sections, values of L_D can also be extracted from a variety of transient PL measurements. In these measurements, samples are excited with a short excitation pulse, usually from a laser, and the PL is measured as a function of time. These measurements can be conducted in either bilayer[105,136,138,139] or bulk quenching architectures.[80,132,140–143] In bilayer architectures, the transient decay of a quenched sample is compared to the decay of an unquenched sample and is measured as a function of increasing film thickness. The luminescence intensity at time t is proportional to the exciton density, integrated over the thickness of the film. Solving Eqn. 3.9 in the transient regime allows for the decays to be fit for D. Combining this with τ, determined from the unquenched sample, L_D can be extracted while providing additional insight into exciton dynamics that are not accessible from a steady-state PL quenching measurement alone. The diffusion length can also be determined from fluorescence decays in bulk quenching architectures. Here a small amount of an exciton quencher, often 0.001 - 5 wt.%, is uniformly distributed throughout the film and PL decays are measured as a function of quencher concentration. As the quencher concentration increases, so does the probability of an exciton encountering a quenching molecule, reducing the PL decay time. While the bilayer methods discussed thus far determine a one-dimensional L_D in the direction perpendicular to the substrate, this approach probes diffusion in three-dimensions. Solving a spatially independent exciton decay rate equation, the rate constant for exciton quenching can be easily extracted from the quenched and unquenched decay times. This rate constant can then be fit for D using either a Stern-Volmer analysis,[140] sphere of capture Smoluchowski model,[141,142] or Monte

Carlo simulations.[80,143] With this approach, care should be taken to ensure that the quencher does not aggregate in the film and that the presence of the quencher does not affect the photophysics or morphology of the host material compared to the unquenched sample.

Transient PL decays can also be measured as a function of excitation intensity to extract *D*. In these measurements, the decay of a single unquenched film is measured as a function of excitation intensity causing exciton-exciton annihilation to shorten the PL decay time.[104,105,147] Similarly to the bulk quenching measurements, an exciton-exciton annihilation rate constant can be extracted by fitting the PL decays, which can then be used to determine *D*. While this approach is appealing because it only requires a single film, extracting *D* depends the annihilation radius, which can be difficult to accurately determine. Additionally, films must have good photochemical stability due to the intense laser light required to create exciton densities high enough for annihilation to occur.

5.2.4 Photoluminescence Imaging

Recently, advanced imaging techniques have been used to directly observe the motion of excitons by imaging PL in both the steady-state and transient regimes.[47,82,148–150] These experiments are usually performed on highly crystalline, luminescent materials with micron scale L_D. Excitons are generated by a collimated laser that is focused onto the sample and the PL resulting from excitons diffusing away from the excitation spot is spatially mapped using either a streak camera or a single photon counter which is rastered over the sample. The image of the PL intensity can then be converted to an exciton density distribution, which is then fit to solutions of the diffusion equation, extracting L_D. Additionally, in the transient domain, the temporal dependence of *D* can be used to extract information about how energetic disorder affects exciton diffusion.[47,149] This technique is

limited by the relatively large spot size of the excitation laser compared to L_D, restricting the scope to samples with high D; however, recent work on inorganic quantum dot films has suggested that L_D on the order of tens of nm may be accessible using this method.[149]

5.3 Charge carrier based diffusion length measurements

While PL represents excitons which fail to reach a dissociating interface, charge carrier based techniques probe the number of excitons which are successfully dissociated at a D-A interface. The number of generated charge carriers can be determined by measurements of photocurrent (Fig. 5.7a),[18,151–155] the conductivity in a quenching layer either optically[134,156,157] or electrically[77], or photovoltage,[158] which will be covered extensively in Chapter 7. These techniques do not necessitate that the material of interest be emissive and are therefore capable of probing the diffusion of singlet excitons in materials with low η_{PL} and dark triplet excitons. Additionally, these techniques are often performed in OPV

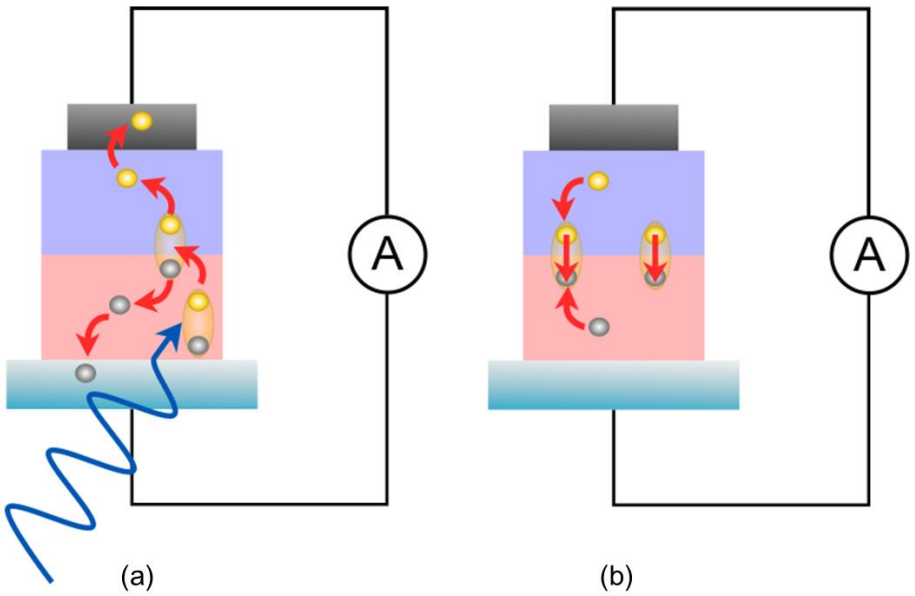

Figure 5.7 (a) Photocurrent-based L_D measurements rely on the collection of generated carriers, measuring the photocurrent created under monochromatic illumination and fitting of the η_{EQE} spectrum. (b) Geminate (right) and non-geminate (left) free carrier recombination mechanisms that may occur during carrier collection. These mechanisms can lead to underestimates of the number of excitons which reached the interface and underestimates of L_D

architectures, rather than films, ensuring that device characteristics like film morphology, substrate interactions, and interfaces accurately reflect the environment the excitons sample during device operation. However, unlike PL-based techniques, these measurements are subject to charge-collection losses, as shown in Fig. 5.7b. In an OPV, excitons which reach the D-A interface are efficiently converted to charge-transfer states; these charge-transfer states can either be dissociated into mobile charge carriers or undergo non-geminate recombination at the interface. Generated charge carriers are either collected at the electrodes as photocurrent or are lost to non-geminate recombination with a charge carrier of opposite polarity, either at the interface or in the bulk of the material.[94,114–117] If geminate and non-geminate recombination are not properly accounted for when using these techniques, the number of generated charge carriers will underestimate the number of excitons which reached the interface and subsequently, underestimate L_D.

5.3.1 Photocurrent based measurements

The most straightforward of the charge carrier-based techniques are photocurrent measurements where a PHJ OPV is illuminated with monochromatic illumination and the steady-state short-circuit current is measured. Repeating this measurement as a function of excitation wavelength allows for the determination of the device η_{EQE}, as shown for a PHJ SubPc-C_{60} device in Fig. 5.8. Recall from Chapter 2 that the η_{EQE} results from five successive photoconversion steps, each characterized by their own efficiency. Using the transfer matrix formalism discussed in Section 5.1 $\eta_A(\lambda)$ can be accurately predicted. Coupling this with solutions to the diffusion equation, $\eta_D(\lambda, L_D)$ is determined based on the flux of excitons at the dissociating interface, with SubPc and C_{60} L_D as the fit parameters. It is usually assumed that in a heterojunction OPV with a sufficient energy offset at the

interface that η_{CT} = 1. However, there are not simple established methods capable of accurately predicting η_{CS} and η_{FC}. As such, if η_{CS} and η_{FC} are naively assumed to be unity, the fitting algorithm will incorporate these losses into η_D and underestimate values of L_D. Figure 5.7 displays three different simulated η_{EQE} curves under varying values of SubPc and C_{60} L_D, when $\eta_{CS}\times\eta_{FC}$ = 1. Here, the experimental η_{EQE} is best fit when the SubPc L_D = 8.3 nm and C_{60} L_D = 14.9 nm. However, when the predicted photocurrent is multiplied by a non-unity charge collection efficiency, for example $\eta_{CS}\times\eta_{FC}$ = 0.8, a nearly identical fit is produced, yielding SubPc L_D = 11.1 nm and C_{60} L_D = 20.1 nm. This demonstrates the disadvantage of this method, where unique fits to the data cannot be achieved without detailed knowledge of charge collection efficiencies in the device at short-circuit.

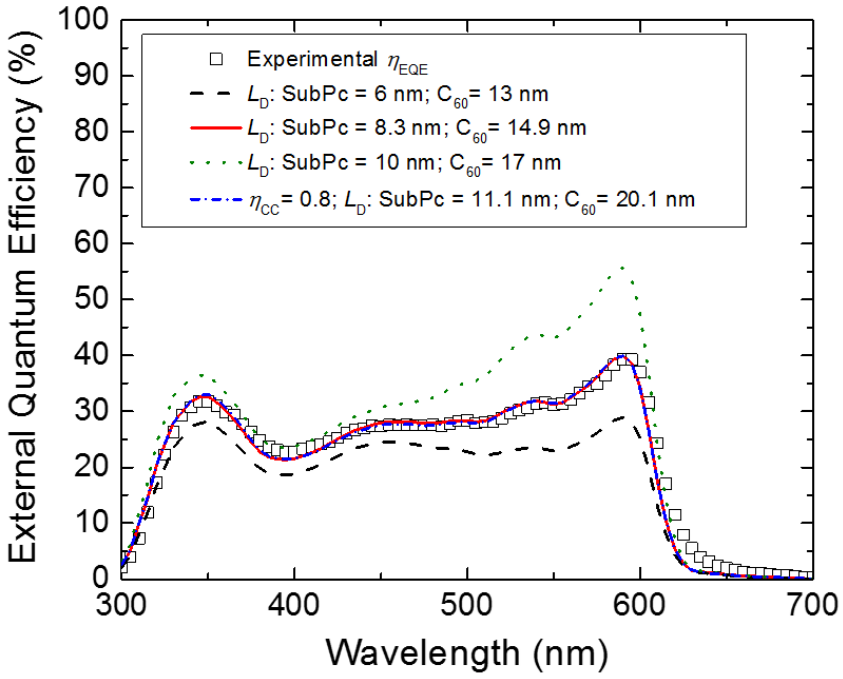

Figure 5.8 Experimental and simulated values of the external quantum efficiency for a PHJ SubPc C_{60} device. The experimental data can be well fit for L_D with good resolution; however, unique fits of the exciton diffusion length (L_D) depend of the charge collection efficiency (η_{CC}), which can be difficult to experimentally determine.

5.3.2 Conductivity based measurements

Another approach to extract L_D through charge carrier measurements is to monitor the change in photoconductivity in a quenching layer. This can be done optically using time-resolved microwave conductivity,[134,156,157] or electrically through surface photoconductivity measurements.[77] Time-resolved microwave conductivity is an electrode-less technique, where a bilayer structure consisting of the material of interest and a quenching layer, often TiO_2, is excited with a short optical pulse and the time dependent conductivity in the quenching layer is monitored based upon the reflected optical power from a microwave cavity. The reflected optical power is proportional to the conductivity in the quenching layer, which depends on the number of dissociated excitons and hence, L_D. This technique requires only a single sample, is capable of probing non-emissive materials, and does not require charge collection, eliminating non-geminate recombination losses; however, rapid interfacial geminate recombination could still affect these measurements. Furthermore, because TiO_2 is not typically used as an acceptor in OPVs, the amount of geminate recombination will be different than in a functioning device.

Surface photoconductivity measurements can be used to determine L_D in highly crystalline materials with anisotropic optical constants. In this technique, electrodes are deposited on the top surface of a crystalline sample and the surface photocurrent, resulting from exciton dissociation at the bare surface or in the presence of a quenching material, is measured as a function incident light polarization angle. In highly crystalline materials, different molecular orientations along different crystallographic directions can result in anisotropic absorption coefficients. Changing the polarization angle will then result in different absorption lengths, causing a periodic variation in the surface conductivity,

provided L_D is sufficiently long. The relative amplitude of the photoconductivity variation is then fit for L_D. Similar to a PL ratio, this normalized photoconductivity cancels many experimental parameters, including the efficiency of exciton dissociation at the surface. This technique requires only a single sample and is convenient for measuring L_D of single crystal samples, which are difficult to implement into device architectures or grow consistently for PL measurements.

5.4 Conclusions

Of the many techniques capable of determining L_D, each has its own advantages, constraints, and assumptions and the appropriate technique to use depends on the information one wishes to extract and the experimental tools that are available. Photoluminescence quenching techniques are not subject to charge collection losses and provide an intrinsic value of L_D for the material under study, but are only applicable to materials with sufficient η_{PL}. Steady-state PL quenching techniques require simple experimental set ups and for spectrally resolved measurements only require one film thickness. Transient PL quenching measurements require fast detection electronics, but are capable of decoupling D and τ using a single measurement. Photoluminescence imaging techniques visualize exciton motion in real time, but are restricted to emissive, highly crystalline samples with micron scale L_D. Charge carrier based techniques like photocurrent and conductivity measurements can probe exciton diffusion in both luminescent and dark materials, but are restricted by charge collection losses which can be difficult to decouple. Values L_D extracted from these experiments will agree with PL values only in the absence of geminate and non-geminate recombination. In the coming chapters, a variety of these techniques will be used to provide a deeper understanding what affects

exciton diffusion in organic semiconductors, new techniques to measure L_D will be developed, and different techniques will be combined to provide a comprehensive understanding of the excitonic and charge carrier recombination mechanisms which limit OPV device performance.

6. The effect of materials purity on exciton transport

The importance of achieving a high material purity is often stressed within the field or organic electronics.[15,47,159–161] Material purities >99% and orders of magnitude greater are often achieved for the source materials used to fabricate organic electronic devices.[15] Impurities that are present in these materials are typically synthesis reaction side products, residual metallic catalysts, or oxidation products.[160–163] Work done on organic field-effect transistors has shown that trace impurities can have a dramatic impact on the measured carrier mobility in these materials.[164] Additionally, it has been demonstrated that impurities can also affect OPV device performance, potentially limiting J_{SC}, V_{OC}, and *FF*, primarily by reducing carrier mobilities and increasing in trap-assisted recombination.[160,163–166] Substantially less attention has been paid to understanding how impurities can impact the magnitude of L_D. Examples in the literature have cited that large variations in L_D can occur depending on the batch and purity of the source material; however, these studies are not quantitative about the level of impurities or nature of the interaction between the impurities and excitons.[47,159]

In this chapter, different types of impurities found in organic semiconductors and their impact on exciton diffusion are discussed. In order to quantify how native molecular impurities can affect exciton diffusion, L_D and other relevant photophysical parameters are measured as impurities are systematically removed from a batch **of** *N*,*N*′-bis(naphthalen-1-yl)-*N*,*N*′-bis(phenyl)-benzidine (α-NPD). The diffusion length is determined by thickness dependent PL quenching using dipyrazino[2,3-f:2',3'-h]quinoxaline-2,3,6,7,10,11-hexacarbonitrile (HATCN) as an exciton quencher due to its favorable energy offset for electron transfer and large energy gap which prevents Förster transfer from α-NPD to

HATCN.[146,167,168] The source material was synthesized by The Dow Chemical Company and was subsequently purified once by thermal gradient sublimation purification and additional increases in thin film purity were realized at different deposition boat temperatures. Thin film purities were measured by The Dow Chemical Company using high-performance liquid chromatography (HPLC). Lastly, the trend of L_D as a function of impurity concentration is modeled in order to extract an impurity free, theoretical maximum value of L_D, providing quantitative insight into the levels of impurities that can be tolerated without being detrimental to exciton diffusion.

6.1 Interactions of excitons with impurity molecules

Impurities can hinder exciton diffusion by trapping, quenching, or dissociating excitons. For organic impurities, the exact mechanism depends on both the nature of the diffusing exciton, namely whether or not is capable of emitting light (Fig. 6.1 a,b), as well as the energetic alignment of the impurity molecule with respect to pure host material (Fig. 6.1 c-e). For fluorescent materials, if there exists an overlap in the emission spectrum of pure host and the absorption spectrum of the impurity molecule, excitons will be able to transfer to the impurity molecule *via* Förster transfer. This type of impurity is likely the most detrimental to exciton diffusion due to the long range dipole-dipole interaction (Fig. 6.1a), consistent with Eqn. 3.3. Once an exciton is transferred to the smaller energy gap impurity, transfer back to the host is energetically unfavorable and the exciton will become trapped and eventually decay. In materials with exceedingly low η_{PL}, if an overlap in resonant energy states still exists, excitons will may transfer to the impurity molecule *via* Dexter transfer (Fig. 6.1b). While the relative energetic alignment (Fig. 6.1c) and end result of these two mechanisms are the same, in this case, there must exist a spatial overlap

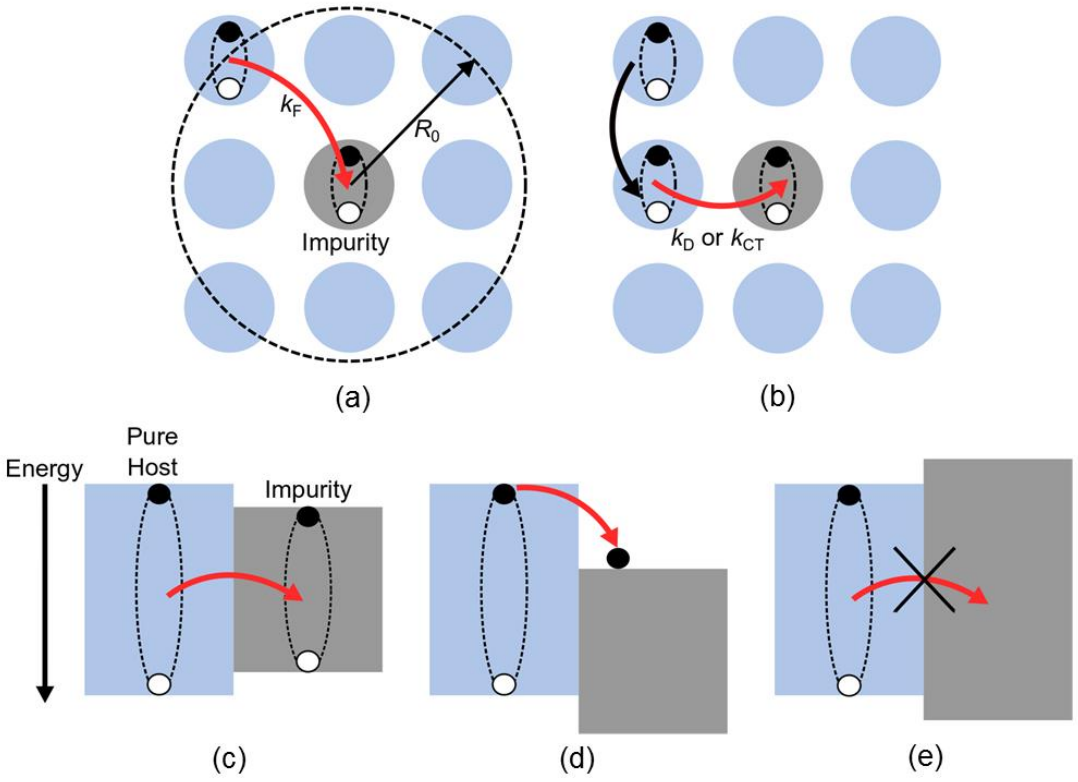

Figure 6.1 (a) Impurity exciton quenching by Förster transfer. Quenching is relatively long range with the rate k_F proportional to the Förster radius, R_0. (b) Impurity quenching by a Dexter or charge transfer mechanism occurring over nearest neighbors with rate k_D or k_{CT}. (c) Energy level alignment required for Förster or Dexter quenching. Processes requires overlap of emission and absorption between pure host and impurity, respectively. The dominant mechanism will be dictated by whether the host is capable of emission. (d) Energy level alignment required for quenching by charge transfer. The impurity will dissociate excitons if the energy offset is greater than the exciton binding energy. (e) Energy level alignment of an inert wide energy gap impurity.

between the electronic orbitals of the two molecules and thus this process occurs on a much shorter, nearest neighbor length scale, consistent with Eqn. 3.7. Therefore, it is expected that Dexter impurities will be less detrimental to exciton diffusion than Förster impurities at a given concentration, due to the smaller capture radius. If no sufficient overlap between emission and absorption exists, but there is an offset in the energy levels which exceeds the exciton binding energy between the impurity molecule and the pure host (Fig. 6.1d); the impurity will be able to dissociate excitons by charge transfer. Charge transfer also requires electronic orbital overlap and occurs on a nearest neighbor length scale.[57] It is

expected that charge transfer impurities will have a similar dependence of L_D on impurity concentration as Dexter impurities. All three of these mechanism will serve to reduce the effective τ of the exciton and negatively impact L_D. The last type of organic impurity that can be present in these systems is an impurity molecule with a wider energy gap than the pure host material (Fig. 6.1e). In this case, energy transfer to the impurity molecule is not energetically favorable and these types of impurities are not expected to affect L_D in trace quantitates. At larger concentrations however, these molecules could begin to alter the photophysics of the host material and impact exciton diffusion.[67]

Metallic impurities present from residual catalysts or diffusion of metal atoms from the cathode into an organic layer will also negatively impact exciton diffusion. A large number of studies have demonstrated that a layer of metallic material can quench excitons through a long range CPS interaction, named for Chance, Prock, and Silbey who developed the theory in 1975.[169–172] In this type of interaction, the dipole created by the exciton interacts with the metal electron gas, transferring its energy non-radiatively with a rate proportion to x^{-3}, where x is the distance to the quenching metallic interface. Studies have also shown that individual metal atoms, where an electron gas is not present, are capable of quenching excitons through a long range Förster like process, reducing the magnitude of L_D.[173–176] With these mechanisms in mind, we can now begin to quantitatively examine the relationship between material purity and L_D.

6.2 Increasing and quantifying material purity

6.2.1 Thermal gradient sublimation purification

Thermal gradient sublimation is a common method used to purify small molecule organic semiconductors. This technique uses a temperature gradient to exploit differences

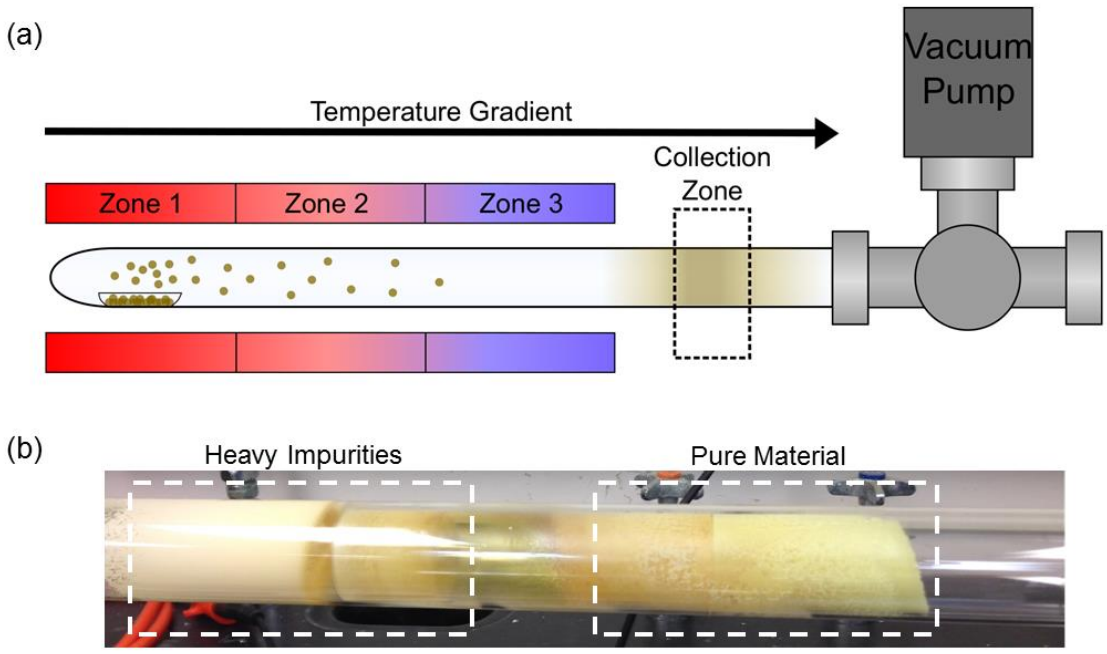

Figure 6.2 (a) Schematic of thermal gradient sublimation purification set up. Source material is loaded into a long quartz tube, placed under vacuum, and inserted into a three zone furnace. Sublimed material transports down the length of the tube and the temperature gradient spatially separates material based on the volatility. (b) Picture of the collection zone in a purification of α-NPD. Pure α-NPD zone can be seen as spatially separated from heavy impurities which are closer to source material.

in vapor pressure in order to spatially separate a pure target material from impurities present in the source material.[161,177] A schematic of this experimental set up is shown in Fig. 6.2a. Source material is first loaded into the sealed end of a long quartz tube. The tube is then placed under vacuum and inserted into a three zone furnace in order to apply a temperature gradient. The source material at one end is heated above the sublimation temperature and the sublimed material begins to transport down the length of the tube. Along the temperature gradient, molecules will begin to deposit onto the walls, spatially separated based on their volatility. Materials with a low vapor pressure, often high molecular weight impurities, will either remain in the deposition boat or deposit in the hotter regions of the tube. Materials with higher vapor pressures, often low molecular weight impurities, will deposit further down the tube, spatially separated from the pure

target material, which deposits between these two regions.[178] In order to facilitate material collection, the inside of the tube is lined with quartz sleeves that can be removed and material is then collected by scraping these sleeves.

To minimize contamination, the glassware used in these experiments were rinsed with DI water, isopropanol, and acetone and etched using a 3:1 sulfuric acid and 30% hydrogen peroxide mixture and then baked at 500 ºC overnight to remove any residual solvents. An initial quantity of 11.4 g of the starting source material was loaded into a deposition boat and placed at the end of the quartz tube. In order to bake off any residual solvent present in the source material, the system was pumped down to a base pressure of 1.8×10^{-6} Torr and all three zones of the furnace were set at 120 ºC and left overnight. The sample material was then purified by setting all three furnace zones to 260 ºC at a base pressure of 3.4×10^{-7} Torr and left for 8 days, in accord with previous purifications of this material.[161] Separation was achieved by a linear temperature gradient which starts at the output of the furnace, at the end of zone 3. After the completion of the purification, the system was crash cooled to room temperature by turning off and removing the furnace and then 9.1 g of target material was collected from the 3rd and 4th quartz sleeves, shown in Fig. 6.2b. For more complete details of the purification, see Appendix C.

6.2.2 High-performance liquid chromatography

Thin film purities were measured by HPLC by Wayne Blaylock at The Dow Chemical Company. In this technique, the material of interest is dissolved into a solvent and the solution is pressurized and passed through a column filled with an adsorbent material. Each molecule present in solution will have a slightly different adsorbent interaction within the packed column. This will cause a different flow rate for each type of molecule, separating

the solution.[179]As the different components exit the column, the absorbance of the solution is monitored as a function of time using ultraviolet-visible spectroscopy (UV/Vis). From this data, the relative quantities of each component in the solution can be determined based upon their absorbance area, assuming the molar absorbance is similar for each component. In addition to UV/Vis, it is common to also use mass spectrometry to determine the chemical structure of each component; however, no such analysis was used in this study.

Solutions used for HPLC analysis were prepared from ~100 nm films of α-NPD deposited on glass microscope slides. In order to ensure that these films were representative of the samples used to measure L_D, the slides remained on the deposition chuck throughout the duration of a growth, incorporating all layers of the thickness dependent PL quenching samples. These films were dissolved in tetrahydrofuran at concentrations of 2 mg/mL. Samples were measured on an Agilent 1200 Series HPLC system with an injection volume of 10 μL and a flow rate of 1 mL/min. Purity was determined by HPLC area percent assay and error bars are based upon the standard deviation in HPLC % across six different solutions prepared from six different slides. The results of these measurements, reported as HPLC % versus elution time, are given in Table 6.1 for the four different purities

Elution Time (min)	97.1% Sample (HPLC %)	98.3% Sample (HPLC %)	98.8% Sample (HPLC %)	99.0% Sample (HPLC %)
4.09	1.44 ± 0.72	0.94 ± 0.50	0.58 ± 0.12	0.27 ± 0.15
7.98 (α-NPD)	97.12 ± 1.22	98.29 ± 0.84	98.83 ± 0.20	99.03 ± 0.31
8.35	0.10 ± 0.04	0.13 ± 0.01	0.00 ± 0.00	0.09 ± 0.06
9.40	0.08 ± 0.03	0.02 ± 0.02	0.00 ± 0.00	0.00 ± 0.00
9.57	0.30 ± 0.01	0.09 ± 0.01	0.21 ± 0.01	0.25 ± 0.01
10.5	0.84 ± 0.42	0.45 ± 0.29	0.38 ± 0.10	0.36 ± 0.19
11.71	0.12 ± 0.08	0.08 ± 0.06	0.00 ± 0.00	0.00 ± 0.00

Table 6.1 Experimental HPLC data of elution time and HPLC purity, determined by HPLC area percent assay. Error bars were determined by the standard deviation in HPLC % across six measured samples for each purity. Data was taken from 100 nm films of α-NPD deposited on glass substrates and dissolved in tetrahydrofuran at concentrations of 2 mg/mL.

considered in this study. Here, each different peak that is measured at a different elution time represents a different type of impurity molecule that is present in the film.

6.3 α-NPD diffusion length as a function of purity

6.3.1 α-NPD diffusion length measurements

Films deposited from the as synthesized source material yield L_D = (3.9 ± 0.5) nm with a corresponding thin film organic purity of (97.1 ± 1.2) %. The source material was then purified by thermal gradient sublimation purification and films grown under the same deposition conditions show an increased value of L_D = (4.7 ± 0.5) nm and purity of (98.3 ± 0.8) %. No further increases in L_D were realized with successive purifications of the source material. Interestingly, it was also observed that the value of L_D and thin film purity showed a dependence on the deposition boat temperature. Initial films were grown at boat temperature of (258 ± 10) ºC, corresponding to a deposition rate of 0.3 Å/s. As the boat

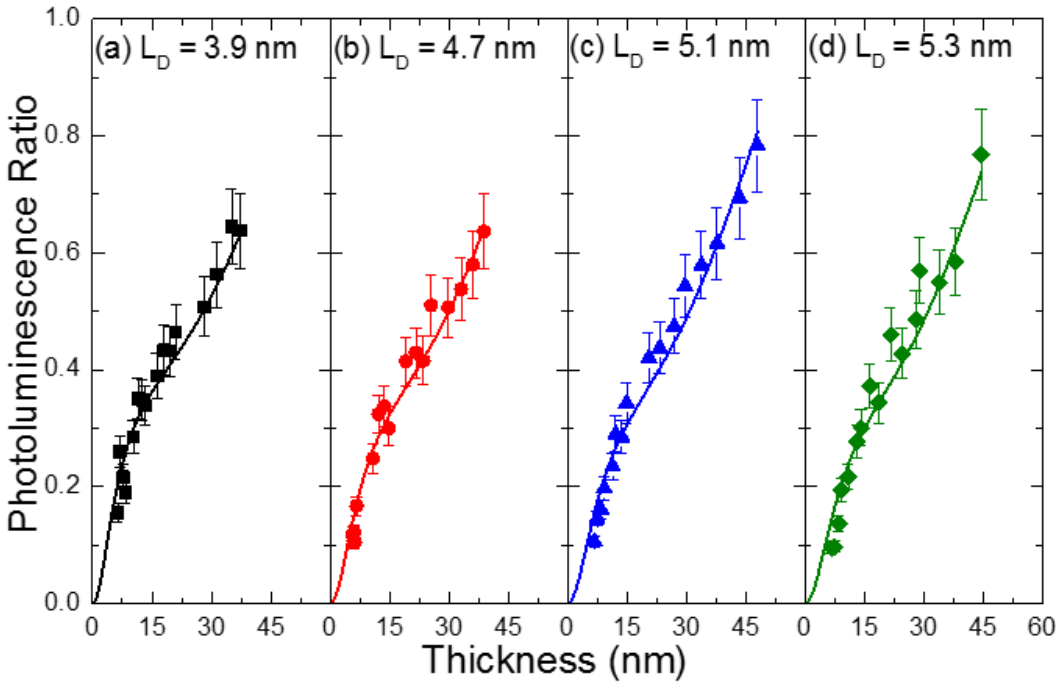

Figure 6.3 Photoluminescence ratios versus film thickness for α-NPD films with organic purities of (a) 97.1% (b) 98.3% (c) 98.8% (d) 99.0% along with the corresponding exciton diffusion lengths (L_D). Solid lines represent fits based on a one-dimensional steady state exciton diffusion model at the given values of L_D.

temperature was increased to (324 ± 10) ºC with a deposition rate of 8.8 Å/s, films deposited from the purified source material increased systematically in both L_D and purity, resulting in values of (5.3 ± 0.9) nm and (99.0 ± 0.3) %, respectively. This represents a 36% increase in L_D for a 1.9% increase in thin film purity. Photoluminescence ratios and L_D fits are shown in Fig. 6.3.

In order to determine if changes in crystallinity are contributing to increases in L_D with increasing deposition rate, X-ray diffraction spectra were measured; however, no scattering peaks were observed.[66,143,144] Therefore, we conclude that increases in material purity are driving the increase in L_D and the dependence on deposition rate is caused by additional material purification during the deposition process. One scenario in which this could occur is if impurities are preferentially sublimed while ramping the deposition rate to the set point. For higher deposition rates, more material will be sublimed during the ramp phase, potentially leaving a higher purity source material when the deposition process begins.

6.3.2 α-NPD photophysics and diffusion length predictions

In order to determine what is changing photophysically in the system as a function of purity, η_{PL} and τ were measured in concert with L_D. Results of these measurements are listed in

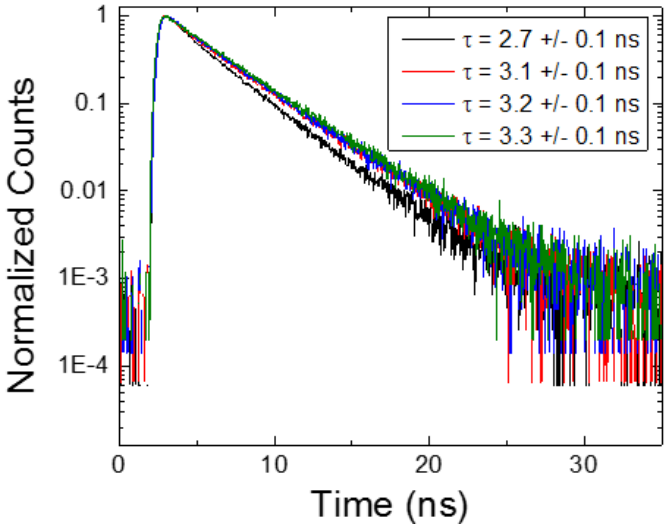

Figure 6.4 Transient photoluminescence decays of 40 nm α-NPD films with corresponding purities of 99.0% (green), 98.8% (blue), 98.3% (red) and 97.1% (black) and their fitted exciton lifetimes as measured by time correlated single photon counting. Error bars were determined by the standard deviation in measured lifetime across twelve samples and three separate depositions.

Table 6.2 and lifetime decays are shown in Fig. 6.4. It was observed that increases in L_D coincide with concomitant increases in both η_{PL} and τ; increasing from η_{PL} = (25 ± 1) % and τ = (2.7 ± 0.1) ns for the 97.1% pure films to η_{PL} = (37 ± 1) % and τ = (3.3 ± 0.1) ns for the 99.0% pure films. Based on these measurements, values of k_R and k_{NR} can be decoupled using Eqns. 2.2 and 2.3. As the purity increases from 97.1% to 99.0%, k_{NR} systematically decreases from (28 ± 2)×10^7 s^{-1} to (19 ± 1)×10^7 s^{-1}. This reduction drives an increase in τ, offering the exciton more time to diffuse before it recombines. For the same change in purity, k_R increases from (9.3 ± 0.5)×10^7 s^{-1} to (11 ± 1)×10^7 s^{-1}. As detailed in Section 3.3, for materials which transfer their energy *via* Förster transfer, *D* is directly proportional to the magnitude of k_R. Thus, the increase in k_R is also driving an increase in *D*, due to an enhanced Förster radius.

Based on the observed enhancement in the photophysics, predictions of L_D can be made using a convention model of diffusion by Förster transfer using Eqn. 3.13. A value of d = 0.58 nm was calculated from the volume averaged radius using the crystal density of α-NPD.[70,180] Additionally, no shift in emission or change in optical constants were observed, leaving only the measured η_{PL} to drive the increase in predicted L_D. These results, listed in Table 6.2, are in good agreement with the measured values of L_D, validating this model of

Organic Purity (%)	L_D (nm)	η_{PL} (%)	τ (ns)	Predicted L_D (nm)
97.1 ± 1.2	3.9 ± 0.5	25 ± 1	2.7 ± 0.1	4.3 ± 0.6
98.3 ± 0.8	4.7 ± 0.6	33 ± 1	3.1 ± 0.1	4.8 ± 0.7
98.8 ± 0.2	5.1 ± 0.6	34 ± 1	3.2 ± 0.1	4.9 ± 0.7
99.0 ± 0.3	5.3 ± 0.9	37 ± 1	3.3 ± 0.1	5.1 ± 0.7

Table 6.2 Experimentally determined values of the thin film purity, exciton diffusion length (L_D), photoluminescence efficiency (η_{PL}), exciton lifetime (τ), and predicted L_D calculated using an exciton diffusion model based on Förster theory.

diffusion and confirming that changes to k_R and k_{NR} caused by the decrease in concentration of exciton quenching impurities are responsible for the observed trend in L_D. While the decrease in k_{NR} and increase in τ were expected to occur as exciton quenching impurities are removed from the films, the increase in k_R and D was unexpected.

6.3.3 Modeling the exciton diffusion length as a function of purity

Along with the measured L_D values, it is informative to model this trend of L_D versus purity in order to better understand what increases can be realized at thin film purities beyond 99.0%. The effect impurities have on L_D can be modeled by a simple one-dimensional steady state diffusion equation incorporating a term accounting exciton quenching by impurities:

$$0 = D\frac{\partial^2 n}{\partial x^2} - \frac{n}{\tau_0} + G - nk_Q, \tag{6.1}$$

where τ_0 is the natural lifetime of the exciton in the absence of impurities and k_Q is the average rate of exciton quenching by impurities in the steady state. Previously, it was demonstrated that impurities can dramatically affect k_{NR}. If k_{NR} is expressed as the sum of the component losses, $k_{NR} = (k_{NR}^0 + k_Q)$, where k_{NR}^0 is the intrinsic non-radiative decay rate, an effective lifetime can be expressed as $1/\tau = (k_R + k_{NR}^0 + k_Q) = 1/\tau_0 + k_Q$. In this formalism, the change in the non-radiative exciton decay rate due to impurity quenching is significantly larger than the corresponding change in the radiative decay rate. In order to incorporate the dependence of impurity concentration into this model a quenching mechanism must be assumed. Here, we will consider impurity quenching by Förster transfer, because of the fluorescent nature of α-NPD this will be the most detrimental type of organic impurity found in these systems. The transfer rate for an exciton on a single host molecule to an impurity molecule can be described by Eqn. 3.3. It has previously been

argued however, that for an exciton interacting with a distribution of impurity molecules, the quenching rate must be multiplied by the molecular density of the impurity molecules and integrated over all of space.[181] Here, the density of impurity molecules can be expressed by multiplying the fraction of impurity molecules, *Q*, by the total molecular density, given by $\left(\frac{4}{3}\pi d^3\right)^{-1}$, where *d* is the volume averaged radius. The total steady state rate of impurity quenching can then be determined as:

$$k_Q = 4\pi \int_d^\infty \frac{1}{\tau_0}\left(\frac{R_I}{r}\right)^6 \frac{3Q}{4\pi d^3} r^2 dr = \frac{{R_I}^6 Q}{\tau_0 d^6}, \tag{6.2}$$

where *R*I is the average Förster radius between α-NPD and the impurities. Inserting Eqn. 6.2 into Eqn. 6.1 and solving yields a simple expression for the effective L_D as function of impurity concentration

$$L_D = \sqrt{\frac{D\tau_0}{1+\frac{{R_I}^6 Q}{d^6}}} = \sqrt{\frac{{L_{D,0}}^2}{1+\frac{{R_I}^6 Q}{d^6}}}. \tag{6.3}$$

Here, $L_{D,0}$ represents the diffusion length in the absence of impurities. Using Eqn. 6.3, the experimental values of L_D can be well fit as a function of impurity fraction, shown in Fig. 6.5. This fit yields a Förster radius of R_I = (1.3 ± 0.1) nm and $L_{D,0}$ = (7.0 ± 1.0) nm. In Fig. 6.5 it can be seen that large increases in L_D occur at purities beyond 99%, stressing the importance of attaining a high thin film purity to maximize *L*D.

While the model does a good job of fitting the trend of L_D as a function of purity, the actual physics of the interaction of excitons with impurities in the film will be far more complicated. With multiple different types of impurities present, the extracted R_I represents an average Förster radius for all impurities within in the film. In actuality the interaction of an exciton with each separate type of impurity will be different. Furthermore, there is no way to distinguish between the different types of quenching mechanisms outlined in

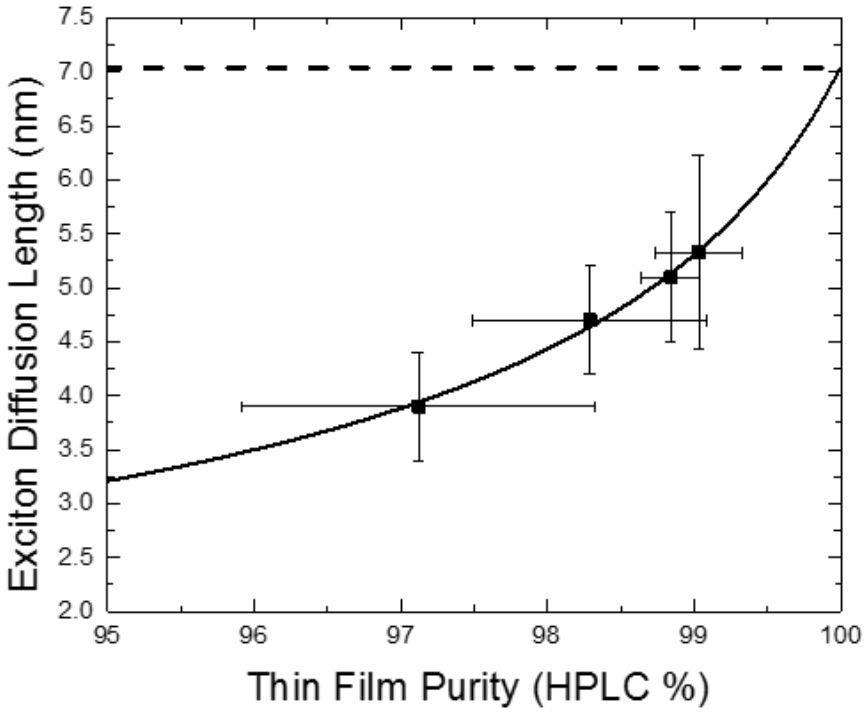

Figure 6.5 Exciton diffusion length (L_D) of α-NPD as a function of thin film purity as measured by high performance liquid chromatography (HPLC). Solid line represents a fit of L_D as a function of impurity concentration assuming exciton quenching by impurities via a Förster mechanism. The fit yields a Förster radius from α-NPD to the impurity of R_I = 1.3 nm and an impurity free, maximum L_D value of $L_{D,0}$ = 7.0 nm, represented by the dashed line.

section 6.1 by the data set of Fig. 6.5. If for example, Eqn. 3.7, were inserted in to Eqn. 6.2 for a Dexter transfer impurity, the same dependence of $Q^{-1/2}$ would be determined, resulting in the same fit to the data.

6.4 Conclusions

In this chapter we have demonstrated that molecular impurities present in organic semiconductors can impede exciton diffusion by measuring L_D as native impurities were systematically removed from films of α-NPD. Increases in L_D were caused by a reduction in the concentration of exciton quenching impurities, which caused systematic decreases in k_{NR} and increases in k_R, D, and τ. When the trend of L_D versus purity was fit with a model that assumes exciton quenching by Förster transfer, large increases in L_D were predicted at

purities beyond 99%. This stresses the importance of attaining a high thin film purity in order to optimize exciton diffusion in these types of systems.

6.5 Experimental Methods

Sample Preparation: The α-NPD source material was synthesized by The Dow Chemical Company and HATCN was purchased from the Luminescence Technology Corporation. All samples were grown by thermal vacuum sublimation at base pressures of 7×10^{-7} Torr, with deposition pressures $\leq 9\times10^{-7}$ Torr. Additionally, fresh source material was loaded into a clean boat before each deposition in order to assure a constant starting source material purity for each deposition. Photoluminescence quenching and τ samples were deposited on glass substrates and η_{PL} samples were deposited on quartz substrates. Additionally, τ samples were encapsulated using a UV cured epoxy in order to eliminate photo-oxidation affecting the measurements.

Photoluminescence and X-ray measurements: Photoluminescence was measured under monochromatic illumination at λ = 350 nm at an incident angle of θ = 65º with s-polarized light under a N_2 purge. In addition to measurements of L_D, τ was measured by time-correlated single photon counting and fit by a single-exponential decay and η_{PL} was measured in an integrating sphere. X-ray diffraction spectra were measured on 80 nm thick α-NPD films deposited on silicon substrates using a Bruker Co. Kα source x-ray diffractometer. For additional experimental details, see Appendix B.

7. Measurements of exciton diffusion using photovoltage

Excitons are charge-neutral quasi-particles; therefore, it is difficult to directly probe exciton diffusion by electrical means. Consequently, measurements of L_D rely on tracking end-of-life products, specifically photons or charge carriers. As discussed in Chapters 5 and 6, PL quenching measurements work well for materials which emit light; however, there is a large class of understudied materials with exceedingly low η_{PL} that are inaccessible by these traditional measurements.[18,65,67,68,70,105,133,135,137,146,182] Often, L_D of these non-luminescent, dark excitonic materials are determined by device-based photocurrent measurements. In these measurements, the material of interest is used as either an electron donor or electron acceptor in a PHJ OPV and the η_{EQE} is fit for L_D by combining rigorous simulations of the generating optical field[79] with solutions to the diffusion equation.[18,151,155,183,184] While excellent fits to the experimental data are often achieved with these measurements, photocurrent collection is subject to charge collection losses which can be difficult to quantify. If η_{CS} or η_{FC} are not unity, there will not be a one-to-one relationship between the number of collected charge carriers and the number of excitons which reached the D-A interface. Subsequently, extracted values of L_D will be underestimates if the model does not properly account for these losses. As such, better methods are needed to measure L_D of these dark excitonic materials.

In this chapter, a new technique is presented which determines L_D by measuring photovoltage in an OPV at open-circuit. When an exciton reaches the D-A interface of an OPV and the resulting CT state is dissociated, the generated free carriers occupy sites of disparate potential energy, producing a measureable photovoltage. This results in a direct relationship between the number of generated charge carriers, which is proportional to the

number of dissociated excitons, and the magnitude of the voltage produced by the device.[185–187] In order to measure L_D using a photovoltage-based technique, the exact relationship between voltage and number of carriers must be known, and it must be demonstrated that non-geminate recombination losses are negligible. Under open-circuit conditions, no current will flow and the only active recombination pathway for carrier loss is through non-geminate recombination.[114–116,122] If the voltage can be measured immediately after exciton dissociation, before significant non-geminate recombination losses occur, this measurement will eliminate a non-unity η_{FC} from influencing the extracted L_D. However, CT states which undergo rapid geminate recombination at the D-A interface will not accumulate in numbers sufficient to generate a measureable photovoltage; therefore, this loss pathway will be included in these measurements. Additionally, because this technique measures L_D in a working OPV, the measurement will account for effects specific to the device, such as interface roughness, molecular ordering, and substrate interactions. Therefore, the L_D extracted from these measurements will yield a device relevant L_D value which represents the fraction of excitons that are able to be dissociated and are capable of producing a useable photocurrent. Here, the L_D of boron subphthalocyanine chloride (SubPc) and C_{60} are measured using photovotolage and the value of SubPc is compared with previous PL-based measurements. The technique is then expanded to measure L_D in a series of previously inaccessible archetypical dark excitonic materials.

7.1 Probing exciton diffusion with photovoltage

Figure 7.1a shows the device architecture used to demonstrate the photovoltage-based technique for measuring L_D. The OPV is a PHJ device comprised of the electron donating

material SubPc paired with the electron accepting material C_{60}. The device is capped with an exciton blocking layer of bathocuproine (BCP) and a 100 nm thick aluminum cathode. Exciton diffusion in SubPc and C_{60} can be separately probed by selective excitation of their absorption spectra. Figure 7.1b displays the extinction coefficients of SubPc and C_{60} compared to the emission spectra of the two light emitting diodes (LEDs) used to excite the device. Here, a blue LED (λ_{peak} = 455 nm) is used to excite C_{60} and a green LED (λ_{peak} = 530 nm) is used to excite SubPc. When the device is held at open-circuit and illuminated with a 10 μs pulse from one of the LEDs, the photovoltage transients shown in Fig. 7.1c are generated. Since SubPc and C_{60} do not have completely distinct extinction coefficients, excitons originating from SubPc comprise about 79% and 9% of the photovoltage response for the green and blue LED pulses, respectively.[79] The photovoltage response shown in Fig. 7.1c can be characterized by four regions termed dark, rise, pre-recombination, and decay. In the dark region, the LED is initially off and no carriers are present in the device, corresponding to zero photovoltage. During the rise phase, the LED is turned on and optical absorption generates excitons, some of which will diffuse to reach the D-A interface and dissociate, generating charge carriers which produce a measurable photovoltage. The accumulation of these charge carriers generates the linear voltage rise. Once generated, there is a rate for charge carriers to undergo recombination, leading to the long time-scale photovoltage decay after the LED is turned off. The eventual decay in photovoltage is attributed to non-geminate charge carrier recombination, but the timescale for this process is slow enough that the photovoltage can be measured before a substantial number of charge carriers can recombine. This is demonstrated by the photovoltage 'plateau' observed initially after the LED is turned off in the pre-recombination region.

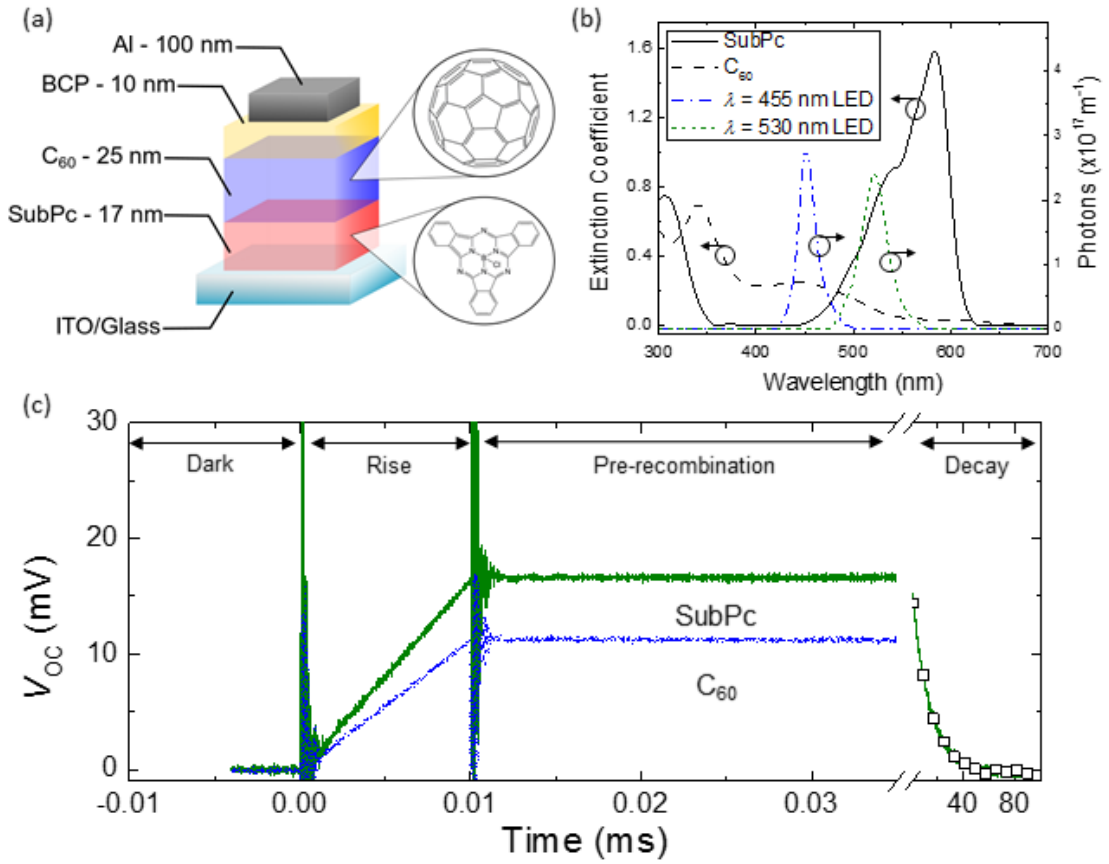

Figure 7.1 (a) Device architecture and molecular structures of active layers in SubPc-C_{60} OPV. (b) Pump spectra for LEDs peaked at wavelengths of λ = 455 nm and λ = 550 nm compared to the thin film extinction coefficients of SubPc and C_{60}. Representative plot of the open-circuit voltage response to a 10 μs incident light pulse showing four data sets. There are two data sets shown in the regions labeled Dark, Rise, and Pre-recombination, where SubPc data is show in green and C_{60} data is shown in blue. The region labeled "Decay" shows two photovoltage decays, one is for primarily pumping C_{60} (squares) and one for primarily pumping SubPc (green line in decay). Both decays correspond to a peak voltage of 16.5 mV and have time constants of 13.6 ms. The equivalence of the decays demonstrates that the photovoltage decay only depends on the number of carriers and not which material is being pumped.

The behavior of Fig. 7.1c can be approximated by different regimes of the rate equation governing the number of carriers (n) in the OPV:

$$\frac{dn}{dt} = -\frac{n^{\alpha}}{\tau_{rec}} + G \approx \begin{cases} G & LED\ on, t \ll \tau_{rec} \quad Rise \\ 0 & LED\ off, t \ll \tau_{rec} \quad Pre-recombination \\ -n^{\alpha}/\tau_{rec} & LED\ off, t \geq \tau_{rec} \quad Decay \end{cases} \tag{7.1}$$

where G is the generation rate of charge carriers, τ_{rec} is the non-geminate charge carrier recombination time, and α represents the order of recombination.[188] The plateau observed in Fig. 7.1c verifies that τ_{rec} is sufficiently long such that a voltage can be measured in this

experiment before any appreciable non-geminate recombination has occurred, enabling an accurate measure of the number of charge carriers generated at the interface.

7.2 Relating photovoltage to the number of charge carriers

In order to extract L_D from the magnitude of the photovoltage plateau, the relationship between the number of generated charge carriers and voltage must be determined. This relationship can be difficult to calculate,[185,186] but can be directly measured using charge extraction (CE) methods.[189–191] The CE scheme used here, shown schematically in Fig 7.2, relies on two transistors which flip on and off oppositely from one another. One transistor is connected to the LED, turning it on and off, and the other transistor is connected to the device, switching between open-circuit and shot-circuit. Initially, the LED is turned on and

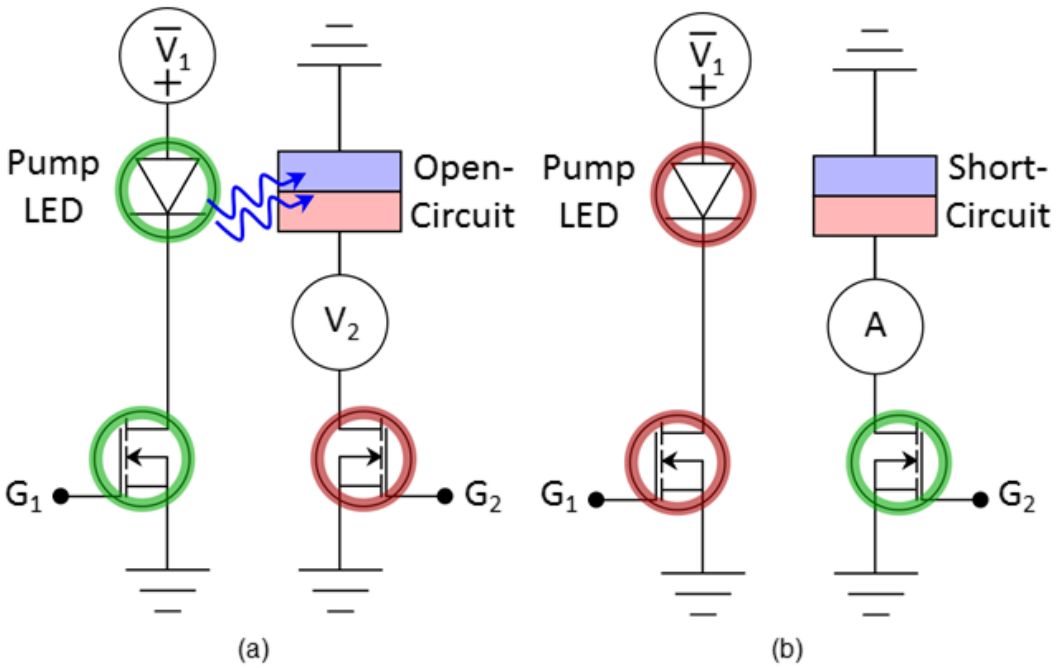

Figure 7.2 Schematic of charge extraction measurement. (a) Open-circuit voltage measurement of an OPV. A DC voltage (V_1) is applied to LED and a positive voltage to gate of the transistor (G_1) connected to the LED, turning the LED on. The transistor connected to the OPV is off, leaving the device at open-circuit, while steady-state voltage (V_2) is recorded. (b) Current transient measurement of an OPV. Transistor connected to LED is off, turning the LED off. A positive voltage is applied the gate of the transistor (G_2) connected the OPV, providing a short-circuit pathway to discharge the device and the resulting current transient is measured (A).

the device is held at open-circuit until a steady-state voltage is reached and recorded (Fig 7.2a). Then, simultaneously, the LED is turned off and the device is switched to short-circuit and the resulting current transient is recorded (Fig. 7.2b). The integral of the current transient yields the number of charge carriers stored in the OPV, determining the relationship between the number of carriers and the photovoltage.[94,187]

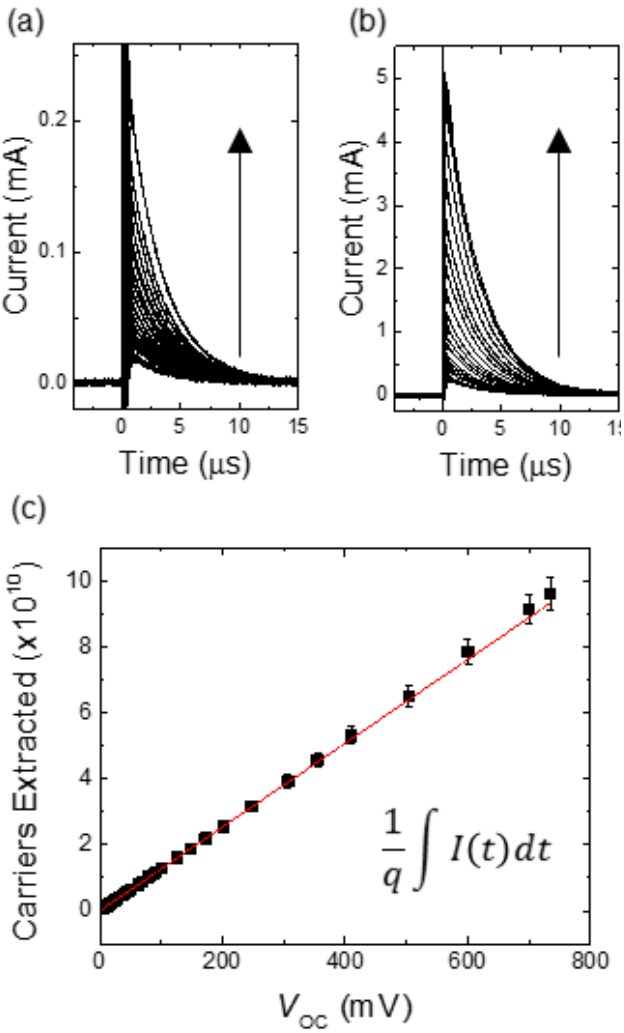

Figure 7.3 (a), (b) Current transients obtained by switching the SubPc-C_{60} device in Fig. 1b from open-circuit (steady-state) to short-circuit. The arrow points in the direction of increasing optical illumination and hence, V_{OC} prior to switching to short-circuit. In (a), the V_{OC} is varied from 3.4 mV to 37.6 mV while in (b), the V_{OC} is varied from 40.8 mV to 735 mV. (c) The trend of carrier number as a function of photovoltage obtained by integrating parts (a) and (b) with respect to time. A linear fit (solid red line) to the data is also shown with an intercept of zero and a slope of 1.31 x 10^{11} carriers per Volt.

Figures 7.3a,b show the current transients recorded for the SubPc-C_{60} device as a function of illumination intensity. As the illumination intensity is increased, more carriers are generated, leading to a higher V_{OC} and larger time-integrated current. Figure 7.3a displays the current transients corresponding to V_{OC} ranging from 3.4 mV to 37.6 mV and Figure 7.3b displays current transients for V_{OC} from 40.8 mV to 735 mV. Figure 7.3c

displays the current transients integrated with respect to time, yielding the number of charges stored in the device at a given photovoltage. Using this plot, any measure of photovoltage can be converted into a measure of the number of charge carriers present in the device.

It may seem contradictory that the advantage of the photovoltage measurement is that it circumvents charge collection, while the measurement used to establish the relationship between charge carriers and voltage relies on charge collection. During the CE measurement some charges will certainly be lost to non-geminate recombination; however, the amount of charge lost to this mechanism is negligible compared to the charge collected in the current transients. Figures 7.4a,b show the decays of the photovoltage compared to CE. During the photovoltage experiment at open-circuit, the

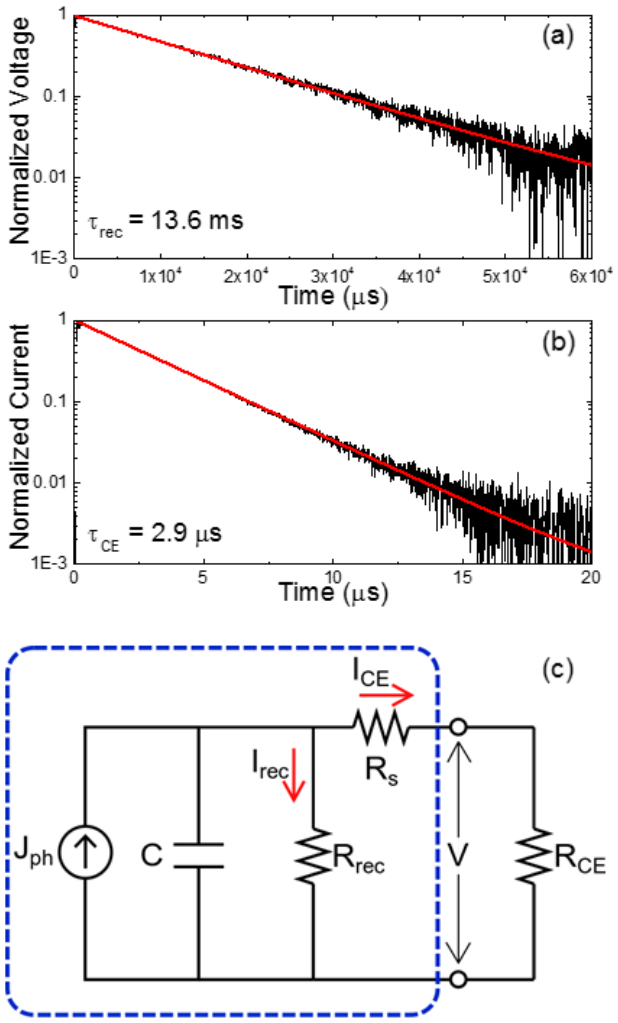

Figure 7.4 (a) Decay of SubPc photovoltage transient shown in Fig 7.1c. Red line represents a single exponential fit, resulting in characteristic recombination time (τ_{rec}) of 13.6 ms. (b) Characteristic charge extraction current decay from Fig. 7.3b with a corresponding fit of 2.9 μs. The large difference in decay times between (a) and (b) suggests non-geminate recombination is negligible in the charge extraction measurement. (c) Equivalent circuit diagram of an OPV connected to an external resistor (R_{CE}). Components contained in blue line represent OPV. See text for details of operation in photovoltage and charge extraction measurements.

dominant pathway for carrier loss is non-geminate recombination. Figure 7.4a shows that the characteristic timescale for this process is τ_{rec} = 13.6 ms. During the CE measurement, shown in Fig. 7.4b, the characteristic timescale for charge collection is τ_{CE} = 2.9 μs, orders of magnitude shorter than τ_{rec}. Additionally, it is instructive to think about this experiment in terms of an equivalent circuit diagram, shown in Fig. 7.4c. Here, the OPV is shown in the blue box and is connected to an external resistor (R_{CE}) which measures V_{OC} when R_{CE} = 1MΩ and the current transient (I_{CE}) when R_{CE} = 50Ω, near short-circuit. Inside the device, carrier generation at the D-A interface acts as a current source (J_{ph}) when the LED is on and the device is at open-circuit, storing the charge in the active layers of the device, which acts as a capacitor (C). Additionally, there are two resistors in parallel to the capacitor, one which represents non-geminate recombination (R_{rec}) and one which represents the series resistance of the device (R_s). Previous reports have measured R_s of OPVs ranging from 1-100Ω, here we assume R_s = 50Ω.[18,186] When the LED is off and J_{ph} = 0, the circuit will behave like a discharging RC circuit where R is given by the total resistance (R_{tot}) of the device and external circuit:

$$R_{tot} = \left(\frac{1}{R_{rec}} + \frac{1}{R_s + R_{CE}}\right)^{-1}. \quad (7.2)$$

Using the results of Fig. 7.3c and Fig. 7.4a, R_{rec} can be estimated. Given the linear relationship shown in Fig 7.3c, the capacitance of the device can be calculated by multiplying the slope of curve, 1.31×10^{11} carriers volt^{-1}, by the elementary charge, giving C = 21 nF. In reality, the device will never truly be at open-circuit or short-circuit when a voltage is being measured through a resistor; thus, in the photovoltage measurement τ_{rec} reflects the response of the total circuit, which approximates open-circuit conditions with a R_{CE} = 1 MΩ. As a result, in this measurement R_{tot} is given by τ_{rec}/C. Solving Eqn. 7.2 for

R_{rec} yields a value of 1.8 MΩ. During the CE measurement, when R_{CE} = 50Ω, the ratio of the recombination current (I_{rec}) to I_{CE} will provide insight into whether non-geminate recombination is affecting the CE measurements. In a discharging RC circuit, the current can be determined by:

$$I(t) = \frac{-Q_0}{R_{tot}C} e^{-t/\tau_{CE}}, \tag{7.3}$$

where Q_0 is the initial charge stored on the capacitor. Inserting Eqn. 7.2 into Eqn. 7.3 and expressing I_{rec} and I_{CE} in terms of their component resistances, the current ratio at any time *t* is given by:

$$\frac{I_{rec}}{I_{CE}} = \frac{R_{CE}+R_S}{R_{rec}} = 5.6 \times 10^{-5}. \tag{7.4}$$

Thus, we conclude that impact of non-geminate recombination on the charge extraction measurement is negligible, in agreement with a previous analysis.[189]

7.3 Extracting the exciton diffusion length

With the relationship between photovoltage and number of carriers established, as well as the knowledge that recombination can be ignored, the L_D of SubPc and C_{60} can now be determined. Using the measured relationship shown in Fig. 7.3c, the voltage plateaus can be converted into a measure of the number generated charge carriers or equivalently, in the absence of non-geminate recombination, dissociated excitons. For SubPc, the 16.6 mV photovoltage plateau corresponds to 2.09×10^9 dissociated excitons. Additionally, the number of incident photons needs to be determined. The LED spectra are measured with a spectrometer and the pulse power is measured using a silicon photodiode. For the green pulse used to establish the 16.6 mV photovoltage rise in Fig. 7.1c, it is determined that 8.64×10^9 photons were incident on the device.

Knowing the incident number of photons and resulting number of dissociated excitons, L_D can be extracted by modeling η_A and η_D of the device. A transfer matrix formalism is used to calculate the exciton generation profile in the device as a function of incident photon wavelength, which determines η_A.[79] Using this generation profile, the exciton diffusion equation can be solved to calculate $\eta_D(\lambda,L_D)$. Example calculations of $\eta_A\eta_D$ for varying values of SubPc L_D are shown in Fig.7.5a. Multiplying $\eta_A\eta_D$ by the number incident photons (P_{inc}) and integrating with respect to wavelength yields the number of carriers that would be generated from exciton dissociation (n_{gen}) as a function of L_D:

$$n_{gen} = \int \eta_A \eta_D(\lambda, L_D) P_{inc}(\lambda) d\lambda. \quad (7.5)$$

Values of L_D are then iterated until n_{gen} determined from Eqn. 7.5 matches the measured number of 2.09×10^9 dissociated excitons. Figure 7.5b shows the results of Eqn. 7.5 at varying values of the SubPc L_D, demonstrating that in this example the L_D of SubPc is 8.4 nm. A similar analysis is used to extract the C_{60} L_D from the C_{60} photovoltage transient shown in Fig. 7.1c, resulting from excitation from the blue LED. The LED pump spectra and simulated $\eta_A\eta_D$ under varying values of C_{60} L_D are shown in Fig. 7.5c. Applying Eqn. 7.5 to the curves in Fig. 7.5c generates Fig. 7.5d. In this example, the C_{60} L_D is determined to be 11.5 nm.

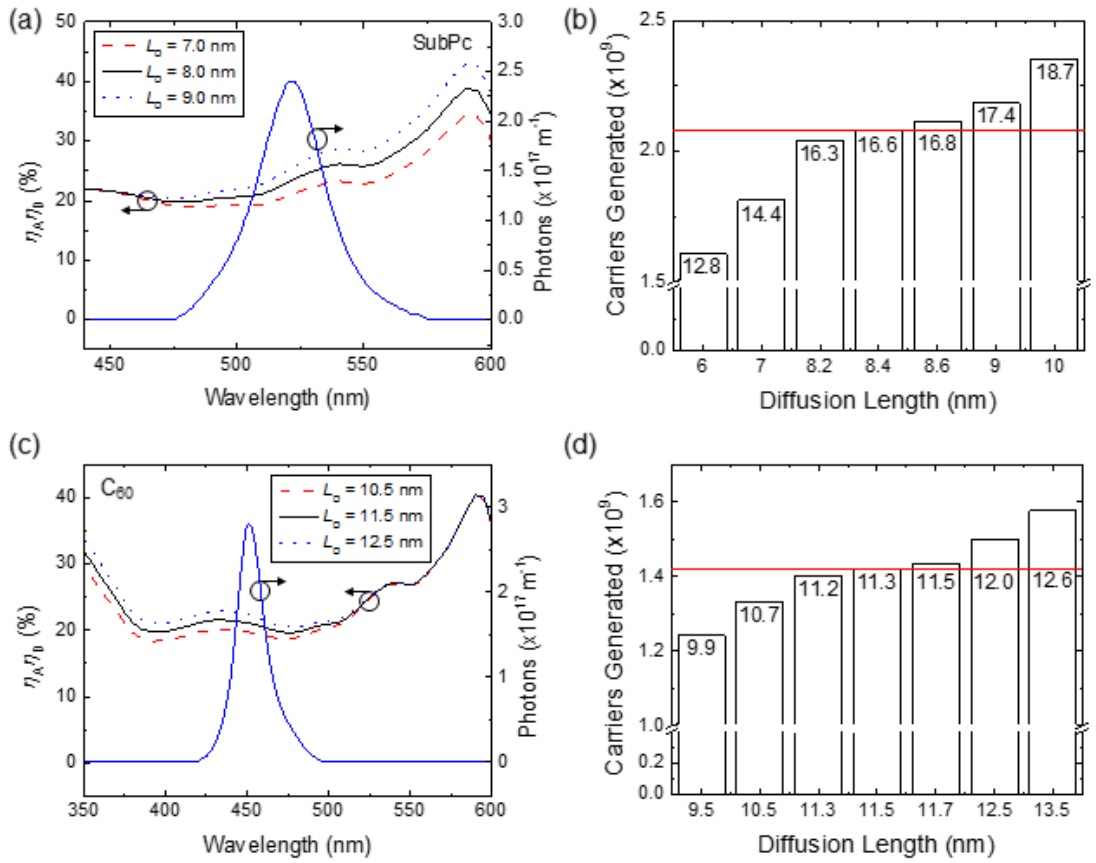

Figure 7.5 (a) Simulated $\eta_A\eta_D$ for variable values of the SubPc L_D, with a constant C_{60} L_D of 11.5 nm. Also shown, is the total number of photons incident on the device over a 10 μs pulse (solid blue line). (b) The number of charge carriers predicted to be generated for different SubPc L_D values. The horizontal line (red) marks the experimentally measured number of charge carriers generated. The labels on the bars represent the photovoltage (in millivolts) the device would generate for each value of L_D, showing the sensitivity of the technique. (c) Simulated $\eta_A\eta_D$ for variable values of the C_{60} L_D, with a constant SubPc L_D of 8.4 nm, and the total number of incident photons over a 10 μs pulse (solid blue line). (d) The predicted number of generated charge carriers for different values of the C_{60} L_D. The horizontal line (red) marks the experimentally measured number of charge carriers generated, while the bar labels represent the generated photovoltage (in millivolts) for each value of L_D.

Figures 7.5b,d demonstrate the sensitivity of the photovoltage measurements. Each bar is labelled by the photovoltage (in mV) that would be measured for the corresponding L_D value and number of generated charge carriers. The oscilloscope used to measure the photovoltage transients has a resolution of ~0.2 mV, which corresponds to an L_D resolution of about ±0.2 nm for this device. While L_D can be determined within this small error for a single device, there remain uncontrolled effects in device fabrication that lead to more

substantial device-to-device variation. In order to account for this, the standard deviation across twelve devices is used to determine the error in L_D, resulting in values of (8.5 ± 1.0) nm and (11.5 ± 1.2) nm for SubPc and C_{60}, respectively.

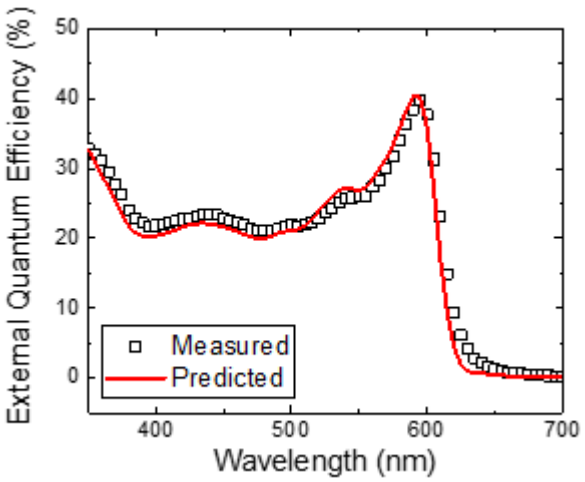

Figure 7.6 Comparison of the measured device η_{EQE} to that predicted using L_D values extracted from photovoltage with $\eta_{CC} = 1$. Since the measurement of L_D intrinsically reflects the impact of geminate recombination, the agreement between the measured and simulated η_{EQE} suggests that non-geminate recombination is negligible in this device at short circuit.

To put these measurements into context and validate the photovoltage approach, it is instructive to compare these results to the L_D measured by established techniques. Figure 7.6 shows the SubPc-C_{60} device η_{EQE} determined from the experimentally measured photocurrent spectra. This is compared to the $\eta_A\eta_D$ that is predicted from the photovoltage L_D values, resulting in excellent agreement. Direct fitting of the η_{EQE} data using the same model yields L_D values of 8.0 nm and 12.2 nm for SubPc and C_{60}, respectively, similar to those obtained from photovoltage. The agreement between these two measurements suggests that non-geminate recombination losses, which are circumvented by the photovoltage measurements, are negligible near short-circuit for this device.

Geminate recombination at the D-A interface will account for the difference in L_D measured by PL quenching and photovoltage. Previous PL quenching measurements of SubPc cite an L_D of 10.7 nm, larger than what is reported here using photovoltage.[67] This suggests that substantial geminate recombination present at the D-A interface results in an

underestimate of the intrinsic L_D value. Thus, the L_D determined from photovoltage measurements represent a device relevant value which determines the fraction of excitons that are dissociated and capable of producing a useable photocurrent. The exact relationship between these measurement techniques and methods to quantify and decouple recombination mechanisms, as well as determine intrinsic L_D values from photovoltage measurements will be examined extensively in Chapter 8.

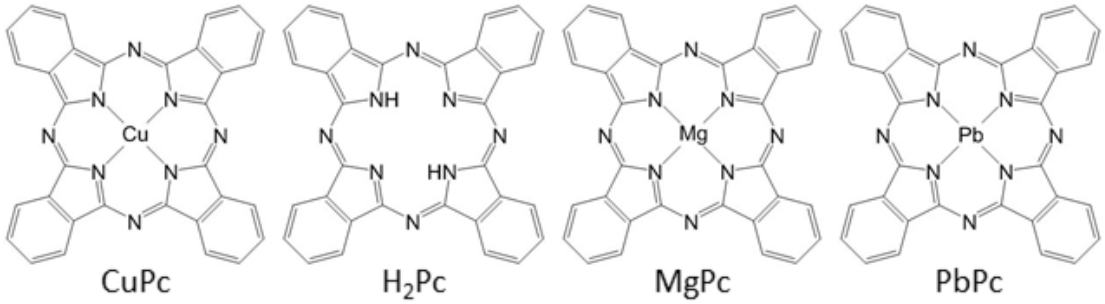

Figure 7.7 Series of archetypical non-luminescent, dark phthalocyanine molecules that are commonly used as OPV donors. Copper phthalocyanine (CuPc), metal-free phthalocyanine (H_2Pc), magnesium phthalocyanine (MgPc), and lead phthalocyanine (PbPc) differ only by their central coordinating atom.

7.4 Measuring dark exciton transport in phthalocyanine devices

Now that the technique has been demonstrated on a luminescent material and the constraints and assumptions of the photovoltage measurements are understood, it can be expanded to measure L_D of dark excitonic materials The method can be broadly applied to any material of interest that can be implemented as either a donor or acceptor layer in a PHJ OPV (*i.e.* it produces a photovoltage) without the need to optimize the device or reach high efficiency. Some of the most ubiquitously used dark materials in OPVs, in addition to C_{60}, are phthalocyanine donors. Here, we measure L_D for a series of dark phthalocyanine molecules which differ only in their central coordinating atom (Fig. 7.7).

An example of a copper phthalocyanine (CuPc) photovoltage L_D measurement is displayed in Fig. 7.8. Figure 7.8a displays the device architecture, consisting of a

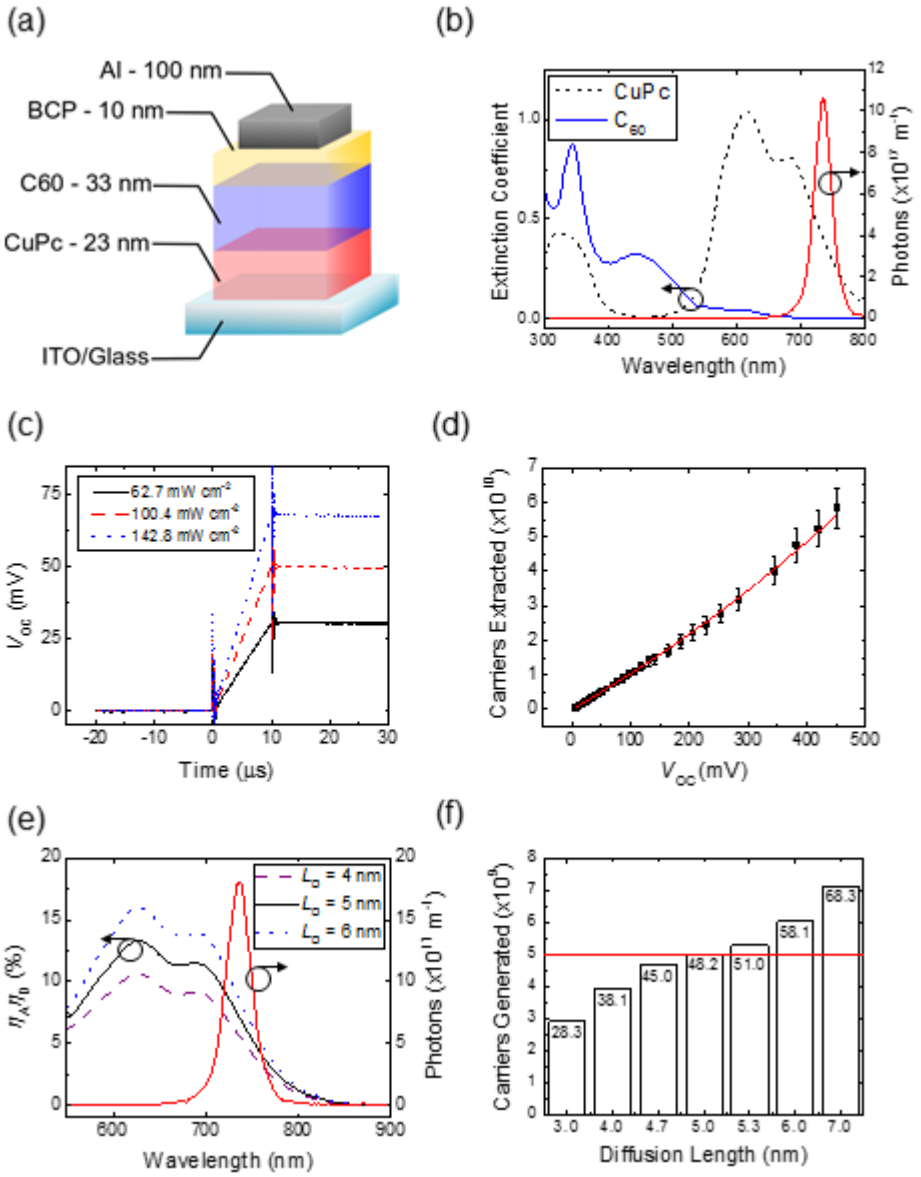

Figure 7.8 (a) Architecture for the planar heterojunction OPV based on the donor-acceptor pairing of CuPc-C_{60}. (b) Comparison of the extinction coefficients for CuPc and C_{60} as well as the spectrum of the LED pulse (λ_{peak} = 735 nm) used to pump CuPc. (c) Three photovoltage rises recorded when pumping CuPc with the λ = 735 nm LED at intensities of 62.7 mW cm^{-2} (black), 100.4 mW cm^{-2} (red) and 142.8 mW cm^{-2} (blue). (d) The relationship between charge carriers and voltage in the CuPc-C_{60} device obtained using the charge extraction method and an exponential fit to the data. (e) Simulated $\eta_A\eta_D$ curves for three CuPc L_D values with a constant C_{60} L_D of 12.1 nm compared to the time integrated LED pump spectrum. (f) Comparison of the predicted number of charge carriers generated (for multiple values of the CuPc L_D) to the photovoltage-based measurement (horizontal line). The V_{OC} (in millivolts) that would be measured for the corresponding number of charge carriers is labeled for each bar.

LED (λ_{peak} = 735 nm) is absorbed by CuPc. Three photovoltage transients taken under varying excitation intensity from a 10 μs LED pulse are displayed in Fig. 7.8c. As the intensity of LED pulse increases, more excitons will be generated and dissociated, leading to higher number of generated charge carriers and photovoltage plateau. These photovoltage plateaus can be converted to a number of dissociated excitons using the CE relation in Fig 7.8d. Figure 7.8e shows the calculated $\eta_A\eta_D$ for three CuPc L_D values overlaid with the LED spectrum at an intensity of 100.4 mW cm^{-2}. Figure 7.8f gives the results of applying Eqn. 7.5 to a series of $\eta_A\eta_D$ curves for the 100.4 mW cm^{-2} pump. In this examples, an L_D of 5.0 nm is extracted for CuPc. By varying the intensity of LED, each photovoltage transient provides an individual measurement of L_D. Values of L_D extracted for the other pump intensities agree with this example, resulting in L_D = 4.94 nm for the 67.3 mW cm^{-2} pulse and L_D = 4.97 nm for the 142.8 mW cm^{-2} pulse.

Figure 7.9 shows the resulting photovoltage L_D values measured for the other dark phthalocyanine materials which differ only in the central coordinating metal atom: copper (CuPc) L_D = 4.7 nm, metal-free (H_2Pc) L_D = 4.7 nm, magnesium (MgPc) L_D = 2.8 nm, and lead (PbPc) L_D = 4.6 nm. Device architectures,

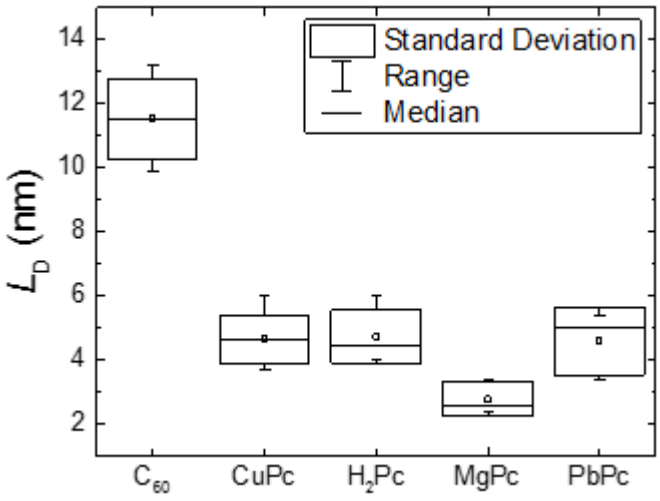

Figure 7.9 Values of L_D extracted using the photovoltage-based technique for C_{60} and a series of phthalocyanine molecules differing in the coordinating metal atom: metal-free (H_2Pc), magnesium (MgPc), copper (CuPc), and lead (PbPc). The small square symbol represents the mean of all measured devices.

photovoltage transients, CE measurements, $\eta_A\eta_D$ plots, and photovoltage sensitivity plots for the remaining materials are displayed in Appendix D. In addition to demonstrating the wide applicability of the photovoltage approach, Fig. 7.9 also demonstrates an interesting trend. The average L_D for all the phthalocyanine materials fall with a range of less than two nanometers despite the nature of the exciton being very different in the materials. The exciton in H_2Pc is likely a singlet exciton with a lifetime of 250ps, whereas the excitons in the materials with a heavy metal atom, like CuPc and PbPc, are likely long-lived triplets, providing a unique opportunity to contrast the motion of singlet and triplet excitons in similar environments.[192]

7.5 Conclusions

This chapter has demonstrated a new photovoltage-based measurement technique which probes exciton harvesting in OPVs. The technique is generally applicable to any material that can facilitate exciton dissociation in a PHJ OPV. The approach relies on the direct relationship between photovoltage and number of charge carriers present in the active layers of the device. It was established that photovoltage measurements can be made before any substantial non-geminate recombination occurs, which implies that the number of charge carriers equals the number of dissociated excitons. The measurement is still subject to geminate recombination losses, meaning the measured L_D yields a device relevant value that represents the fraction of excitons which are able to be dissociated and extracted as photocurrent. Photovoltage provides a useful tool to probe exciton harvesting in non-luminescent dark excitonic materials which are inaccessible by conventional PL quenching techniques. In the next chapter, photovoltage measurements will be used to quantify charge carrier recombination losses and it will be demonstrated that intrinsic L_D

values of dark materials can be extracted when photovoltage and PL quenching measurements are combined.

7.6 Experimental methods

Device preparation: All materials were used as received. Materials were obtained from the following suppliers: H_2Pc and MgPc from Sigma-Aldrich; CuPc from Acros Organics; lead phthalocyanine from TCI America; BCP and Al from Alfa Aesar; SubPc and UGH2 from Luminescence Technology Corporation; and C_{60} from MER Corporation. All devices were capped with a 10-nm-thick exciton blocking layer of BCP and a 100-nm-thick cathode layer of Al. All devices have an active area of 0.25 cm^2. For additional experimental details, see Appendix B.

Charge extraction: Charge extraction experiments were performed in atmosphere using an M455F1, M530F1, M625F1, or M735L3 LED from Thorlabs as the light source. The n-channel MOSFETs used to switch the LED and the OPV were manufactured by STmicroelectronics (STP27N3LH5). Integrated gate driver circuits were used to simultaneously switch the LED transistor and the OPV transistor. Since the transistors controlling the LED and the OPV must switch states in opposite directions at the same time, an inverting gate driver (Microchip Technology TC4421AVPA) was connected to the LED transistor and a non-inverting gate driver (Microchip Technology TC4422AVPA) was connected to the OPV transistor. The gate drivers were operated by the same pulses from an Agilent 33220A pulse generator, and the current transients were recorded using a Tektronix TDS5104B oscilloscope. The error bars in Fig. 2c and Fig. 5e represent the standard deviation across eight devices.

Voltage transients: Voltage transients were measured in atmosphere. The same LEDs used in the charge extraction experiment were used to obtain the voltage transients. The LEDs were powered by a Hewlett-Packard 8114A pulse generator, and the voltage transients were recorded by a Tektronix TDS5104B oscilloscope. The spectrum of each LED was measured using an Ocean Optics HR4000 spectrometer and the power output of the LEDs was recorded using a Thorlabs PDA36A amplified silicon photodetector. The values of L_D obtained were (11.5 ± 1.2) nm for C_{60}, (8.5 ± 1.0) nm for SubPc, (4.7 ± 0.7) nm for H_2Pc, (2.8 ± 0.4) nm for MgPc, (4.7 ± 0.7) nm for CuPc, and (4.6 ± 0.9) nm for PbPc. Values of L_D for a single device were determined by averaging three to five voltage transient measurements using LED intensities ranging from about 10 to 150 mW cm^{-2}. Reported L_D values are obtained by averaging measurements of twelve C_{60}, twelve SubPc, six H_2Pc, three MgPc, fourteen CuPc, and three PbPc devices. The error is the standard deviation across all devices and LED intensities.

Acknowledgement: The work in this chapter was conducted in collaboration with Tyler Mullenbach.

8. Decoupling photocurrent loss mechanisms

As discussed in Chapter 5, a variety of different techniques can be used to measure L_D. Each technique comes with its own set of constraints and assumptions and often L_D measurements of the same material using different techniques do not agree.[80] Thus far in this work, three different techniques have been used to extract L_D: PL quenching, photovoltage-, and photocurrent-based methods. When one considers what is physically being measured by each of these techniques, it is apparent that each technique actually probes a different point in the photoconversion process, as shown in Fig. 8.1. Photoluminescence quenching measurements probe the fraction of excitons which do not reach the dissociating interface. Therefore, this technique probes absorption, diffusion, and charge transfer, offering an intrinsic value of L_D for the material under study, provided η_{CT} = 1. Photovoltage measurements require that the generated CT state be dissociated into free carriers, thus probing absorption, diffusion, and charge transfer, as well as CT state

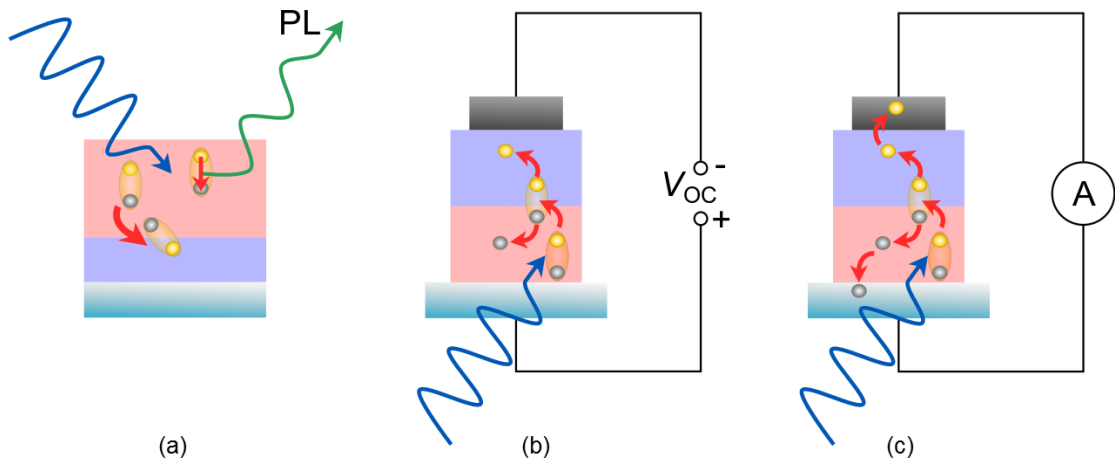

Figure 8.1 Different exciton diffusion length measurement techniques probe different points in the photoconversion process. (a) Photoluminescence quenching experiments probe diffusion and charge transfer, offering intrinsic value of the diffusion length. (b) Photovoltage measurements require charge transfer state dissociation and probe diffusion, charge transfer, and charge transfer state dissociation. (c) Photocurrent measurements require collection of carriers and probe all steps of photoconversion.

dissociation, subject to geminate recombination losses. Photocurrent based methods require that charges be physically collected at the electrodes, probing all five steps of the photoconversion process, subject to both geminate and non-geminate carrier losses. In this chapter we will employ each of these techniques on a PHJ SubPc-C_{60} device. Given that each technique probes different steps in the overall photoconversion process, comparing them yields a quantitative measure of both the diffusive behavior of the exciton, as well as the active recombination pathways in the device.

8.1 Photocurrent loss mechanisms

The current-voltage behavior of an OPV result from the sum of two contributions: the diode behavior of the device, which produces a rectifying dark current (J_{dark}) from carrier injection at the electrodes and recombination at the D-A interface and photocurrent (J_{photo}) generated from the five step mechanism presented in Section 4.1. As a function of forward bias voltage throughout the fourth quadrant, the values of η_D, η_{CS}, and η_{FC} can be reduced due to exciton- and polaron-driven losses.[94,98–100,110–112,114,115,117,118] These parasitic loss pathways often result in a steep reduction in the photocurrent as a function of forward bias voltage, leading to low device *FF* that limits the maximum operating power of a device.[94,114,116] Reductions in η_D can result from excitonic losses caused by increases in exciton-polaron quenching.[97–100] It has been established that there is a direct relationship between the voltage and the number of charge carriers present in the device.[158,185–187] Therefore, it follows that as the forward bias voltage increases, so does the number of polarons, increasing the probability of exciton-polaron quenching occurring prior to dissociation. Charge transfer state[94,110–112] and free charge carrier[94,114,115,117,118] losses can also increase as function of forward bias voltage. The difference in work function between

the anode and cathode in an OPV creates a built-in electric field in the active layers of the device. The force exerted on electrons and holes by this built-in field will act in opposite directions, as shown in Fig. 8.2a. Due to these opposing forces, the internal electric field can aid in both CT state dissociation, by spatially separating the CT state, and free carrier collection, by causing electrons and holes to drift to the cathode and anode, respectively. However, when the device is under forward bias, an electric field is induced which opposes the built-in field, reducing the overall internal electric field within the device and driving force for CT state separation and free carrier collection, as shown in Fig 8.2b. This reduction has been demonstrated to reduce η_{CS} and η_{FC} in many systems due to increases in both geminate and non-geminate recombination, respectively. In BHJ OPVs, the internal electric field determines η_{FC}; however, PHJ OPVs have an additional contribution from diffusion sweeping charge carriers away from the interface and the dependence of η_{FC} on electric field is expected to be reduced in these devices.[122] The effects of these loss

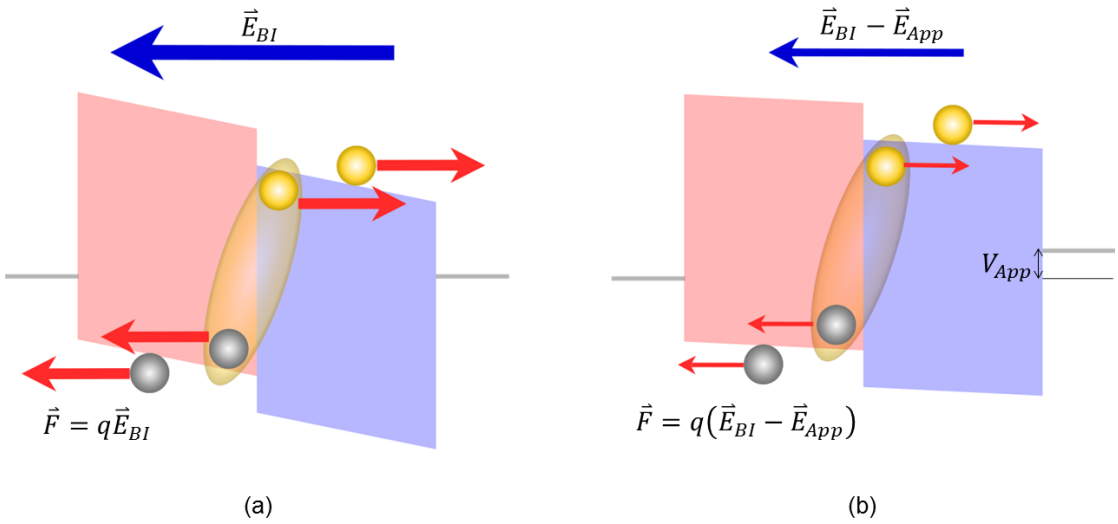

Figure 8.2 (a) At short-circuit the built in electric field ($\vec{E}_{BI}$) exerts a force ($\vec{F}$) on electrons and holes which acts in opposite directions. This $\vec{F}$ can aid in both charge transfer state dissociation and free carrier collection. (b) Under forward bias (V_{App}), an applied electric field ($\vec{E}_{App}$) opposes $\vec{E}_{BI}$ and reduces the $\vec{F}$ on electrons and holes, which can increase geminate and non-geminate recombination.

processes are often convoluted and difficult to decouple. In order to make informed decisions about materials and device design to mitigate these losses and improve device performance, there needs to be a quantitative understanding of which recombination mechanisms are dominant and limiting device performance at a given operating voltage.

In this study, a PHJ device based on the D-A pairing of SubPc-C_{60} is measured by PL quenching, photovoltage, and photocurrent techniques in order to demonstrate a method to quantitatively decouple η_D, η_{CS}, and η_{FC} as a function of forward bias voltage and provide a better understanding of the mechanisms which limit photocurrent generation. First, the effective L_D will be measured as function of forward bias by photovoltage measurements in order to determine the effects of geminate recombination. When these values are compared to photocurrent-based η_{EQE} measurements, the amount of non-geminate recombination present at short-circuit will be elucidated. Single carrier devices are fabricated to determine the effects of exciton-polaron quenching as a function of voltage. The effective L_D are then used to predict J_{photo} as a function of voltage in order to differentiate which loss mechanisms are dominant. Lastly, when PL-quenching and photovoltage measurements are combined, the intrinsic L_D of SubPc and C_{60} can be determined and values of η_{CS} and η_{FC} are quantified as a function of forward bias voltage.

8.2 Measuring L_D as a function of voltage

To elucidate the recombination mechanisms responsible for photocurrent loss in the fourth quadrant, the effective L_D must be measured as a function of voltage to help determine the role of geminate recombination and exciton-polaron quenching. Recently, it has been established that the total number of carriers in a device is the same at a given voltage, whether the device is at open-circuit or an operating voltage.[187] Therefore, the L_D

extracted under open-circuit conditions in the photovoltage measurement is equivalent to the value that would be extracted at the same operating voltage. This measurement, is identical to the photovoltage and charge extraction measurements described in Chapter 7, except that during the photovoltage measurement a constant background illumination is applied in order to bias the device to a desired voltage.

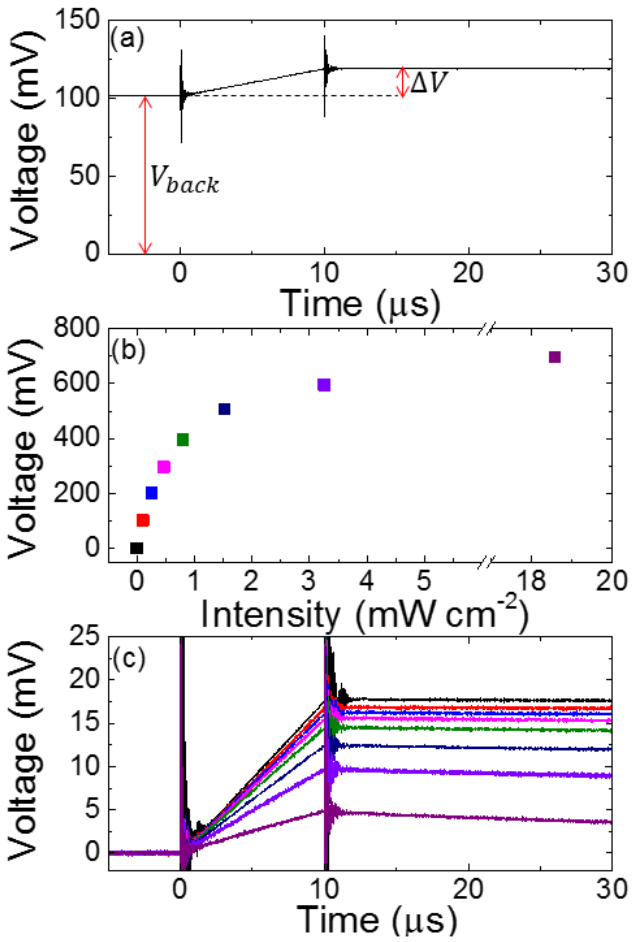

Figure 8.3 (a) Photovoltage transient used to extract the effective exciton diffusion length as a function of forward bias voltage. A constant background illumination is applied to the device in order to establish a steady-state baseline voltage (V_{back}). Exciton diffusion is then probed by a 10 μs LED pulse which creates a small voltage rise (ΔV) on top of V_{back}. (b) Baseline voltages as a function of light intensity from blue LED (λpeak = 455 nm) (c) Photovoltage transients, normalized to $V_{back} = 0$, used to extract the effective diffusion length for SubPc. As V_{back} is increased ΔV decreases, signifying a reduction in effective diffusion length. Colors of voltage transients in Figures 8.3b and 8.3c are consistent.

For SubPc, the baseline voltage (V_{back}, Fig. 8.3a) is established by selectively exciting the C_{60} acceptor with a constant light bias from a blue LED (λ_{peak} = 455 nm). This blue light is absorbed primarily by the C_{60} acceptor. Excitons generated in the C_{60} layer then diffuse and dissociate to create a steady-state voltage (and polaron density) across the device. Figure 8.3b shows that incremental increases in the intensity from the background blue LED, from

0 to 18.6 mW cm^{-2}, lead to a steady-state device voltage that increases from 0 to 700 mV. In addition to this background illumination, the device is also excited by a 10 μs pulse from a green LED (λ_{peak} = 530 nm) with an intensity of 13.0 mW cm^{-2}. The green pulse is primarily absorbed by the SubPc layer, creating a small voltage rise (ΔV, Fig. 8.3a) on top of V_{back}, which probes exciton diffusion on SubPc. Using this technique, the voltage across the device can be varied, while minimizing changes in the exciton density in the layer of interest due to the weak absorption of the background LED. Figure 8.3c shows the photovoltage measurements with a normalized V_{back} to emphasize the decrease in ΔV as a function of forward bias, signifying a reduction in the effective L_D.

The photovoltage transients shown if Fig. 8.3c can be used to extract an effective L_D. The method used to determine L_D in this study is subtly different than what is presented in Chapter 7. In this method, instead of simulating η_A and η_D at an arbitrary excitation intensity, the intensity and spectral shape of the LED excitation is directly input into the diffusion model and converted to an exciton generation rate.[79] Solving a diffusion equation yields the exciton density profile, $n(x)$. From this profile, the number of dissociated excitons can be determined from the time-integrated exciton flux at the D-A interface as:

$$N_{DE} = \tau_{pulse} AD \left.\frac{dn(x)}{dx}\right|_{D-A\ Interface}, \tag{8.1}$$

where N_{DE} is the total number of dissociated excitons, τ_{pulse} is the duration of the LED pulse (τ_{pulse}=10μs), A is the excitation area, and D is the exciton diffusivity. This methodology assumes η_{CT} and η_{CS} are unity, an approximation we will revisit later. Values of L_D are then iterated until the simulated N_{DE} matches the number determined from ΔV. This method will yield the same value of L_D as the method presented in Chapter 7; however, it provides an accurate measure of the exciton density needed to gain a better understanding of the

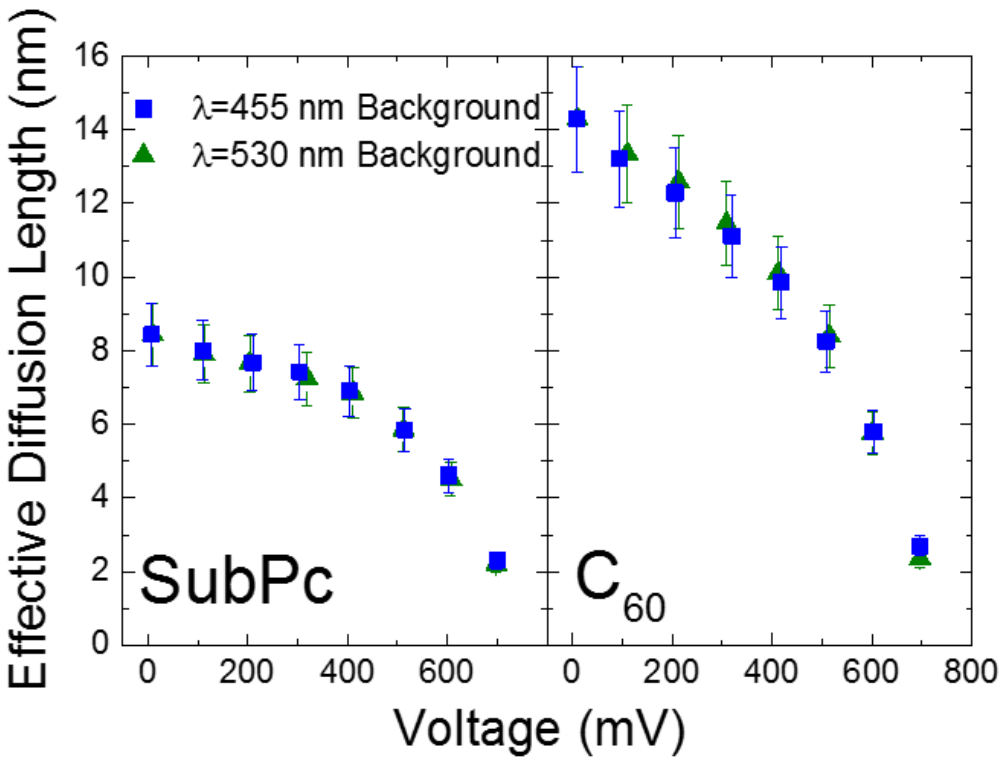

Figure 8.4 The effective exciton diffusion length determined *via* photovoltage, incorporating geminate recombination, of (a) SubPc and (b) C_{60} as a function of forward bias voltage. Blue squares represent measurements taken with a λ = 455 nm LED used as constant background illumination and green triangles represent measurements taken with a λ = 530 nm LED background. The agreement between these measurements suggests that exciton-exciton annihilation is not contributing to the observed reduction in effective L_D.

excitonic loss mechanisms. The results of this analysis are presented in Fig. 8.4. The effective values of L_D for SubPc and C_{60} are found to decrease from (8.4 ± 0.8) nm and (14.3 ± 1.4) nm, respectively, at 0 mV, to (2.3 ± 0.2) nm and (2.4 ± 0.2) nm, respectively, at 700 mV. At a voltage of 500 mV, corresponding to the maximum power output of the device, the effective values of L_D for SubPc and C_{60} are (5.9 ± 0.6) nm and (8.4 ± 0.8) nm, respectively. These reductions could be caused by decreases in η_D due to exciton-polaron quenching or η_{CS} due to an increase in the geminate recombination rate. To our knowledge, this is the first technique capable of accurately probing exciton harvesting at device relevant operating conditions, where secondary loss mechanisms are active.

8.3 Excitonic loss mechanisms

Due to the increasing light intensity used to establish the voltage, exciton-exciton annihilation could also become significant and contribute to a reduction in the effective L_D.[102,104,108] In order to determine if this secondary loss mechanism is affecting the results of the measurement, L_D is again measured as a function of voltage, except now with a background light bias corresponding to absorption on the layer of interest, *i.e.* the LED peaked at λ = 530 nm for SubPc and λ = 455 nm for C_{60}. This leads to a much larger background exciton density in the layer of interest, which will scale as a function of voltage. If exciton-exciton annihilation is contributing to the reduction in effective L_D, it is expected that L_D in this second experiment will decrease more rapidly as a function of voltage, due to the increased exciton densities and quadratic dependence of exciton-exciton annihilation on the exciton density.[97,102,104]

For the case of SubPc, the background light bias (at λ = 530 nm) was incrementally increased from 0 to 13.0 mW cm^{-2} to increase the voltage from 0 to 700 mV in ~100 mV steps. This corresponds to an increase in the background exciton density by about an order of magnitude with respect to the blue light background (at λ = 455 nm). For example, in the measurement taken at 700 mV, the background exciton density is increased from 3.09 $\times 10^{11}$ cm^{-3} to 3.15 $\times 10^{12}$ cm^{-3} in the SubPc layer. However, as shown in Figure 8.4, the trend of the effective L_D versus voltage is the same for both SubPc and C_{60} irrespective of which light bias, and consequently exciton density, is used. This suggests that exciton-exciton annihilation is not contributing to the reduction in effective L_D using this measurement technique.

Next, the effect of exciton-polaron quenching needs to be determined in order to decouple the relative contributions of excitonic and CT state losses to the reduction in effective L_D. In this device, as the voltage is increased to 700 mV, the spatially averaged polaron density increases from 2.6×10^{16} cm^{-3} and 1.6×10^{16} cm^{-3} near 0 mV to 2.2×10^{18} cm^{-3} and 1.1×10^{18} cm^{-3} at 700 mV for the SubPc and C_{60} layers, respectively. Here, the polaron densities are calculated by converting the average voltage of a given photovoltage transient into a total number of generated carriers using the CE relation and dividing by the volume of the layer of interest. To determine if exciton-polaron quenching is active at these densities, single carrier devices, hole-only for SubPc (Fig. 8.5a) and electron-only for C_{60} (Fig. 8.5b), were fabricated and PL was measured as a function of increasing current density, and hence polaron density.[168,193,194]

In the presence of exciton-polaron quenching, the steady-state one-dimensional exciton rate equation can be expressed as[102,109]

$$0 = -\frac{n_{ex}}{\tau} + G - k_{ex-p} n_{ex} n_{pol}, \tag{8.2}$$

where n_{ex} is the exciton density, τ is the exciton lifetime, G is the optical generation rate, $k_{ex\text{-}p}$ is the exciton-polaron quenching rate, and n_{pol} is the polaron density. In order to extract $k_{ex\text{-}p}$, PL from SubPc and C_{60} are measured as a function of unipolar current density in the device, which then needs to be converted to a measure of the polaron density. The models used to fit these measurements assume that the device is operating in a space charge limited current regime. This means that current flow through the device is dominated by carrier injection from the contacts and that the current is controlled by the mobility of the carriers and not the intrinsic material carrier densities. The simplest and perhaps most widely used model of this type is the Mott-Gurney law.[195,196] Here, Ohm's law ($J = \rho\mu E$) is combined

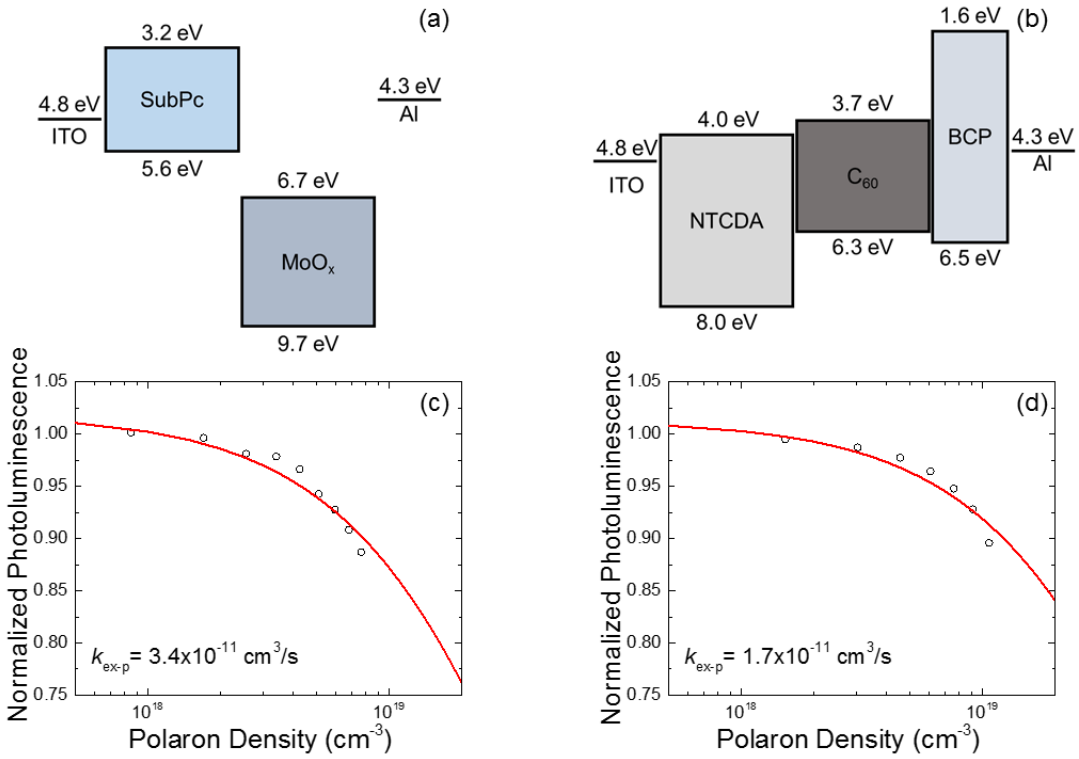

Figure 8.5 Energy level diagrams of device architectures for (a) hole-only SubPc devices and (b) electron only C_{60} devices. Fitting the normalized photoluminescence of these devices as a function of current density yields the exciton-polaron quenching rate ($k_{ex\text{-}p}$) for SubPc (c) and (d) C_{60}.

with Gauss' law $\left(\frac{dE}{dx} = \frac{\rho}{\varepsilon}\right)$ and solved in order to express a current voltage relationship for the device, where $J \propto V^2$. The devices used here did not display this quadratic behavior, so the current voltage relation was fit with a more complicated model which incorporates an exponential distribution of charge carrier traps in the active layers of the device.[196] This model assumes a drift current that is controlled by a linear voltage drop across the device, yielding $J = \rho_f \mu {}^{V}/_{L}$, where ρ_f is the free carrier density, μ is the electron or hole mobility, L is the thickness of the device, and V is the voltage. Here, L ranged from 84.1 nm to 168.3 nm for the C_{60} devices and from 89.6 nm to 176.3 nm for the SubPc devices. The free carrier density is then expressed in terms of a temperature activated carrier density resulting

from an exponential distribution of traps. Inserting this expression for ρ_f into the equation for J yields[109,196,197]

$$V = \left(\frac{2l+1}{l+1}\right)\left[\frac{J}{e\mu N_c}L^{2l+1}\left(\frac{eN_0(l+1)}{\epsilon l}\right)^{l}\right]^{\frac{1}{l+1}} = CJ^{\frac{1}{l+1}}, \quad (8.3)$$

where l is the ratio of the temperature of the trap distribution to the ambient temperature, N_C is the density of trap states at the transport level, ϵ is the permittivity, e is the elementary charge, and C is a constant. Next, J needs to be converted into a measure of n_{pol}. Inserting Eqn. 8.3 into Gauss' law $\left(-\frac{d^2V}{dx^2} = \frac{qn_{pol}}{\varepsilon}\right)$ and solving yields

$$n_{pol} = \frac{\epsilon V}{eL^2}\left(\frac{2l+1}{l+1}\right)^{\frac{l}{l+1}}. \quad (8.4)$$

Plots of the normalized PL as a function of n_{pol} are shown in Fig. 8.5c and 8.5d, for SubPc and C_{60}, respectively; from which, $k_{ex\text{-}p}$ can be determined. The photoluminescence efficiency in the presence of polaron quenching can be expressed as $\eta_{PL} = k_r \Big/ k_r + k_{nr} + n_{pol}k_{ex-p}$. Using this relation, the PL intensity normalized to the PL in the absence of polaron quenching can be fit to

$$\frac{PL(n_{pol})}{PL_0} = \frac{1}{1+\tau n_{pol}k_{ex-p}}, \quad (8.5)$$

where τ is the exciton lifetime in the absence of polaron quenching. Inputting τ of 0.5 ns and 0.59 ns for SubPc and C_{60}, respectively, results in $k_{ex\text{-}p}$ of $(3.4 \pm 0.4 \times 10^{-11})$ cm^3 s^{-1} for SubPc and $(1.7 \pm 0.2 \times 10^{-11})$ cm^3 s^{-1} for C_{60}, as shown in Figs. 8.5c,d.[67,159] Here, the error bars are determined as a statistical error from the fitted data. Assuming that exciton-polaron quenching will not affect the diffusivity, L_D can be expressed as $\sqrt{D\left(\tau^{-1} + k_{ex-p}n_{pol}\right)^{-1}}$. Inputting the values of $k_{ex\text{-}p}$ into this equation, L_D of both SubPc and C_{60} are both reduced

by 0.1 nm at the maximum n_{pol}, allowing us to conclude that this mechanism is not a dominant loss pathway at the range of polaron densities accessed in these measurements. However, it should be noted that this conclusion relies on the assumption of a spatially averaged, flat polaron density. While this may be a reasonable assumption at open-circuit when the current density is equal to zero, this assumption may break down at operating voltages when current is flowing through the device. From the charge extraction measurement we only know the total number of polarons in the active layer, but nothing about their spatial distribution. In a PHJ device, all of the polaron generation takes place at the D-A interface. At a given operating voltage, if a large majority of the polarons are located within a few nanometers of the D-A interface the density in this region would be much higher than our spatially averaged approximation. This could lead result in exciton-polaron quenching that could potentially reduce L_D and would not be accounted for in this simple model. With that being said, in the absence of significant exciton-exciton and exciton-polaron quenching, an increased geminate recombination rate as a function of voltage remains as the cause for the observed reduction in effective L_D in this device.

8.4 Decoupling photocurrent loss mechanisms

To fully decouple the pathways responsible for photocurrent loss, the effect of non-geminate recombination must be quantitatively determined throughout the fourth quadrant. At short-circuit this can be accomplished by comparing values of L_D determined from photovoltage measurements to photocurrent measurements which are subject to non-geminate collection losses. As shown in Fig. 8.6, when the effective L_D values determined from photovoltage are used to predict the experimental η_{EQE}, excellent agreement with the

experimental data is observed. This implies that there is no non-geminate recombination at short-circuit, consistent with previous reports.[94,122,158]

To determine if non-geminate recombination contributes to the photocurrent loss at higher voltages, J_{photo} is predicted from the effective L_D values measured by photovoltage, which are subject to geminate losses only. The experimentally measured J_{photo} is shown in Fig. 8.7 (green line) is extracted by illuminating the device with AM 1.5G illumination at 100 mW cm^{-2} and filtering out the dark current (J_{dark}) contribution with a lock-in amplifier. The effective L_D values are input into a diffusion model with a generation term equivalent to the same one-sun illumination and the predicted J_{photo} (black squares) can be determined by

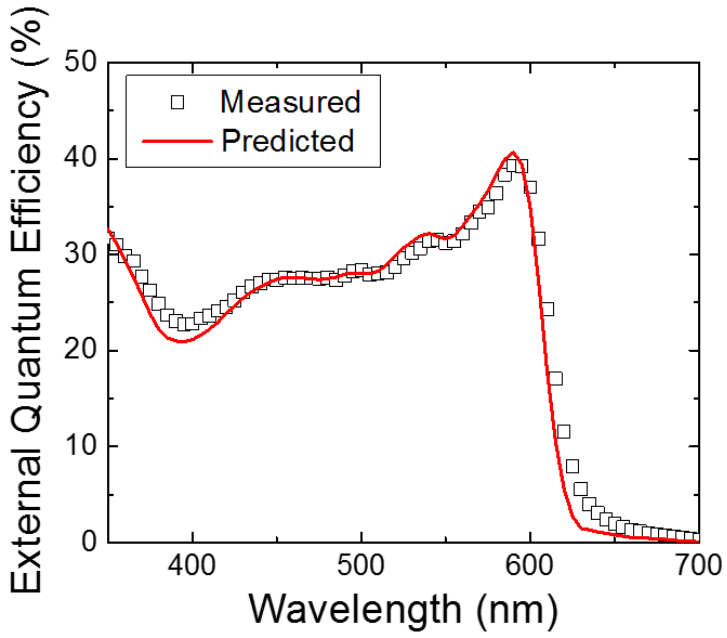

Figure 8.6 Comparison of the experimental η_{EQE} to the prediction of η_{EQE} based on the effective L_D measured by photovoltage. Agreement suggests that non-geminate recombination losses are negligible near short-circuit.

$$J_{Photo} = \eta_{FC} q D \frac{\partial n(x)}{\partial x}|_{D-A\ Interface}, \quad (8.6)$$

where q is the elementary charge. In this model, η_{FC} will account for the different between the measured and predicted J_{phoro}; however, Fig. 8.7 demonstrates that J_{photo} is best reproduce with a unity $\eta_{FC,}$ suggesting non-geminate recombination does not contribute to the loss in J_{photo} in this device, even at higher voltages. Consequently, the reduction in J_{photo}

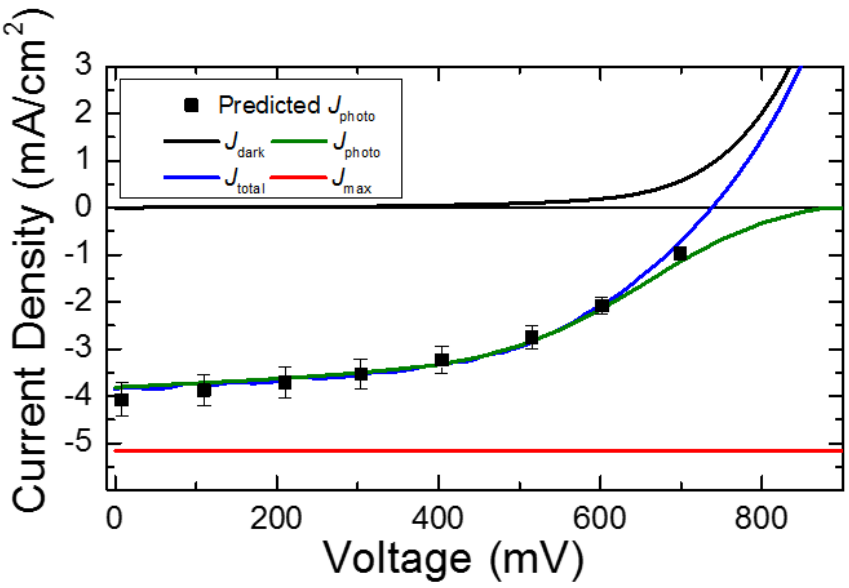

Figure 8.7 Experimentally measured dark current density (J_{dark}), photocurrent density (J_{photo}) and total-current density (J_{total}) of the SubPc-C_{60} device illuminated by AM 1.5G at 100 mW cm^{-2}. Black squares represent the predicted J_{photo} determined from the effective L_D measured by photovoltage. Agreement between the measured and predicted J_{photo} suggests that geminate recombination is responsible for photocurrent losses in the fourth quadrant. The red line (J_{max}) represents the J_{photo} that would be extracted from the device in the absence of carrier recombination losses determined from the intrinsic L_D values.

is caused by an increasing geminate recombination rate, likely due to a reduction in the internal electric field with increasing voltage.

8.5 Quantifying geminate and non-geminate recombination

Now that the mechanism responsible for photocurrent loss has been elucidated, values of η_D, η_{CS}, and η_{FC} need to be quantitatively determined. To do this, the intrinsic L_D values in the absence of any carrier recombination are determined by a thickness-dependent PL quenching measurement of SubPc. Here, a 15.6 nm thick layer of C_{60} is used an exciton quencher to preserve the interface that is present in the device measurements. Photoluminescence spectra were measured for a series of ten SubPc films ranging in thickness from 5.3 nm to 39.5 nm. Photoluminescence ratios and L_D fit are shown in Fig. 8.8a, yielding an intrinsic $L_D = (11.2 \pm 1.0)$ nm for SubPc.

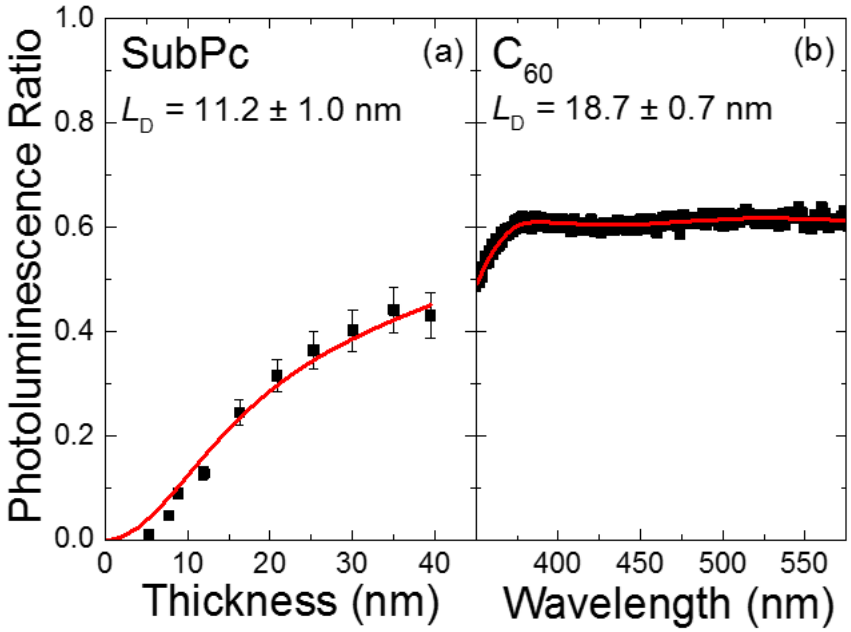

Figure 8.8 (a) Thickness dependent photoluminescence quenching diffusion length measurement of SubPc using a C_{60} exciton quencher. Measurement offers an intrinsic value of the exciton diffusion length. (b) Spectrally resolved diffusion length measurement of C_{60} film using a HATCN exciton quencher. Agreement of this measurement with the C_{60} diffusion length determined from photovoltage and SubPc photoluminescence quenching measurement helps validate the method of decoupling charge-transfer state separation efficiency.

Knowing the intrinsic value of L_D for SubPc, η_{CS} and the intrinsic L_D of C_{60} can now be determined. When the photovoltage data for SubPc is re-fit using an L_D of (11.2 ± 1.0) nm, a value of η_{CS} = (79.1 ± 8.8) % is obtained near 0 mV. Re-fitting the C_{60} photovoltage data with η_{CS} = (79.1 ± 8.8) % results in an intrinsic C_{60} L_D of (19.4 ± 1.7) nm. Additionally, to ensure the validity of this approach, the C_{60} L_D was also measured by PL quenching. Due to the exceedingly low luminescence efficiency of C_{60}, L_D was determined by spectrally resolved PL quenching on a relatively thick 46.1 nm film of C_{60}, deposited on quartz, with a 12.9 nm HATCN exciton quencher deposited on top of the C_{60} film. Additionally, for the unquenched film, a 12.7 nm layer of BCP was deposited on top of C_{60} in order to avoid effects of oxidation. As shown in Fig. 8.8b, this experiment is in agreement with the previous measurements yielding an intrinsic C_{60} L_D = (18.7 ± 0.7) nm. Importantly, this

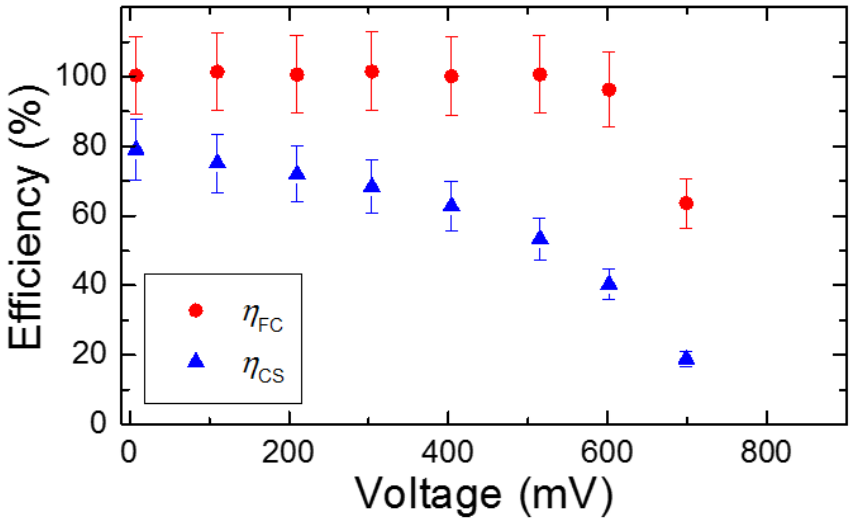

Figure 8.9 Charge-transfer state separation efficiency (η_{CS}) and free carrier collection efficiency (η_{FC}) as a function of voltage. The charge separation efficiency is determined by the ratio of the predicted J_{photo} to J_{max} and η_{FC} is determined by the ratio of J_{total} to predicted J_{photo}. Error bars are propagated based on the uncertainty in L_D associated with both the photoluminescence quenching and photovoltage measurements.

result validates this approach and demonstrates that if a dark material is paired with a luminescent donor or acceptor, the intrinsic L_D of the dark material can be accurately decoupled from photovoltage measurements.

The intrinsic L_D values of (11.2 ± 1.0) nm and (19.4 ± 1.7) nm for SubPc and C_{60}, respectively, are input into the photocurrent model. Under one-sun illumination, Eqn. 8.6, with $\eta_{FC} = 1$, yields a diffusion-limited maximum J_{photo} (J_{max}) of (5.16 ± 0.34) mA cm^{-2} (red line, Fig. 8.7). This represents the photocurrent that would be produced in the absence of any carrier recombination losses. With this value, η_{CS} can be determined as a function of voltage by dividing the predicted J_{photo}, which incorporates geminate recombination *via* the effective L_D, by J_{max}. As shown in Fig. 8.9, η_{CS} is reduced from (79.1 ± 8.8) % near short-circuit to (18.9 ± 2.1) % at 700 mV, nearing V_{OC}.

When the device is at V_{OC}, the rate of carrier generation at the interface is precisely canceled by the rate of non-geminate recombination, such that no current flows out of the

device.[114–116,122] For the SubPc-C_{60} device considered here, it has been established that geminate recombination is responsible for the voltage dependent losses in photocurrent. Therefore, in this device, non-geminate recombination accounts for the difference between J_{photo} and J_{total}. In general, η_{FC} can be calculated from the ratio of J_{total}, which incorporates all losses, to the J_{photo} predicted from photovoltage, which incorporates diffusion and geminate losses. In this device, η_{FC} is near unity throughout the majority of the fourth quadrant, even near the optimal operating voltage of 500 mV, shown in Fig. 8.9. Non-geminate recombination only starts to become significant at voltages beyond 600 mV and does not affect the photocurrent or maximum power output of the device. While the balance of η_{CS} and η_{FC} will be affected by layer thickness, device architecture, and materials selection, the method presented here can be generally applied to any PHJ device that contains one material which emits light in order to gain insight into materials and device properties that limit device photocurrent.

8.6 Conclusions

In this chapter three different techniques which are typically used to extract L_D are compared to probe exciton harvesting and decouple the active recombination pathways as a function of voltage in a PHJ SubPc-C_{60} OPV. Photovoltage measurements are used to determine a device relevant, effective L_D throughout the power generating fourth quadrant in the presence of diffusion and geminate recombination losses. When photovoltage L_D values are compared to photocurrent based η_{EQE} measurements, excellent agreement is observed, suggesting non-geminate recombination is negligible at short-circuit conditions. The effective L_D values are then used to predict the photocurrent as a function of voltage in the device and it is determined that increases in geminate recombination are responsible

for photocurrent loss. Lastly, PL quenching measurements are used to determine the intrinsic L_D of both materials in the absence of any carrier recombination losses. When these measurements are combined, the values of η_{CS} and η_{FC} can be quantitatively decoupled as a function of voltage. This work demonstrates that differences in the charge and exciton populations probed by popular L_D measurement techniques allow for a deeper understanding of exciton harvesting within a PHJ OPV and the active recombination pathways that determine device performance. With this knowledge more informed decisions of materials selection and device design can be made in order to limit these losses and ultimately produce more efficient devices.

8.7 Experimental methods

Device preparation: The devices considered in this work consisted of an 18.2-nm-thick donor layer of SubPc, a 35.6-nm-thick acceptor layer of C_{60}, a 10 nm-thick exciton blocking layer of bathocuproine (BCP), and a 100-nm-thick cathode layer of Al. All materials were used as received without further purification. SubPc was purchased from Luminescence Technology Corp.; C_{60} from the MER corporation; and BCP and Al, 1,4,5,8-naphthalenetetracarboxylic dianhydride (NTCDA), and molybdenum oxide (MoO_x) from Alfa Aesar. In order to ensure consistency in the films considered across this study, the same batches of material and processing conditions were used for all deposited films of the same type. For additional experimental details, see Appendix B.

Charge extraction: Charge extraction measurements were collected in atmosphere on devices illuminated using M455F1 and M530F1 LEDs from Thorlabs with an illumination area of $\pi \times 0.075^2$ cm^2. The LEDs and OPV were simultaneously switched using n-channel MOSFETs and integrated gate driver circuits. MOSFETs were purchased from

STmicroeletronics (STP27N3LH5) and gate drivers were purchased from Microchip Technology. In order for the MOSFETs connected to the LED and OPV to switch in opposite directions simultaneously, an inverting gate driver (TC4421AVPA) was connected to the LED transistor and a non-inverting gate driver (TC4422AVPA) was connected to the OPV transistor. Gate drivers were switched using a 10V, 200 ms period square wave generated from an Agilent 33220A pulse generator and current transients were recorded using a Tektronix TDS5104B oscilloscope.

Voltage transients: Voltage transient measurements were taken in atmosphere. The same LEDs used in the charge extraction measurements were used to obtain the voltage transients. A λ=455 nm LED was used to probe C_{60} and a λ=530 nm LED was used to probe SubPc. LEDs were excited by a Hewlett-Packard 8114A pulse generator. The steady-state background LED light was powered by a Sorensen XHR 600 DC power supply. The illumination from the LEDs was focused onto the OPV using a bifurcated fiber bundle (BFY1000HS02) and fiber collimator (F220SMA-532), both purchased from Thorlabs. Voltage transients were recorded by a Tektronix TDS5104B oscilloscope. All LED spectra were measured using an Ocean Optics HR4000 spectrometer and the power output of all LEDs were recorded using a Thorlabs PDA36A amplified silicon photodetector. Peak exciton densities in SubPc during photovoltage measurements range from 3.6×10^{12} cm^{-3} to 6.0×10^{12} cm^{-3}. By comparison the peak exciton density in SubPc at one-sun is 7.2×10^{12} cm^{-3}. Error bars in L_D were determined based on the standard deviation across a statistically significant number of devices. Error associated with the extracted η_{CS} and η_{FC} were propagated based on the uncertainty in both the photovoltage and photoluminescence quenching L_D measurements.

Current-voltage measurements: Dark and total illuminated current-voltage measurements were taken using an Agilent 4155C semiconductor parameter analyzer. Total illuminated and photocurrent measurements were carried out under AM1.5G solar radiation at 100 mW cm^{-2} with an illumination area of $\pi \times 0.075^2$ cm^2. Photocurrent measurements were made using a Stanford Research Systems (SRS) SR810 lock-in amplifier and illumination was chopped using an SRS SR540 optical chopper to filter out the dark current and pre-amplifier was used to apply a forward bias to the device.

Single carrier devices: Hole- and electron-only devices were fabricated on glass substrates pre-patterned with a 150-nm-thick layer of indium-tin-oxide (ITO). Hole-only devices consisted of 89.6 nm to 176.3 nm of SubPc deposited on the ITO-coated substrate, capped with an 11.4-nm-thick MoO_x electron-blocking layer and a 100-nm-thick Al cathode. Electron-only devices were fabricated with a 13.7-nm-thick NTCDA hole-blocking layer deposited on the ITO-coated substrate, followed by 84.1 nm to 168.3 nm of C_{60}, and capped with a 10.0-nm-thick hole-blocking layer of BCP and a 100-nm-thick Al cathode. Photoluminescence spectra were collected using a Photon Technology International Quantum Master 4 Fluorimeter. Devices were biased and current measurements were taken using a Kiethly 2604B source meter.

External quantum efficiency measurements: External quantum efficiency measurements were taken under monochromatic illumination from a 300 W xenon arc lamp coupled into a Cornerstone 130 1/8 meter monochromator and chopped with an SRS SR540 optical chopper. Current measurements were taken using an SRS SR810 lock-in amplifier.

Photoluminescence quenching measurements: Photoluminescence quenching measurements were taken using a Photon Technology International Quantum Master 4 Fluorimeter. Measurements were performed under a N_2 purge at an incident angle of 65° to the substrate normal. Samples were illuminated using a Xe lamp coupled into a monochrometer selected to wavelength of $\lambda = 500$ nm. Incident light was passed through a wire grid polarizer to select s-polarization. Error bars given for photoluminescence quenching L_D measurements are determined based on the statistical error associated with the fit of the PL ratios.

9. Exciton diffusion in singlet fission materials

Singlet fission is a multiple exciton generation process that occurs in a select number of organic semiconductors. In these materials, optically generated singlet excitons are able to share their energy with an adjacent molecule in the ground state to produce two triplet excitons, each with energies of roughly half of the initially generated singlet, $2E(T_1) \approx E(S_1)$.[51,52] This is a spin allowed process, where the resulting triplet pair has a net overall singlet character, with total spin = 0, allowing for fast and efficient conversion.[51] The phenomenon was first reported by Singh *et al.* in 1965 to explain the observed delayed fluorescence in anthracene crystals,[198] but has received renewed interest in recent years due to the potential to increase OPV device performance through enhanced photocurrents.[45,46,51,52,199–202] Additionally, these materials are also being explored for their potential as a sensitization layer for traditional inorganic Silicon PVs. In this scheme, the organic singlet fission layer is deposited on the Si cell, absorbing high energy light above the Si bandgap, which then transfers generated carriers into the Si layer *via* a dissociating PbSe interlayer, increasing the photocurrent of the cell.[200] Organic photovoltaic devices based on these materials have already demonstrated η_{EQE} of over 100% at peak absorption, meaning that more than one electron is being collected for every photon that is incident on the device.[44,203] Additionally, theoretical considerations report that devices based on singlet fission materials have the potential to overcome the Shockley-Queisser limit, increasing the thermodynamic efficiency limit of a single junction solar cell from 34% to 44%, when singlet fission materials are paired with a material that absorbs photons with energies equal to the difference between $E(S_1)$ and $E(T_1)$.[51,199,204]

In addition to enhancing the photocurrent of a device through multiple exciton generation, OPVs based on singlet fission materials have to potential to exploit macroscopically long L_D, as single crystals of these materials have yielded the longest reported L_D to date.[77,47,82] This would allow devices to be made with active layer thicknesses comparable to absorption length of light, overcoming the exciton bottleneck associated with simple PHJ devices.[18,14] In endoergic singlet fission materials, that is materials where $E(T_1)$ is slightly more than half of $E(S_1)$, efficient triplet fusion can occur, where two triplets join to form one singlet.[51,52,205,84] The resulting singlet exciton generated from triplet fusion can then radiatively decay, producing delayed fluorescence.[51,52,47,84,206,207] Direct imaging of delayed fluorescence,[47,82] as well as surface conductivity measurements,[77] have yielded L_D of up to 4 μm and 8 μm in single crystals of tetracene and rubrene, respectively. This is orders of magnitude longer than the vast majority of organic semiconductors, where L_D are typically on the order of ~ 10 nm.[70,63,80,83] However, the implementation of single crystals into functioning OPVs has thus far been limited. As such, it is important to study exciton diffusion in polycrystalline films of singlet fission materials implemented in device architectures to better understand if long range exciton diffusion can be achieved to enhance OPV performance. Previous work examining diffusion of both singlets[144] and triplets[47,84] have reported that the energetic disorder induced by crystalline defects in a polycrystalline film, whether in the bulk or at grain boundaries, are detrimental to exciton diffusion. While these defects have relatively little effect on D, which is controlled by the extent of electron wavefunction overlap for triplets, they can have large effects on τ by either non-radiatively quenching or trapping excitons at low energy sites. Triplet excitons are especially susceptible to these defects because they

have long lifetimes, sampling many molecules, and transfer their energy *via* a nearest neighbor Dexter mechanism, limiting the number of available transfer sites once trapped.[84,56]

In this chapter we explore exciton diffusion as a function of polycrystalline grain size in films of pentacene that are implemented into OPV devices. Pentacene is an exoergic singlet fission material where $E(S_1) - 2E(T_1) = -0.11$ eV,[208–210] causing efficient singlet fission, occurring on timescales of 80 fs,[210] with triplet yields approaching 200%.[44] Conversely, triplet fusion is inefficient and delayed fluorescence is not appreciable. Measurements of L_D in exoergic dark singlet fission materials are limited; however, these materials are arguably of more interest in devices due to their fast fission rates and high triplet yields, which will maximize the generated photocurrent.[51,211,155,184] First, device architectures and film morphologies will be discussed, demonstrating that the polycrystalline grain size can be controlled by varying the thin film deposition rate. Then, device performance will be assessed and L_D is measured using a unique photovoltage approach which is capable of measuring L_D in non-emissive materials. This work demonstrates how the photovoltage method can be used to determine L_D in dark singlet fission materials and also provides insight into the relationship between crystalline order and the magnitude of triplet L_D.

9.1 Device architectures and fabrication

The devices used in this work are based on the D-A pairing of pentacene and C_{60}, respectively, consisting of a 20 nm poly(3-hexylthiphene-1,5-diyl) (P3HT) layer spun coat onto a patterned ITO coated glass substrate, with a 45 nm pentacene donor layer, 34 nm C_{60} acceptor layer, 11 nm BCP exciton blocking layer, and 100 nm Al cathode. Energy

level alignments of the device are shown in Fig. 9.1.[168,193,212,90] Pentacene layers were grown at deposition rates of 0.05 Å/s, 2 Å/s, and 10 Å/s in order to vary the polycrystalline grain size and the C_{60} layer was grown at 8 Å/s in order to provide consistency in both morphology and photoconversion efficiency in the C_{60} layer across all three devices. The primary purpose of the P3HT layer for the context of this work is to planarize the rough ITO surface, reducing the nucleation density of pentacene, which allows the crystalline grain size can be controlled by the deposition rate. Pentacene films deposited directly onto ITO showed no change in grain size as a function of deposition rate. Additionally, the large gap of P3HT relative to pentacene confines excitons in the pentacene layer, preventing exciton quenching at the anode. Previous work has also demonstrated that a P3HT layer at the anode interface aids in hole extraction and also acts as a singlet fission sensitizer by injecting singlet excitons into the pentacene layer through long range Förster transfer, which can subsequently undergo singlet fission and

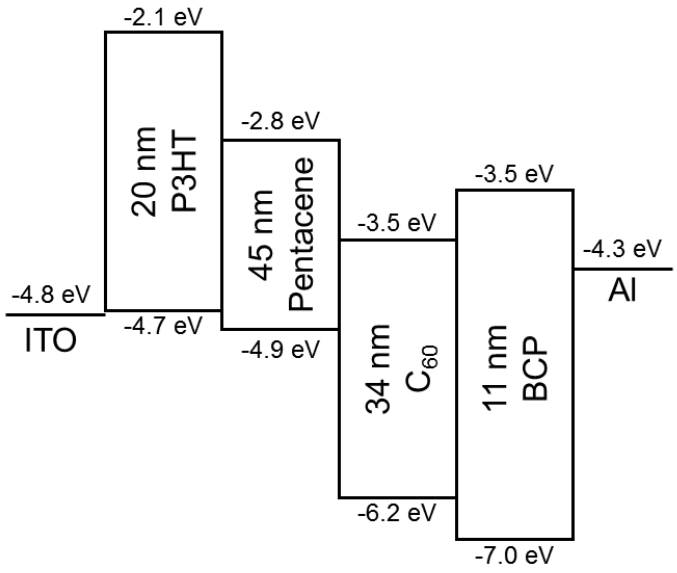

Figure 9.1 Energy diagram and layer thicknesses of the devices used for photovoltage diffusion length measurements. Three different devices using this structure were fabricated with pentacene layers of varying polycrystalline grain size. The polycrystalline grain size was controlled by varying deposition rate of the pentacene layer at rates of 0.05 Å/s, 2 Å/s, and 10 Å/s.

dissociate.[44,213] While this sensitization is beneficial to device performance, it must be rigorously accounted for when fitting for L_D.

9.2 Engineering pentacene grain size

The crystalline grain size of the pentacene layers are controlled by varying the deposition rate from 0.05 Å/s to 10 Å/s. Pentacene crystallizes in a layered herringbone packing motif with the long axis of the molecule oriented nearly perpendicular to the substrate, as shown in Fig. 9.2.[214,215] This general structure can exist in a number of different polymorphs depending on the type of substrate, substrate temperature during deposition, rate of deposition, and film thickness, where different polymorphs are identified based on their d_{001} spacing.[214,216–223] Single crystal bulk pentacene forms a triclinic $P\bar{1}$ structure with a d_{001} spacing of 14.1 Å.[214,215] Additionally, there exist a variety of different "thin film phase" polymorphs, the majority of which also form triclinic

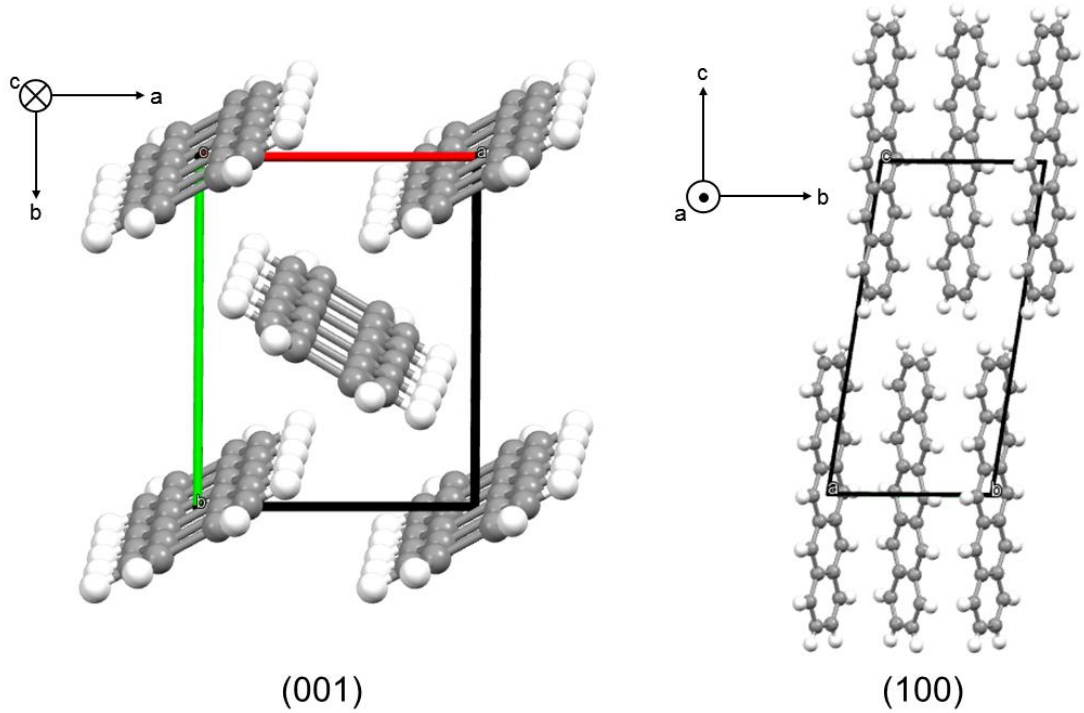

Figure 9.2 Triclinic crystal structure of single crystalline pentacene. (a) (001) plane showing the herringbone packing motif of pentacene. (b) (100) plane representing how pentacene molecules stand nearly vertically on the substrate.

structures which are characterized by varying tilt angles of the pentacene molecules relative to the substrate.[214,216–223] Previous reports demonstrate that structural evolutions can occur as a function of film thickness as the tilt of the pentacene molecule gradually increases further away from the substrate.[222,223] A similar effect is observed here as function of deposition rate and crystalline grain size.

Diffraction spectra, shown in Fig. 9.3, were measured using a Bruker D8 Discover 2D X-ray diffractometer with Co K_α radiation on device relevant architectures consisting of 45 nm films of pentacene grown at 0.05 Å/s, 2 Å/s, and 10 Å/s, deposited on 20 nm P3HT and an ITO coated glass substrate. Here, a small peak centered at 2θ = 6.4º is observed for a P3HT coated substrate, consistent with previous reports of crystalline P3HT.[224,225] Pentacene samples display evidence of polymorphism, which increases as a function of decreasing deposition rate. Two (001) diffraction peaks can be observed, one centered at 2θ = 6.8º, labeled (001'), corresponding to a $d_{001'}$ spacing of 15.1 Å, which is consistent with a previously observed triclinic thin film phase of pentacene,[218]

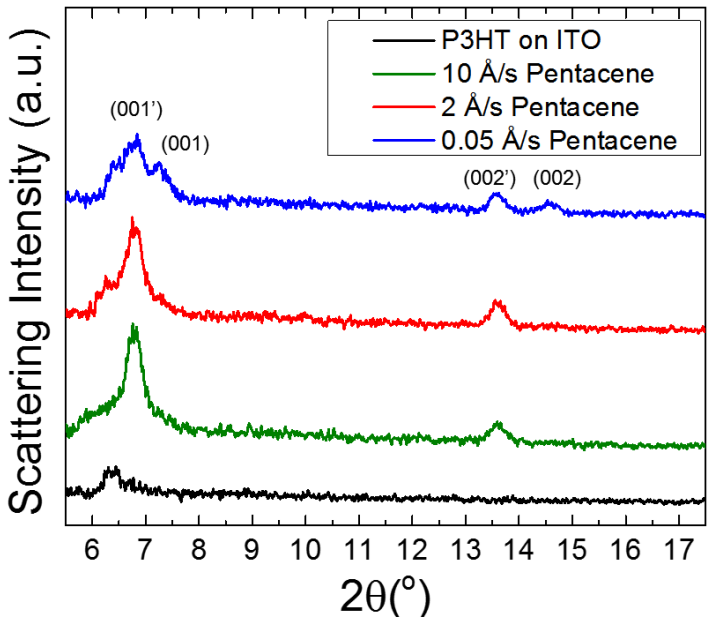

Figure 9.3 X-ray diffraction spectra of 45 nm films of pentacene deposited at varying deposition rates on a 20 nm P3HT layer and ITO coated glass substrate. All pentacene layers produce a (001') diffraction peak consistent with a thin film phase of pentacene and the film deposited at 0.05 Å/s also displays a (001) diffraction peak, consistent with the single crystal triclinic phase of pentacene.

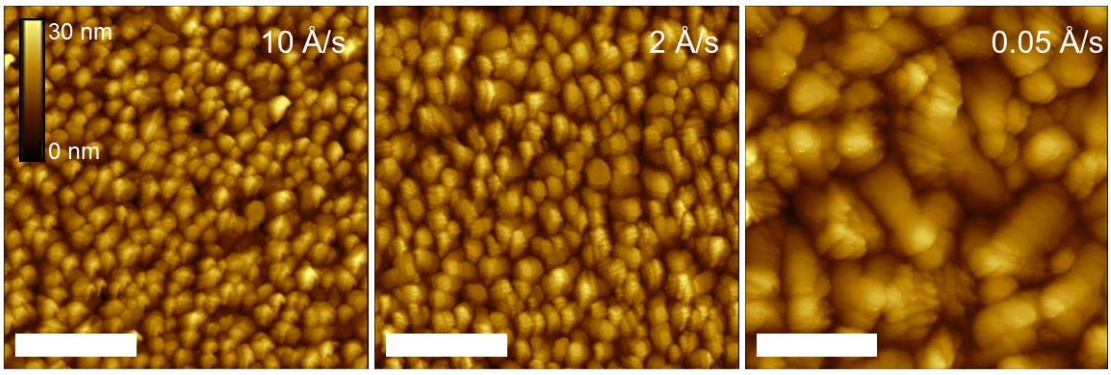

Figure 9.4 AFM height images showing the surface morphology of pentacene films deposited at 10 Å/s, 2 Å/s, 0.05 Å/s, displaying the increase in polycrystalline grain size as a function of decreasing deposition rate. Scale bars are 1 μm.

and another centered at $2\theta = 7.2°$, labeled (001), corresponding to a d_{001} spacing of 14.1 Å, consistent with the bulk single crystalline triclinic phase of pentacene. Second order reflections of these peaks are also observed at larger angles.[214,218,222,223] In these films, the 2 Å/s and 10 Å/s films only display the thin film phase, while the 0.05 Å/s film also displays the single crystalline triclinic diffraction peak, signifying an increased tilt in the pentacene molecules, likely changing as a function of thickness.

Film morphology is characterized by atomic force microscopy (AFM). Previous studies have demonstrated that the grain size of pentacene can be increased by lowering the deposition rate.[221,226] These reports describe pentacene nucleation and growth by diffusion limited aggregation, where the nucleation density increases as a function of deposition rate, and coarsening effects begin to dominate as the grains begin to merge.[221,223,226] Atomic force micrographs of films similar to those used in the X-ray diffraction (XRD) measurements are shown in Fig. 9.4. These images demonstrate a clear increase in the average grain size as a function of decreasing deposition rate. The samples all had a similar root mean squared surface roughness of 4.2 nm, 4.4 nm, and 4.4 nm for the 0.05 Å/s, 2 Å/s,

and 10 Å/s samples, respectively. With the change in grain size coinciding with similar interface roughness, the effect of grain size on L_D can be determined.

The correlation between grain size and polymorphism in these structures is interesting to note. It has previously been observed that a similar transformation from a thin film phase to a bulk triclinic phase can occur as a function of film thickness.[222,223] The mechanism for this transformation is attributed to pentacene molecules, away from the substrate, growing on the inclined plane of a crystalline grain, which gradually increases the tilt angle of the pentacene molecule relative to the substrate. In the films used in this work, the smaller grain sizes appear to suppress this transformation, perhaps caused by the merging of crystalline grains closer to the substrate, which locks in the thin film phase morphology.

Figures 9.5 and 9.6 show XRD spectra and AFM images for 34 nm C_{60} films deposited at 8 Å/s on top of the pentacene samples. Figure 9.5 demonstrates that when C_{60} is deposited on the pentacene films a diffraction peak centered at $2\theta = 12.9^{o}$, corresponding to a *d* spacing of 8.0 Å, is produced consistently across all three samples. This peak is slightly off from the 8.2 Å spacing commonly reported for the (111) plane of the face centered cubic C_{60} crystal

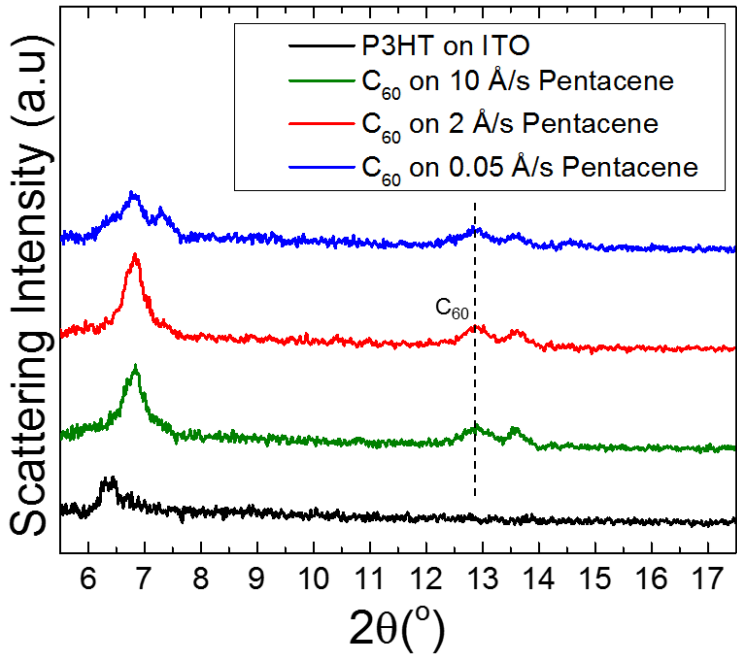

Figure 9.5 X-ray diffraction spectra of 34 nm C_{60} films deposited at 8 Å/s on pentacene, P3HT, and an ITO coated glass substrate. The C_{60} layers produce a consistent diffraction peak across three pentacene films that were grown at different deposition rates.

structure,[227–230] but agrees with a previously observed diffraction peak in C_{60} films.[228] Figure 9.6 displays that C_{60} forms small circular grains which nucleate on the molecular terraces of the pentacene under layer, with an average step size consistent with the d_{001} spacing of pentacene. The domain size and XRD spectra of the C_{60} layers are very consistent across all three samples. This consistent morphology yields similar photoconversion behavior in the C_{60} layers for the devices, allowing for clear comparisons of the photophysical changes in the pentacene layers across devices.

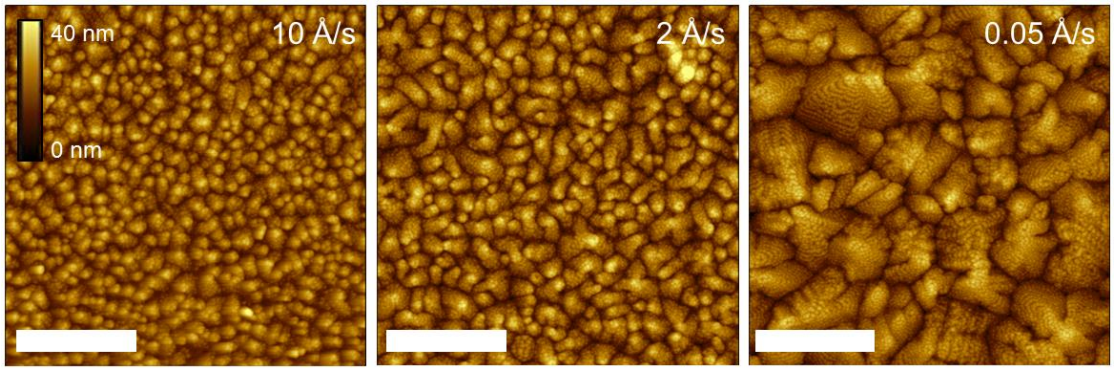

Figure 9.6 AFM height images showing the surface morphology of 34 nm C_{60} films deposited on pentacene films of varying crystalline grain size, P3HT, and an ITO coated glass substrate. C_{60} forms small circular grains that nucleate on the molecular terraces of the pentacene under layer. Scale bars are 1 μm

9.3 Relation between grain size and device performance

Increases in the pentacene grain size coincided with improved OPV device performance. Figure 9.7 shows the device η_{EQE} compared to the extinction coefficients for pentacene and C_{60}. In these devices, the η_{EQE} corresponding to predominantly C_{60} absorption, peaked at λ = 345 nm, remains relatively constant across all three devices, while the η_{EQE} associated with pentacene absorption, peaked at λ = 670 nm, shows a systematic increase as a function of increasing grain size, resulting in an 8.8% increase in the magnitude of η_{EQE} at peak absorption. The absorption spectrum of pentacene remained relatively unchanged across all three deposition rates; therefore, this asymmetric increase

in η_{EQE} suggests that the C_{60} L_D remains constant and the pentacene L_D systematically increases. Additionally, this behavior also suggests that at short-circuit, η_{CS} and η_{FC} are constant across all three devices, as a change in either of these parameters would cause a broadband reduction in η_{EQE}. It would be serendipitous if a change in either η_{CS} or η_{FC} was precisely offset by a change in C_{60} L_D to generate the observed agreement, given the similarity in the morphology of the C_{60} layers.

In addition to an increase in η_{EQE}, the larger crystalline grain size also improved OPV device performance. Figure 9.8 shows the performance metrics of the devices measured under AM1.5G illumination at 100 mW cm^{-2}. The short-circuit current density of the devices improved from (4.3 ± 0.1) mA cm^{-2} for the device containing the pentacene layer deposited at 10 Å/s to (5.4 ± 0.1) mA cm^{-2} for the 0.05 Å/s device. The trend of J_{SC} is predicted within 5% from the integrated η_{EQE} spectra, suggesting that this 26% improvement in J_{SC} is due to the increase in pentacene L_D. The devices also displayed an increase in V_{OC} with lower

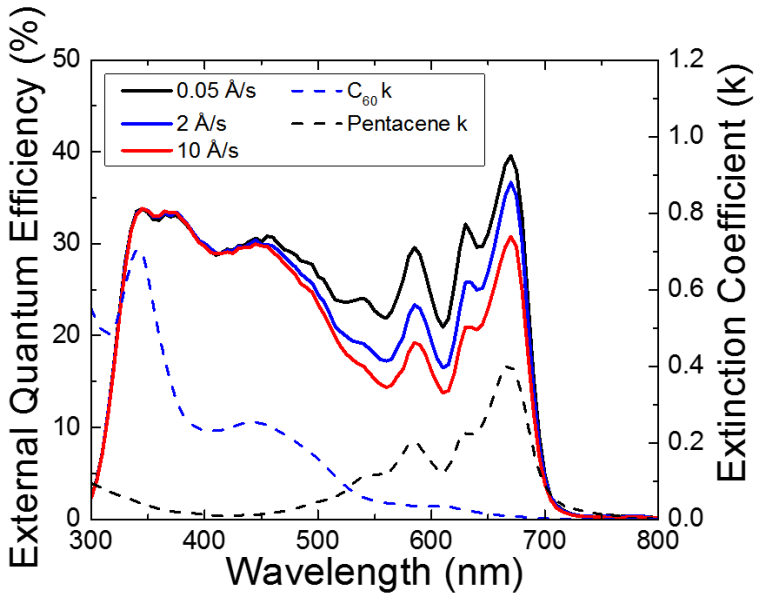

Figure 9.7 External quantum efficiency measurements of pentacene-C_{60} devices compared to the extinction coefficients of the active layers. The portion of the spectra corresponding to C_{60} absorption is constant across all three devices, while the portion corresponding to pentacene absorption shows a systematic increase as a function of decreasing thin film deposition rate and increasing polycrystalline grain size, suggesting an increase in pentacene L_D.

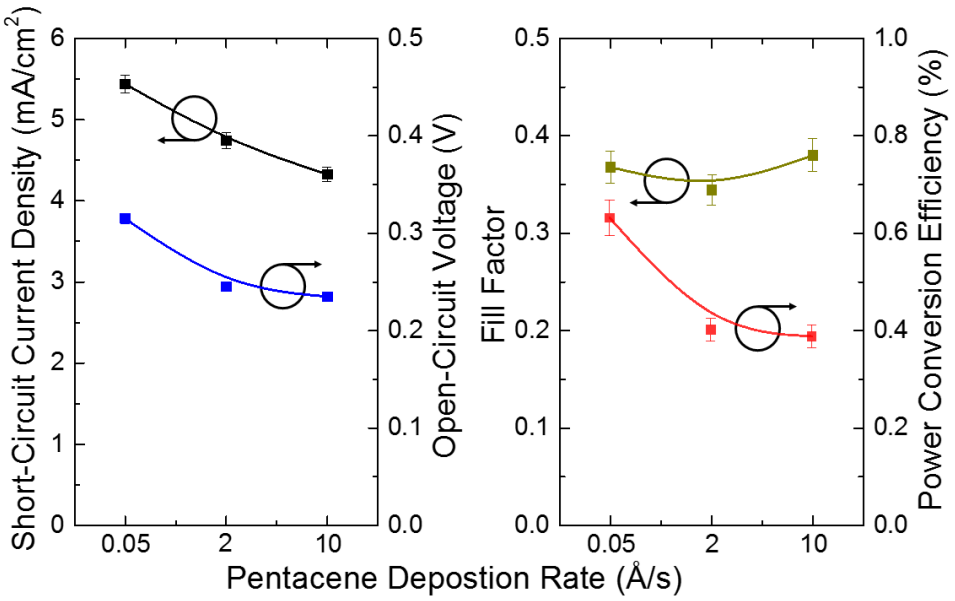

Figure 9.8 Device performance metrics for pentacene-C_{60} devices fabricated with varying pentacene deposition rates under AM1.5G illumination at 100 mW cm^{-2}. Error bars are based on the standard deviation across 8 devices. Error in the open-circuit voltage is smaller than the size of the data point.

pentacene deposition rates, which was caused by a decrease in the magnitude of the dark current throughout the fourth quadrant. This could be caused by a decrease in non-geminate recombination at positive voltages due to either a decrease in trap-assisted recombination or an increase in the carrier mobility, which has previously been correlated with pentacene grain size.[217,221,231] These improvements, along with a relatively constant *FF*, result in a 63% improvement in the power conversion efficiency of the 0.05 Å/s relative to the 10 Å/s device. The *FF* and J_{SC} in these devices is reduced compared to similar devices in the literature.[184,222,152] We attribute this reduction due to increased geminate and non-geminate recombination resulting from the increased pentacene and C_{60} layer thicknesses used in this study, compared to optimized devices, which are needed to accurately extract the relatively long L_D.

9.4 Photovoltage diffusion length measurements in singlet fission materials

9.4.1 Modeling diffusion in singlet fission materials

The photovoltage technique presented in Chapter 6 can be used to measure L_D of dark triplet excitons in materials which exhibit singlet fission. In order to achieve accurate measurements of the intrinsic pentacene L_D, η_{CS} must be decoupled from these measurements, the injection of excitons from P3HT into pentacene needs to be properly accounted for, and the diffusion of triplet excitons in the pentacene layers needs to be accurately modeled. The diffusion of singlet and triplet excitons in singlet fission materials can be described by two coupled steady-state equations:

$$0 = D_s \frac{\partial^2 n_s(x)}{\partial x^2} - \frac{n_s(x)}{\tau_s} + G(x) - k_{fis} n_s(x) + \frac{1}{2} k_{fus} n_t(x)^2, \quad (9.1)$$

and

$$0 = D_t \frac{\partial^2 n_t(x)}{\partial x^2} - \frac{n_t(x)}{\tau_t} + 2k_{fis} n_s(x) - k_{fus} n_t(x)^2, \quad (9.2)$$

where the subscripts *s* and *t* denote singlet and triplet quantities, respectively, *n* is the exciton density, τ is the natural exciton lifetime, *D* is the diffusivity, *G* is the optical generation rate, k_{fis} is the rate of singlet fission, and k_{fus} is the rate of triplet fusion. In exoergic singlet fission materials like pentacene these equations can be simplified significantly. Transient absorption measurements on polycrystalline films of pentacene have demonstrated that singlet fission is very efficient and unidirectional, since two triples do not have sufficient energy to regenerate the singlet, allowing for k_{fus} terms to be neglected.[208,210,232,46] In polycrystalline pentacene, reported values of k_{fis} are equal to 1.3×10^{13} s^{-1}, this has been shown to be competitive with vibrational relaxation, leading to negligible PL in films of pentacene and allows singlet exciton decay back to the ground state to be ignored.[208,210,232] Additionally, magnetic field dependent photocurrent

measurements in pentacene-C_{60} devices have suggested that in pentacene films thicker than 5 nm triplet yields approach 200%, as singlet fission outcompetes the rate of singlet exciton dissociation and the singlet hopping rate; therefore the singlet diffusion term can also be ignored.[44] Under these assumptions, Eqn. 9.1 can be simplified to $G(x) = k_{fis} n_s(x)$, inserting this expression into Eqn. 9.2, the diffusion of triplet excitons in pentacene can be described by:

$$0 = D_t \frac{\partial^2 n_t(x)}{\partial x^2} - \frac{n_t(x)}{\tau_t} + 2G(x). \tag{9.3}$$

Thus, the generation profile of triplet excitons can be modeled from $G(x)$, which can be rigorously accounted for through the use of a transfer matrix formalism,[79] and it is assumed that all dissociated excitons are triplets and the triplet yield is 200%.

9.4.2 C_{60} photoluminescence quenching measurements

In order to extract an intrinsic value of L_D for pentacene using the photovoltage approach, the intrinsic C_{60} L_D value must be determined in order to decouple the effects of interfacial geminate recombination. This can be accomplished with spectrally resolved PL quenching measurements

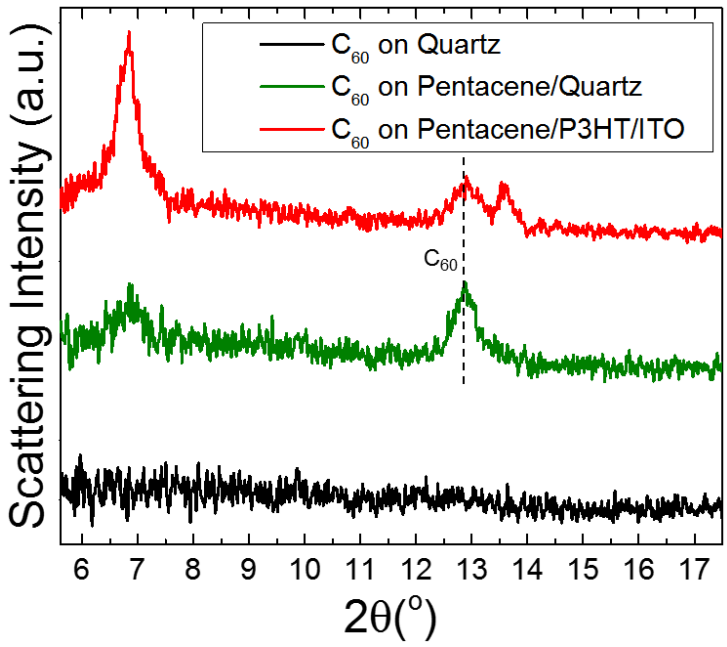

Figure 9.9 X-ray diffraction spectra of C_{60} films used for spectrally resolved photoluminescence quenching measurements. C_{60} films deposited on quartz reveal no diffraction peaks, while the C_{60} film deposited on pentacene and quartz produces the same diffraction peak that is observed for the C_{60} layers in devices.

which only rely on efficient charge transfer and not charge transfer state dissociation.[70,135] Additionally, it must be ensured that the structure of the C_{60} film used in this measurement is the same as the crystalline C_{60} layer in the devices. Figure 9.9 shows that when X-ray diffraction spectra are measured on a 46 nm film of C_{60} deposited at 8 Å/s on quartz no scattering peaks are revealed; however, when the same film is deposited on an 18 nm layer of pentacene on quartz, the same crystalline phase that occurs in the devices is produced, generating a diffraction peak centered at $2\theta = 12.9^{\circ}$. Thus, PL quenching measurements must be conducted on C_{60} films deposited on top of a pentacene under layer in order to ensure the sample is representative of films used in devices.

With the presence of the dissociating pentacene interface introduced in this structure, the approach to the spectrally resolved PL quenching measurement must be modified. Typically, PL quenching measurements compare the magnitude of PL resulting from an unquenched film to a quenched film with one adjacent exciton dissociating layer. In this case, the PL resulting from a C_{60} film deposited on a dissociating pentacene layer must be compared to the PL from a film with a dissociating material present on each side of the C_{60} layer. As shown in Fig. 9.10a, one structure consists of the pentacene and C_{60} layers deposited on quartz that is capped with a film of BCP, which serves as an exciton blocking

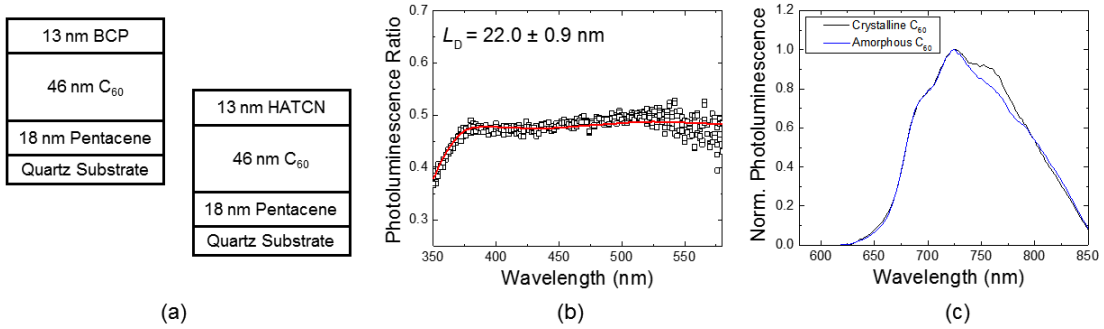

Figure 9.10 (a) Film structure of the samples used for spectrally resolved photoluminescence quenching measurements. (b) Photoluminescence ratios and corresponding fit for C_{60} L_D. (c) C_{60} emission spectra for an amorphous film of C_{60} deposited on quartz and a crystalline film of C_{60} deposited on a film pentacene and quartz.

layer and also prevents oxidation. This film is modeled with a quenching boundary condition ($n(x) = 0$) at the pentacene-C_{60} interface and a reflecting boundary condition ($\frac{dn(x)}{dx} = 0$) at the C_{60}-BCP interface. The other structure consists of the same pentacene and C_{60} layer, but is capped with a dissociating HATCN layer. In this case, both interfaces are modeled as dissociating. The resulting PL ratio and fit are shown in Fig. 9.10b, yielding a value of $L_D = (22.0 \pm 0.9)$ nm. This was a slight increase over the $L_D = (18.7 \pm 0.7)$ nm that is determined for the amorphous C_{60} layer (see Fig. 7.8b). Normalized PL spectra of the amorphous and crystalline C_{60} emission spectra are shown in Fig. 9.10c, which displays an extra vibronic peak that grows in for the crystalline C_{60} sample; however, it should be noted that the spectra are truncated on the near infrared side of the spectrum due to the responsivity of the detector. With this intrinsic value of L_D for the crystalline C_{60} layer, the L_D of pentacene can now be determined.

9.4.3 Accounting for singlet fission sensitization

Due to the spectral overlap between the emission spectrum of P3HT and the absorption spectrum of pentacene, as shown in Fig 9.11a, exciton injection from the P3HT layer into pentacene can occur through long range Förster transfer and must be quantitatively accounted for when fitting for L_D.[233,234,146] The process that leads to the dissociation of optically generated excitons in P3HT is shown schematically in Fig. 9.11b. Here, optically generated singlet excitons in the P3HT layer transfer their energy to pentacene by Förster transfer, creating a singlet exciton in pentacene which can then undergo singlet fission, generating two triplets that can diffuse to the donor acceptor interface and dissociate. Not properly accounting for this singlet fission sensitization will lead to an overestimate of the

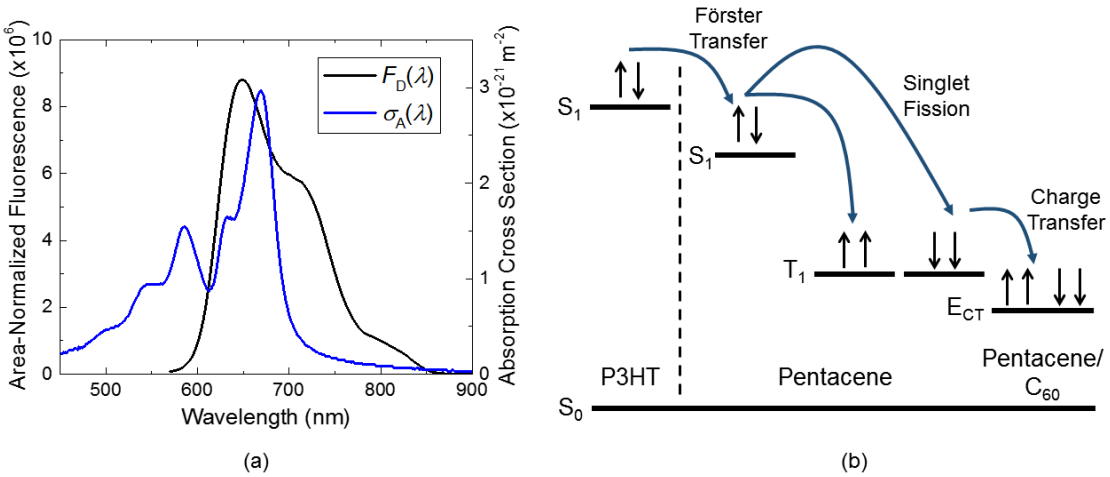

Figure 9.11 (a) Area normalized emission spectrum of P3HT ($F_D(\lambda)$) and absorption cross section (σ_A) of pentacene, which in part determines the Förster radius and number of excitons injected from P3HT into pentacene. (b) Process of singlet fission sensitization. Optically generated singlet excitons (S_1) in P3HT transfer to the singlet energy level of pentacene *via* Förster transfer, which rapidly undergoes singlet fission to two triplets (T_1), which can then diffuse to the pentacene-C_{60} interface and charge transfer (E_{CT}).

number of carriers generated from direct absorption on pentacene and C_{60}, causing an overestimate of L_D.

Within the P3HT layer, exciton diffusion can be modeled by a steady-state exciton diffusion equation incorporating a term which accounts for Förster transfer:

$$D\frac{\partial^2 n(x)}{\partial x^2} - \frac{n(x)}{\tau} + G(x) - n(x)k_f(d) = 0, \tag{9.4}$$

where $n(x)$ is the exciton density at a given position in the P3HT layer and k_f is the rate of Förster transfer for excitons in P3HT to the pentacene film. Previous work has demonstrated that when Förster energy transfer occurs between an excited molecule and a film of material, the distance dependence is relaxed from r^{-6} to d^{-3}, where d is the distance to the planar interface, given by $d = x - L$, x is the position in the layer, and L is the thickness.[234,146,235] In this architecture, the k_f is given by:

$$k_f = \frac{\rho_A}{\tau}\frac{\pi {R_0}^6}{6d^3}, \tag{9.5}$$

where ρ_A is the molecular density of the acceptor and R_0 is the Förster radius, which is calculated to be R_0 = 2.2 nm between P3HT and Pentacene, using Eqn. 3.4.

In order to model the singlet fission sensitization from P3HT Eqn. 9.4 must be solved numerically. Here, a centered finite difference approximation is used which can be found in Appendix E. In this method the x domain is discretized into small steps (Δx) relative to the thickness of the film and the differential equation is transformed into a set of linear equations which are solved for $n(x)$. Using this method to solve Eqn. 9.4 with R_0 = 2.2 nm, $\rho_A = 3.02 \times 10^{27}$ molecules m^{-3}, and L_D = 8.5 nm, the total injection rate of excitons from the entire P3HT layer into pentacene can be determined as:[105]

$$G_{inj} = \frac{1}{\Delta x_{pent}} \int_0^L n(x) k_f(x) dx, \tag{9.6}$$

where Δx_{pent} is the bin spacing in the pentacene layer. Here, we approximate that all of the excitons are injected into the first monolayer of pentacene. In the actual system this is not necessarily true; however, the rate of injection into the first monolayer will always be the greatest and the thickness of the pentacene layers are much greater than R_0, making this a reasonable approximation. The resulting exciton diffusion equation for triplet excitons in pentacene at the P3HT-pentacene interface (x = 0) is then given by:

$$D_t \frac{\partial^2 n_t(0)}{\partial x^2} - \frac{n_t(0)}{\tau} + 2G(0) + 2G_{inj} = 0. \tag{9.7}$$

Here, G_{inj} is multiplied by a factor of 2 to account for singlet fission. With the ability to properly determine the effects of injection from P3HT and geminate recombination at the interface, the photovoltage results can be now be interpreted to extract intrinsic values of L_D for pentacene.

9.4.4 Dependence of the triplet diffusion length on crystalline grain size in pentacene

Photovoltage L_D measurements of the three pentacene-C_{60} devices are conducted using a blue (λ_{peak} = 455 nm) and red (λ_{peak} = 625 nm) LED to probe diffusion in the C_{60} and pentacene layers, respectively. Photovoltage transients of the three devices measured under λ_{peak} = 625 nm illumination at four different excitation intensities and their corresponding charge extraction relations are shown in Fig. 9.12. These plots demonstrate that the relationship between carriers and voltage is similar across all three devices; however, the magnitude of the voltage plateau at a given excitation intensity clearly increases as a function of pentacene grain size, suggesting an enhancement in the pentacene L_D. Results of the photovoltage analysis are summarized in Table 9.1. Device relevant C_{60} L_D values, which assume η_{CS} = 1, are relatively constant across all three devices, ranging from (15.8 ± 1.5) nm in the device containing the 10 Å/s pentacene layer, to (15.1 ± 1.5) nm in the

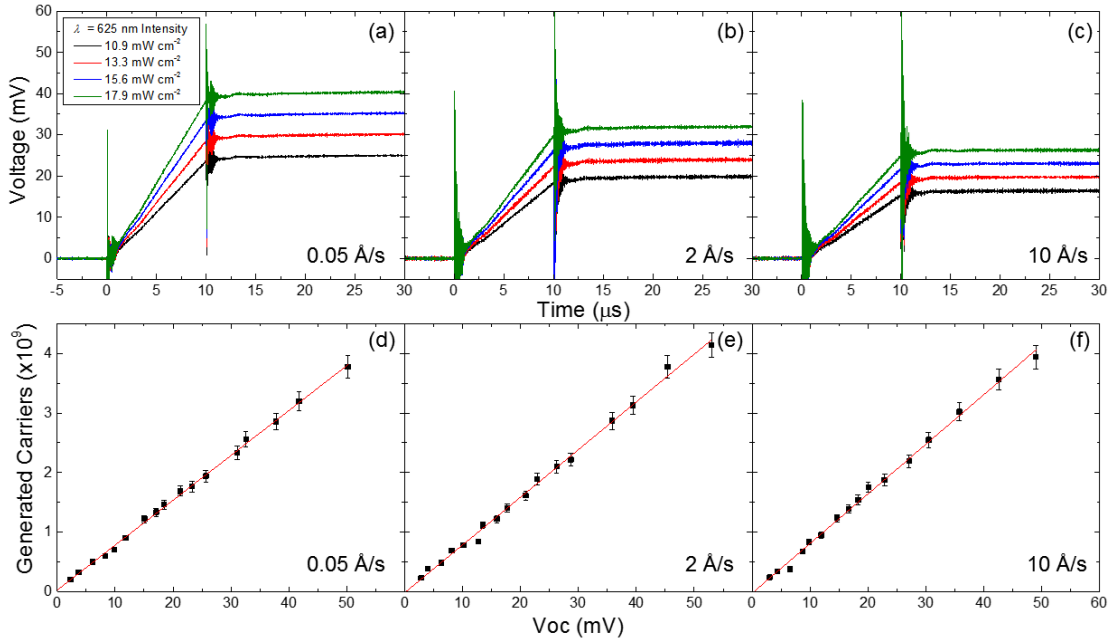

Figure 9.12 Photovoltage measurements taken under λ = 625 nm excitation at four excitation intensities (a-c) and charge extraction measurements (d-f) used to determine pentacene L_D. (a) and (d) correspond to devices with pentacene layers grown at 0.05 Å/s, (b) and (e) at 2 Å/s, and (c) and (f) at 10 Å/s.

Pentacene Deposition Rate (Å/s)	Photovoltage C_{60} L_D (nm)	η_{CS} (%)	Pentacene L_D (nm)
0.05	15.3 ± 1.5	75.1 ± 2.3	33.4 ± 3.5
2	15.1 ± 1.5	73.9 ± 2.2	26.6 ± 2.8
10	15.8 ± 1.6	77.6 ± 2.3	20.9 ± 2.2

Table 9.1 Photovoltage L_D measurements as a function of pentacene layer deposition rate. Photovoltage C_{60} measurements are subject to geminate recombination losses and yield similar values across all three devices. These values are compared to photoluminescence quenching measurements, which yield C_{60} L_D = (22.0 ± 0.9), to determine the charge transfer state separation efficiency (η_{CS}). With η_{CS} intrinsic pentacene L_D can be determined from photovoltage measurements, demonstrating a systematic increase as a function of polycrystalline grain size.

device with the 2 Å/s pentacene layer. When this data is instead fit for η_{CS} using a C_{60} L_D = (22.0 ± 0.9) nm, determined from PL quenching measurements, similar values of η_{CS} are determined for all devices, ranging from (73.9 ± 2.3)% to (77.6 ± 2.3)%. With the combination of these two measurements the effect of interfacial geminate recombination can be decoupled from the photovoltage measurements, allowing for the measurement of intrinsic pentacene L_D values. When the photovoltage transients in Fig. 9.12 a-c are fit with η_{CS}, the pentacene L_D is found to systematically increase as a function of polycrystalline grain size, from (20.9 ± 2.9) nm in the pentacene layer deposited at 10 Å/s, to (33.4 ± 3.5) nm in the pentacene layer deposited at 0.05 Å/s.

Similar trends between L_D and crystalline grain size have previously been reported in fluorescent and endoergic singlet fission materials.[47,144] These studies have found that the change in L_D is driven by increases in τ as a function of grain size, which is attributed to non-radiative quenching and trapping of excitons at crystalline defects and grain boundaries. In these types of materials, the exact energy levels of a molecule are determined, in part, by the surrounding dielectric environment. In a single crystal the orientation of surrounding environment is identical for each molecule leading to a very

narrow density of states for the triplet energy level. When this symmetry is broken, at a grain boundary for instance, local fluctuations in the dielectric environment broaden the distribution of triplet energies, creating some low energy states which are capable of trapping excitons.[84,37] We expect a similar effect is driving the change in L_D in this system; however, in order to decouple the relative contributions of D and τ additional measurements are needed. In emissive materials, decoupling these effects can accomplished by measuring τ directly *via* transient PL measurements. In dark materials, measurements of τ must be extracted from transient absorption measurements. One study using this technique has reported a τ_t = 5 ns in polycrystalline pentacene.[46] This is relatively short for triplet excitons and perhaps accounts for the discrepancy between the nanoscopic L_D reported here and the microscopic L_D reported in single crystals of singlet fission materials, which display τ_t on the order of hundreds of ns to tens of μs.[47,84] Additionally, one should not that in Eqn. 9.7 we are extracting a one-dimensional L_D in the direction perpendicular to the substrate, while grain growth is taking place parallel to the substrate. Physically, an exciton is taking a three-dimensional random. Thus the probability of a grain boundary due to motion in the x-y plane is affected by both grain size and the three-dimensional L_D. These factors will influence L_D in the projection along the z-axis, perpendicular to the D-A interface, extracted here.

9.5 Conclusions

Singlet fission is a unique process which occurs in a select number of organic semiconductors, where optically generated singlet excitons are able to be transformed into two triplet excitons. This mechanism has the potential to increase photocurrents in devices in order to realize more efficient OPVs. Additionally, single crystals of these materials

have yielded the longest reported L_D to date. In this chapter, L_D of pentacene is measured as a function of polycrystalline grain size using a photovoltage method in order to explore the relationship between L_D and crystalline grain size in functioning OPVs and demonstrate a method to determine L_D in previously inaccessible dark singlet fission materials. It is found that the polycrystalline grain size could be controlled by varying the deposition rate of pentacene and L_D shows systematic increases as a function of increasing grain size, suggesting that grain boundaries can inhibit exciton diffusion by trapping or non-radiatively quenching excitons. Future work should focus on engineering the morphology of these pentacene films for even larger grain sizes in order to realize further enhancements in L_D by growing at slower deposition rates, exploring different planarizing layers, and growing at elevated temperatures. Additionally, the methodology presented here should be expanded to other dark singlet fission materials with longer τ_t in order to understand which materials are capable of yielding microscopic L_D when implemented into device architectures. If this can be achieved, simple PHJ devices which are capable of overcoming the exciton bottleneck can be possible.

9.6 Experimental methods

Sample preparation: Pentacene layers were grown at deposition rates of 0.05, 2, and 10 Å/s, C_{60} layers were grown at 8 Å/s, BCP and HATCN layers were grown at 2 Å/s. Aluminum cathodes were deposited at a rate of 3 Å/s through a shadow mask. All devices have an active area of 0.25 cm^2 and were encapsulated in glass to avoid degradation in atmosphere. P3HT layers were spin coat at 1500 RPM for 30 s from a P3HT solution dissolved in chlorobenzene at a concentration of 5 mg mL^{-1}. The devices considered in this work consisted of a 20-nm-thick planarizing layer of P3HT, a 45-nm-thick pentacene

donor layer, a 34-nm-thick acceptor layer of C_{60}, an 11 nm-thick exciton blocking layer of BCP, and a 100-nm-thick cathode layer of Al. Photoluminescence quenching measurements were conducted on films containing an 18 nm pentacene layer deposited at 2 Å/s, a 46 nm layer of C_{60} deposited at 8 Å/s, and a BCP or HATCN layer deposited at 2 Å/s. All materials were used as received without further purification. Pentacene, P3HT, and HATCN were purchased from Luminescence Technology Corp.; C_{60} from the MER corporation; and BCP and Al from Alfa Aesar. For additional experimental details, see Appendix B.

Charge extraction: Charge extraction measurements were collected in atmosphere on devices illuminated using an M625F2 LED from Thorlabs with an illumination area of $\pi \times 0.075^2$ cm^2. The LEDs and OPV were simultaneously switched using n-channel MOSFETs and integrated gate driver circuits. MOSFETs were purchased from STmicroeletronics (STP27N3LH5) and gate drivers were purchased from Microchip Technology. In order for the MOSFETs connected to the LED and OPV to switch in opposite directions simultaneously, an inverting gate driver (TC4421AVPA) was connected to the LED transistor and a non-inverting gate driver (TC4422AVPA) was connected to the OPV transistor. Gate drivers were switched using a 10V, 200 ms period square wave generated from an Agilent 33220A pulse generator and current transients were recorded using a Tektronix TDS5104B oscilloscope.

Voltage transients: Voltage transient measurements were taken in atmosphere. Devices were illuminated with M455F1 and M625F2 LEDs from Thorlabs to obtain the voltage transients. A λ=455 nm LED was used to probe C_{60} and a λ=625 nm LED was used to probe Pentacene. LEDs were excited by a Hewlett-Packard 8114A pulse generator. The

illumination from the LEDs was focused onto the OPV using a bifurcated fiber bundle (BFY1000HS02) and fiber collimator (F220SMA-532), both purchased from Thorlabs. Voltage transients were recorded by a Tektronix TDS5104B oscilloscope. All LED spectra were measured using an Ocean Optics HR4000 spectrometer and the power output of all LEDs were recorded using a Thorlabs PDA36A amplified silicon photodetector. Error bars in L_D were determined based on the standard deviation across a statistically significant number of devices. Error associated with the extracted η_{CS} were propagated based on the uncertainty in both the photovoltage and photoluminescence quenching L_D measurements.

Current-voltage measurements: Current-voltage measurements were taken using an Agilent 4155C semiconductor parameter analyzer. Total illuminated and photocurrent measurements were carried out under AM1.5G solar radiation at 100 mW cm^{-2} with an illumination area of $\pi \times 0.075^2$ cm^2.

External quantum efficiency measurements: External quantum efficiency measurements were taken under monochromatic illumination from a 300 W xenon arc lamp coupled into a Cornerstone 130 1/8 meter monochromator and chopped with an SRS SR540 optical chopper. Current measurements were taken using an SRS SR810 lock-in amplifier.

Photoluminescence quenching measurements: Photoluminescence quenching measurements were taken using a Photon Technology International Quantum Master 4 Fluorimeter. Measurements were performed under a N_2 purge at an incident angle of 70° to the substrate normal. Samples were illuminated using a Xe lamp coupled into a monochrometer selected to excitation wavelengths of λ = 350 - 580 nm and photoluminescence intensity was monitored at an emission wavelength of 750 nm. Error

bars given for photoluminescence quenching L_D measurements are determined based on the statistical error associated with the fit of the PL ratios.

10. Transient photovoltage measurements

Chapters 5 and 7 demonstrate the difficulty of attaining accurate measures of L_D for dark excitonic materials where traditional PL based measurement techniques are not applicable. A similar problem exists for measuring τ in dark materials. Charge carrier based techniques, which are capable of probing diffusion in dark materials, determine the magnitude of $L_{D,}$ but often D and τ must be decoupled to understand the physics of what controls or is changing L_D in a material, as was the case for triplet excitons in Pentacene in the previous chapter. This can be accomplished if values of L_D are combined with a measure of D or τ. Exciton lifetimes in luminescent materials are typically measured from transient PL decays, where a film is excited with a short laser pulse and the PL is measured as a function of time and fit to some sort of exponential decay.[67–69,139,140] For dark materials, τ is generally measured by transient absorption.[46,159,192,210,236] In these measurements, films are initially excited with a short, monochromatic laser pulse and the absorption spectrum of the film is measured as a function of delay time after the initial excitation, using a white light probe. The initial excitation will lead to an excited state (exciton) absorption feature that is proportional to the optically generated exciton density. The transient decay of this excited state absorption feature can be fit with a model similar to those used to treat PL decays and determine τ. However, these measurements can be involved, requiring complex experimental set ups with fast detection electronics and interpretations of convoluted transient absorption spectra. In this chapter, transient photovoltage measurements are explored for the potential to examine exciton dynamics in real time and extract values of τ in dark materials. A model to fit the photovoltage transients will be presented and experimental findings, shortcomings, and future potentials will be discussed.

10.1 Exciton dynamics of transient photovoltage measurements

As discussed in Chapter 7, the magnitude of the photovoltage in an OPV is directly proportional to the number of dissociated excitons.[185–187] When the device is held at open-circuit and illuminated, a photovoltage is produced resulting from the buildup of charge carriers in the active layers of the device due to exciton dissociation at the D-A interface. If this measurement is carried out in the transient regime, then the rise in photovoltage will potentially represent a real time measure of exciton dissociation at the D-A interface. The total number of excitons that have reached the interface at a given time will depend both on the rate at which the exciton arrives at the interface, proportional to D, and the average time that an exciton can diffuse before recombination occurs, given by τ. Thus, fitting this photovoltage rise with solutions to the transient exciton diffusion equation allows for τ to be extracted if the value of L_D is known.

To examine the validity of this approach, the fluorescent material tris-(8-hydroxyquinoline)aluminum (Alq_3) is first considered. A PHJ device based on the D-A pairing of 4,4′-cyclohexylidenebis[N,N-bis(4-methylphenyl)benzenamine] (TAPC) and Alq_3, respectively, was held at open-circuit and illuminated with a short pulse from a N_2 dye laser with an excitation wavelength of λ = 400 nm. Molecular structures for these materials are shown in Fig. 10.1a. The pulse width (τ_{pulse}) of the laser was measured to be $\leq$ 1.8 ns and at this excitation wavelength, nearly all of the absorption occurs on Alq_3. The resulting normalized photovoltage transient is shown in Fig 10.1b, which demonstrates that the photovoltage rise persists long after the end of the excitation pulse, eventually plateauing, due to the diffusion and dissociation of excitons generated away from the D-A interface. Transient photoluminescence of a film of Alq_3 was separately measured using

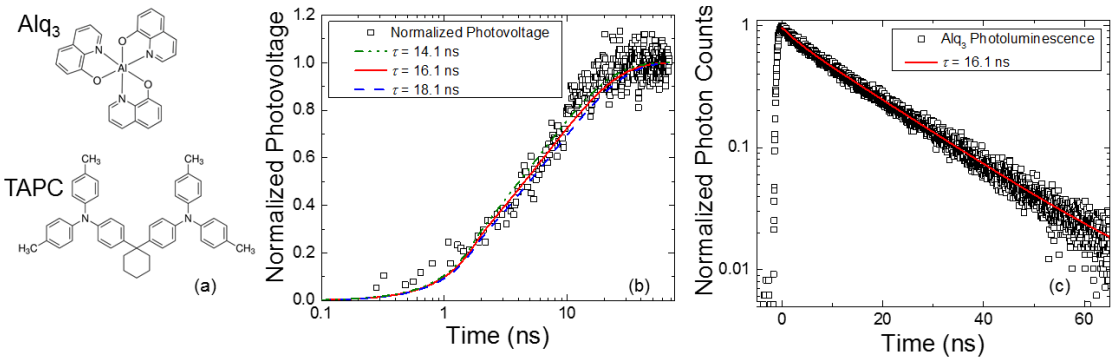

Figure 10.1 (a) Molecular structures of tris-(8-hydroxyquinoline)aluminum (Alq_3) 4,4′-cyclohexylidenebis[N,N-bis(4-methylphenyl)benzenamine] (TAPC). (b) Normalized transient photovoltage rise when Alq_3 layer of the device is optically excited with a 1.8 ns pulse and predicted photovoltage rises under varying values of the exciton lifetime (τ). (c) Transient photoluminescence of Alq_3 film and corresponding exponential fit for τ.

time correlated single photon counting, shown in Fig. 10.1c. The PL decay was fit with a single exponential, determining τ = 16.1 ns.

Given the linear relationship between the voltage and number of carriers in a device, the photovoltage at any time t is equivalent to the total number of dissociated excitons up to time t. Additionally, the photovoltage rise normalized to the plateau voltage will be identical to the normalized number of accumulated carriers. Therefore, the photovoltage rise can be can be predicted using solutions to the transient exciton diffusion equation:

$$\frac{\partial n(x)}{\partial t} = \frac{{L_D}^2}{\tau}\frac{\partial^2 n(x)}{\partial x^2} - \frac{n(x)}{\tau} + G(x), \tag{10.1}$$

where $n(x)$ is the exciton density, τ is the exciton lifetime, and $G(x)$, the exciton generation rate, is determined by a transfer matrix formalism for $t < \tau_{pulse}$ and $G(x) = 0$ for $t > \tau_{pulse}$.[79] Solving Eqn. 10.1 with a quenching boundary condition at the D-A interface ($n(x = 0) = 0$), the normalized voltage transient can be fit by the integrated flux of excitons arriving at the interface normalized to the total number of dissociated excitons:

$$\hat{V}_{OC}(t) = \frac{\int_0^t \frac{\partial n(x,t',L_D,\tau)}{\partial x}\Big|_{x=L} dt'}{\int_0^\infty \frac{\partial n(x,t',L_D,\tau)}{\partial x}\Big|_{x=L} dt'}. \tag{10.2}$$

A value of L_D = (5.7 ± 0.8) nm was determined for Alq_3 from a thickness dependent PL quenching measurement using HATCN as an exciton quencher, leaving τ as the only unknown parameter. Solving Eqns. 10.1 and 10.2 numerically with values of τ = 16.1 ns, L_D = 5.7 nm, and τ_{pulse} = 1.8 ns yields the solid red line in Fig. 10.1b. This model does a good job of reproducing the experimentally measured photovoltage rise, which is remarkable considering the inputs to the model are all independently measured values, providing confidence in this approach. With a lifetime and photovoltage rise this long the resolution of this measurement is not ideal, changing τ in the model to 14.1 ns and 18.1 ns also does a reasonably good job of reproducing the experimental data; however this resolution will be improved in materials with τ.

With the high intensity laser pulses used to excite the device in these measurements, care must be taken to ensure that exciton-exciton annihilation is not contributing to a reduction in the effective exciton lifetime.[104,192] Exciton-exciton annihilation is often observed to occur at exciton densities greater than ~10^{18} excitons cm^{-3}. When the 220 kW cm^{-2} 1.8 ns laser pulse is incident on the device, a peak exciton density of 5.1×10^{11} cm^{-3} is generated due to weak absorption of Alq_3 and presence of the dissociating interface, well below the reported threshold for annihilation. Additionally, the photovoltage rise was measured over five decades of intensity and showed no significant change in the photovoltage rise, suggesting exciton-exciton annihilation is not significant in this system.

10.2 Transient photovoltage of dark excitonic materials

The technique was further expanded to determine τ in dark materials which are inaccessible by traditional transient PL measurements. As demonstrated in Chapter 7, the intrinsic L_D of a dark material can be extracted when it is paired with a luminescent donor

or acceptor and photovoltage L_D measurements are combined it PL quenching measurements of luminescent material. Therefore, the intrinsic L_D of a dark material can be determined allowing for the extraction of τ as the only fit parameter. Planar heterojunction devices based on the D-A pairing of CuPc and C_{60} were fabricated at a variety of layer thicknesses. The N_2 dye laser used to excite the devices can be tuned to different wavelengths, so that τ of each material could be independently measured. Here, a λ = 400 nm pulse was used to probe C_{60} and a λ = 579 nm pulse was used to probe CuPc. At λ = 400 nm 94% of the dissociated excitons originate from C_{60} and at λ = 579 nm 85% of the dissociated excitons originate from CuPc. The normalized photovoltage transient at each of these excitation wavelengths are shown for a device consisting of 35.4 nm CuPc and 31.8 nm C_{60} in Fig. 10.2a. Here it can be seen that the photovoltage transients generated from probing each material are nearly identical. This agreement was present for six different devices that were tested, which vary in layer thickness. Additionally, the agreement of photovoltage transients between the donor and acceptor was also observed in a PHJ H_2Pc-C_{60} device. It would be serendipitous for the rise time in both materials to be identical, and suggests that there may be some other rate limiting step inherent in the device or measurement which occurs between the arrival of excitons at the D-A interface and the measurement of the photovoltage, controlling the timescale of the photovoltage rise. The two most obvious mechanisms which could be responsible are the timescale of charge transfer state dissociation or the timescale charge carrier collection.

In these experiments, the open-circuit voltage is measured by connecting the device to a 1 MΩ terminal of an oscilloscope. The measurement of a voltage in this set up requires a small current to flow through this terminal. This behavior could be explained if the

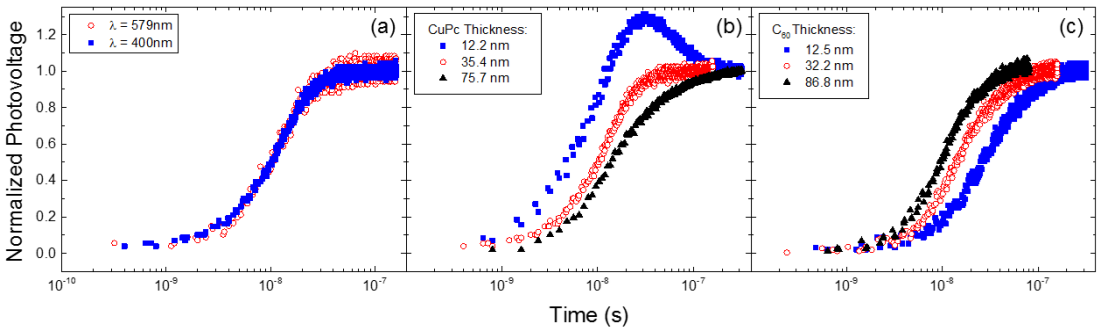

Figure 10.2 (a) Photovoltage transient of a CuPc-C_{60} device. The photovoltage rise is independent of which material is excited and suggests some other rate limiting step controls the timescale of the photovoltage rise in this device. (b) Photovoltage rise as a function of CuPc layer thickness. Longer rise times are consistent with the model, as excitons generated further away from the interface take longer to dissociate. (c) Photovoltage rise as a function of increasing C_{60} thickness. Displaying counterintuitive behavior where rise time gets faster with thicker layers, which does not agree with the photovoltage model.

measurement is limited by a charge carrier transit time between the interface and electrode. To investigate this, photovoltage transients were measured as a function donor and acceptor layer thickness. It stands to reason that if this measurement is limited by some sort of charge carrier transit time, the thicker the device, the slower the photovoltage rise due to the longer pathway for charge collection. Figure 10.2b displays the photovoltage rise for three devices with a constant C_{60} thickness of 31.8 nm and varying CuPc thickness, where demonstrates that the photovoltage rise time increases as a function of donor layer thickness. The photovoltage transients shown in Figs. 10.2b and 10.2c correspond to λ = 400 nm excitation; however, the transients generated from λ = 579 nm excitation produce the same results. It should also be noted that this trend could be explained by exciton diffusion, where if L_D is sufficiently long, the photovoltage rise time will trend with thickness due to the dissociation of excitons generated further away from the D-A interface. Devices with a constant CuPc thickness of 18.6 nm and an increasing C_{60} thickness are shown in Fig. 10.2c. These devices display the opposite dependence, where the rise time decreases as a function of increasing C_{60} thickness. This behavior was unexpected and contrary to both

exciton diffusion and charge collection arguments. Lastly, 1:1 CuPc:C_{60} BHJ devices were measured at different active layer thicknesses. In this architecture, the timescale for an exciton to reach the D-A interface should be minimized and equivalent between the two devices. Figure 10.3 shows the resulting photovoltage transients with both log and linear time scales for 31.5 nm and 61.9 nm thick BHJ devices. These devices displayed similar, counterintuitive behavior that was observed in PHJ devices with an increasing C_{60} thickness, where the photovoltage rise was the same regardless of which material is initially excited and plateaued faster in thicker devices.

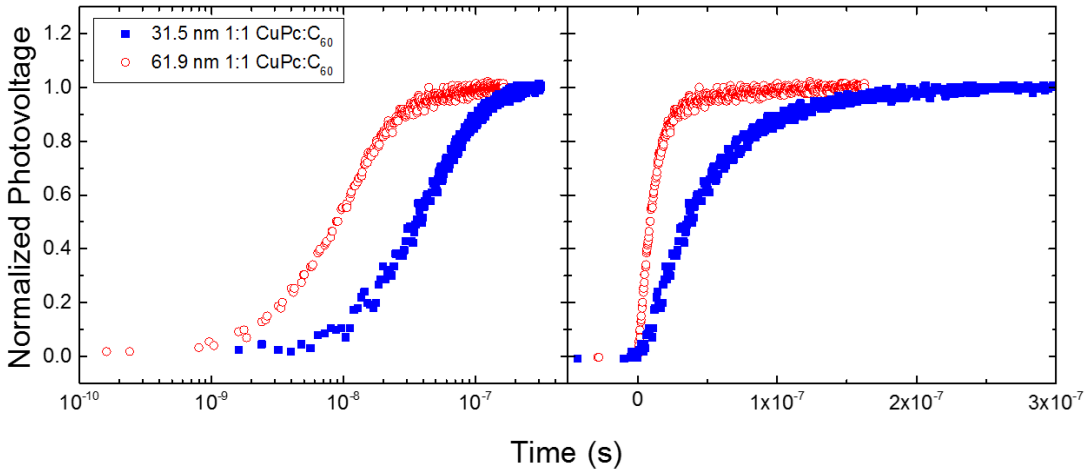

Figure 10.3 Transient photovoltage rise of a 1:1 CuPc-C_{60} bulk heterojunction device on both log (left) and linear (right) timescales. Bulk heterojunction devices should minimize the timescale for exciton dissociation and display similar counterintuitive behavior where the rise time is longer for thicker devices.

10.3 Conclusions and future directions

Probing excitons in non-emissive materials is an inherently difficult problem. Charge carrier based L_D measurements probe the magnitude of this parameter, but often L_D must be decoupled with a measure of D or τ in order to provide a deeper understanding of what processes control exciton diffusion. The results presented in this chapter offer a unique and experimentally simple approach to measure τ in dark excitonic materials compared to traditional transient absorption measurements. The photovoltage produced by a device is

directly proportional to the number of dissociated excitons. Measuring a photovoltage transient resulting from a short excitation pulse has the potential to probe the dissociation of excitons in real time, which can be fit for τ provided that L_D is known. However, more work needs to be done in order to understand the physics associated with the photovoltage transients. Initial measurements of Alq_3 show consistency between the experimental and modeled photovoltage transients using only experimentally measured inputs of L_D from photoluminescence quenching and τ from time-correlated single photon measurements. When the method was applied to PHJ CuPc-C_{60} and H_2Pc-C_{60} devices, the normalized photovoltage transients were nearly identical regardless of which layer was excited by optical excitation. This suggests that there is some rate limiting step inherent in the device or measurement that occurs between the arrival of excitons at the D-A interface and the measurement of voltage, possibly either the timescale for charge transfer state dissociation or the timescale for charge transit. Devices displayed counterintuitive behavior where the photovoltage rise time systematically decreased as a function of increasing C_{60} thickness and systematically increased as a function of increasing CuPc thickness. Additionally, 1:1 CuPc:C_{60} BHJ devices showed a decrease in photovoltage rise time with increasing thickness. Future work should focus on trying to understand this result in order to elucidate what controls the timescale of photovoltage transients. Other D-A pairings should be investigated to see if this behavior is specific to C_{60} or is general to all PHJ and BHJ devices. In order for this measurement to be successful the photovoltage transient must reflect the timescale of excitons arriving at the D-A interface. This could potentially be accomplished by efforts to minimize the timescale for exciton dissociation and charge collection by making increasingly thinner devices to maximize the internal electric field at

the D-A interface or measuring the photovoltage rise under a constant reverse bias voltage to increase field assisted charge transfer state dissociation and free carrier collection.

10.4 Experimental Methods

Device Preparation: Alq_3 devices consisted of a 11.0 nm TAPC donor layer, paired with a 13.0 nm Alq_3 acceptor layer, deposited on ITO and capped with a 10.2 nm BCP exciton blocking layer and 100 nm Al cathode. H_2Pc-C_{60} devices consisted of a 16.6 nm H_2Pc layer, 22.8 nm C_{60} layer, 10.2 nm BCP layer and 100 nm Al cathode deposited on an ITO coated glass substrate. For the devices used in thickness dependent CuPc-C_{60} measurements, a constant 31.8 nm C_{60} layer was paired with 12.2 nm, 35.4 nm, and 75.6 nm CuPc donor layers, with a 10.3 nm BCP layer and 100 nm Al cathode, and a constant 18.6 nm CuPc layer was paired with 12.5 nm, 32.2 nm and 86.8 nm C_{60} acceptor layers, with a 10.4 m BCP layer and 100 nm Al cathode.

Transient photovoltage measurements: All devices were excited with a N_2 laser operating at 1 Hz. Dye cells were inserted into the laser to down convert the λ = 337 nm exciton to λ = 400 nm and λ = 579 nm. The pulse width was measured with a Thorlabs PDA10 Si amplified detector. Photovoltage transients were measured at open-circuit by connecting the anode of the device to a 1 MΩ terminal of a Tektronix TDS5104B oscilloscope capable of a 250 GS/s sample rate with a voltage resolution of eight bits. The cathode of the device was grounded directly to the shield of the device probe with a copper wire, which was found to reduce the noise associated with the photovoltage transient.

Transient photoluminescence measurements: Transient photoluminescence of Alq_3 was measured on an 11.3 nm film of deposited on glass and encapsulated with a glass microscope slide and epoxy to avoid oxidation. The decay was measured via time

correlated singe photon counting with a PicoQuant PDL800-B laser pulse driver and laser diode operating at λ = 375 nm. Timing was measured using a PicoQuant NanoHarp 250 processor with a 31 ps time resolution and instrument response time of ~ 0.5 ns.

Photoluminescence quenching measurements were performed on a series of 12 Alq_3 films ranging from 4.6 to 38.8 nm with a 14.2 nm HATCN quenching layer. Films were excited at under monochromatic illumination at a wavelength of λ = 350 nm at an incident angle of 65° with s-polarized light.

11. Conclusions and future work

11.1 Summary and conclusions

Organic photovoltaic devices are an emerging renewable energy technology that has the potential to provide low cost solar energy to a variety of unique applications that are not accessible by traditional photovoltaics. In order to be economically viable and carve out a space in the marketplace device efficiencies and operating lifetimes need to be improved. Consequently, there needs to be a better understanding of the underlying mechanisms of device operation in order to design materials and device architectures capable of producing more efficient OPVs. This dissertation has focused on the development of measurement techniques which are capable of accessing new material sets, providing a deeper understanding of the physics of device operation; as well as, the manipulation of material parameters in order to increase diffusion efficiencies for the realization of more efficient devices.

Chapter 6 investigated the effects of materials purity on exciton transport, as native molecular impurities were systematically removed from films of α-NPD. This study aimed to explore what levels of impurities could be tolerated before exciton diffusion was significantly hampered. With this knowledge, better insight into the degree of material purification needed optimize device performance can be obtained. It was found that an increase in HPLC purity from 97.1% to 99.0% coincided with concomitant increases in L_D from (3.9 ± 0.5) nm to (5.3 ± 0.9), due to a reduction in the concentration of exciton quenching impurities, which primarily acted to reduce k_{NR} and increase τ. Fitting this trend with a diffusion model based on Förster energy transfer suggested that large increases in

L_D occur at thin film purities beyond 99%, stressing the importance of achieving very high film purities to optimize exciton diffusion.

Chapter 7 presented a new method to determine L_D in device relevant architectures utilizing a photovoltage-based measurement. This technique is equally capable of probing exciton harvesting in luminescent and dark excitonic materials. When a photovoltage is measured at open-circuit charge collection is not necessary, eliminating non-geminate recombination losses that lead to underestimates of L_D in established photocurrent based methods. This technique is subject to geminate recombination of interfacial CT states and thus yields a device relevant value of L_D, which represents the fraction of excitons that are able to be harvested as useable photocurrent in a device. When a dark material is paired with a luminescent donor or acceptor, which are accessible by PL based L_D measurement techniques, η_{CS} can be decoupled, elucidating intrinsic values of L_D for the dark material. The photovoltage approach offers a unique tool to learn about exciton diffusion in non-luminescent materials, including triplets, which remain an understudied faction of organic semiconductors.

Chapter 8 presented a series of experiments which can be combined to probe exciton harvesting and quantitatively decouple the active recombination pathways as a function of forward bias voltage in a PHJ OPV. Three techniques which are typically only used to extract values of L_D were considered in concert with one another and demonstrated that each technique actually probes a separate point in the photoconversion process. With these three techniques, the intrinsic L_D of each material was determined and the effects of geminate and non-geminate recombination were quantified and decoupled throughout the power generating fourth quadrant. For the particular SubPc-C_{60} device under study, it was

found that geminate recombination was the dominant loss pathway and that non-geminate recombination only began to take effect past the maximum operating power point. This work demonstrates a methodology which can be used to learn about where the inefficiencies in photoconversion occur during device operation. With this knowledge, materials and device architectures can be designed to minimize dominant loss pathways for more efficient operation.

Chapter 9 utilized the photovoltage method presented in Chapter 7 to measure L_D in the dark singlet fission based material pentacene. Singlet fission is a process capable of producing two excitons per absorbed photon, which enhances photocurrents and can potentially produce more efficient OPVs. Additionally, single crystals of emissive singlet fission materials have yielded the longest reported L_D to date; however, relatively little is known about the diffusive behavior of triplet excitons in dark singlet fission materials. In this study, L_D was demonstrated to systematically increase as a function of polycrystalline grain size due to the reduction in exciton quenching at grain boundaries. The reported L_D ranged from (20.9 ± 2.2) nm to (33.4 ± 3.5) nm. This is relatively long compared to many reported values of L_D for singlet excitons; however, it was well short of the micron scale L_D observed in single crystals. Future work should explore different material sets to see if other singlet fission systems are capable of producing microscopic L_D in device architectures. This would allow for the use of optically thick films and simple PHJ architectures which are capable of overcoming the exciton bottleneck.

Chapter 10 expanded the photovoltage technique to the transient regime. In these measurements, the rise in photovoltage was measured after excitation from a short laser pulse. Generated photovoltage transients potentially represent exciton dissociation in real

time and can be fit for τ if a value of L_D is known. This would allow for experimentally simple measurements of τ in dark materials, where traditional transient PL measurements are not applicable. To demonstrate the method, transient photovoltage and PL measurements of the emissive material Alq_3 were compared and observed to be in a good agreement. However, when the technique was expanded to dark materials, counterintuitive behavior was observed. In these devices, the photovoltage rise time was independent of which material was excited and got shorter as a function of increasing acceptor layer thickness, in disagreement with the model. In order for this technique to be successful more work needs to be done to understand this behavior and different device architectures and experimental set ups should explored in order to optimize the rate of CT state dissociation.

Each of these studies advanced the understanding OPV device operation in some way or provided tools to learn about underlying device physics. However, a lot more work needs to be done in order to advance the understanding of these devices to the point where power conversion efficiencies are high enough to compete in the marketplace. Many companies are nearing the point of commercialization and time will tell whether OPVs can be an economic solution capable of providing low cost renewable energy.

11.2 Future work

In order for OPVs to overcome the exciton bottleneck in simple PHJ devices, materials with L_D on the order of the absorption length of light, which are able to be successfully implemented into device architectures must be realized. It should be noted that even in BHJ devices a longer L_D will be beneficial by increasing η_D or relaxing the constraint on phase morphology. As discussed in Section 3.6, triplet excitons present the best opportunity for this to be achieved due the fact that D and τ are not coupled. If triplet materials can be

fabricated with sufficiently long τ, then microscopic L_D are possible, which has been demonstrated in single crystals of rubrene and tetracene.[47,77,82] Additionally, devices based on singlet fission materials have the potential of increasing power conversion efficiencies through enhanced photocurrents by generating two excitons per absorbed photon. The techniques developed throughout this work provide tools to study exciton diffusion in these systems. Chapter 9 demonstrated that the photovoltage approach could be used measure L_D in pentacene; however, this is the simplest case to study because singlet fission is fast and efficient and triplet fusion is inefficient. Future work should focus on expanding upon this work to study triplet exciton diffusion in singlet fission materials with more complicated exciton dynamics.

11.2.1 Decoupling singlet and triplet diffusion lengths in rubrene

Rubrene provides an interesting test case to combine photovoltage and PL quenching measurements to decouple singlet and triplet L_D in a singlet fission based material. In rubrene, S_1 (2.29 eV) and $2T_1$ (2.28 eV) are approximately isoergic, as shown in Fig. 11.1a.[237] Consequently, both singlet fission and triplet fusion occur readily at room temperature.[237–240] This complicates the photovoltage analysis significantly, as you can no longer assume a 2:1 ratio of generated excitons to absorbed photons. In this case, Eqns. 9.1 and 9.2 cannot be simplified and must be solved as two coupled differential equations. Additionally, there are now six unknown parameters: D_s, τ_s, D_t, τ_t, k_{fis}, and k_{fus}. Previously, with only one type of diffusing exciton, L_D was the only fit parameter. In the steady-state, with only one diffusing species, the fraction of dissociated excitons is only proportional to the product of D and τ and not the magnitude of either individual component. That is not the case for rubrene, where the rate of singlet exciton dissociation, which is proportional

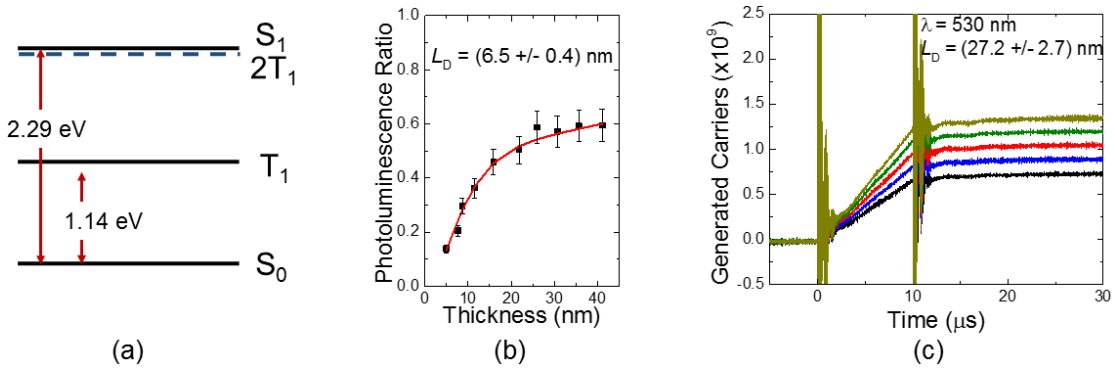

Figure 11.1 (a) Singlet (S_1) and triplet (T_1) energy levels of rubrene. (b) Photoluminescence quenching and (c) photovoltage based L_D measurements of rubrene, assuming a single diffusive species. Discrepancy between these measurements demonstrates that a large fraction of triplets are dissociated.

to D_S, will compete with k_{fis}, and similarly the rate of triplet exciton dissociation, which is proportional to D_T, will compete with k_{fus}. With one experiment and six unknowns, it is clear that photovoltage measurements alone are not enough to solve this problem and must be combined with photoluminescence quenching, transient absorption, and transient PL measurements in order to be able to achieve a unique fit for the singlet and triplet L_D.

Figures 11.1b and 11.1c demonstrate preliminary PL quenching and photovoltage measurements, respectively. Here, both measurements are fit with a model that naively neglects singlet fission and triplet fusion, assuming a single diffusive species where one absorbed photon generates one exciton. Photoluminescence quenching measurements, which probe the magnitude of the singlet exciton density yield a value of L_D = (6.5 ± 0.5) nm. However, when photovoltage measurements are conducted on a rubrene based OPV, which are sensitive to the dissociation of both singlets and triplets, a value of L_D = (27.2 ± 2.7) nm is extracted. The device measured here consists of a 31.3 nm rubrene film deposited on ITO, paired with a 21.8 nm C_{60} acceptor, 11.8 nm BCP exciton blocking layer, and 100 nm Al cathode and is excited with λ_{peak} = 530 nm excitation. The disagreement between these two measurements suggests a significant number of triplet excitons reach the

dissociating interface; however, a more rigorous treatment is needed to quantitatively decouple the singlet and triplet L_D.

When transient PL of rubrene is measured, it displays near biexponential behavior where there is a short-lived prompt fluorescence component, τ_{prompt}, which is dominated by singlet excitons rapidly undergoing fission to two triplets, as well as a long lived delayed fluorescence component, resulting from triplet fusion repopulating the singlet state, which then radiatively decays.[51,238,240] Transient absorption measurements are capable of monitoring the singlet and triplet exciton densities as a function of time and can extract the sum of $2k_{fis} + k_{fus}$.[237] If transient absorption measurements are combined with transient PL measurements and it is assumed that $\tau_{prompt} \approx k_{fis}^{-1}$, which is a good approximation if $k_{fis}^{-1} << \tau_S$, then reasonable measures of k_{fis} and k_{fus} can be obtained. From Eqn. 9.1 it can be inferred that the intensity of the delayed fluorescent component is proportional to n_t^2. Previous reports have argued that at very long times when the triplet density is low enough, that the delayed fluorescence component transitions form a power law t^{-2} dependence to a single exponential dependence, where the decay is determined by τ_t. If these experiment can successfully determine k_{fis}, k_{fus}, and τ_t, this leaves three remaining unknown parameters: D_s, D_t, and τ_s.

If photovoltage measurements are combined with PL quenching measurements, then two sets of differential equations can be solved simultaneously in order to fit the remaining three parameters. The data that is fit from PL quenching measurements is:

$$PL_{Ratio} = \frac{\int n_{S,Q}(x)dx}{\int n_{S,UQ}(x)dx} \tag{11.1}$$

where $n_{s,Q}$ and $n_{s,UQ}$ are the quenched and unquenched singlet exciton densities, respectively. Photovoltage measurements will determine the total number of dissociated

excitons (N_{DE}) including singlets and triplets. Additionally, η_{CS} will need to be decoupled, as demonstrated in Chapters 8 and 9. Photovoltage data can then be fit using an equation similar to Eqn. 8.1, incorporating both species of exciton:

$$N_{DE} = \tau_{pulse} A \left(D_S \frac{dn_s(x)}{dx} + D_t \frac{dn_t(x)}{dx} \right) |_{D-A\ Interface}, \tag{11.2}$$

where τ_{pulse} is the excitation pulse width and A is the excitation area.

If this series of experiments is successfully able to extract values of D_s, D_t, and τ_s, then the singlet and triplet L_D can be extracted. In this sort of a two state system however, L_D is not simply given by $\sqrt{D\tau}$. The balance of k_{fis} and k_{fus} determine effective lifetimes for which the exciton exists in each state. It has previously been demonstrated that in this sort of a two state system L_D and the effective lifetime can be determined as:[40]

$$L_{D,s}{}^2 = D_s \frac{k_{fus} + \tau_t{}^{-1}}{k_{fus}\tau_s{}^{-1} + k_{fis}\tau_t{}^{-1} + \tau_s{}^{-1}\tau_t{}^{-1}} \tag{11.3}$$

$$L_{D,t}{}^2 = D_t \frac{k_{fis}}{k_{fus}\tau_s{}^{-1} + k_{fis}\tau_t{}^{-1} + \tau_s{}^{-1}\tau_t{}^{-1}}. \tag{11.4}$$

Decoupling singlet and triplet L_D in singlet fission materials which display triplet fusion is far more complicated than the method used for determining triplet L_D in exoergic singlet fission materials demonstrated in Chapter 9. However, this series of experiments offers a unique opportunity to study the interplay of diffusing excitons in a two state system. The films used in the experiments shown in Figs. 11.1b and 11.1c are amorphous and reveal no scattering peaks. If these experiments can successfully decouple singlet and triplet L_D, then the approach could be expanded to explore how this relationship is affected as a function of crystallinity.

11.2.2 Intramolecular singlet fission sensitization

Singlet fission materials can enhance photocurrents by generating two excitons for every absorbed photon; however, the linear acenes and their derivatives, which make up the majority of singlet fission materials, are characteristically weak absorbers limiting device efficiencies.[51] In order to overcome this problem, studies have tried to decouple absorption from singlet fission through singlet fission sensitization.[44,213] Similar to the exciton injection scheme discussed in Section 9.4.3, a strongly absorbing material is paired with a singlet fission layer, such that optical absorption on the strongly absorbing material generates singlet excitons, which can then undergo Förster transfer to the singlet fission material to generate two triplets. The problem with this approach is that while it successfully decouples absorption from singlet fission, it doesn't take advantage of the potentially long L_D of triplet excitons. If two triplet excitons could instead be transferred back to the strongly absorbing material after fission occurs, then triplet excitons, with potentially long L_D, could be generated on the absorber and thicker films could be used to boost optical absorption, while still employing the benefits of singlet fission.

Generally, singlet fission is a bimolecular process where an excited molecule shares its energy with a neighboring molecule in the ground state. This process is highly sensitive to the packing of the two molecules and is generally more efficient in highly crystalline systems.[51,52,240] Recently however, dimer-like molecules which display efficient intramolecular singlet fission have been synthesized. In these molecules an exciton undergoes singlet fission to create two triplets on the same molecule, relaxing the restriction on molecular packing.[241,242] This type of molecule could be doped into a strongly

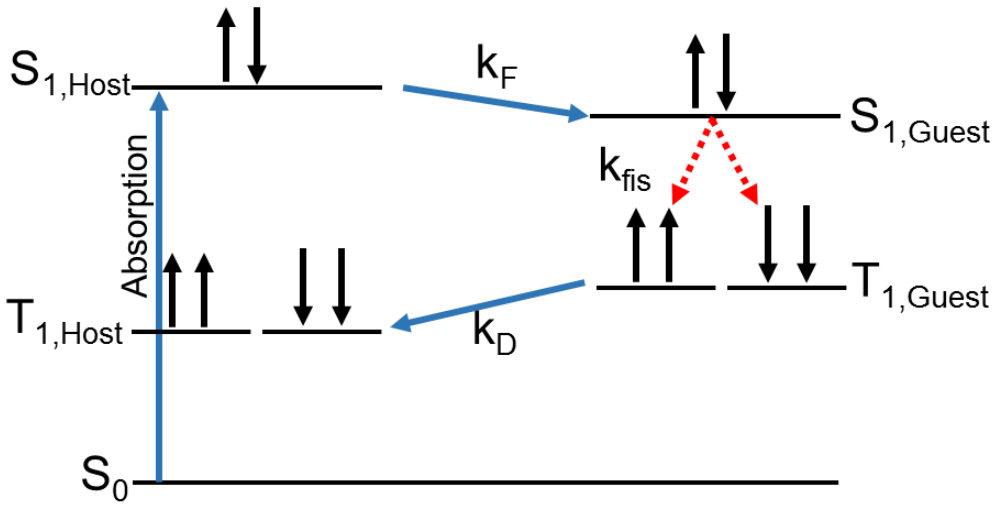

Figure 11.2 Energy level diagram of an intramolecular singlet fission sensitized host-guest system. Optically generated singlet excitons on the host ($S_{1,Host}$) undergo Förster transfer to $S_{1,Guest}$. Intramolecular singlet fission converts the singlet exciton to two triplets. Triplet excitons can then transfer back to the host triplet level by Dexter transfer.

absorbing film in a host-guest architecture, similar to what has been demonstrated with phosphorescent sensitizers.[119,151,243] Previous work phosphorescent sensitizers has demonstrated that triplet excitons can be generated on a fluorescent host by doping in a small fraction of a phosphorescent molecule. In this scheme the host transfers an optically generated singlet exciton to phosphorescent guest, which rapidly converts the singlet exciton to a triplet due to strong spin-orbit coupling and is then transferred to the triplet energy level of the host. If the energy levels of the host and guest are chosen correctly this same sort of transfer could occur, while simultaneously generating an extra exciton through singlet fission.

In order for such a host-guest system to operate effectively two criteria must be satisfied: first, the energy of lowest excited singlet state of the host, $S_{1,host}$, must be greater than the lowest excited singlet state of the guest, $S_{1,guest}$. This ensures that there is adequate spectral overlap between the emission spectrum of the host and the absorption spectrum of the guest, such that optically generated singlet excitons on the host can be transferred to

the guest *via* a Förster mechanism. The exciton on the guest can then undergo singlet fission to generate two triplet excitons, with energy $T_{1,guest}$. Second, $T_{1,guest}$ must be greater than the first excited triplet energy level of the host, $T_{1,host}$, so that converted triplet excitons can be transferred back to the host. This energetic offset ensures that triplet excitons will not be trapped on the guest. This pathway of triplet exciton generation on the host is shown schematically in Fig. 11.2.

One material system which could potentially satisfy this criteria is SubPc and the molecule BET-B, which consists of two covalently linked cofacial 5-ethynyl-tetracene dimers. BET-B has demonstrated efficient intramolecular singlet fission occuring on timescale of 1 ps, with high triplet yields of 154%.[241] There exists a spectral overlap between the emission spectrum of SubPc and the absorption spectrum of BET-B, ensuring Förster transfer can occur. Additionally, the two molecules have resonant triplet energy levels of 1.4 eV, which would allow triplet excitons to undergo Dexter transfer back to SubPc.[244] In this system, the strong visible aborption of SubPc can be utilized, while two long lived triplet excitons, with potentially long L_D, can be generated on SubPc. This decouples the process of singlet fission and absorption and also allows diffusion of triplet excitons to occur on the absorber, so that thicker films could be used to boost optical absorption

If this is energy transfer process is able to occur efficiently, η_{EQE} spectra and current-voltage characteristics should first be measured as a function of BET-B concentration in order to optimize photocurrent and the magnitude of the SubPc η_{EQE} peak. This will ensure that the balance between the energy transfer scheme shown in Fig. 11.2 and triplet transport on SubPc is optimized. If too little of the guest is doped into the host, then singlet excitons

will be dissociated without encountering a BET-B molecule. If too much of the guest is doped into the host, then transport along BET-B will compete with triplet transport in SubPc.

If an increase in photocurrent or η_{EQE} can be demonstrated, then photovoltage measurements can be used to determine if the triplet L_D on SubPc is enhanced relative to neat SubPc. The model for fitting L_D in this system will also be complicated. As a first order approximation, at the optimized doping level it can be assumed that every SubPc singlet exciton is able to undergo Förster transfer to the guest before it is dissociated. In this case, the 154% triplet yield can be incorporated into the diffusion equation as:

$$0 = D_t \frac{\partial^2 n_t(x)}{\partial x^2} - \frac{n_t(x)}{\tau_t} + 1.54G(x). \quad (11.5)$$

This scheme provides an opportunity to simultaneously employ the strong absorption of SubPc and the benefits of singlet fission, by generating two triplet excitons through and intramolecular singlet fission sensitizer. If the generated triplets display an enhanced L_D relative to neat film, then thicker active layers can be used increase η_A and the photocurrent will be increased due to both singlet fission and increases in L_D.

12. Bibliography

(1) *Intergovermental Panel on Climate Change - Climate Change 2014: Mitigation of Climate Chage*; Camdridge University Press, 2015; Vol. 3.

(2) Nasa. Climate change: How do we know? https://climate.nasa.gov/evidence/.

(3) U.S. Energy Information Administration - International Energy Outlook 2017 https://www.eia.gov/outlooks/ieo/.

(4) Fröhlich, C.; Lean, J. Solar Radiative Output and Its Variability: Evidence and Mechanisms. *Astron. Astrophys. Rev.* **2004**, *12* (4), 273–320.

(5) Jean, J.; Brown, P. R.; Jaffe, R. L.; Buonassisi, T.; Bulović, V. Pathways for Solar Photovoltaics. *Energy Environ. Sci.* **2015**, *8* (4), 1200–1219.

(6) Reilich, G.; Crucchiola, J. The Amount Of Land Required To Run America On Solar Power Is Shockingly Small https://www.good.is/infographics/solar-power-all-of-america.

(7) Mazzio, K. A.; Luscombe, C. K. The Future of Organic Photovoltaics. *Chem. Soc. Rev.* **2015**, *44* (1), 78–90.

(8) U.S. Energy Infromation Administration - Electric Power Monthly https://www.eia.gov/electricity/monthly/.

(9) Schmalensee, R. *The Future of Solar Energy - An Interdisciplinary MIT Study*; Massachusetts Institute of Technology, 2015.

(10) Haegel, N. M.; Margolis, R.; Buonassisi, T.; Feldman, D.; Froitzheim, A.; Garabedian, R.; Green, M.; Glunz, S.; Henning, H. M.; Holder, B.; et al. Terawatt-Scale Photovoltaics: Trajectories and Challenges. *Science (80-.).* **2017**, *356* (6334), 141–143.

(11) Swanson, A.; Plumer, B. Trump's Solar Tariffs Are Clouding the Industry's Future. *New York Times*. New York January 2018.

(12) Philipps, S. Fraunhofer Instutute for Solar Energy Systems ISE - Photovoltaics Report https://www.ise.fraunhofer.de/en/publications/studies/photovoltaics-report.html.

(13) Yang, W. S.; Park, B.; Jung, E. H.; Jeon, N. J. Iodide Management in Formamidinium-Lead-Halide – Based Perovskite Layers for Efficient Solar Cells. *Science (80-.).* **2017**, *356* (6345), 1376–1379.

(14) Forrest, S. R. The Limits to Organic Photovoltaic Cell Efficiency. *MRS Bull.* **2005**, *30* (January), 28–32.

(15) Forrest, S. R. The Path to Ubiquitous and Low-Cost Organic Electronic Appliances on Plastic. *Nature* **2004**, *428*, 911–918.

(16) Kippelen, B.; Brédas, J.-L. Organic Photovoltaics. *Energy Environ. Sci.* **2009**, *2* (3), 251.

(17) Krebs, F. C.; Espinosa, N.; Hösel, M.; Søndergaard, R. R.; Jørgensen, M. 25th Anniversary Article: Rise to Power - OPV-Based Solar Parks. *Adv. Mater.* **2014**, *26* (1), 29–39.

(18) Peumans, P.; Yakimov, A.; Forrest, S. R. Small Molecular Weight Organic Thin-Film Photodetectors and Solar Cells. *J. Appl. Phys.* **2003**, *93* (7), 3693–3723.

(19) Mulligan, C. J.; Wilson, M.; Bryant, G.; Vaughan, B.; Zhou, X.; Belcher, W. J.; Dastoor, P. C. A Projection of Commercial-Scale Organic Photovoltaic Module Costs. *Sol. Energy Mater. Sol. Cells* **2014**, *120* (PART A), 9–17.

(20) Günes, S.; Neugebauer, H.; Sariciftci, N. S. Conjugated Polymer-Based Organic Solar Cells. *Chem. Rev.* **2007**, *107* (4), 1324–1338.

(21) Yu, G.; Gao, J.; Hummelen, J. C.; Wudl, F.; Heeger, A. J. Polymer Photovoltaic Cells : Enhanced Efficiencies via a Network of Internal Donor- Acceptor Heterojunctions. *Science (80-.).* **1995**, *270*, 1789–1791.

(22) Zhou, H.; Zhang, Y.; Mai, C. K.; Collins, S. D.; Bazan, G. C.; Nguyen, T. Q.; Heeger, A. J. Polymer Homo-Tandem Solar Cells with Best Efficiency of 11.3%. *Adv. Mater.* **2015**, *27* (10), 1767–1773.

(23) Heliatek. Heliatek sets new Organic Photovoltaic world record efficiency of 13.2% http://www.heliatek.com/en/press/press-releases/details/heliatek-sets-new-organic-photovoltaic-world-record-efficiency-of-13-2.

(24) Lunt, R. R.; Bulovic, V. Theoretical Limits for Visibly Transparent Photovoltaics. *Appl. Phys. Lett.* **2012**, *98* (11).

(25) Ubiquitous Energy - Clearview Power Technology for Windows http://ubiquitous.energy/windows/.

(26) Pope, M.; Swenberg, C. *Electronic Processes in Organic Crystals*, 1st ed.; Oxford University Press, 1982.

(27) McMurry, J.; Simanek, E. *Fundamentals of Organic Chemistry*, 6th ed.; Thompson Brooks/Cole: Belmont, Ca, 2007.

(28) Turro, N.; Ramamurthy, V.; Scaiano, J. C. *Principles of Modern Molecular Photochemsitry*; 2009.

(29) Gregg, B. A.; Hanna, M. C. Comparing Organic to Inorganic Photovoltaic Cells: Theory, Experiment, and Simulation. *J. Appl. Phys.* **2003**, *93* (6), 3605.

(30) Kittel, C. *Introduction to Solid State Physics*, 8th ed.; John Wiley Sons, I., Ed.; 2005.

(31) Volksen, W.; Miller, R. D.; Dubois, G. Low Dielectric Constant Materials. *Chem. Rev.* **2010**, *110*, 56–110.

(32) Nagle, J. K. Atomic Polarizability and Electronegativity. *J. Am. Chem. Soc.* **1990**, *112* (12), 4741–4747.

(33) Forrest, S. R. Ultrathin Organic Films Grown by Organic Molecular Beam Deposition and Related Techniques. *Chem. Rev.* **1997**, *97* (6), 1793–1896.

(34) Knupfer, M. Exciton Binding Energies in Organic Semiconductors. *Appl. Phys. A Mater. Sci. Process.* **2003**, *77* (5), 623–626.

(35) Kasha, M. Characterization of Electronic Transitions in Complex Molecules. *Discuss. Faraday Soc.* **1950**, *9*, 14–19.

(36) David J. Griffiths. *Introduction to Quantum Mechanics*; Pearson Education, Inc., 2004.

(37) Köhler, A.; Bässler, H. Triplet States in Organic Semiconductors. *Mater. Sci. Eng. R Reports* **2009**, *66* (4–6), 71–109.

(38) Shao, Y.; Yang, Y. Efficient Organic Heterojunction Photovoltaic Cells Based on Triplet Materials. *Adv. Mater.* **2005**, *17*, 2841–2844.

(39) Baldo, M. A.; O'Brien, D. F.; You, Y.; Shoustikov, A.; Sibley, S.; Thompson, M. E.; Forrest. R. Highly Efficient Phosphorescent Emission from Organic Electroluminescent Devices. *Nature* **1998**, *395*, 151–154.

(40) Menke, S. M.; Holmes, R. J. Exciton Transport in an Organic Semiconductor Exhibiting Thermally Activated Delayed Fluorescence. *J. Phys. Chem. C* **2016**, *120*, 8502–8508.

(41) Uoyama, H.; Goushi, K.; Shizu, K.; Nomura, H.; Adachi, C. Highly Efficient Organic Light-Emitting Diodes from Delayed Fluorescence. *Nature* **2012**, *492*, 234–238.

(42) Goushi, K.; Yoshida, K.; Sato, K.; Adachi, C. Organic Light-Emitting Diodes Employing Efficient Reverse Intersystem Crossing for Triplet-to-Singlet State Conversion. *Nat. Photonics* **2012**, *6* (April), 253–258.

(43) Niwa, A.; Kobayashi, T.; Nagase, T.; Goushi, K.; Adachi, C.; Naito, H. Temperature Dependence of Photoluminescence Properties in a Thermally Activated Delayed Fluorescence Emitter. *Appl. Phys. Lett.* **2014**, *104*, 213303.

(44) Congreve, D. N.; Lee, J.; Thompson, N. J.; Hontz, E.; Yost, S. R.; Reusswig, P. D.; Bahlke, M. E.; Reineke, S.; Van Voorhis, T.; Baldo, M. A. External Quantum Efficiency Above 100% in a Singlet-Exciton-Fission–Based Organic Photovoltaic Cell. *Science (80-.).* **2013**, *340*, 334–337.

(45) Lee, J.; Jadhav, P.; Reusswig, P. D.; Yost, S. R.; Thompson, N. J.; Congreve, D. N.; Hontz, E.; Van Voorhis, T.; Baldo, M. A. Singlet Exciton Fission Photovoltaics. *Acc. Chem. Res.* **2013**, *46* (6), 1300–1311.

(46) Rao, A.; Wilson, M.; Hodgkiss, J.; Albert-Seifried, S.; Bassler, H.; Friend, R. H. Exciton Fission and Charge Generation via Triplet Excitons in Pentacene/C60 Bilayers. *J. Am. Chem. Soc.* **2010**, *132*, 12698–12703.

(47) Akselrod, G. M.; Deotare, P. B.; Thompson, N. J.; Lee, J.; Tisdale, W. A.; Baldo,

M. A.; Menon, V. M.; Bulović, V. Visualization of Exciton Transport in Ordered and Disordered Molecular Solids. *Nat. Commun.* **2014**, *5*, 3646.

(48) Pichler, K.; Graham, S.; Gelsen, O. M.; Friend, R. H.; Romanow, W. J.; McCauley, J. P.; Coustel, N.; Fischer, J. E.; Smith III, A. B. Photophysical Properties of Solid Films of Fullerene, C60. *J. Phys. Condens. Matter* **1991**, *3* (9259–9270).

(49) Ebbesen, T. W.; Tanigaki, K.; Kuroshima, S. Excited-State Properties of C60. *Chem. Phys. Lett.* **1991**, *181* (6), 501–504.

(50) Goudsmit, G.; Paul, H. Time-Resolved EPR Investigation of Triplet State C60. Triplet-Triplet Annihilation , CIDEP , and Quenching by Nitroxide Radicals. *Chem. Phys. Lett.* **1993**, *208* (1,2), 73–78.

(51) Smith, M. B.; Michl, J. Singlet Fission. *Chem. Rev.* **2010**, *110*, 6891–6936.

(52) Smith, M. B.; Michl, J. Recent Advances in Singlet Fission. *Annu. Rev. Phys. Chem.* **2013**, *64*, 361–386.

(53) Förster, T. 10th Spiers Memorial Lecture: Transfer Mechanisms of Electronic Excitation. *Discuss. Faraday Soc.* **1959**, *27*, 7–17.

(54) Förster, T. Zwischenmolekulare Energiewanderung Und Fluoreszenz. *Ann. Phys.* **1948**, *2*, 55–75.

(55) Scholes, G. D. Long-Range Resonance Energy Transfer in Molecular Systems. *Annu. Rev. Phys. Chem.* **2003**, *54* (18), 57–87.

(56) Dexter, D. L. A Theory of Sensitized Luminescence in Solids. *J. Chem. Phys.* **1953**, *21* (5), 836.

(57) Köhler, A.; Bässler, H. What Controls Triplet Exciton Transfer in Organic Semiconductors? *J. Mater. Chem.* **2011**, *21* (12), 4003.

(58) Andrews, D. L.; Curutchet, C.; Scholes, G. D. Resonance Energy Transfer: Beyond the Limits. *Laser Photon. Rev.* **2011**, *5* (1), 114–123.

(59) Yost, S. R.; Hontz, E.; Yeganeh, S.; Van Voorhis, T. Triplet vs Singlet Energy Transfer in Organic Semiconductors: The Tortoise and the Hare. *J. Phys. Chem. C* **2012**, *116* (33), 17369–17377.

(60) Förster, T. Experimentelle Und Theoretische Untersuchung Des Zwischenmolekularen Übergangs von Elektronenanregungsenergie. *Zeitschrift für Naturforsch.* **1949**, *4a*, 321.

(61) Kawamura, Y.; Brooks, J.; Brown, J. J.; Sasabe, H.; Adachi, C. Intermolecular Interaction and a Concentration-Quenching Mechanism of Phosphorescent Ir(III) Complexes in a Solid Film. *Phys. Rev. Lett.* **2006**, *96* (1).

(62) Baldo, M. A.; Adachi, C.; Forrest, S. R. Transient Analysis of Organic Electrophosphorescence. II. Transient Analysis of Triplet-Triplet Annihilation. *Phys. Rev. B* **2000**, *62* (16), 10967–10977.

(63) Menke, S. M.; Holmes, R. J. Exciton Diffusion in Organic Photovoltaic Cells. *Energy Environ. Sci.* **2014**, *7*, 499–512.

(64) Maksimov, M. Z.; Rozman, I. M. On Energy Transfer in Solid Solutions. *Opt. Spectrosc.* **1962**, *12*, 337–338.

(65) Rim, S.-B.; Fink, R. F.; Schöneboom, J. C.; Erk, P.; Peumans, P. Effect of Molecular Packing on the Exciton Diffusion Length in Organic Solar Cells. *Appl. Phys. Lett.* **2007**, *91* (17), 173504.

(66) Sim, M.; Shin, J.; Shim, C.; Kim, M.; Jo, S. B.; Kim, J.; Cho, K. Dependence of Exciton Diffusion Length on Crystalline Order in Conjugated Polymers. *J. Phys. Chem. C* **2014**, *118*, 760–766.

(67) Menke, S. M.; Luhman, W. A.; Holmes, R. J. Tailored Exciton Diffusion in Organic Photovoltaic Cells for Enhanced Power Conversion Efficiency. *Nat. Mater.* **2013**, *12* (2), 152–157.

(68) Mullenbach, T. K.; McGarry, K. A.; Luhman, W. A.; Douglas, C. J.; Holmes, R. J. Connecting Molecular Structure and Exciton Diffusion Length in Rubrene Derivatives. *Adv. Mater.* **2013**, *25* (27), 3689–3693.

(69) Curtin, I. J.; Blaylock, D. W.; Holmes, R. J. Role of Impurities in Determining the Exciton Diffusion Length in Organic Semiconductors. *Appl. Phys. Lett.* **2016**, *108*, 163301.

(70) Lunt, R. R.; Giebink, N. C.; Belak, A. a.; Benziger, J. B.; Forrest, S. R. Exciton Diffusion Lengths of Organic Semiconductor Thin Films Measured by Spectrally Resolved Photoluminescence Quenching. *J. Appl. Phys.* **2009**, *105* (5), 53711.

(71) Gregg, B. A. Evolution of Photophysical and Photovoltaic Properties of Perylene Bis(phenethylimide) Films upon Solvent Vapor Annealing. *J. Phys. Chem.* **1996**, *100* (2), 852–859.

(72) You, Z.; Hsu, C. The Fragment Spin Difference Scheme for Triplet-Triplet Energy Transfer. *J. Chem. Phys.* **2010**, *133*, 74105.

(73) Murphy, C. B.; Zhang, Y.; Troxler, T.; Ferry, V.; Martin, J. J.; Jones, W. E. Probing Förster and Dexter Energy-Transfer Mechanisms in Fluorescent Conjugated Polymer Chemosensors. *J. Phys. Chem. B* **2004**, *108*, 1537–1543.

(74) Monguzzi, A.; Tubino, R.; Meinardi, F. Upconversion-Induced Delayed Fluorescence in Multicomponent Organic Systems: Role of Dexter Energy Transfer. *Phys. Rev. B* **2008**, *77*, 155122.

(75) Namdas, E. B.; Ruseckas, A.; Samuel, I. D. W.; Lo, S.-C.; Burn, P. L. Triplet Exciton Diffusion in Fac-tris(2-Phenylpyridine) iridium(III)-Cored Electroluminescent Dendrimers. *Appl. Phys. Lett.* **2005**, *86* (9), 91104.

(76) Athanasopoulos, S.; Hennebicq, E.; Beljonne, D.; Walker, A. B. Trap Limited Exciton Transport in Conjugated Polymers. *Phys. Chem. C* **2008**, *112* (V), 11532–11538.

(77) Najafov, H.; Lee, B.; Zhou, Q.; Feldman, L. C.; Podzorov, V. Observation of Long-Range Exciton Diffusion in Highly Ordered Organic Semiconductors. *Nat. Mater.* **2010**, *9* (11), 938–943.

(78) Powell, R. C.; Soos, Z. G. Singlet Exciton Energy Transfer in Organic Solids. *J. Lumin.* **1975**, *11*, 1–45.

(79) Pettersson, L. A. A.; Roman, L. S.; Inganäs, O. Modeling Photocurrent Action Spectra of Photovoltaic Devices Based on Organic Thin Films. *J. Appl. Phys.* **1999**, *86* (1), 487–496.

(80) Mikhnenko, O. V; Blom, P. W. M.; Nguyen, T.-Q. Exciton Diffusion in Organic Semiconductors. *Energy Environ. Sci.* **2015**, *8*, 1867–1888.

(81) Ahn, T.-S.; Wright, N.; Bardeen, C. J. The Effects of Orientational and Energetic Disorder on Forster Energy Migration along a One-Dimensional Lattice. *Chem. Phys. Lett.* **2007**, *446* (1–3), 43–48.

(82) Irkhin, P.; Biaggio, I. Direct Imaging of Anisotropic Exciton Diffusion and Triplet Diffusion Length in Rubrene Single Crystals. *Phys. Rev. Lett.* **2011**, *107* (1), 17402.

(83) Hedley, G. J.; Ruseckas, A.; Samuel, I. D. W. Light Harvesting for Organic Photovoltaics. *Chem. Rev.* **2017**, *117*, 796–837.

(84) Burdett, J. J.; Müller, A. M.; Gosztola, D.; Bardeen, C. J. Excited State Dynamics in Solid and Monomeric Tetracene: The Roles of Superradiance and Exciton Fission. *J. Chem. Phys.* **2010**, *133* (14), 144506.

(85) Gregg, B. A. Excitonic Solar Cells. *J. Phys. Chem. B* **2003**, *107*, 4688–4698.

(86) Tang, C. W. Two-layer Organic Photovoltaic Cell. *Appl. Phys. Lett.* **1986**, *48* (2), 183–185.

(87) Harima, Y.; Yamashita, K.; Suzuki, H. Spectral Sensitization in an Organic P-N-Junction Photovoltaic Cell. *Appl. Phys. Lett.* **1984**, *45* (1984), 1144–1145.

(88) Sun, S.-S.; Sariciftci, N. S. *Organic Photovoltaics Mechanims, Materials, and Devices*; Taylor & Francis Group: Boca Raton, Fl, 2005.

(89) Rand, B. P.; Burk, D. P.; Forrest, S. R. Offset Energies at Organic Semiconductor Heterojunctions and Their Influence on the Open-Circuit Voltage of Thin-Film Solar Cells. *Phys. Rev. B* **2007**, *75*, 115372.

(90) Kahn, A.; Koch, N.; Gao, W. Electronic Structure and Electrical Properties of Interfaces between Metals and P-Conjugated Molecular Films. *J. Polym. Sci. Part B Polym. Phys.* **2003**, *41* (21), 2529–2548.

(91) Heremans, P.; Cheyns, D.; Rand, B. P. Strategies for Increasing the Efficiency of Heterojunction Organic Solar Cells : Material Selection and Device Architecture. *Acc. Chem. Res.* **2009**, *42* (11).

(92) Marcus, R.; Sutin, N. Electron Transfers in Chemistry and Biology. *Biochim.*

Biophys. Acta-Reviews Bioenerg. **1985**, *811*, 265–322.

(93) Deibe, C.; Strobe, T.; Dyakonov, V. Role of the Charge Transfer State in Organic Donor-Acceptor Solar Cells. *Adv. Mater.* **2010**, *22* (37), 4097–4111.

(94) Credgington, D.; Jamieson, F. C.; Walker, B.; Nguyen, T.; Durrant, J. R. Quantification of Geminate and Non-Geminate Recombination Losses within a Solution-Processed Small-Molecule Bulk Heterojunction Solar Cell. *Adv. Mater.* **2012**, *24*, 2135–2141.

(95) Braun, C. L. Electric Field Assisted Dissociation of Charge Transfer States as a Mechanism of Photocarrier Production. *J. Chem. Phys.* **1984**, *80* (4157).

(96) Hodgkiss, J. M.; Tu, G.; Albert-seifried, S.; Huck, W. T. S.; Friend, R. H. Ion-Induced Formation of Charge-Transfer States in Conjugated Polyelectrolytes. *J. Am. Chem. Soc.* **2009**, *131*, 8913–8921.

(97) Baldo, M. A.; Holmes, R. J.; Forrest, S. R. Prospects for Electrically Pumped Organic Lasers. *Phys. Rev. B* **2002**, *66*, 35321.

(98) Ferguson, A. J.; Kopidakis, N.; Shaheen, S. E.; Rumbles, G. Quenching of Excitons by Holes in Poly (3-Hexylthiophene) Films. *J. Phys. Chem. C* **2008**, *112*, 9865–9871.

(99) Hodgkiss, J. M.; Albert-Seifried, S.; Rao, A.; Barker, A. J.; Campbell, A. R.; Marsh, R. A.; Friend, R. H. Exciton-Charge Annihilation in Organic Semiconductor Films. *Adv. Funct. Mater.* **2012**, *22*, 1567–1577.

(100) Verreet, B.; Bhoolokam, A.; Brigeman, A.; Dhanker, R.; Cheyns, D.; Heremans, P.; Stesmans, A.; Giebink, N. C.; Rand, B. P. Reducing Exciton-Polaron Annihilation in Organic Planar Heterojunction Solar Cells. *Phys. Rev. B* **2014**, *90* (11), 115304.

(101) Hertel, D.; Meerholz, K. Triplet-Polaron Quenching in Conjugated Polymers. *J. Phys. Chem. B* **2007**, *1111*, 12075–12080.

(102) Reineke, S.; Walzer, K.; Leo, K. Triplet-Exciton Quenching in Organic Phosphorescent Light-Emitting Diodes with Ir-Based Emitters. *Phys. Rev. B* **2007**, *75* (12), 125328.

(103) Siboni, H. Z.; Aziz, H. Triplet-Polaron Quenching by Charges on Guest Molecules in Phosphorescent Organic Light Emitting Devices Triplet-Polaron Quenching by Charges on Guest Molecules in Phosphorescent Organic Light Emitting Devices. *Appl. Phys. Lett.* **2012**, *101*, 63502.

(104) Engel, E.; Leo, K.; Hoffmann, M. Ultrafast Relaxation and Exciton–exciton Annihilation in PTCDA Thin Films at High Excitation Densities. *Chem. Phys.* **2006**, *325* (1), 170–177.

(105) Shaw, P. E.; Ruseckas, A.; Samuel, I. D. W. Exciton Diffusion Measurements in poly(3-Hexylthiophene). *Adv. Mater.* **2008**, *20* (18), 3516–3520.

(106) Mężyk, J.; Kalinowski, J.; Meinardi, F.; Tubino, R. Singlet Exciton Interactions in Solid Films of Alq3. *Chem. Phys. Lett.* **2004**, *395* (4–6), 321–326.

(107) Völker, S. F.; Schmiedel, A.; Holzapfel, M.; Renziehausen, K.; Engel, V.; Lambert, C. Singlet-Singlet Exciton Annihilation in an Exciton-Coupled Squaraine-Squaraine Copolymer: A Model toward Hetero-J-Aggregates. *J. Phys. Chem. C* **2014**, *118* (31), 17467–17482.

(108) Shao, M.; Yan, L.; Mingxing, L.; Ilia, I.; Hu, B. Triplet–charge Annihilation versus Triplet–triplet Annihilation in Organic Semiconductors. *J. Phys. Chem. C* **2013**, *1*, 1330–1336.

(109) Hershey, K. W.; Holmes, R. J. Unified Analysis of Transient and Steady-State Electrophosphorescence Using Exciton and Polaron Dynamics Modeling. *J. Appl. Phys.* **2016**, *120*, 195501.

(110) Dibb, G. F. A.; Jamieson, F. C.; Maurano, A.; Nelson, J.; Durrant, J. R. Limits on the Fill Factor in Organic Photovoltaics: Distinguishing Nongeminate and Geminate Recombination Mechanisms. *J. Phys. Chem. Lett.* **2013**, *4*, 803–808.

(111) Mingebach, M.; Walter, S.; Dyakonov, V.; Deibel, C. Direct and Charge Transfer State Mediated Photogeneration in Polymer-Fullerene Bulk Heterojunction Solar Cells. *Appl. Phys. Lett.* **2012**, *100*, 193302.

(112) Zhang, Y.; Liu, J.; Nguyen, T.-Q. Photoresponse of Donor/Acceptor Blends in Organic Transistors : A Tool for Understanding Field-Assisted Charge Separation in Small Molecule Bulk Heterojunction Solar Cells. *Appl. Mater. Interfaces* **2013**, *5*, 2347–2353.

(113) Langevin, P. Recombinaison et Mobilites Des Ions Dans Les Gaz. *Ann. Chim. Phys* **1903**, *28* (433), 122.

(114) Proctor, C. M.; Kuik, M.; Nguyen, T.-Q. Charge Carrier Recombination in Organic Solar Cells. *Prog. Polym. Sci.* **2013**, *38*, 1941–1960.

(115) Lakhwani, G.; Rao, A.; Friend, R. H. Bimolecular Recombination in Organic Photovoltaics. *Annu. Rev. Phys. Chem.* **2014**, *65*, 557–581.

(116) Credgington, D.; Hamilton, R.; Atienzar, P.; Nelson, J.; Durrant, J. R. Non-Geminate Recombination as the Primary Determinant of Open-Circuit Voltage in Polythiophene : Fullerene Blend Solar Cells : An Analysis of the Influence of Device Processing Conditions. *Adv. Funct. Mater.* **2011**, *21*, 2744–2753.

(117) Mauer, R.; Howard, I. A.; Laquai, F. Effect of Nongeminate Recombination on Fill Factor in Polythiophene/Methanofullerene Organic Solar Cells. *J. Phys. Chem. Lett.* **2010**, *24*, 3500–3505.

(118) Albrecht, S.; Schindler, W.; Kurpiers, J.; Kniepert, J.; Blakesley, J. C.; Dumsch, I.; Allard, S.; Fostiropoulos, K.; Scherf, U.; Neher, D. On the Field Dependence of Free Charge Carrier Generation and Recombination in Blends of PCPDTBT/PC70BM: Influence of Solvent Additives. *J. Phys. Chem. Lett.* **2012**, *3*, 640–645.

(119) Rand, B. P.; Girotto, C.; Mityashin, A.; Hadipour, A.; Genoe, J.; Heremans, P.; Photocurrent Enhancement in Polymer : Fullerene Bulk Heterojunction Solar Cells Doped with a Phosphorescent Molecule. *Appl. Phys. Lett.* **2009**, *95*, 173304.

(120) Mihailetchi, V. D.; Koster, L. J. A.; Hummelen, J. C.; Blom, P. W. M. Photocurrent Generation in Polymer-Fullerene Bulk Heterojunctions. *Phys. Rev. Lett.* **2004**, *93* (21), 216601.

(121) Park, S. H.; Roy, A.; Beaupré, S.; Cho, S.; Coates, N.; Moon, J. S.; Moses, D.; Leclerc, M.; Lee, K.; Heeger, A. J. Bulk Heterojunction Solar Cells with Internal Quantum Efficiency Approaching 100%. *Nat. Photonics* **2009**, *3* (5), 297–303.

(122) Foertig, A.; Wagenpfahl, A.; Gerbich, T.; Cheyns, D.; Dyakonov, V.; Deibel, C. Nongeminate Recombination in Planar and Bulk Heterojunction Organic Solar Cells. *Adv. Energy Mater.* **2012**, *2*, 1483–1489.

(123) Chiu, S.-W.; Lin, L.-Y.; Lin, H.-W.; Chen, Y.-H.; Huang, Z.-Y.; Lin, Y.-T.; Lin, F.; Liu, Y.-H.; Wong, K.-T. A Donor–acceptor–acceptor Molecule for Vacuum-Processed Organic Solar Cells with a Power Conversion Efficiency of 6.4%. *Chem. Commun.* **2012**, *48* (13), 1857–1859.

(124) Menke, S. M.; Holmes, R. J. Energy-Cascade Organic Photovoltaic Devices Incorporating a Host-Guest Architecture. *ACS Appl. Mater. Interfaces* **2015**, *7* (4), 2912–2918.

(125) Griffith, O. L.; Forrest, S. R. Exciton Management in Organic Photovoltaic Multidonor Energy Cascades. *Nano Lett.* **2014**, *13*, 2353–2358.

(126) Barito, A.; Sykes, M. E.; Huang, B.; Bilby, D.; Frieberg, B.; Kim, J.; Green, P. F.; Shtein, M. Universal Design Principles for Cascade Heterojunction Solar Cells with High Fill Factors and Internal Quantum Efficiencies Approaching 100%. *Adv. Energy Mater.* **2014**, 1400216.

(127) Cnops, K.; Rand, B. P.; Cheyns, D.; Verreet, B.; Empl, M. a; Heremans, P. 8.4% Efficient Fullerene-Free Organic Solar Cells Exploiting Long-Range Exciton Energy Transfer. *Nat. Commun.* **2014**, *5*, 3406.

(128) Menke, S. M.; Mullenbach, T. K.; Holmes, R. J. Directing Energy Transport in Organic Photovoltaic Cells Using Interfacial Exciton Gates. *ACS Nano* **2015**, *9* (4), 4543–4552.

(129) Yang, Y.; Liu, Y.; Chen, C. C.; Hong, Z.; Gao, J.; Michael Yang, Y.; Zhou, H.; Dou, L.; Li, G. Solution-Processed Small-Molecule Solar Cells: Breaking the 10% Power Conversion Efficiency. *Sci. Rep.* **2013**, *3*, 3356.

(130) Zou, Y.; Holst, J.; Zhang, Y.; Holmes, R. J. 7.9% Efficient Vapor-Deposited Organic Photovoltaic Cells Based on a Simple Bulk Heterojunction. **2014**, *Journal of Mat. Chem. A.*, 12397–12402.

(131) Menke, S. M. Exciton Transport in Organic Semiconductors, University of Minnesota, 2015.

(132) Markov, D.; Blom, P. Anisotropy of Exciton Migration in Poly(p-Phenylene Vinylene). *Phys. Rev. B* **2006**, *74* (8), 85206.

(133) Scully, S. R.; McGehee, M. D. Effects of Optical Interference and Energy Transfer on Exciton Diffusion Length Measurements in Organic Semiconductors. *J. Appl. Phys.* **2006**, *100* (3), 34907.

(134) Kroeze, J. E.; Kroeze, J. E.; Savenije, T. J.; Savenije, T. J.; Vermeulen, M. J. W.; Vermeulen, M. J. W.; Warman, J. M.; Warman, J. M. Contactless Determination of the Photoconductivity Action Spectrum, Exciton Diffusion Length, and Charge Separation Efficiency in Polythiophene-Sensitized TiO2 Bilayers. *J. Phys. Chem. B* **2003**, *107*, 7696–7705.

(135) Bergemann, K. J.; Forrest, S. R. Measurement of Exciton Diffusion Lengths in Optically Thin Organic Films. *Appl. Phys. Lett.* **2011**, *99*, 243303.

(136) Markov, D. E.; Amsterdam, E.; Blom, P. W. M.; Sieval, A. B.; Hummelen, J. C. Accurate Measurement of the Exciton Diffusion Length in a Conjugated Polymer Using a Heterostructure with a Side-Chain Cross-Linked Fullerene Layer. *J. Phys. Chem. A* **2005**, *109* (24), 5266–5274.

(137) Mikhnenko, O. V; Cordella, F.; Sieval, A. B.; Hummelen, J. C.; Blom, P. W. M.; Loi, M. A. Temperature Dependence of Exciton Diffusion in Conjugated Polymers. *J. Phys. Chem. B* **2008**, *112* (37), 11601–11604.

(138) Markov, D.; Hummelen, J.; Blom, P.; Sieval, A. Dynamics of Exciton Diffusion in Poly(p-Phenylene Vinylene)/fullerene Heterostructures. *Phys. Rev. B* **2005**, *72* (4), 1098–0121.

(139) Markov, D.; Tanase, C.; Blom, P.; Wildeman, J. Simultaneous Enhancement of Charge Transport and Exciton Diffusion in Poly(p-Phenylene Vinylene) Derivatives. *Phys. Rev. B* **2005**, *72* (4), 45217.

(140) Mikhnenko, O. V.; Kuik, M.; Lin, J.; van der Kaap, N.; Nguyen, T.-Q.; Blom, P. W. M. Trap-Limited Exciton Diffusion in Organic Semiconductors. *Adv. Mater.* **2014**, *26*, 1912–1917.

(141) Ward, A. J.; Ruseckas, A.; Samuel, I. D. W. A Shift from Diffusion Assisted to Energy Transfer Controlled Fluorescence Quenching in Polymer − Fullerene Photovoltaic Blends. *J. Phys. Chem. C* **2012**, *116*, 23931–23937.

(142) Hedley, G. J.; Ward, A. J.; Alekseev, A.; Howells, C. T.; Martins, E. R.; Serrano, L. A.; Cooke, G.; Ruseckas, A.; Samuel, I. D. W. Determining the Optimum Morphology in High-Performance Polymer-Fullerene Organic Photovoltaic Cells. *Nat. Commun.* **2013**, *4*, 1–10.

(143) Mikhnenko, O. V; Lin, J.; Shu, Y.; Anthony, J. E.; Blom, P. W. M.; Nguyen, T.-Q.; Loi, M. A. Effect of Thermal Annealing on Exciton Diffusion in a Diketopyrrolopyrrole Derivative. *Phys. Chem. Chem. Phys.* **2012**, *14* (41), 14196–14201.

(144) Lunt, R. R.; Benziger, J. B.; Forrest, S. R. Relationship between Crystalline Order

and Exciton Diffusion Length in Molecular Organic Semiconductors. *Adv. Mater.* **2010**, *22* (11), 1233–1236.

(145) Menke, S. M.; Holmes, R. J. Evaluating the Role of Energetic Disorder and Thermal Activation in Exciton Transport. *J. Mater. Chem. C* **2016**, *4*, 3437–3442.

(146) Luhman, W. A.; Holmes, R. J. Investigation of Energy Transfer in Organic Photovoltaic Cells and Impact on Exciton Diffusion Length Measurements. *Adv. Funct. Mater.* **2011**, *21* (4), 764–771.

(147) Shin, H.-Y.; Woo, J. H.; Gwon, M. J.; Barthelemy, M.; Vomir, M.; Muto, T.; Takaishi, K.; Uchiyama, M.; Hashizume, D.; Aoyama, T.; et al. Exciton Diffusion in near-Infrared Absorbing Solution-Processed Organic Thin Films. *Phys. Chem. Chem. Phys.* **2013**, *15* (8), 2867–2872.

(148) Mu, A. M.; Bardeen, C. J. Using a Streak Camera to Resolve the Motion of Molecular Excited States with Picosecond Time Resolution and 150 Nm Spatial Resolution. *J. of Phys. Chem. C.* **2007**, 12483–12489.

(149) Akselrod, G. M.; Prins, F.; Poulikakos, L. V; Lee, E. M. Y.; Weidman, M. C.; Mork, A. J.; Willard, A. P.; Bulovic, V.; Tisdale, W. A. Subdiffusive Exciton Transport in Quantum Dot Solids. *Nano Lett.* **2014**, *14*, 3556–2562.

(150) Adams, D. M.; Kerimo, J.; O'Connor, D. B.; Barbara, P. F. Spatial Imaging of Singlet Energy Migration in Perylene Bis(phenethylimide) Thin Films. *J. Phys. Chem. A* **1999**, *103* (49), 10138–10143.

(151) Luhman, W. A.; Holmes, R. J. Enhanced Exciton Diffusion in an Organic Photovoltaic Cell by Energy Transfer Using a Phosphorescent Sensitizer. *Appl. Phys. Lett.* **2009**, *94* (15), 153304.

(152) Yoo, S.; Domercq, B.; Kippelen, B. Efficient Thin-Film Organic Solar Cells Based on pentacene/C60 Heterojunctions. *Appl. Phys. Lett.* **2004**, *85* (22), 5427–5429.

(153) Terao, Y.; Sasabe, H.; Adachi, C. Correlation of Hole Mobility, Exciton Diffusion Length, and Solar Cell Characteristics in Phthalocyanine/fullerene Organic Solar Cells. *Appl. Phys. Lett.* **2007**, *90* (10), 103515.

(154) Kurrle, D.; Pflaum, J. Exciton Diffusion Length in the Organic Semiconductor Diindenoperylene. *Appl. Phys. Lett.* **2008**, *92* (13), 133306.

(155) Tabachnyk, M.; Ehrler, B.; Bayliss, S.; Friend, R. H.; Greenham, N. C. Triplet Diffusion in Singlet Exciton Fission Sensitized Pentacene Solar Cells. *Appl. Phys. Lett.* **2013**, *103*, 155302.

(156) Fravventura, M. C.; Hwang, J.; Suijkerbuijk, J. W. A.; Erk, P.; Siebbeles, L. D. A.; Savenije, T. J. Determination of Singlet Exciton Diffusion Length in Thin Evaporated C60 Films for Photovoltaics. *J. Phys. Chem. Lett.* **2012**, *3*, 2367–2373.

(157) Kroeze, J. E.; Savenije, T. J.; Candeias, L. P.; Warman, M.; Siebbeles, L. D. A. Triplet Exciton Diffusion and Delayed Interfacial Charge Separation in a Tio2/PdTPPC Bilayer : Monte Carlo Simulations. *Sol. Energy Mater. Sol. Cells*

2005, *85*, 189–203.

(158) Mullenbach, T. K.; Curtin, I. J.; Zhang, T.; Holmes, R. J. Probing Dark Exciton Diffusion Using Photovoltage. *Nat. Commun.* **2017**, *8*, 14215.

(159) Bergemann, K. J.; Liu, X.; Panda, A.; Forrest, S. R. Singlets Lead to Photogeneration in C_{60}-Based Organic Heterojunctions. *Phys. Rev. B* **2015**, *92* (3), 35408.

(160) Kaake, L.; Dang, X.-D.; Leong, W. L.; Zhang, Y.; Heeger, A.; Nguyen, T.-Q. Effects of Impurities on Operational Mechanism of Organic Bulk Heterojunction Solar Cells. *Adv. Mater.* **2013**, *25* (25), 1706–1712.

(161) Morgan, N. T.; Zhang, Y.; Molitor, E. J.; Bell, B. M.; Holmes, R. J.; Cussler, E. L. Understanding Rate-Limiting Processes for the Sublimation of Small Molecule Organic Semiconductors. *AIChE J.* **2014**, *60* (4), 1374–1354.

(162) Nikiforov, M. P.; Lai, B.; Chen, W.; Chen, S.; Schaller, R. D.; Strzalka, J.; Maser, J.; Darling, S. B. Detection and Role of Trace Impurities in High-Performance Organic Solar Cells. *Energy Environ. Sci.* **2013**, *6* (5), 1513–1520.

(163) Salzman, R.; Xue, J.; Rand, B.; Alexander, A.; Thompson, M.; Forrest, S. The Effects of Copper Phthalocyanine Purity on Organic Solar Cell Performance. *Org. Electron.* **2005**, *6*, 242–246.

(164) Bisri, S. Z.; Takenobu, T.; Takahashi, T.; Iwasa, Y. Electron Transport in Rubrene Single-Crystal Transistors. *Appl. Phys. Lett.* **2010**, *96* (18), 183304.

(165) Drechsel, J.; Petrich, A.; Koch, M.; Pfützner, S.; Meerheim, R.; Scholz, S.; Walzer, K.; Pfeiffer, M.; Leo, K. Influence of Material Purification by Vacuum Sublimation on Organic Optoelectronic Device Performance. *Dig. Tech. Pap.* **2006**, *37* (4), 1962–1965.

(166) Cowan, S. R.; Leong, W. L.; Banerji, N.; Dennler, G.; Heeger, A. J. Identifying a Threshold Impurity Level for Organic Solar Cells : Enhanced First-Order Recombination Via Well- Efined PC84BM Traps in Organic Bulk Heterojunction Solar Cells. *Adv. Funct. Mater.* **2011**, *21*, 3083–3092.

(167) Numata, M.; Yasuda, T.; Adachi, C. High Efficiency Pure Blue Thermally Activated Delayed Fluorescence Molecules Having 10H-Phenoxaborin and Acridan Units. *Chem. Commun.* **2015**, *51* (46), 9443–9446.

(168) Djurovich, P. I.; Mayo, E. I.; Forrest, S. R.; Thompson, M. E. Measurement of the Lowest Unoccupied Molecular Orbital Energies of Molecular Organic Semiconductors. *Org. Electron.* **2009**, *10*, 515–520.

(169) Chance, R. R.; Prock, A.; Silbey, R. Decay of an Emitting Dipole between Two Parallel Mirrors. *J. Chem. Phys.* **1975**, *62* (3), 771.

(170) Burin, A. L.; Ratner, M. A. Exciton Migration and Cathode Quenching in Organic Light Emitting Diodes †. *J. Phys. Chem. A* **2000**, *104* (20), 4704–4710.

(171) Mei, J.; Bradley, M.; Bulović, V. Photoluminescence Quenching of Tris-(8-Hydroxyquinoline) Aluminum Thin Films at Interfaces with Metal Oxide Films of Different Conductivities. *Phys. Rev. B* **2009**, *79* (23), 235205.

(172) Kalinowski, J.; Fattori, V.; Marco, P. Di. Surface Reactions of Singlet Excitons in Solid Films of 8-Hydroxyquinoline Aluminium (Alq 3). *Chem. Phys.* **2001**, *266*, 85–96.

(173) Choong, V.; Park, Y.; Shivaparan, N.; Tang, C. W.; Gao, Y. Deposition-Induced Photoluminescence Quenching of Tris-(8-Hydroxyquinoline) Aluminum. *Appl. Phys. Lett.* **1997**, *71*, 1005–1007.

(174) Choong, V.; Park, Y.; Gao, Y.; Wehrmeister, T.; Müllen, K.; Hsieh, B. R.; Tang, C. W. Dramatic Photoluminescence Quenching of Phenylene Vinylene Oligomer Thin Films upon Submonolayer Ca Deposition. *Appl. Phys. Lett.* **1996**, *69* (10), 1492–1494.

(175) Wu, Y.; Wu, H. R.; Wang, M. L.; Lu, M.; Song, Q. L.; Ding, X. M.; Hou, X. Y. Metal-Induced Photoluminescence Quenching in Thin Organic Films Originating from Noncontact Energy Transfer between Single Molecule and Atom. *Appl. Phys. Lett.* **2007**, *90* (15), 154105.

(176) Wu, Y.; Zhou, Y. C.; Wu, H. R.; Zhan, Y. Q.; Zhou, J.; Zhang, S. T.; Zhao, J. M.; Wang, Z. J.; Ding, X. M.; Hou, X. Y. Metal-Induced Photoluminescence Quenching of Tri-(8-Hydroxyquinoline) Aluminum. *Appl. Phys. Lett.* **2005**, *87* (4), 44104.

(177) Morgan, N. T.; Zhang, Y.; Grandbois, M. L.; Bell, B. M.; Holmes, R. J.; Cussler, E. L. Mechanism for the Separation of Organic Semiconductors via Thermal Gradient Sublimation. *Org. Electron.* **2015**, *24*, 212–218.

(178) Shalev, O.; Shtein, M. Effect of Crystal Density on Sublimation Properties of Molecular Organic Semiconductors. *Org. Electron.* **2013**, *14* (1), 94–99.

(179) Matuszewski, B. K.; Constanzer, M. L.; Chavez-Eng, C. M. Strategies for the Assessment of Matrix Effect in Quantitative Bioanalytical Methods Based on HPLC – MS/MS. *Anal. Chem.* **2003**, *75* (13), 3019–3030.

(180) Cheng, J.-A.; Cheng, P.-J. Crystal Study of N,N′-Diphenyl-N,N′-bis(1-Naphthyl)-1,1′-Biphenyl-4,4′-Diamine. *J. Chem. Crystallogr.* **2010**, *40* (6), 557–560.

(181) Farchioni, R.; Grosso, G. *Organic Electronic Materials: Conjugated Polymer and Low Molecular Weight Organic Solids*; Zunger, A., Hull, R., Osgood, R. M., Sakaki, H., Eds.; Springer: Berlin, 2001.

(182) Theander, M.; Yartsev, A.; Zigmantas, D.; Sundström, V.; Mammo, W.; Andersson, M. R.; Inganäs, O. Photoluminescence Quenching at a polythiophene/C_{60} Heterojunction. *Phys. Rev. B* **2000**, *61* (19), 12957–12963.

(183) Halls, J. J. M.; Pichler, K.; Friend, R. H.; Moratti, S. C.; Holmes, A. B. Exciton Diffusion and Dissociation in a Poly(p-phenylenevinylene)/C-60 Heterojunction Photovoltaic Cell. *Appl. Phys. Lett.* **1996**, *68* (22), 3120–3122.

(184) Yoo, S.; Potscavage, W. J.; Domercq, B.; Han, S. H.; Li, T. De; Jones, S. C.; Szoszkiewicz, R.; Levi, D.; Riedo, E.; Marder, S. R.; et al. Analysis of Improved Photovoltaic Properties of pentacene/C60 Organic Solar Cells: Effects of Exciton Blocking Layer Thickness and Thermal Annealing. *Solid. State. Electron.* **2007**, *51*, 1367–1375.

(185) Giebink, N. C.; Wiederrecht, G. P.; Wasielewski, M. R.; Forrest, S. R. Ideal Diode Equation for Organic Heterojunctions. I. Derivation and Application. *Phys. Rev. B* **2010**, *82* (15), 155305.

(186) Cheyns, D.; Poortmans, J.; Heremans, P.; Deibel, C.; Verlaak, S.; Rand, B. P.; Genoe, J. Analytical Model for the Open-Circuit Voltage and Its Associated Resistance in Organic Planar Heterojunction Solar Cells. *Phys. Rev. B* **2008**, *77* (16), 165332.

(187) Mullenbach, T. K.; Holmes, R. J. Relating Photocurrent, Photovoltage, and Charge Carrier Density to the Recombination Rate in Organic Photovoltaic Cells. *Appl. Phys. Lett.* **2015**, *107* (12), 123303.

(188) Pivrikas, A.; Sariciftci, N. S.; Juška, G.; Österbacka, R. A Review of Charge Transport and Recombination in Polymer/fullerene Organic Solar Cells. *Prog. Photovoltaics Res. Appl.* **2007**, *15* (8), 677–696.

(189) Shuttle, C. G.; Maurano, A.; Hamilton, R.; O'Regan, B. C.; de Mello, J. C.; Durrant, J. R. Charge Extraction Analysis of Charge Carrier Densities in a Polythiophene/fullerene Solar Cell: Analysis of the Origin of the Device Dark Current. *Appl. Phys. Lett.* **2008**, *93* (18), 183501.

(190) Peter, L. M.; Duffy, N. W.; Wang, R. L.; Wijayantha, K. G. U. Transport and Interfacial Transfer of Electrons in Dye-Sensitized Nanocrystalline Solar Cells. *J. Electroanal. Chem.* **2002**, *524–525*, 127–136.

(191) Duffy, N. W.; Peter, L. M.; Rajapakse, R. M. G.; Wijayantha, K. G. U. A Novel Charge Extraction Method for the Study of Electron Transport and Interfacial Transfer in Dye Sensitised Nanocrystalline Solar Cells. *Electrochem. commun.* **2000**, *2* (9), 658–662.

(192) Caplins, B. W.; Mullenbach, T. K.; Holmes, R. J.; Blank, D. A. Intermolecular Interactions Determine Exciton Lifetimes in Neat Films and Solid State Solutions of Metal-Free Phthalocyanine. *J. Phys. Chem. C* **2015**, *119* (49), 27340–27347.

(193) Sugiyama, K.; Ishii, H.; Ouchi, Y.; Seki, K. Dependence of Indium–tin–oxide Work Function on Surface Cleaning Method as Studied by Ultraviolet and X-Ray Photoemission Spectroscopies. *J. Appl. Phys.* **2000**, *87* (1), 295–298.

(194) Zou, Y.; Holmes, R. J. Influence of a MoOx Interlayer on the Open-Circuit Voltage in Organic Photovoltaic Cells. *Appl. Phys. Lett.* **2013**, *103* (5), 53302.

(195) Mott, N. F.; Gurney, R. W. *Electronic Processes in Ionic Crystals*, 1st ed.; Oxford University Press, 1940.

(196) Lampert, M. A. Volume-Controlled Current Injection in Insulators. *Reports Prog.*

Phys. **1964**, *27*, 329–364.

(197) Giebink, N. C.; Andrade, B. W. D.; Weaver, M. S.; Brown, J. J.; Forrest, S. R. Direct Evidence for Degradation of Polaron Excited States in Organic Light Emitting Diodes. *J. Appl. Phys.* **2009**, *105*, 124514.

(198) Singh, S.; Jones, W. J.; Siebrand, W.; Stoicheff, B. P.; Schneider, W. G. Laser Generation of Excitons and Fluorescence in Anthracene Crystals. *J. Chem. Phys.* **1965**, *42* (1), 330–342.

(199) Hanna, M. C.; Nozik, A. J. Solar Conversion Efficiency of Photovoltaic and Photoelectrolysis Cells with Carrier Multiplication Absorbers. *J. Appl. Phys.* **2006**, *100* (7), 754510.

(200) Ehrler, B.; Musselman, K. P.; Böhm, M. L.; Friend, R. H.; Greenham, N. C.; Friend, R. H. Exciton Fission Hybrid Pentacene / a-Silicon Solar Cells Utilizing Multiple Carrier Generation via Singlet Exciton Fission. *Appl. Phys. Lett.* **2012**, *101*, 1153507.

(201) Sanders, S. N.; Kumarasamy, E.; Pun, A. B.; Trinh, M. T.; Choi, B.; Xia, J.; Ta, E. J.; Low, J. Z.; Miller, J. R.; Roy, X.; et al. Quantitative Intramolecular Singlet Fission in Bipentacenes. *J. Am. Chem. Soc.* **2015**, *137*, 8965–8972.

(202) Jankus, V.; Snedden, E. W.; Bright, D. W.; Arac, E.; Dai, D.; Monkman, A. P. Competition between Polaron Pair Formation and Singlet Fission Observed in Amorphous Rubrene Films. *Phys. Rev. B* **2013**, *87* (22), 224202.

(203) Thompson, N. J.; Congreve, D. N.; Goldberg, D.; Menon, V. M.; Baldo, M. A. Slow Light Enhanced Singlet Exciton Fission Solar Cells with a 126% Yield of Electrons per Photon. *Appl. Phys. Lett.* **2013**, *103* (26), 263302.

(204) Shockley, W.; Queisser, H. J. Detailed Balance Limit of Efficiency of P-N Junction Solar Cells. *J. Appl. Phys.* **1961**, *32* (3), 510–519.

(205) Zimmerman, P. M.; Bell, F.; Casanova, D.; Head-Gordon, M. Mechanism for Singlet Fission in Pentacene and Tetracene: From Single Exciton to Two Triplets. *J. Am. Chem. Soc.* **2011**, *133* (49), 19944–19952.

(206) Burdett, J. J.; Piland, G. B.; Bardeen, C. J. Magnetic Field Effects and the Role of Spin States in Singlet Fission. *Chem. Phys. Lett.* **2013**, *585*, 1–10.

(207) Ern, V. Anisotropy of Triplet Exciton Diffusion in Anthracene. *Phys. Rev. Lett.* **1969**, *22* (8), 22–24.

(208) Jundt, C.; Klein, G.; Sipp, B.; Lemoigne, J.; Joucla, M.; Villaeys, A. A. Exciton Dynamics in Pentacene Thin-Films Studied by Pump-Probe Spectroscopy. *Chem. Phys. Lett.* **1995**, *241*, 84–88.

(209) Burgos, J.; Pope, M.; Swenberg, C. E.; Alfano, R. R. Heterofission in Pentacene-doped Tetracene Single Crystals. *Phys. Status Solidi* **1977**, *83*, 249–256.

(210) Wilson, M. W. B.; Rao, A.; Clark, J.; Kumar, R. S. S.; Brida, D.; Cerullo, G.;

Friend, R. H. Ultrafast Dynamics of Exciton Fission in Polycrystalline Pentacene. *J. Am. Chem. Soc.* **2011**, *133*, 11830–11833.

(211) Yost, S. R.; Lee, J.; Wilson, M. W. B.; Wu, T.; McMahon, D. P.; Parkhurst, R. R.; Thompson, N. J.; Congreve, D. N.; Rao, A.; Johnson, K.; et al. A Transferable Model for Singlet-Fission Kinetics. *Nat. Chem.* **2014**, *6* (6), 492–497.

(212) Guan, Z. L.; Bok Kim, J.; Loo, Y. L.; Kahn, A. Electronic Structure of the poly(3-Hexylthiophene):indene-C60 Bisadduct Bulk Heterojunction. *J. Appl. Phys.* **2011**, *110* (4), 43719.

(213) Reusswig, P. D.; Congreve, D. N.; Thompson, N. J.; Baldo, M. A. Enhanced External Quantum Efficiency in an Organic Photovoltaic Cell via Singlet Fission Exciton Sensitizer. *Appl. Phys. Lett.* **2012**, *101* (2012), 113304.

(214) Mattheus, C. C.; De Wijs, G. A.; De Groot, R. A.; Palstra, T. T. M. Modeling the Polymorphism of Pentacene. *J. Am. Chem. Soc.* **2003**, *125* (20), 6323–6330.

(215) Holmes, D.; Kumaraswamy, S.; Matzger, A. J.; Vollhardt, K. P. C. On the Nature of Nonplanarity in the [N] Phenylenes. *Chem. Eur. J.* **1999**, *5*, 3399–3412.

(216) Bouchoms, I. P. M.; Schoonveld, W. A.; Vrijmoeth, J.; Klapwijk, T. M. Morphology Identification of the Thin Film Phases of Vacuum Evaporated Pentacene on SIO2 Substrates. *Synth. Met.* **1999**, *104*, 175–178.

(217) Knipp, D.; Street, R. A.; Völkel, A.; Ho, J. Pentacene Thin Film Transistors on Inorganic Dielectrics: Morphology, Structural Properties, and Electronic Transport. *J. Appl. Phys.* **2003**, *93* (1), 347–355.

(218) Wu, J. S.; Spence, J. C. H. Electron Diffraction of Thin-Film Pentacene. *J. Appl. Crystallogr.* **2004**, *37* (1), 78–81.

(219) Wisz, G.; Kuzma, M.; Virt, I.; Sagan, P.; Rudyj, I. Growth Modes of Pentacene Films Obtained by Pulsed Laser Deposition. *Appl. Surf. Sci.* **2011**, *257* (12), 5319–5323.

(220) Fritz, S. E.; Martin, S. M.; Frisbie, C. D.; Ward, M. D.; Toney, M. F. Structural Characterization of a Pentacene Monolayer on an Amorphous SiO2 Substrate with Grazing Incidence X-Ray Diffraction. *J. Am. Chem. Soc.* **2004**, *126* (13), 4084–4085.

(221) Yang, J.; Nguyen, T. Q. Effects of Thin Film Processing on pentacene/C60 Bilayer Solar Cell Performance. *Org. Electron.* **2007**, *8*, 566–574.

(222) Hwang, J.; Sunesh, C. D.; Chandran, M.; Lee, J.; Choe, Y. Performance Characteristics of Pentacene-Based Organic Photovoltaic Cells. *Org. Electr.* **2012**, *13*, 1809–1818.

(223) Cheng, H. L.; Mai, Y. S.; Chou, W. Y.; Chang, L. R.; Liang, X. W. Thickness-Dependent Structural Evolutions and Growth Models in Relation to Carrier Transport Properties in Polycrystalline Pentacene Thin Films. *Adv. Funct. Mater.* **2007**, *17*, 3639–3649.

(224) Sugiyama, K.; Kojima, T.; Fukuda, H.; Yashiro, H.; Matsuura, T.; Shimoyama, Y. ESR and X-Ray Diffraction Studies on Thin Films of Poly-3-Hexylthiophene: Molecular Orientation and Magnetic Interactions. *Thin Solid Films* **2008**, *516* (9), 2691–2694.

(225) Dai, M. K.; Lian, J. T.; Lin, T. Y.; Chen, M. C.; Tai, Y.; Chen, Y. F. High-Performance Polythiophene Thin-Film Transistors with Nematic Liquid Crystal Modification. *Org. Electron. physics, Mater. Appl.* **2012**, *13* (11), 2229–2234.

(226) Meyer zu Heringdorf, F.-J.; Reuter, M. C.; Tromp, R. M. Growth Dynamics of Pentacene Thin Films. *Nature* **2001**, *412* (6846), 517–520.

(227) Pandey, R.; Gunawan, A. A.; Mkhoyan, K. A.; Holmes, R. J. Efficient Organic Photovoltaic Cells Based on Nanocrystalline Mixtures of Boron Subphthalocyanine Chloride and C60. *Adv. Funct. Mater.* **2012**, *22* (3), 617–624.

(228) Pfuetzner, S.; Mickel, C.; Jankowski, J.; Hein, M.; Meiss, J.; Schuenemann, C.; Elschner, C.; Levin, A. A.; Rellinghaus, B.; Leo, K.; et al. The Influence of Substrate Heating on Morphology and Layer Growth in C60: ZnPc Bulk Heterojunction Solar Cells. *Org. Electron. physics, Mater. Appl.* **2011**, *12* (3), 435–441.

(229) Hong, Z. R.; Maennig, B.; Lessmann, R.; Pfeiffer, M.; Leo, K.; Simon, P. Improved Efficiency of Zinc Phthalocyanine/ C60 Based Photovoltaic Cells via Nanoscale Interface Modification. *Appl. Phys. Lett.* **2007**, *90* (20), 1–4.

(230) Zhennan, G.; Jiuxin, Q.; Xihaung, Z.; Yongqing, W. Buckminsterfullerene C60: Synthesis, Spectroscopic Characterization, and Structure Analysis. *J. Phys. Chem.* **1991**, *95* (24), 9615–9618.

(231) Edura, T.; Takahashi, H.; Nakata, M.; Onozato, H.; Mizuno, J.; Tsutsui, K.; Haemori, M.; Itaka, K.; Koinuma, H.; Wada, Y. Single Grain and Single Grain Boundary Resistance of Pentacene Thin Film Characterized Using a Nanoscale Electrode Array. *Jpn. J. Appl. Phys.* **2006**, *45* (4B), 3708–3711.

(232) Wilson, M. W. B.; Rao, A.; Ehrler, B.; Friend, R. H. Singlet Exciton Fission in Polycrystalline Pentacene: From Photophysics toward Devices. *Acc. Chem. Res.* **2013**, *46* (6), 1330–1338.

(233) Forster, T. 10th Spiers Memorial Lecture Transfter Mechanisms of Electronic Excitation. *R. Soc. Chemsitry* **1959**, *27*, 7–17.

(234) Scully, S. R.; Armstrong, P. B.; Edder, C.; Fréchet, J. M. J.; Mcgehee, M. D. Long-Range Resonant Energy Transfer for Enhanced Exciton Harvesting for Organic Solar Cells. *Adv. Mater.* **2007**, *19*, 2961–2966.

(235) Kuhn, H. Classical Aspects of Energy Transfer in Molecular Systems. *J. Chem. Phys.* **1970**, *53* (1), 101–108.

(236) Schlosser, M.; Lochbrunner, S. Exciton Migration by Ultrafast Forster Transfer in Highly Doped Matrixes. *J. Phys. Chem. B* **2006**, *110*, 6001–6009.

(237) Ma, L.; Zhang, K.; Kloc, C.; Sun, H.; Michel-Beyerle, M. E.; Gurzadyan, G. G. Singlet Fission in Rubrene Single Crystal: Direct Observation by Femtosecond Pump–probe Spectroscopy. *Phys. Chem. Chem. Phys.* **2012**, *14* (23), 8307.

(238) Ryasnyanskiy, A.; Biaggio, I. Triplet Exciton Dynamics in Rubrene Single Crystals. *Phys. Rev. B - Condens. Matter Mater. Phys.* **2011**, *84* (19), 2–5.

(239) Biaggio, I.; Irkhin, P. Extremely Efficient Exciton Fission and Fusion and Its Dominant Contribution to the Photoluminescence Yield in Rubrene Single Crystals. *Appl. Phys. Lett.* **2013**, *103* (26).

(240) Piland, G. B.; Burdett, J. J.; Kurunthu, D.; Bardeen, C. J.; Piland, B.; Burdett, J. J.; Kurunthu, D.; Bardeen, C. J. Magnetic Field Effects on Singlet Fission and Fluorescence Decay Dynamics in Amorphous Rubrene. *Phys. Chem. C* **2013**, *117* (3), 1224–1236.

(241) Korovina, N. V.; Das, S.; Nett, Z.; Feng, X.; Joy, J.; Haiges, R.; Krylov, A. I.; Bradforth, S. E.; Thompson, M. E. Singlet Fission in a Covalently Linked Cofacial Alkynyltetracene Dimer. *J. Am. Chem. Soc.* **2016**, *138* (2), 617–627.

(242) Xia, J.; Sanders, S. N.; Cheng, W.; Low, J. Z.; Liu, J.; Campos, L. M.; Sun, T. Singlet Fission: Progress and Prospects in Solar Cells. *Adv. Mater.* **2017**, *29* (20).

(243) Rand, B. P.; Schols, S.; Cheyns, D.; Gommans, H.; Girotto, C.; Genoe, J.; Heremans, P.; Poortmans, J. Organic Solar Cells with Sensitized Phosphorescent Absorbing Layers. *Org. Electron.* **2009**, *10*, 1015–1019.

(244) González-rodríguez, D.; Torres, T.; Guldi, D. M.; Rivera, J.; Ángeles, M.; Echegoyen, L. Subphthalocyanines : New Tuneable Tectons for Intramolecular Electron and Energy Transfer Processes. *J. Am. Chem. Soc.* **2004**, No. 2, 1–36.

13. Appendix

A. List of publications and presentations

Publications:

1) Curtin, I.J.; Blaylock, D.W.; Holmes R.J.; Role of impurities in determining the exciton diffusion length in organic semiconductors. *Appl. Phys. Lett.* **2016**, 108, 163301.

2) Mullenbach, T.K.*; Curtin, I.J.*****; Zhang, T.; Holmes, R.J.; Probing dark exciton harvesting using photovoltage. *Nature Comm.* **2017**, 8, 14215.
*Authors contributed equally

3) Curtin, I.J.; Holmes, R.J.; Decoupling Photocurrent Loss Mechanisms in Photovoltaic Cells Using Complementary Measurements of Exciton Diffusion. *Advanced Energy Materials.* **2018**, 1702339.

4) Curtin, I.J.; Fielitz, T.R.; Holmes, R.J., Understanding and engineering exciton transport. *World Scientific Handbook of Organic Electronics.* **2018.**

5) Curtin, I.J.; Shi, K.; Holmes, R.J.; Measuring triplet diffusion lengths as a function of polycrystalline grain size in singlet fission pentacene, *In Preparation*

Presentations:

Oral Presentations:

1) Curtin, I.J., Holmes, R.J., Exciton Transport in Materials Exhibiting Singlet Fission, Industrial Partnership for Research in Interfacial Materials and Engineering, Minneapolis, MN, May 31, 2017

2) Curtin I.J., Holmes, R.J., Photocurrent Loss in Organic Photovoltaic Cells due to Exciton-Polaron Quenching, International Conference of Electroluminescence and Optoelectronic Devices, Raleigh, NC, October 6, 2016

3) Curtin, I.J., Holmes, R.J., Photocurrent Loss in Organic Photovoltaic Cells due to Exciton-Polaron Quenching, Industrial Partnership for Research in Interfacial Materials and Engineering, Minneapolis, MN, June 1, 2016

4) Curtin, I.J., Holmes, R.J., The Role of Molecular Impurities in Determining the Exciton Diffusion Length in Organic Semiconductors, Industrial Partnership for Research in Interfacial Materials and Engineering, Minneapolis, MN, May 27, 2015

Poster Presentations:

1) Curtin, I.J., Holmes, R.J., Exciton Transport in Materials Exhibiting Singlet Fission, Industrial Partnership for Research in Interfacial Materials and Engineering, Minneapolis, MN, May 31, 2017

2) Curtin, I.J., Holmes, R.J., Photocurrent Loss in Organic Photovoltaic Cells due to Exciton-Polaron Quenching, 3M Poster Symposium, St. Paul, MN, July 11, 2016

3) Curtin, I.J., Holmes, R.J., The Role of Molecular Impurities in Determining the Exciton Diffusion Length in Organic Semiconductors, Materials Research Society, Boston, MA, November 27-December 2, 2016

4) Curtin, I.J., Holmes, R.J., The Role of Molecular Impurities in Determining the Exciton Diffusion Length in Organic Semiconductors, Industrial Partnership for Research in Interfacial Materials and Engineering, Minneapolis, MN, May 27, 2015

B. Experimental methods

Substrate cleaning procedure:

All substrates used in this work were cleaned prior to film deposition with the following procedure:

1) Sonication for 5 minutes in a dilute solution of Tergitol and deionized water
2) Sonication for 5 minutes in deionized water
3) Sonication for 5 minutes in acetone
4) Sonication for 5 minutes in a second acetone bath
5) Boiling for 5 minutes in isopropyl alcohol
6) Boiling for 5 minutes in a second isopropyl alcohol bath

Additionally, substrates of ITO were exposed to an ultraviolet-ozone atmosphere for 10 minutes prior to deposition.

Film and device preparation:

Unless otherwise noted:

Films and device active layers used in this work were fabricated using thermal vacuum sublimation. Organic layers were deposited at 0.2 nm s^{-1}, and the Al cathode was deposited at 0.3 nm s^{-1} at a base pressure of 10^{-7} Torr. All materials were used as received without further purification. Materials were obtained from the following suppliers: H_2Pc and MgPc from Sigma-Aldrich; CuPc from Acros Organics; PbPc from TCI America; BCP, NTCDA, MoO_x and Al from Alfa Aesar; HATCN, SubPc and UGH2 from Luminescence Technology Corporation; α-NPD from The Dow Chemical Company; and C_{60} from MER Corporation.

All devices were fabricated on an ITO coated glass substrate with a sheet resistance of 15 Ω per square and were capped with a 10-nm-thick exciton blocking layer of BCP and a 100-nm-thick cathode layer of Al deposited through a shadow mask. Devices deposited on

pre-patterned ITO have an active area of 0.25 cm^2 and devices deposited on unpatterned ITO have an active area of $\pi \times 0.0025\,cm^2$. All patterned devices were encapsulated with a glass microscope slide and UV cured epoxy to avoid device degradation in atmosphere.

C. α-NPD photoluminescence spectra and purification details

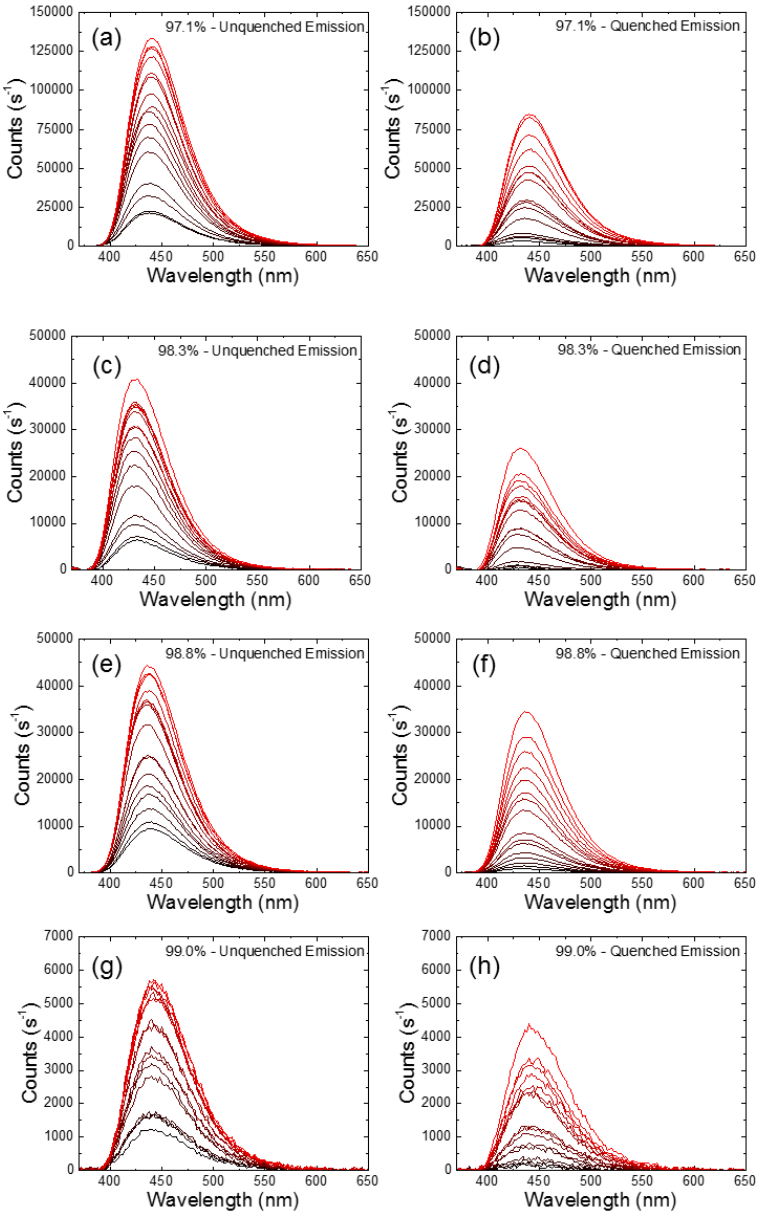

Figure 13.1 Photoluminescence (PL) spectra of α-NPD films used to calculate PL ratios for L_D fits in Fig. 6.3. (a) Unquenched and (b) quenched spectra of 97.1% pure films corresponding to 6.4, 6.9, 7.8, 8.3, 10.3, 11.5, 12.3, 13.3, 16.4, 18.0, 19.7, 21.0, 28.2, 31.4, 35.2, and 37.3 nm thicknesses in order increasing intensity. (c) Unquenched and (d) quenched spectra of 98.3% pure films corresponding to 5.6, 6.1, 6.3, 6.7, 10.9, 12.3, 13.7, 14.8, 19.2, 21.7, 23.6, 25.5, 29.9, 33.1, 36.1, and 38.9 nm thicknesses in order increasing intensity. (e) Unquenched and (f) quenched spectra of 98.8% pure films corresponding to 6.8, 7.5, 8.4, 9.3, 11.4, 12.2, 13.7, 14.9, 20.5, 23.3, 27.0, 29.7, 33.8, 37.8, 43.4, and 48.0 nm thicknesses in order increasing intensity. (g) Unquenched and (h) quenched spectra of 99.0% pure films corresponding to 6.7, 7.5, 8.5, 9.2, 10.9, 13.1, 14.1, 16.5, 18.7, 21.7, 24.5, 28.0, 28.9, 33.9, 38.1, 44.5 nm thicknesses in order increasing intensity. Counts axis between different purities is arbitrary.

α-NPD purification details:

α-NPD was purified once by thermal gradient sublimation purification. Prior to purification all glassware was cleaned by rinsing in acetone, isopropanol, and DI water three times to remove the majority of the organic material left from previous purifications. The remaining residual organic material was then removed with a piranha etch, consisting of a 3:1 sulfuric acid (H_2SO_4) to hydrogen peroxide (H_2O_2) ratio. Here, 150 mL of 99% sulfuric acid is mixed with 50 mL of 30% hydrogen peroxide in the purification tube, this is repeated three times until the glassware is submerged, with a total of 600 mL of solution in the tube. The glassware was rinsed three times with piranha etch and on the third rinse the solution was left in the purification tube overnight in a fume hood in order to ensure that all organic material was completely etched. All glassware was subsequently rinsed with water and isopropanol to remove any sulfuric acid and hydrogen peroxide.

All glassware was then allowed to dry before being inserted into the thermal gradient sublimation purification setup. Empty glassware was placed under vacuum at a base pressure of 2.2×10^{-6} Torr, heated to 500 ºC, and left overnight to remove any residual water, solvent, or organic material. The next day, 11.4 g of α-NPD was loaded into the deposition boat and inserted into the purification tube, along with five glass sleeves which are used to collect the sublimed material. The purification tube was evacuated to a base pressure of 1.8×10^{-6} Torr and all three zones of the furnace were set to 120 ºC and left overnight to bake off any volatiles and residual solvent in the source material. The next day, all three zones of the furnace were increased to 260 ºC at a starting base pressure of 3.4×10^{-7} Torr. While all three zones of the furnace were set to the same temperature, separation was achieved by the linear temperature gradient out of the end of the furnace. After eight days, once the purification was complete, all three zones of the furnace were

turned off and the furnace was removed, allowing the purification tube to be crash cooled to room temperature. Once the tube had cooled to room temperature and was brought up to room pressure, 9.1 g of pure material was collected from the end of the third and beginning of the fourth sleeve, as shown in Fig. 6.2b, by manually scraping the inside of collection sleeves.

D. Photovoltage L_D measurements of dark phthalocyanine materials

The following figures display the charge extraction and photovoltage results used to measure L_D in dark phthalocyanine materials presented in Chapter 7.

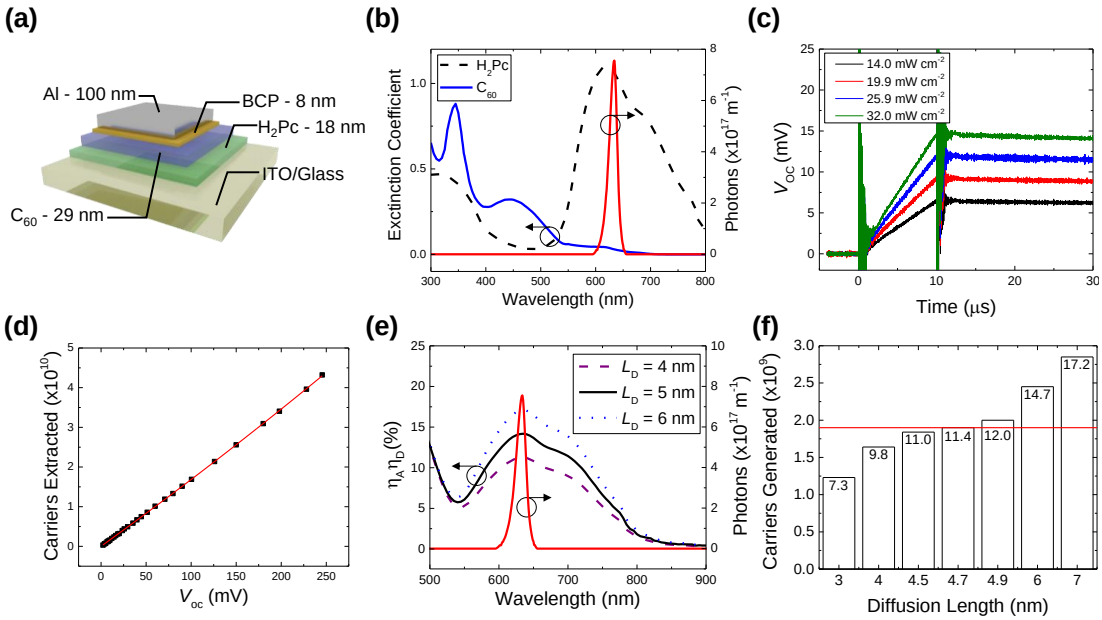

Figure 13.2: Measuring the L_D of H_2Pc: (a) Architecture for the planar heterojunction organic photovoltaic cell (OPV) based on the donor-acceptor pairing of metal-free phthalocyanine (H_2Pc)-C_{60}. (b) Comparison of the extinction coefficients for H_2Pc and C_{60} as well as the spectrum of the LED pulse (λ_{peak} = 625 nm) used to pump H_2Pc. (c) Four photovoltage rises recorded when pumping H_2Pc with the λ = 625 nm LED at intensities of 14.0 mW cm^{-2} (black), 19.9 mW cm^{-2} (red), 25.9 mW cm^{-2} (blue) and 32.0 mW cm^{-2} (green). (d) The relationship between charge carriers and voltage for the H_2Pc-C_{60} device obtained using the charge extraction method and a linear fit to the data. (e) Simulated $\eta_A\eta_D$ curves for three H_2Pc L_D values compared to the time integrated LED pump spectrum. (f) Comparison of the predicted number of charge carriers generated (for multiple values of the H_2Pc L_D) to the photovoltage-based measurement (horizontal line). The V_{OC} (in millivolts) that would be measured for the corresponding number of charge carriers is labeled for each bar.

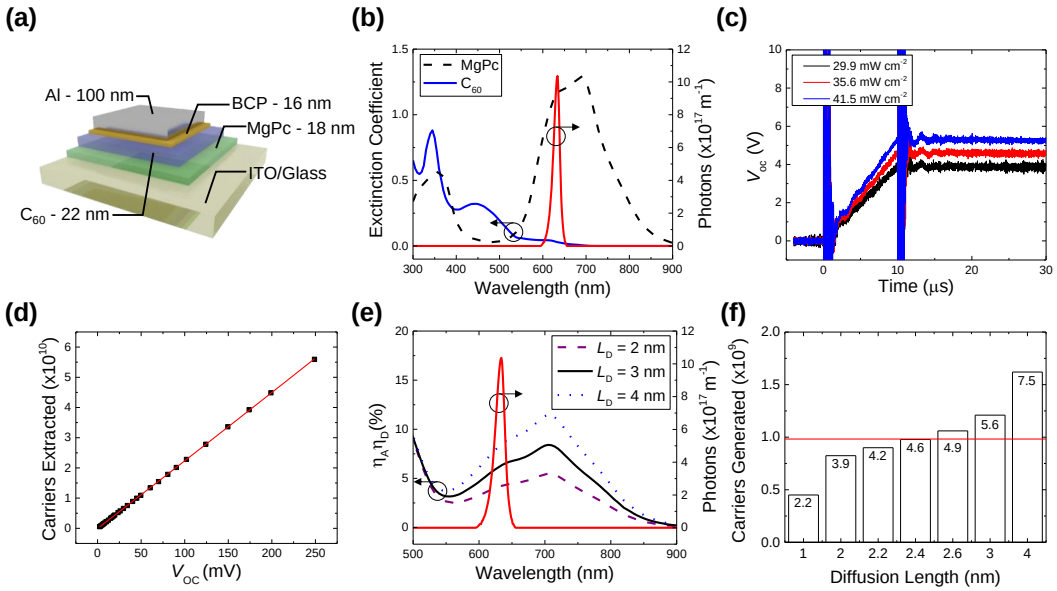

Figure 13.3 Measuring the L_D of MgPc: (a) Architecture for the planar heterojunction OPV based on the donor-acceptor pairing of magnesium phthalocyanine (MgPc)-C_{60}. (b) Comparison of the extinction coefficients for MgPc and C_{60} as well as the spectrum of the LED pulse (λ_{peak} = 625 nm) used to pump MgPc. (c) Three photovoltage rises recorded when pumping MgPc with the λ = 625 nm LED at intensities of 29.9 mW cm^{-2} (black), 35.6 mW cm^{-2} (red), 41.5 mW cm^{-2} (blue). (d) The relationship between charge carriers and voltage for the MgPc-C_{60} device obtained using the charge extraction method and a linear fit to the data. (e) Simulated $\eta_A\eta_D$ curves for three MgPc L_D values compared to the time integrated LED pump spectrum. (f) Comparison of the predicted number of charge carriers generated (for multiple values of the MgPc L_D) to the photovoltage-based measurement (horizontal line). The V_{OC} (in millivolts) that would be measured for the corresponding number of charge carriers is labeled for each bar.

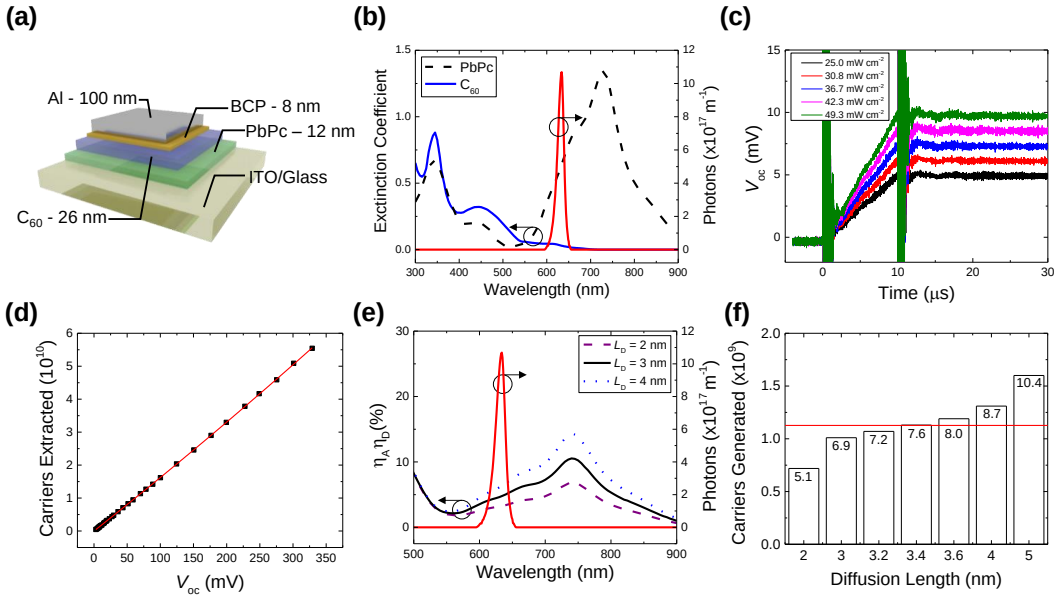

Figure 13.4: Measuring the L_D of PbPc: (a) Architecture for the planar heterojunction OPV based on the donor-acceptor pairing of lead phthalocyanine (PbPc) -C_{60}. (b) Comparison of the extinction coefficients for PbPc and C_{60} as well as the spectrum of the LED pulse (λ_{peak} = 625 nm) used to pump PbPc. (c) Five photovoltage rises recorded when pumping PbPc with the λ = 625 nm LED at intensities of 25.0 mW cm^{-2} (black), 30.8 mW cm^{-2} (red), 36.7 mW cm^{-2} (blue), 42.3 mW cm^{-2} (pink) and 49.3mW cm^{-2} (green). (d) The relationship between charge carriers and voltage in the PbPc-C_{60} device obtained using the charge extraction method and an exponential fit to the data. (e) Simulated $\eta_A\eta_D$ curves for three PbPc L_D values compared to the time integrated LED pump spectrum. (f) Comparison of the predicted number of charge carriers generated (for multiple values of the PbPc L_D) to the photovoltage-based measurement (horizontal line). The V_{OC} (in millivolts) that would be measured for the corresponding number of charge carriers is labeled for each bar.

E. Solving the diffusion equation with the centered finite difference approximation

In some cases it is necessary to use a numerical solution to the exciton diffusion equation in order to account for processes like Förster transfer to a quencher, exciton-polaron quenching, *etc*. One approach is to solve the exciton diffusion equation with the centered finite difference approximation. This is a numerical method which approximates derivatives as finite differences and transforms an ordinary differential equation into a set of algebraic equations on the form $\bar{\bar{A}}\bar{x} = \bar{b}$, where $\bar{x}$ and $\bar{b}$ are vectors and $\bar{\bar{A}}$ is a tridiagonal matrix. In this approach the domain, *x*, will be discretized into a set of *N* points ranging from x_1 to x_N and the exciton density, $n(x_i)$, will be approximated at each point.

The first step in this method is to approximate derivatives using a Taylor series expansion of $n(x)$ around an arbitrary point *x*, given by:

$$n(x) = n(x_i) + n'(x_i)(x - x_i) + \frac{1}{2}n''(x_i)(x - x_i)^2 + \cdots \tag{12.1}$$

Now, let $x = x_{i+1}$ and $\Delta x = x_{i+1} - x_i$. Then the first forward finite difference is given by:

$$n(x_{i+1}) = n(x_i) + n'(x_i)\Delta x + \frac{1}{2}n''(x_i)\Delta x^2 + \cdots \tag{12.2}$$

Rearranging Eqn. 12.2, we can approximate the derivative as:

$$n'(x_i) = \frac{n(x_{i+1}) - n(x_i)}{\Delta x} - \frac{1}{2}n''(x_i)\Delta x \tag{12.3}$$

Taking only first order terms, this can be simplified to:

$$n'(x_i) \cong \frac{n(x_{i+1}) - n(x_i)}{\Delta x} \tag{12.4}$$

Similarly, letting $x = x_{i-1}$ and $\Delta x = x_i - x_{i-1}$ the first backward finite difference is given by:

$$n(x_{i+1}) = n(x_i) + n'(x_i)(-\Delta x) + \frac{1}{2}n''(x_i)\Delta x^2 + \cdots \tag{12.5}$$

$$n'(x_i) = \frac{n(x_i) - n(x_{i-1})}{\Delta x} + \frac{1}{2}n''(x_i)\Delta x \tag{12.6}$$

$$n'(x_i) \cong \frac{n(x_i) - n(x_{i-1})}{\Delta x} \tag{12.7}$$

The centered finite difference approximation is then given by combining the first forward and first backward finite differences to approximate the first and second derivatives as:

$$(12.4) + (12.7) \rightarrow \; n'(x_i) \cong \frac{n(x_{i+1}) - n(x_{i-1})}{2\Delta x} \tag{12.8}$$

$$(12.3) - (12.6) \rightarrow \; n''(x) = \frac{n(x_{i+1}) - 2n(x_i) + n(x_{i-1})}{(\Delta x)^2} \tag{12.9}$$

Now Eqn. 12.9 can be used to transform the diffusion equation into a series of linear equations. Here, the exciton density and spatial position are discretized into a series of N points as $n \; \rightarrow \; n_1 \ldots n_N$ and $x \; \rightarrow \; x_1 \ldots x_N$ where x_1 is the left interface and x_N is the right interface of an arbitrary film. In the simplest form, the one-dimensional steady-state exciton diffusion equation is given by:

$$0 = D\frac{d^2n(x)}{dx^2} - \frac{n(x)}{\tau} + G(x) \rightarrow 0 = \frac{d^2n(x)}{dx^2} - \frac{n(x)}{{L_D}^2} + \frac{G(x)}{D} \tag{12.10}$$

Inserting Eqn. 12.9 into 12.10, at any point x_i, the diffusion equation can be approximated as:

$$0 = \frac{n_{i+1} - 2n_i + n_{i-1}}{(\Delta x)^2} - \frac{n_i}{{L_D}^2} + \frac{G_i}{D} \tag{12.11}$$

Rearranging this equation yields:

$$\frac{-(\Delta x)^2}{D} G_i = n_{i+1} - \left(\frac{(\Delta x)^2}{{L_D}^2} + 2\right) n_i + n_{i-1} \tag{12.12}$$

The entire domain can be expressed in matrix form using an N×N tridiagonal matrix as:

$$\begin{bmatrix} \frac{-(\Delta x)^2}{D} G_1 \\ \vdots \\ \frac{-(\Delta x)^2}{D} G_N \end{bmatrix} =$$

$$\begin{bmatrix} -\left(\frac{(\Delta x)^2}{{L_D}^2} + 2\right) & 1 & 0 & & \\ 1 & -\left(\frac{(\Delta x)^2}{{L_D}^2} + 2\right) & 1 & \emptyset & \\ 0 & 1 & -\left(\frac{(\Delta x)^2}{{L_D}^2} + 2\right) & 1 & \\ & \emptyset & & & \ddots \end{bmatrix} \begin{bmatrix} n_1 \\ \vdots \\ n_N \end{bmatrix} \tag{12.13}$$

Now we have a matrix in the form $\bar{\bar{A}}\bar{x} = \bar{b}$ which can be solved using the *linsolve* function in Matlab, for example. Next, quenching and reflecting boundary conditions can be applied by changing the first and last rows of this matrix. As an example, we will apply a reflecting boundary condition at the left interface and a quenching boundary condition at the right interface, as would be the case for exciton donor. However, this method can be used to determine quenching or reflecting boundary conditions at both interfaces. For a reflecting boundary condition, we can use Eqn. 12.8 to determine:

$$\frac{dn_1}{dx} = 0 = \frac{n_2 - n_0}{2\Delta x} \rightarrow n_2 = n_0 \tag{12.14}$$

Inserting this into Eqn. 12.12 yields:

$$\frac{-(\Delta x)^2}{D} G_1 = -\left(\frac{(\Delta x)^2}{{L_D}^2} + 2\right) n_1 + 2n_2 \tag{12.15}$$

Similarly, for a quenching boundary condition at the right interface, we want to enforce that:

$$n_N = 0 \tag{12.16}$$

Inserting Eqns. 12.15 and 12.16 into Eqn. 12.13, we now have a system of linear equations which can be solved to determine the exciton density from the diffusion equation as a

function of position, *x*, with a reflecting boundary condition on the left side and quenching boundary condition on the right side as:

$$\begin{bmatrix} \frac{-(\Delta x)^2}{D} G_1 \\ \vdots \\ \frac{-(\Delta x)^2}{D} G_{N-1} \\ 0 \end{bmatrix} =$$

$$\begin{bmatrix} -\left(\frac{(\Delta x)^2}{{L_D}^2}+2\right) & 2 & 0 & & \\ 1 & -\left(\frac{(\Delta x)^2}{{L_D}^2}+2\right) & 1 & & \emptyset \\ 0 & 1 & -\left(\frac{(\Delta x)^2}{{L_D}^2}+2\right) & 1 & \\ & \emptyset & & & \ddots \\ & & & 0 & 1 \end{bmatrix} \begin{bmatrix} n_1 \\ \vdots \\ n_N \end{bmatrix} \tag{12.17}$$

Note that in Eqn. 12.17, the first and last rows are changed from Eqn. 12.13. A similar approach can be used to modify Eqn. 12.13 for a left quenching boundary condition by switching and reversing the first and last rows. Using this approach, different boundary conditions and other quenching and generation terms can easily be incorporated into the diffusion equation without the need for complex analytical solutions for each variation.

F. Optical field simulation code

The following Matlab function uses a transfer matrix formalism to generate an electric field profile in a given multilayer stack. The primary inputs of this function are incident wavelength(s) of light, thickness of the active absorbing layers, complex indices of refraction, light polarization angle, and angle of incident illumination. The code then outputs vectors of optical field, and absorbed power to calculate the optical generation rate.

```
function
[alpha,q,xi,L,S,Scheck,Spr,Sprpr,Tj,Q,Q1,E,Intensity,Beta,DC,Refl] =
ElectricFieldGeneration(d,n,K,Ld,AM15,tau,x,epsilon,c,charge,plank,phi,
lambda)

for z = 1:size(lambda,1)
    %Cycles through layers and calculates constants for each layer
    Refl(z,1) = abs((1*cos(phi)-n(1,z)*sqrt(1-
(1*sin(phi)/n(1,z))^2))/(1*cos(phi)+n(1,z)*sqrt(1-
(1*sin(phi)/n(1,z))^2)))^2; %Reflection of Air/Glass Interface - S-
Polarized
    %Refl(z,1) = abs((1*sqrt(1-(1*sin(phi)/n(1,z))^2)-
n(1,z)*cos(phi))/(1*sqrt(1-(1*sin(phi)/n(1,z))^2)-n(1,z)*cos(phi)))^2;
%Reflection of Air/Glass Interface - P-Polarized
    for j =1:1:size(d,2)
        %Absporption Coefficient (1/m)
        alpha(z,j) = (4*pi*K(j,z))/lambda(z,1);

        %Optical Constants Relation
        q(z,j)=((n(j,z))^2-(n(1,z)^2)*(sin(phi)^2))^.5;

        % xi*dj is layer phase thickness corresponding to phase change
as wave goes through layer j
        xi(z,j) = (2*pi*q(z,j))/(lambda(z,1));

        %Layer Matrix describes propogation of wave through layer j
        L(:,:,j,z) = [exp(-1i*xi(z,j)*d(1,j)) 0; 0
exp(1i*xi(z,j)*d(1,j))];

        %Diffusion Coefficient
        DC(j) = (Ld(j)^2)/tau(j);

        %Beta = 1/Ld
        Beta(j) = 1/Ld(j);
    end

    %Calculates complex Fresnel Reflection and Transmission
Coefficients and Interface Matrix
    for j = 1:1:(size(d,2)-1)
        %S-Polarized Light
        rjk(z,j) = (q(z,j)-q(z,j+1))/(q(z,j)+q(z,j+1));
        tjk(z,j) = (2*q(z,j))/(q(z,j)+q(z,j+1));

        %P-Polarized Light
```

```
        %rjk(z,j) = (-
n(j+1,z)^2*q(z,j)+n(j,z)^2*q(z,j+1))/(n(j+1,z)^2*q(z,j)+n(j,z)^2*q(z,j+
1));
        %tjk(z,j) =
(2*n(j+1,z)*n(j,z)*q(z,j))/(n(j+1,z)^2*q(z,j)+n(j,z)^2*q(z,j+1));

        %Interface Matrix
        Ijk(:,:,j,z) = (1/tjk(z,j))*[1 rjk(z,j);rjk(z,j) 1];
    end

    %Calculates Total System Transfer/Scattering Matrix S(:,:,z)
    S(:,:,z) = [1 0;0 1];
    for j = 1:1:(size(d,2)-2)
        S(:,:,z) = S(:,:,z)*Ijk(:,:,j,z)*L(:,:,j+1,z);
    end
    S(:,:,z) = S(:,:,z)*Ijk(:,:,(size(d,2)-1),z);

    %Total Reflection and Transmission Coefficients (Assumes E- of
Substrate = 0)
    r(z) = S(2,1,z)/S(1,1,z); %Reflection Coefficient Eo-/Eo+
    t(z) = 1/S(1,1,z); %Transmission Coeffiecient E+substrate/Eo+

    %Partial System Transfer/Scattering Matrices
    for j = 2:1:(size(d,2)-1)
        Spr(:,:,j,z) = [1 0; 0 1]; %SjPrime in Patterson et al
        Sprpr(:,:,j,z) = [1 0; 0 1]; %SjPrimePrime in Patterson et al
        for v = 1:1:(j-2)
            Spr(:,:,j,z) = Spr(:,:,j,z)*Ijk(:,:,v,z)*L(:,:,v+1,z);
        end
        Spr(:,:,j,z) = Spr(:,:,j,z)*Ijk(:,:,j-1,z);
        for v = j:1:(size(d,2)-2)
            Sprpr(:,:,j,z) = Sprpr(:,:,j,z)*Ijk(:,:,v,z)*L(:,:,v+1,z);
        end
        Sprpr(:,:,j,z) = Sprpr(:,:,j,z)*Ijk(:,:,(size(d,2)-1),z);
        Scheck(:,:,j,z) = Spr(:,:,j,z)*L(:,:,j,z)*Sprpr(:,:,j,z);
    end

    %Partial Reflection and Transmission Coefficients of Partial System
Transfer Matrices
    for j = 1:1:(size(d,2)-1)
        rpr(j,z) = Spr(2,1,j,z)/Spr(1,1,j,z); % r prime
        tpr(j,z) = 1/Spr(1,1,j,z);
        rprpr(j,z) = Sprpr(2,1,j,z)/Sprpr(1,1,j,z); % r prime prime
        tprpr(j,z) = 1/Sprpr(1,1,j,z);
        tplus(j,z) = tpr(j,z)/(1-(-
Spr(1,2,j,z)/Spr(1,1,j,z))*rprpr(j,z)*exp(1i*2*xi(z,j)*d(1,j)));
%Internal Transfer Coefficient of wave in +x direction
        tminus(j,z) = tplus(j,z)*rprpr(j,z)*exp(1i*2*xi(z,j)*d(1,j));
%Internal Transfer Coefficient of wave in -x direction
        rho(j,z) = abs(rprpr(j,z));
        delta(j,z) = angle(rprpr(j,z));
        Tj(j,z) =
(real(n(j,z))/real(n(1,z)))*(tplus(j,z)*conj(tplus(j,z)));
    end

    %Creates x positions inside each layer
```

```
    NumberofSteps = 100;
    for j = 1:1:(size(d,2)-1)
        for l = 1:1:(NumberofSteps+1)

            %Electric Field Calculations
            Eo(z) = 1;
            E(j,z,l) =
tplus(j,z)*(exp(1i*xi(z,j)*x(j,l))+rprpr(j,z)*exp(1i*xi(z,j)*(2*d(1,j)-
x(j,l))))*Eo(z);
            E1(j,z,l) =
(tplus(j,z)*(exp(1i*xi(z,j)*x(j,l)))+tminus(j,z)*(exp(-
1i*xi(z,j)*x(j,l))))*Eo(z);

            %Time average absorbed power in layer j per second at
position x (W/m^3)
            Q(j,z,l) =
.5*c*epsilon*alpha(z,j)*real(n(j,z))*(E(j,z,l)*conj(E(j,z,l)));
            Q1(j,z,l) = alpha(z,j)*Tj(j,z)*AM15(z)*(1-Refl(z,1))*(exp(-
alpha(z,j)*x(j,l))+(rho(j,z)^2)*exp(-alpha(z,j)*(2*d(1,j)-
x(j,l)))+2*rho(j,z)*exp(-
alpha(z,j)*d(1,j))*cos(((4*pi*real(n(j,z)))/lambda(z,1))*(d(1,j)-
x(j,l))+delta(j,z)));
        end
    end
    Intensity = E.*conj(E);
end
```

G. Analytical solution to diffusion equation

The following Matlab code analytically solves the one-dimensional steady-state exciton diffusion equation with different quenching and reflecting boundary conditions. The inputs to this model are wavelength(s), layer thicknesses, complex indices of refraction, partial transfer matrices, boundary conditions, and diffusion coefficients. The function outputs the exciton density as a function of layer position and the photocurrent.

```
function
[ExcDen,ExcDenTot,Jphotod,Jphoto0]=AnalyticalModel(lambda,d,n,x,alpha,B
eta,Spr,Sprpr,Tj,AM15,BC,c,charge,plank,theta1,theta2,DC,Refl,GlassTran
s)

ExcDenTot = zeros(size(d,2)-1,101);

%Cyles through all wavelenghts
for z = 1:1:size(lambda,1)
    nu(z) = c/lambda(z,1); %Frequency of Light (1/s)
    Nflux(z) = AM15(z)*(1-Refl(z,1))*GlassTrans(z,1)/(plank*nu(z));
%Incident Photon Flux (1/m^2*s)
    %Cycles through layers and calculates constants for each layer
    for j = 1:1:(size(d,2)-1)
        rpr(j,z) = Spr(2,1,j,z)/Spr(1,1,j,z); % r prime
        tpr(j,z) = 1/Spr(1,1,j,z);
        rprpr(j,z) = Sprpr(2,1,j,z)/Sprpr(1,1,j,z); % r prime prime
        tprpr(j,z) = 1/Sprpr(1,1,j,z);
        rho(j,z) = abs(rprpr(j,z));
        delta(j,z) = angle(rprpr(j,z));
        gamma(j,z) = 4*pi*real(n(j,z))/lambda(z);
        C1(j,z) = (rho(j,z)^2)*exp(-2*alpha(z,j)*d(j));
        C2(j,z) = ((Beta(j)^2 -
alpha(z,j)^2)/(Beta(j)^2+(gamma(j,z)^2)))*2*rho(j,z)*exp(-
alpha(z,j)*d(j));

        %Boundary Conditions in each layer
        if BC(j) == 1
            Abc(j,z) = (-(alpha(z,j)*exp(Beta(j)*d(j))+Beta(j)*exp(-
alpha(z,j)*d(j)))+C1(j,z)*(alpha(z,j)*exp(Beta(j)*d(j))-
Beta(j)*exp(alpha(z,j)*d(j)))+C2(j,z)*(exp(Beta(j)*d(j))*gamma(j,z)*sin
(gamma(j,z)*d(j)+delta(j,z))-Beta(j)*cos(delta(j,z))))/(Beta(j)*(exp(-
Beta(j)*d(j))+exp(Beta(j)*d(j))));
            Bbc(j,z) = ((alpha(z,j)*exp(-Beta(j)*d(j))-Beta(j)*exp(-
alpha(z,j)*d(j)))-C1(j,z)*(alpha(z,j)*exp(-
Beta(j)*d(j))+Beta(j)*exp(alpha(z,j)*d(j)))-C2(j,z)*(exp(-
Beta(j)*d(j))*gamma(j,z)*sin(gamma(j,z)*d(j)+delta(j,z))+Beta(j)*cos(de
lta(j,z))))/(Beta(j)*(exp(-Beta(j)*d(j))+exp(Beta(j)*d(j))));
            %Photocurrent at x = d for each layer (A/m^2)
            Jphotod(j,z) =
((charge*theta1*theta2*alpha(z,j)*Tj(j,z)*Nflux(z))/(Beta(j)^2-
alpha(z,j)^2))*(Beta(j)*Abc(j,z)*exp(-Beta(j)*d(j))-
Beta(j)*Bbc(j,z)*exp(Beta(j)*d(j))+alpha(z,j)*exp(-alpha(z,j)*d(j))-
alpha(z,j)*C1(j,z)*exp(alpha(z,j)*d(j))-
gamma(j,z)*C2(j,z)*sin(delta(j,z)));
        elseif BC(j) == 2
```

```
            Abc(j,z) = ((-alpha(z,j)*exp(-alpha(z,j)*d(j))-
Beta(j)*exp(Beta(j)*d(j)))+C1(j,z)*(alpha(z,j)*exp(alpha(z,j)*d(j))-
Beta(j)*exp(Beta(j)*d(j)))+C2(j,z)*(-
Beta(j)*exp(Beta(j)*d(j))*cos(gamma(j,z)*d(j)+delta(j,z))+gamma(j,z)*si
n(delta(j,z))))/(Beta(j)*(exp(-Beta(j)*d(j))+exp(Beta(j)*d(j))));
            Bbc(j,z) = ((alpha(z,j)*exp(-alpha(z,j)*d(j))-Beta(j)*exp(-
Beta(j)*d(j)))-C1(j,z)*(alpha(z,j)*exp(alpha(z,j)*d(j))+Beta(j)*exp(-
Beta(j)*d(j)))-C2(j,z)*(Beta(j)*exp(-
Beta(j)*d(j))*cos(gamma(j,z)*d(j)+delta(j,z))+gamma(j,z)*sin(delta(j,z)
)))/(Beta(j)*(exp(-Beta(j)*d(j))+exp(Beta(j)*d(j))));
            %Photocurrent at x = 0 for each layer (A/m^2)
            Jphoto0(j,z) =
((charge*theta1*theta2*alpha(z,j)*Tj(j,z)*Nflux(z))/(Beta(j)^2-
alpha(z,j)^2))*(-Beta(j)*Abc(j,z)+Beta(j)*Bbc(j,z)-
alpha(z,j)+alpha(z,j)*C1(j,z)+gamma(j,z)*C2(j,z)*sin(gamma(j,z)*d(j)+de
lta(j,z)));
        else
            Abc(j,z) = 0;
            Bbc(j,z) = 0;
        end

        for l = 1:1:101
            %exciton density (1/m^3)
            ExcDen(j,z,l) =
((theta1*alpha(z,j)*Tj(j,z)*Nflux(z))/(DC(j)*(Beta(j)^2-
alpha(z,j)^2)))*(Abc(j,z)*exp(-
Beta(j)*x(j,l))+Bbc(j,z)*exp(Beta(j)*x(j,l))+exp(-
alpha(z,j)*x(j,l))+C1(j,z)*exp(alpha(z,j)*x(j,l))+C2(j,z)*cos(gamma(j,z
)*(d(j)-x(j,l))+delta(j,z)));
            %Sum of all exciton densitys over all wavelengths
            ExcDenTot(j,l) = ExcDenTot(j,l)+5*ExcDen(j,z,l);
            %ExcDenTot = 0;
        end
    end
end
stop = 1;
```

H. Numerical solution to the diffusion equation

The following Matlab code numerically solves the one-dimensional steady-state exciton diffusion equation with different quenching and reflecting boundary conditions. This code uses a centered finite difference approximation and allows for additional exciton loss mechanisms to easily be incorporated into the diffusion equation.

```
function [ExcDenNum,JphotoNum,ExcDenTot] =
NumericalModel(plank,nu,Q,Q1,DC,BC,lambda,x,d,Ld,charge,DonorLayer,Acce
ptorLayer)
ExcDenTot = zeros(size(d,2)-1,size(x,2));
for j = DonorLayer:AcceptorLayer
    %Numerically solves the Diffusion Equation to obtain the Exciton
    %Density using the Centered Finite Difference Approximation
    ExcitonDensityMatrix = zeros(size(x,2),size(x,2),size(lambda,1));
    for z = 1:1:size(lambda,1)
        deltax = d(1,j)/size(x,2); %Spacing of each step
        DiagonalElement = -(deltax^2/Ld(j)^2+2); %Diagonal Element of
Matrix A in Ax = b
        Diagonal = zeros(size(x,2),1);
        Diagonal(:,1) = DiagonalElement;
        ExcitonDensityMatrix(:,:,z) = diag(ones(size(x,2)-
1,1),1)+diag(ones(size(x,2)-1,1),-1)+diag(Diagonal); %Tri-Diagonal
Matrix A in Ax = b
        for l = 1:1:size(x,2)
            %b in Ax = b
            b(l,z) = -(deltax^2/DC(j))*(Q1(j,z,l)/(plank*nu(z)));
        end

        %Impose Boundary Conditions
        if BC(j) == 1 %Quenching Right Interface
            ExcitonDensityMatrix(1,2,z) = 2;
            ExcitonDensityMatrix(size(x,2),size(x,2),z) = 1;
            ExcitonDensityMatrix(size(x,2),size(x,2)-1,z) = 0;
            b(size(x,2),z)=0;
            ExcDenNum(j,z,:) =
linsolve(ExcitonDensityMatrix(:,:,z),b(:,z)); %Exiton Density in
Material as function of x in layer
            JphotoNum(j,z) =
DC(j)*charge*(ExcDenNum(j,z,size(ExcDenNum,3)-1)-
ExcDenNum(j,z,size(ExcDenNum,3)))/deltax; %Calculated
        elseif BC(j) == 2 %Quenching Left Interface
            ExcitonDensityMatrix(1,2,z) = 0;
            ExcitonDensityMatrix(1,1,z) = 1;
            ExcitonDensityMatrix(size(x,2),size(x,2)-1,z) = 2;
            b(1,z) = 0;
            ExcDenNum(j,z,:) =
linsolve(ExcitonDensityMatrix(:,:,z),b(:,z)); %Exiton Density in
Material as function of x in layer
            JphotoNum(j,z) = DC(j)*charge*(ExcDenNum(j,z,2)-
ExcDenNum(j,z,1))/deltax;
        end

        for l = 1:1:size(x,2)
```

```
            ExcDenTot(j,l) = ExcDenTot(j,l)+1E-9*ExcDenNum(j,z,l);
%Total (Integrated) Exciton Density summed over all wavelengths
        end
    end
end
```

I. Numerical solution to diffusion equation for singlet fission materials

The following Matlab code numerically solves the one-dimensional steady-state exciton diffusion equation incorporating singlet fission and singlet fission sensitization in Chapter 9. This code accounts for two excitons being generated for every absorbed photon in pentacene and also accounts for injection of excitons from P3HT into pentacene through long range Förster transfer.

```
function [ExcDenNum,JphotoNum,ExcDenTot] =
NumericalModelSFwithInjection(plank,nu,Q,Q1,DC,BC,lambda,x,d,Ld,charge,
DonorLayer,AcceptorLayer)
ExcDenTot = zeros(size(d,2)-1,size(x,2));
%Code solves diffusion equation with singlet fission and singlet
fission
%sensitization
R0 = 2.2*10^-9; %Forster Radius of Donor to Acceptor (m)2.17
RhoQue = 3.0283*10^27; % Molecular Density of Quenching Material (m)

for j = 3:5
    %Numerically solves the Diffusion Equation to obtain the Exciton
    %Density using the Centered Finite Difference Approximation
    %%{
    if j == DonorLayer %For singlet fission layer
        Q1(DonorLayer,:,:) = 2*Q1(DonorLayer,:,:);%Accounts for two
exctions being generated for every absorbed photon
    end
    %%}
    ExcitonDensityMatrix = zeros(size(x,2),size(x,2),size(lambda,1));
    for z = 1:1:size(lambda,1)
        %Impose Boundary Conditions
        if BC(j) == 1 %Quenching Right Interface
            deltax = d(1,j)/size(x,2); %Spacing of each step
            DiagonalElement = -(deltax^2/Ld(j)^2+2); %Diagonal Element
of Matrix A in Ax = b
            Diagonal = zeros(size(x,2),1);
            Diagonal(:,1) = DiagonalElement;
            ExcitonDensityMatrix(:,:,z) = diag(ones(size(x,2)-
1,1),1)+diag(ones(size(x,2)-1,1),-1)+diag(Diagonal); %Tri-Diagonal
Matrix A in Ax = b
            for l = 1:1:size(x,2)
                %b in Ax = b
                b(l,z) = -(deltax^2/DC(j))*(Q1(j,z,l)/(plank*nu(z)));
            end
            ExcitonDensityMatrix(1,2,z) = 2;
            ExcitonDensityMatrix(size(x,2),size(x,2),z) = 1;
            ExcitonDensityMatrix(size(x,2),size(x,2)-1,z) = 0;
            b(size(x,2),z)=0;
            ExcDenNum(j,z,:) =
linsolve(ExcitonDensityMatrix(:,:,z),b(:,z)); %Exiton Density in
Material as function of x in layer
            JphotoNum(j,z) =
DC(j)*charge*(ExcDenNum(j,z,size(ExcDenNum,3)-1)-
ExcDenNum(j,z,size(ExcDenNum,3)))/deltax; %Calculated
        elseif BC(j) == 2 %Quenching Left Interface
```

```
            deltax = d(1,j)/size(x,2); %Spacing of each step
            DiagonalElement = -(deltax^2/Ld(j)^2+2); %Diagonal Element
of Matrix A in Ax = b
            Diagonal = zeros(size(x,2),1);
            Diagonal(:,1) = DiagonalElement;
            ExcitonDensityMatrix(:,:,z) = diag(ones(size(x,2)-
1,1),1)+diag(ones(size(x,2)-1,1),-1)+diag(Diagonal); %Tri-Diagonal
Matrix A in Ax = b
            for l = 1:1:size(x,2)
                %b in Ax = b
                b(l,z) = -(deltax^2/DC(j))*(Q1(j,z,l)/(plank*nu(z)));
            end
            ExcitonDensityMatrix(1,2,z) = 0;
            ExcitonDensityMatrix(1,1,z) = 1;
            ExcitonDensityMatrix(size(x,2),size(x,2)-1,z) = 2;
            b(1,z) = 0;
            ExcDenNum(j,z,:) =
linsolve(ExcitonDensityMatrix(:,:,z),b(:,z)); %Exiton Density in
Material as function of x in layer
            JphotoNum(j,z) = DC(j)*charge*(ExcDenNum(j,z,2)-
ExcDenNum(j,z,1))/deltax;
        elseif BC(j) == 3 %Quenching Right Interface with Forster
transfer
            deltax = d(1,j)/size(x,2); %Spacing of each step
            Diagonal = zeros(size(x,2),1);
            for l = 1:1:size(x,2)
                %b in Ax = b
                b(l,z) = -(deltax^2/DC(j))*(Q1(j,z,l)/(plank*nu(z)));
                di(l) = d(1,j) - (l-1)*deltax - 0.5*deltax; %Distance
to the interface
                Kf(l) =
(RhoQue*pi*(R0^6))/(((Ld(j)^2)/(DC(j)))*6*(di(l)^3));
                DiagonalElement(l) = -
(deltax^2/Ld(j)^2+2+(Kf(l)*(deltax^2/DC(j)))); %Diagonal Element of
Matrix A in Ax = b
                Diagonal(l,1) = DiagonalElement(l);
            end
            ExcitonDensityMatrix(:,:,z) = diag(ones(size(x,2)-
1,1),1)+diag(ones(size(x,2)-1,1),-1)+diag(Diagonal(:,1)); %Tri-Diagonal
Matrix A in Ax = b
            ExcitonDensityMatrix(1,2,z) = 2;
            ExcitonDensityMatrix(size(x,2),size(x,2),z) = 1;
            ExcitonDensityMatrix(size(x,2),size(x,2)-1,z) = 0;
            b(size(x,2),z)=0;
            ExcDenNum(j,z,:) =
linsolve(ExcitonDensityMatrix(:,:,z),b(:,z)); %Exiton Density in
Material as function of x in layer
            JphotoNum(j,z) =
DC(j)*charge*(ExcDenNum(j,z,size(ExcDenNum,3)-1)-
ExcDenNum(j,z,size(ExcDenNum,3)))/deltax; %Calculated

            for l = 1:1:size(x,2)
                KfN(l,z) = Kf(l)*ExcDenNum(j,z,l)*deltax; %Forster rate
times exciton density in P3HT times step size for integration
            end
            TotalKf(z) = sum(KfN(:,z),1); %Integral of Forster rate
times excion density in P3HT
```

```
        elseif BC(j) == 4 %Quenching Right Interface with Injection
from P3HT
            deltax = d(1,j)/size(x,2); %Spacing of each step
            DiagonalElement = -(deltax^2/Ld(j)^2+2); %Diagonal Element
of Matrix A in Ax = b
            Diagonal = zeros(size(x,2),1);
            Diagonal(:,1) = DiagonalElement;
            ExcitonDensityMatrix(:,:,z) = diag(ones(size(x,2)-
1,1),1)+diag(ones(size(x,2)-1,1),-1)+diag(Diagonal); %Tri-Diagonal
Matrix A in Ax = b
            for l = 1:1:size(x,2)
                %b in Ax = b
                b(l,z) = -(deltax^2/DC(j))*(Q1(j,z,l)/(plank*nu(z)));
            end
            ExcitonDensityMatrix(1,2,z) = 2;
            ExcitonDensityMatrix(size(x,2),size(x,2),z) = 1;
            ExcitonDensityMatrix(size(x,2),size(x,2)-1,z) = 0;
            %b(1,z) = -
(deltax^2/DC(j))*((Q1(j,z,l)/(plank*nu(z)))+TotalKf(z));
            b(1,z) = -
(deltax^2/DC(j))*((Q1(j,z,l)/(plank*nu(z)))+2*TotalKf(z)/deltax);%Facto
r of 2 accounts for singlet fission sensitization
            b(size(x,2),z)=0;
            ExcDenNum(j,z,:) =
linsolve(ExcitonDensityMatrix(:,:,z),b(:,z)); %Exiton Density in
Material as function of x in layer
            JphotoNum(j,z) =
DC(j)*charge*(ExcDenNum(j,z,size(ExcDenNum,3)-1)-
ExcDenNum(j,z,size(ExcDenNum,3)))/deltax; %Calculated

        end

        for l = 1:1:size(x,2)
            ExcDenTot(j,l) = ExcDenTot(j,l)+1E-9*ExcDenNum(j,z,l);
%Total (Integrated) Exciton Density summed over all wavelengths
        end
    end
end
```

J. Transient photovoltage simulation

The following Matlab code numerically solves the one-dimensional transient exciton diffusion equation to simulate the normalized photovoltage transients in Chapter 10. This code inputs an exciton generation rate, calculated from a transfer matrix formalism, in $m^{-3}s^{-1}$, an excitation pulse pulse width, exciton diffusion length, and exciton lifetime and outputs a normalized photovoltage transient.

Main program:

```
format long;

clc;
clear;

clear L Ld tau Gen IC2 xlist
global L Ld tau Gen IC2 xlist

L = 1.3037E-8; %Film thickness in m
Ld = 5.7E-9; %Diffusion Length in m
tau = 16.1E-9; %Exciton Lifetime in s
m = 0; %Solving Diff. Eq in cartesian coordinates
tpulse = 1.8E-9; %Pulse Width in s

GenData = xlsread('GenerationData.xlsx');
VocData = xlsread('VocData.xlsx');

x = GenData(:,1); %x in layer of interest
xlist = x;
Gen = GenData(:,2); %Genration rate m-3 s-1
t = VocData(:,1); %Time steps from data s
ExpVoc = VocData(:,2); %Experimental normalized Voc Data



for i = 1:size(t,1)
    if t(i,1) == tpulse;
        pulseindex = i;
        break;
    end
end

tpulselist = t(1:pulseindex,1);
tlist = t(pulseindex:size(t,1),1);

sol = pdepe(m,@PDEFUN,@ICFUN,@BCFUN,x,tpulselist);
ExcitonDensity1 = transpose(sol(:,:,1)); %Exciton Density before the
pulse
IC2 = ExcitonDensity1(:,pulseindex); %Initial condition for after pulse
is turned off
%figure, plot(x,ExcitonDensity1(:,end));
%figure, plot(tpulselist,ExcitonDensity1(end,:));
```

```
sol2 = pdepe(m,@PDEFUN2,@ICFUN2,@BCFUN,x,tlist);
ExcitonDensity2 = transpose(sol2(:,:,1));
%figure, plot(x,ExcitonDensity2(:,end));
%figure, plot(tlist,ExcitonDensity2(end,:));

for j = 1:size(ExcitonDensity1,2)
    %Exciton Density Derivative at x = 0 DA Interface
    dndx1(j,1) = (ExcitonDensity1(2,j)-
ExcitonDensity1(1,j))/(tpulselist(2,1)-tpulselist(1,1));
end

for k = 1:size(ExcitonDensity2,2)
    %Exciton Density Derivative at x = 0 DA Interface
    dndx2(k,1) = (ExcitonDensity2(2,k)-
ExcitonDensity2(1,k))/(tlist(2,1)-tlist(1,1));
end

VocTot1 = trapz(tpulselist,dndx1); %Total Integrated Voc during pulse
VocTot2 = trapz(tlist,dndx2); %Total Integrated Voc after pulse

for l = 2:size(tpulselist,1)
    Voc1(l,1) = trapz(tpulselist(1:l,1),dndx1(1:l,1)); %Integrated Voc
at any time step during pulse
end

for m = 2:size(tlist,1)
    Voc2(m,1) = trapz(tlist(1:m,1),dndx2(1:m,1)); %Integrated Voc at
any time step after pulse
end

NormVoc1 = Voc1(:,1)./(VocTot1+VocTot2);
NormVoc2 = (VocTot1+Voc2(:,1))./(VocTot1+VocTot2);
NormVoc(:,1) = [NormVoc1;NormVoc2(2:end,1)];

%%%%%%%%%%%%%%%%%%%%%%%%%%%%%%%%%%%%%%%%%%%%%%%%%%%%%%%%%%%%%%%%%%%%%%%%%%%
%%%%
%Plotting
figure(1)

subplot(1,2,1)
plot(t,NormVoc,t,ExpVoc);
axis([0 t(end,1) 0 1.5])
xlabel('time (s)')
ylabel('Normalized Voc')
hold on

subplot(1,2,2)
semilogx(t,NormVoc,t,ExpVoc);
axis([0 t(end,1) 0 1.5])
xlabel('time (s)')
ylabel('Normalized Voc')
```

The following function sets the initial condition for $t < t_{pulse}$:

```
function n0 = ICFUN(x)
n0 = 0; %Initial Condition n(x,0) = 0
```

The following function sets the initial condition for $t > t_{pulse}$:

```
function n0 = ICFUN2(x)
global IC2 xlist

index = 0;

for i = 1:size(xlist,1) %Input x is a scalar cycling through all x's
need to find initial condition corresponding to each x
    if x == xlist(i,1)
        index = i;
        break;
    end
end

n0 = IC2(index,1); %Initial Condition n(x,0) = 0
```

The following function defines the transient diffusion equation for $t < t_{pulse}$, where optical generation is present:

```
function [c,f,s] = PDEFUN(x,tpulselist,n,DnDx) %Defines diffusion
equation so Matlab can read it
global L Ld tau Gen
c = 1;
f = (Ld^2/tau)*DnDx;
s = Gen - n/tau;
```

The following function defines the transient diffusion equation for $t > t_{pulse}$, where optical generation rate is zero:

```
function [c,f,s] = PDEFUN2(x,tlist,n,DnDx) %Defines diffusion equation
so Matlab can read it
global L Ld tau Gen
c = 1;
f = (Ld^2/tau)*DnDx;
s = - n/tau;
```

The following function defines the boundary conditions:

```
function [pl,ql,pr,qr] = BCFUN(xL,nL,xR,nR,T)
global L Ld tau


pl = nL;
ql = 0; %Sets neumann BC n(L,t) = 0 at x = 0
pr = 0;
qr = tau/Ld^2; %Sets dirichlet n'(0,t) = 0 at x = L
```

```
%{
pl = 0;
ql = tau/Ld^2; %Sets neumann BC n(L,t) = 0 at x = 0
pr = nR;
qr = 0; %Sets dirichlet n'(0,t) = 0 at x = L
%}
```